Imperial College London

OPTIMISATION OF POSTBUCKLING STIFFENED COMPOSITE STRUCTURES

Department of Aeronautics

Andrea Faggiani

Thesis submitted for the degree of Doctor of Philosophy

July 2008

Abstract

Composite materials are finding an ever increasing use in primary aerostructures so as to meet demanding performance targets while at the same time reducing environmental impact. This thesis presents an FE based optimization methodology which has been developed in order to optimise stiffened composite structures for damage resistance in postbuckling. A limitation of currently available optimization procedures is that they do not account for failure mechanisms that may occur before overall buckling collapse or in-plane structural failure. Such mechanisms are associated primarily with delamination and skin-stiffener debonding which may lead to rapid degradation in structural integrity and eventually collapse as observed experimentally. The optimization procedure developed seeks to address this problem by coupling out-of-pane failure modelling with the optimization process itself.

After a brief introduction to composite material and their history, a literature review is presented for postbuckling stiffened structures. The finite element (FE) modelling of postbuckling stiffened structures is then discussed, relating to how ABAQUS models are set up in order to trace stiffened composite panels' buckling and postbuckling responses. FE models for a hat-stiffened and an I-stiffened panel were developed and their predicted numerical buckling and postbuckling responses compared to previously conducted experimental investigations.

Focus then shifts to failure in composites and its modelling, in particular delamination failure. ABAQUS interface elements are presented and two stiffener runout models, representing two specimens previously tested experimentally, are then setup to illustrate how interface elements may be used to model mixed mode delamination A global-local submodelling approach is then presented which is able to model the debonding at the skin-stiffener interface for an I-stiffened panel.

The thesis then moves on to optimization of composite structures. This starts off with a literature review of existing optimization methodologies and then a genetic algorithm (GA) is devised to maximize the buckling load of a composite plate subject to a variety of biaxial loads, a problem previously treated in literature. The GA is then modified in order to be used for a much more complex problem; that of optimizing an I-stiffened panel for damage resistance in postbuckling subject to a variety of constraints.

Finally, conclusions are drawn and future work is discussed relating to how the presented FE based optimization methodology which is able to account for damage mechanisms may be extended and improved.

Acknowledgements

I am grateful to my parents Marco Faggiani and Giovanna Faggiani for giving me the opportunity to pursue the studies that I have, as well as for their great help and support in these years. This thesis is dedicated to them.

I am grateful for the friendly and supportive supervision provided by my supervisor, Prof. Brian Falzon, who has followed my work with great attention, and has helped its dissemination in publications and international conferences as well as a variety of social and formal meetings.

I would like to thank those members of the Imperial College Aeronautics department staff, as well as staff at institutions I have visited throughout my studies, for the many interesting discussions regarding my work which have helped me gain valuable insight so as to deepen my research.

A big thanks also goes to my colleagues George Sfantos, Paola Apruzzese, and Lucio Raimondo for their help and useful discussions relating to both the research topic and life in general. A final very special thanks goes to all my friends and the Imperial College Football Club who have made my time during my studies what it has been and have helped in providing me with the motivation that I required.

Contents

List of figures

List of tables

Chapter 1

Introduction

The objective of this chapter is to provide a brief introduction to composite materials. The concept of a matrix with a reinforcement is introduced, and then differences between low, medium, and high performance composites recognized. Carbon fibres are discussed, with details of their microstructure explained and their high specific properties identified. Attention then turns to matrix systems and prepreg composites, before discussing advantages a composite material may have over its metallic counterpart, such as higher specific properties, lower weight, and the greater potential for tailoring of properties in an optimization process. A brief history of composites is then given, from the use of fibrous reinforcement in ancient Egypt to the high-performance composites used in the current Airbus A380 and Boeing 787.

Having introduced composites, an explanation is given regarding the current design scenario relating to stiffened composite structures such as panels loaded in compression. The desire to move to a new design scenario, where a structure is allowed to operate deep in its postbuckling regime rather than limiting its use to its buckling load or at most initial postbuckling range, is discussed and its advantages highlighted. The problems and difficulties in allowing a structure to operate in its postbuckling regime are stressed, such as the phenomenon of mode-jumping which is visible in composite stiffened panels loaded in their postbuckling regime which may lead to failure mechanisms promoting the eventual collapse of the whole structure. The need to understand and be able to model such structures and their failure in a numerical fashion without having to revert to excessive and costly experimental testing is emphasized. Finally, the possibilities of engineering design optimization as applied to composite materials are introduced, prior to discussing the aims of this research effort and the layout of this thesis.

1.1 Definition of composite materials

1.1.1 The matrix and reinforcement

The simplest definition for a composite material is a material which consists of two or more distinct phases on a macroscopic scale, and the mechanical properties and performance of the composite material are designed to be superior to those of the individual phases themselves. Typically a composite consists of two components as shown in Figure 1.1; the "matrix" which is the continuous, less stiff, and weaker phase, and the "reinforcement" which is stiffer, stronger, and usually discontinuous. The properties of a composite material depend not only on the individual properties of the matrix and reinforcement, but also on their geometry and distribution, such as the volume fraction of the reinforcement. Currently composites have a wide range of uses, and in low to medium performance applications the reinforcement may provide some stiffening, but typically has a very small strengthening effect since it takes the form of short fibres or particles. In such composites it is the matrix that carries most of the load and largely governs the resultant composite material's mechanical properties. On the other hand, in high-performance structural composites it is the reinforcement – typically in the form of continuous fibres – that largely characterizes the material's stiffness and strength in the fibre direction. The matrix acts as a protector to the fibres, bonding them together and transferring local stresses amongst them. The matrix does however play a very important part in the failure mechanism, failure propagation, and fracture toughness of the composite material.

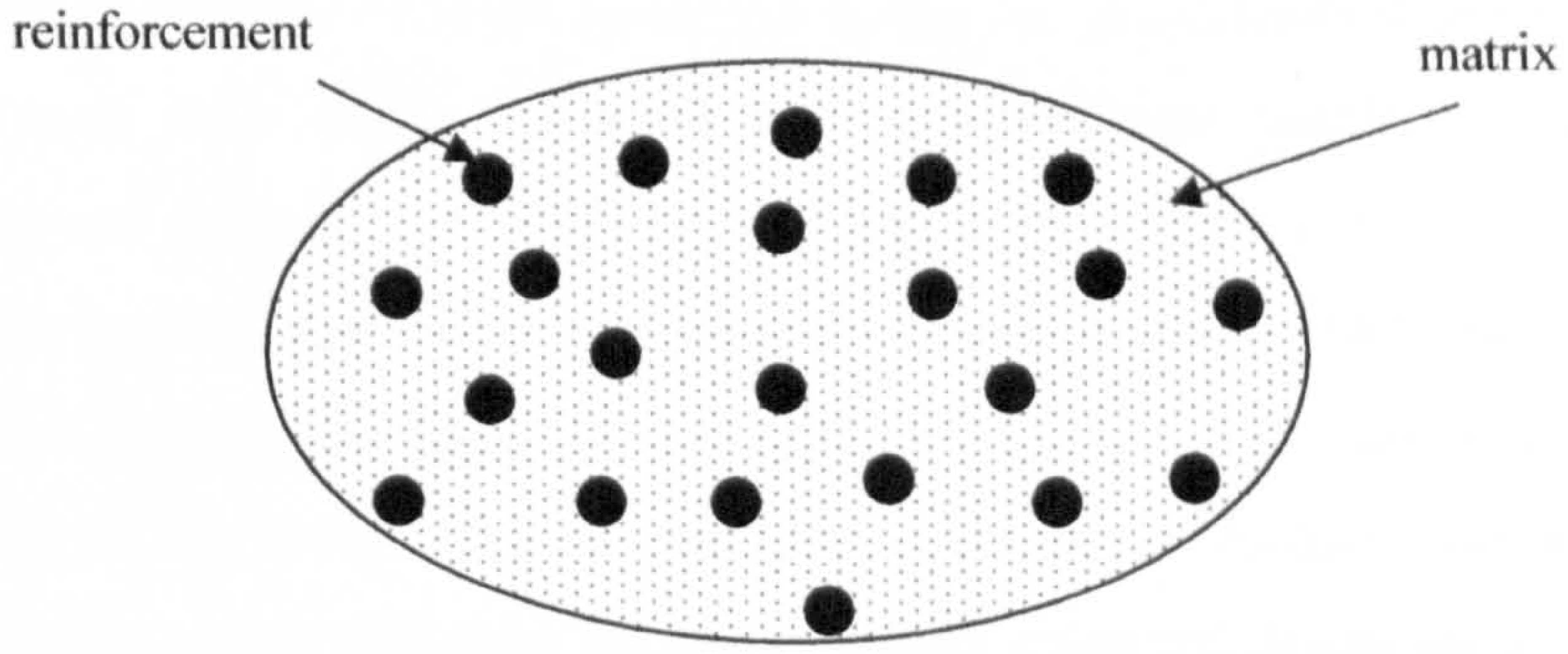

Figure 1.1: Composite material, with continuous matrix phase and discontinuous reinforcement.

1.1.2 Carbon fibre

High-performance composites have found an ever increasing use in the aerospace sector, largely due to the discovery of high-modulus and high-strength carbon fibres in the 1960s. Carbon fibres offer relatively high stiffness-to-weight and strength-to-weight ratios. The high stiffness and strength of carbon fibres, coupled with their low density have made carbon fibre second to just glass fibre in use. High-modulus, high-strength carbon fibres consist of small crystallites of "turbostratic" graphite, and are about 7 to 8 μm in diameter. In a single crystal of graphite the atoms are arranged in hexagonal arrays which are stacked on top of each other. The atoms in each layer are held together by very strong covalent bonds, while weak van der Waal forces exist between the layers, leading to highly anisotropic properties. To achieve a high modulus and strength, the layers of planes of graphite need to be aligned parallel to the axis of the fibre, but the crystalline units are very small and imperfectly aligned with defects. It is the manufacturing route and conditions which determine the degree of alignment and hence resulting properties of the carbon fibres. Needless to say, a trade-off exists in commercially available carbon fibres between their stiffness, strength, and cost.

Three main approaches exist for producing carbon fibres with the graphitic layers oriented in the desired parallel fibre direction [1,2]. The first is the orientation of a polymer precursor by stretching, where PAN (polyacrylonitrile) precursor is used and then heated and stretched to align the structure and remove the non-carbon material. The second is orientation by spinning which involves melt spinning of molten pitch to produce fibres. The third method is orientation during graphitisation, where at very high temperatures carburized fibres made from rayon, pitch or PAN are stretched during the graphitisation stage as the graphite layers slide over each other and further orient the layers parallel to the fibre axis. Graphitization can produce carbon fibres with tensile moduli over 410 GPa, although their tensile strength is somewhat reduced as a result of the process. In fact, each process has its own advantages and disadvantages according to performance, cost, ease of manufacture, and final properties of the fibres. Tensile strengths of carbon fibres can reach as high as 5500 MPa, and it is easy to see why their are attractiveness when comparing them to high strength steel displaying a Young's modulus of about 210 GPa and tensile strength of 1550 MPa.

1.1.3 Matrix systems

The properties of carbon fibres discussed only apply in pure tension, and hence a matrix must provide protection and support of the fibres, as well as transferring local stresses from one fibre to the other [2]. Four different kinds of matrices may be used in composites -

polymeric, metallic, ceramic, and carbon. Most typically a polymeric matrix is used, forming a Carbon Fibre Reinforced Plastic (CFRP). Of polymeric matrices, thermoset polymers are the predominant type, such as polyesters, epoxies, polyimides, and vinylesters. These undergo polymerization and cross-linking during curing with the aid of a hardening agent and heating. Epoxies are the most used out of the thermoset polymers, as they have better thermal and mechanical properties than polyesters. Lower-temperature curing epoxies are typically used in components which are expected to suffer only mild temperature variations in their service life, while higher-temperature curing epoxies are used for high-performance applications such as aircraft components.

1.1.4 Prepreg composites

By combining the matrix and reinforcement, a prepreg may be formed. This consists of a layer of parallel or woven fibres preimpregnated with partially cured resin. Prepregs can be made to a variety of specifications, such as fibre-volume ratio and ply thickness. These can then be laid up in layers at various orientations to yield a composite which has the desired material properties and yet presents a great weight saving when compared to the same aluminium or steel component. Figure 1.2 shows how a multidirectional laminate is formed by stacking up different layers of prepreg at various orientations.

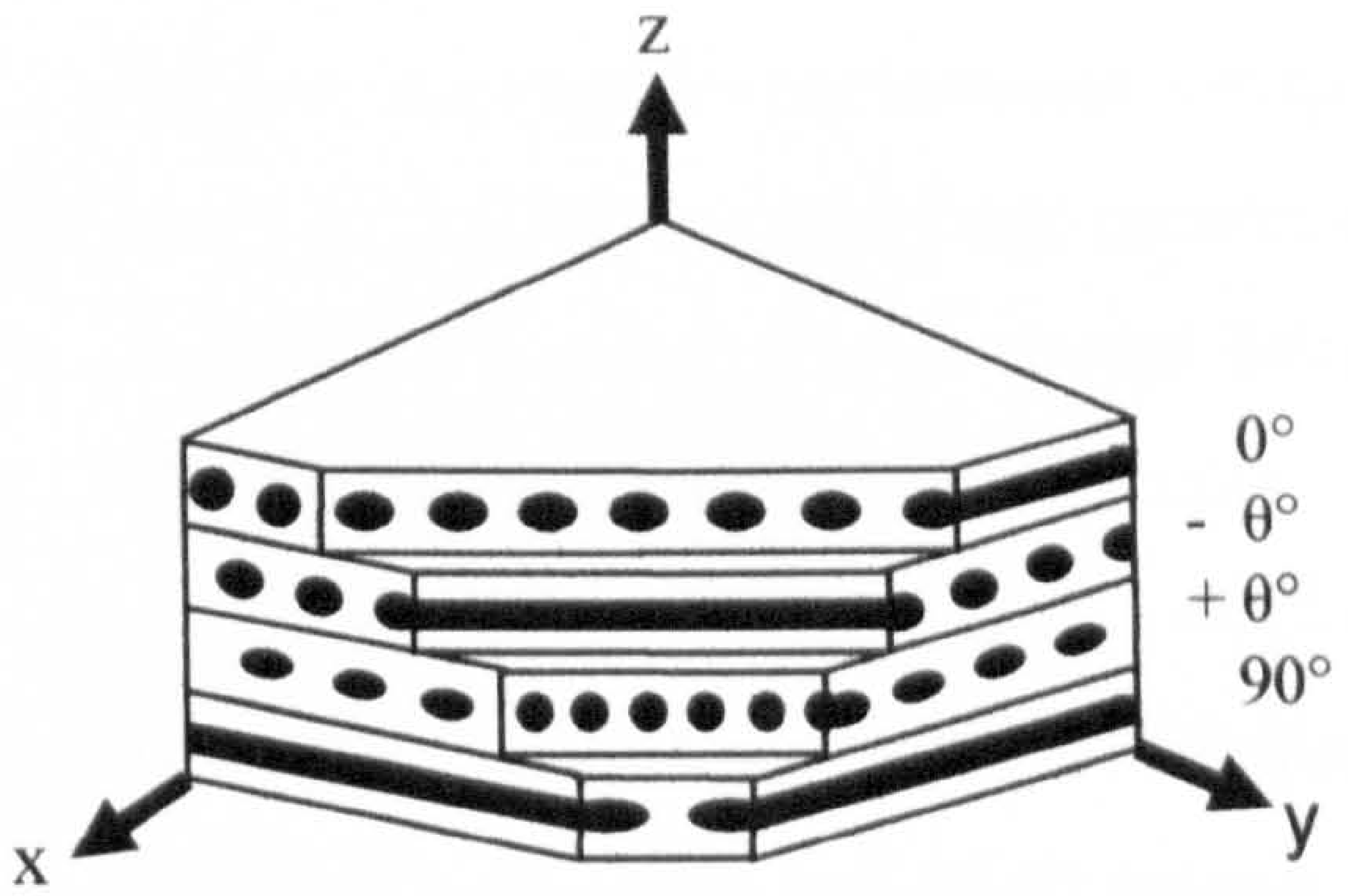

Figure 1.2: Multidirectional laminate composed of four prepreg layers at different orientations.

Weight savings are not the only advantage achievable by the use of composites. Compared to monolithic materials, composites have high strength, high stiffness, long fatigue life, low density, and can also be specifically tailored to suit the function of the structure they compromise. Additionally, they can operate in hostile environments for longer periods of time when compared to, for example, metals. They also offer a reduction in life cycle costs, lower tooling and maintenance costs, and reduced number of joints and parts. Their superior structural performance lies in their high specific strength and specific stiffness ratios (strength to density and stiffness to density ratios) as well as their anisotropic material characteristics. Composites allow the design of the material, manufacturing process, and design of the structure to be undertaken in one contemporaneous process. The design and optimization process for a composite component is much more complex and challenging than that of, for example, a metal component, due to the greater number of degrees of freedom and options available.

1.1.5 The history of composites

The idea of a fibrous reinforcement can be traced back in history to biblical references of straw-reinforced clay bricks in ancient Egypt. In the nineteenth century iron rods reinforced masonry, in much the same way that steel reinforces concrete today. The 1960s saw the introduction in composites of the first high-strength carbon fibres, followed by the use of advanced composites in aircraft structures [1]. Composites started being used in more and more applications in the 1970s, ranging from sporting goods, aircraft, and the maritime, automotive, and biomedical industries. At the present moment in time almost every aerospace company around the globe is developing products which make use of composite materials. After the "birth" of composites in the aerospace industry in the 1960s, when only demonstration specimens made out of composite materials were constructed, components made of composites started being manufactured as replacement components to their metal counterparts. Examples of this were the boron/epoxy fuselage section and horizontal tail on the General dynamics F-111. Eventually, parts of aircraft started being designed of CFRP originally. Examples include the horizontal stabilizer on the Grumman F-14, and the vertical and horizontal stabilizers on the McDonnell-Douglas F-15 [1,2]. On the commercial side of the aircraft industry, Airbus initially employed larger, more demanding primary composite structures with the single piece rudder for the A300 and A310 models, dating back to 1983. The use of composites was then extended to the entire tail plane. Fully composite horizontal stabilizers and elevators are now mainstream on the more recent A320, A330, and A340 models. About 20-22% of the most recent and biggest arrival in the Airbus family, the A380, is made of composites [3]. Naturally other aircraft manufacturers are following the composite route, such as Avions Transporte Regionale. The popular family of regional turboprops ATR 42 and ATR 72 both contain numerous composite structures, with the newer ATR 72 having a fully composite outer wing section and composites making up about 22% of the total aircraft weight. Boeing is also using increasing amounts of composite materials in their aircraft, with the 787 having large portions of its wings and fuselage made of composite material.

1.2 Composites in stiffened aircraft structures

1.2.1 Buckling, postbuckling, and mode-jumping

The next generation of aircraft will no doubt contain more and more composites as a weight percentage. Of particular interest is the use of composite materials in skin-stiffener type structures such as stiffened panels, which can be found in, for example, wing skins and fuselage sections and whose behaviour under high loading must be fully understood. An example of this is the requirement to fully understand the postbuckling behaviour of stiffened composite panels. This is important because, for instance, lower fuselage panels are primarily subject to compressive loads and are also vulnerable to the possibility of in-service damage due to runway debris or maintenance accidents, and accurate understanding of their buckling, postbuckling, and failure will allow the industry to be in an even better position to exploit the high strength and stiffness delivered by composites.

The importance of this research area is evident by the existence of the COCOMAT project, a major European research effort funded by the European Union for the years 2004-2007 and total costs estimated at 6.7 million euros. The project seeks to achieve a "fast and accurate simulation of the collapse load of stringer stiffened CFRP curved panels with taking degradation and cyclic loading into account, in addition to geometrical non-linearity" [4]. It also seeks to change the current design scenario, as shown in Figure 1.3. In the current design scenario, a stiffened panel is allowed to buckle and operate in the postbuckled state. However as can be seen by the position of the limit load, a very limited portion of the panel's postbuckling regime is exploited. In fact for primary composite aerostructures no buckling may be even allowed. For metallic structures, postbuckling is exploited to a much larger extent, with structures operating in the postbuckling regime. Hence, postbuckling needs to be exploited in composite structures too, as weight savings of around ten percent can be gained by operating deep in the postbuckling regime.

The design of current primary composite aerostructures, such as a stiffened composite panel, tends to be conservative due to the susceptibility of the relatively weak skin-stiffener interface. This weakness is due to through-thickness stresses which are exacerbated by deformations due to buckling. Figure 1.3 shows how the future design scenario has the limited load shifted much higher, so that more of the postbuckling regime is exploited. The onset of degradation is now below the ultimate load, and the latter is very close to the collapse load of the structure. In the current design scenario this is not the case, as the ultimate load is well below collapse as well as onset of degradation.

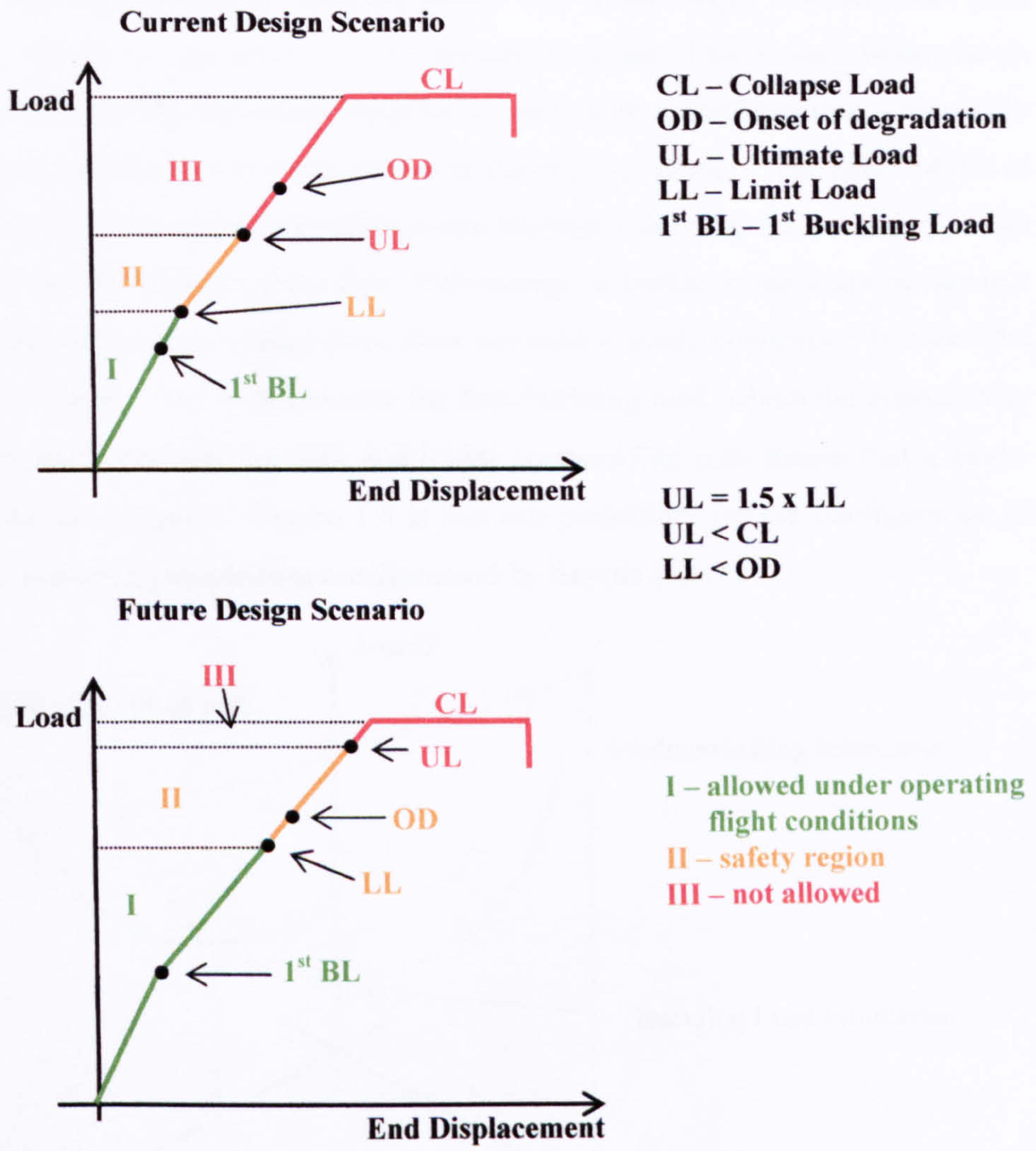

Figure 1.3: COCOMAT aim to change current design scenario - [4].

Closely related to postbuckling is the phenomenon of mode-jumping and how it renders postbuckling behaviour very difficult to predict. When a stiffened panel buckles, it does so in a certain configuration. As the loading of the panel is increased, then mode-jumps may occur, where the panel either gradually or suddenly changes configuration. When a panel buckles, the load-displacement path becomes unstable and hence it "switches" to a stable secondary path. When a mode jump occurs, this secondary path is now itself unstable, and a tertiary stable path is followed as a dynamic change to a higher mode shape occurs. Mode-jumping may release enough energy for damage to occur, in the form of micro-cracking or delamination, and hence its prediction via numerical simulation is of paramount importance.

Figure 1.4 illustrates the phenomenon of mode-jumping graphically. Shown are the equilibrium paths of a simple plate subject to compression, but the concept is easily extended to a stiffened panel. At the buckling load a bifurcation exists where the plate will buckle in either direction. In reality the direction of buckling will depend on imperfections. The plate will buckle into a buckle shape with *n* half-waves as the *n*-mode-shape is stable. As the loading is increased, a point will be reached where this is no longer true and this path becomes unstable, shown by the solid red line becoming dotted. This occurs when the n-mode-shape path intersects the secondary equilibrium path with a configuration – shown in dotted blue – combining the n and m-mode-shapes in the (w_n, w_m) plane. The result of this is the change of the system to a secondary stable m-mode-shape following the secondary stable equilibrium path shown by the solid green line. This change in buckle mode shape occurs in a sudden fashion – the mode-jump – since there does not exist a stable connection between the n and m equilibrium paths. This is different to the first buckling load, where the connectivity between the initial stable prebuckling path and initial postbuckling path means that a mode-jump does not occur at this point. Figure 1.4 is just one possibility for the configuration of equilibrium paths, and other possibilities are discussed by Supple [5,6,7].

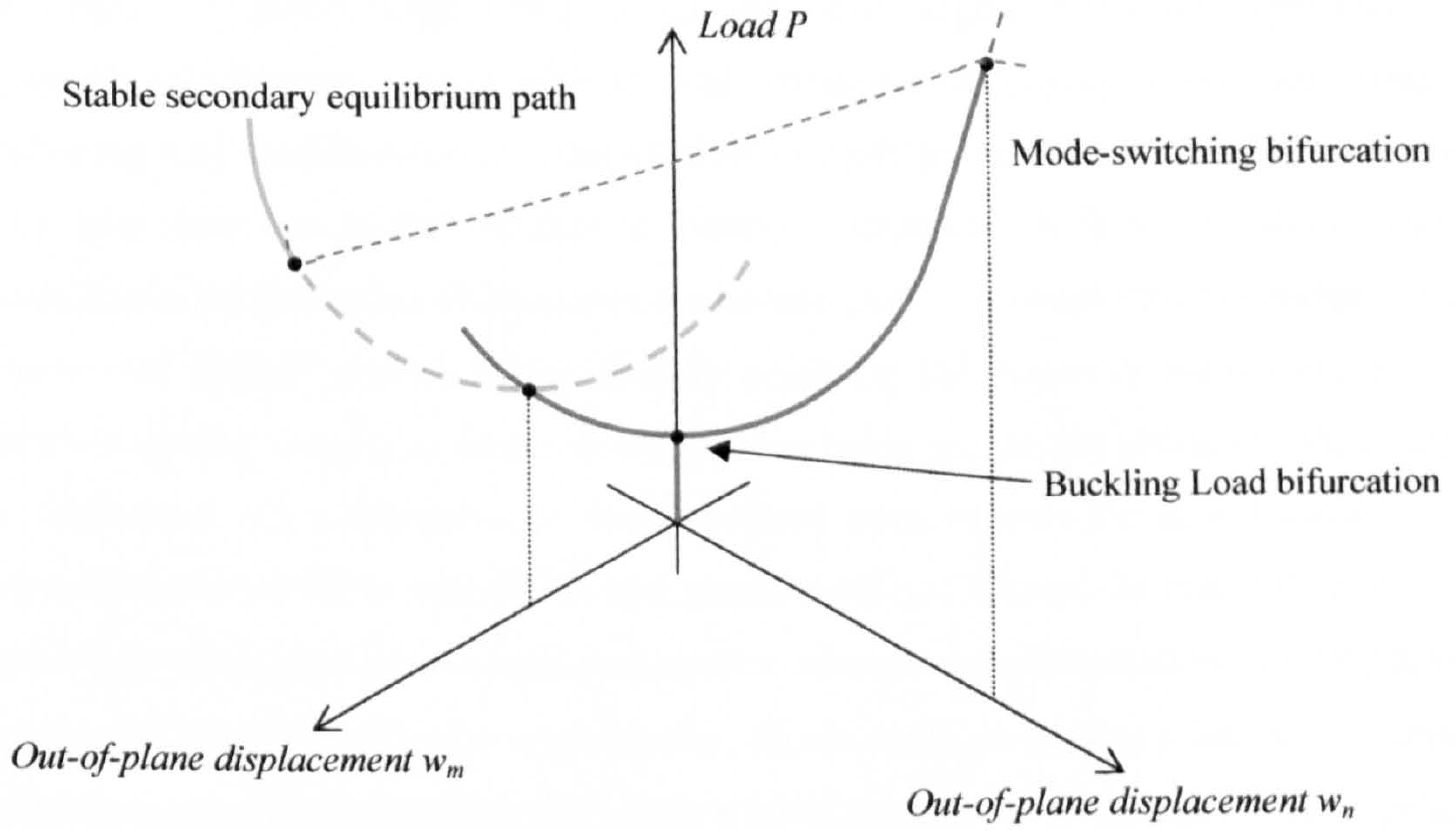

Figure 1.4: Equilibrium paths showing mode-jumping behaviour of a plate under compression.

1.2.2 Failure and its modelling

Once a designer is able to predict a composite structure's postbuckling behaviour in an efficient and accurate manner, then the next step is to try and exploit the structure's postbuckling regime which requires knowledge of its failure characteristics. As mentioned earlier, mode-jumping has been experimentally observed to be closely related to the failure characteristics of composite structures such as stiffened panels. Hence it is imperative for numerical models to be able to predict the failure characteristics of such a panel, in order for the future design scenario of Figure 1.3 to be adopted. Experimental work relating to compression testing indicates that failure occurs predominantly at the skin-stiffener interface in stiffened composite panels in the form of delamination due to the interface being susceptible to through the thickness shear stresses [8]. To model this phenomenon two general approaches exist. The first is the Virtual Crack Closure Technique (VCCT) [9,10], and the second is the use of interface elements [11]. Both methods are widely available in many finite element (FE) packages such as ABAQUS, MSC NASTRAN, and NASTRAN.

1.2.3 Optimization applied to composites

When designing a structure in general, the performance of the structure is usually based on its strength or stiffness, where several specific performance parameters need to be met. Typically the amount of "resources" used are sought to be a minimum, measured in cost or weight. Typically engineering design has been largely based on experience, where essential requirements are identified and structures satisfying these are considered. Following this, modifications to reduce weight or costs are undertaken, but these often take a very long time due to the number of iterations required. It is at this stage where the mathematical optimization of structures comes into play. It transforms the design procedure into a well defined process where designs satisfying the necessary parameters as well as minimizing cost, weight, or whatever objective is being sought, are obtained. Variables such as thicknesses, ply orientations, or cross-sectional areas become the design variables which are optimised in order to achieve the best possible design. Composite materials have added a whole new dimension to structural optimization since as was discussed earlier they allow the designer to tailor their material properties by, for example, composing a laminate by laying up prepreg in specific orientations. This adds a lot of complexity to the optimization process as the number of design variables is greatly increased, since not only structural dimensions but also the properties of the material are optimised for. However, it does offer a much greater scope for even further weight and cost savings, as well as performance improvements over metallic structures in addition to the inherent advantages of composites due to their superior specific properties. The design and optimization of composite structures is extremely challenging, since many of the properties of composites as well as their behaviour, particularly relating to failure initiation and propagation, are still relatively unfamiliar. This highlights the continued need for the development of methodologies and design tools in order to optimise composite structures so as to achieve ever increasing performance gains.

1.3 Research objectives and methodology

1.3.1 Objectives

The aim of the present work is to develop a robust finite element (FE) based optimization methodology for composite structures which is able to account for failure mechanisms which may occur prior to overall buckling collapse. This involves three major aspects. The first is the accurate modelling of the composite structure that is to be optimised. This is done via FE models of various existing structures and the results obtained are validated against experimental tests of the structures themselves. The second aspect is modelling of failure, focusing on delamination at skin-stiffener interfaces. The interface element is introduced, together with its formulation, and then used in modelling the various composite structures considered. Failure characteristics predicted by the model are compared to those observed experimentally. The third aspect is the actual optimization procedure. This can only be applied once the models created for the composite structures have been deemed accurate. The optimization procedure takes the form of a genetic algorithm (GA) which mimics Darwin's theory of evolution in order to find an optimised design. The concepts of GAs are introduced, and then the fashion in which a GA is directly linked to the FE models previously created in order to run the optimization is discussed in detail.

1.3.2 Thesis outline

The thesis is structured in three major sections, each relating to one of the three aspects mentioned in the objectives of the current research effort. After the introduction to composite materials and their use in Chapter 1, Chapter 2 gives a literature review on the experimental testing of stiffened composite structures and the numerical techniques used to model their buckling and postbuckling behaviour. Before discussing composites, Stein's aluminium plate is discussed as historically this is considered as the "pioneer" for all work relating to buckling, postbuckling, and secondary instabilities associated with mode-jumping. Other research on aluminium plates is presented before moving to the buckling and postbuckling of stiffened composite panels. Various panels tested in compression are discussed, with their buckling and postbuckling behaviour analyzed. Numerical models are then introduced, starting with analytical solutions to plate buckling, and moving to detailed FE models.

FE models of various structures are discussed in the thesis, and hence a theoretical background of the analysis techniques used in the FE package ABAQUS are given in Chapter 3. A theoretical foundation to the non-linear algorithms used in FE analysis is given. This includes the standard incremental algorithm and how an iterative procedure may be added so as to provide an accurate solution. This forms the basis of the Newton-Raphson method and its various modifications. Limitations of the latter method are mentioned relating to its convergence difficulties when trying to deal with limit points, and in particular secondary instabilities, such as mode-jumping, when modelling the postbuckling behaviour of stiffened composite panels. To overcome this, the Riks algorithm is discussed followed by the energy dissipation scheme available in ABAQUS.

Having discussed the non-linear solution schemes, these are applied to two FE models of stiffened composite panels to capture their buckling and postbuckling behaviour. The first model corresponds to a hat-stiffened panel, whilst the second to an I-stiffened panel. The FE models created contain conventional shell elements to allow for a computationally efficient solution, the importance of which is highlighted later. Numerical results pertaining to the buckle mode shapes of the panel as well as strains and out-of-plane displacements are compared to those obtained experimentally.

The inability of the FE models of Chapter 4 to capture any form of failure mechanisms in the panel is emphasized in Chapter 5 by the discussion of how composite stiffened panels tested experimentally in various investigations showed out-of-plane damage mechanisms such as skin-stiffener debonding which acted as precursors to final structural collapse. The importance of adding a modelling capability in FE for these damage mechanisms is discussed, before a brief introduction to the basic concepts of fracture mechanics is given. This allows for the introduction of the two main modelling options for out-of-plane damage mechanisms, VCCT and interface elements. The concepts behind VCCT and its implementation into an FE code are mentioned, before discussing the benefits of using interface elements and giving their full formulation for use in the FE package ABAQUS.

Chapter 6 shows how interface elements can be implemented to model the failure characteristics of two stiffener runout specimens tested experimentally. It is shown how an FE model representing the specimens can be created using the continuum shell elements available in ABAQUS and modelling the skin-stiffener interface with interface elements. The ability of the models to capture the failure characteristics is discussed with emphasis on the difference in failure modes of the two specimens. Numerical strain results are also compared to strain gauge readings placed on the experimentally tested runout specimens.

Chapter 7 revisits the I-stiffened panel whose buckling and postbuckling behaviour was modelled in Chapter 4, but this time the objective is to use interface elements to capture the skin-stiffener debonding that can occur in the structure and lead to collapse. A global-local modelling approach is implemented in ABAQUS where the solution to a global model drives a local, more detailed model. For the I-stiffened panel the global model corresponds to the conventional shell model of Chapter 4, whilst the local model is a representative section of the panel with the skin and stiffener modelled using solid elements and interface elements placed in between the two. It is shown how this shell-to-solid submodelling approach is extremely efficient and able to capture the skin-stiffener debonding in the I-stiffened panel.

Chapter 8 introduces the main concepts behind mathematical optimization relating to linear and nonlinear programming. A literature review is conducted of existing optimization work dealing with composite structures before introducing GAs and their suitability to nonlinear integer programming problems. Previous work where GAs have been applied to composite structure optimization is also reviewed. This paves the way for Chapter 9 where a GA is constructed for the buckling load maximization of a composite plate. The aim of this is to validate the GA code for an optimization problem which has been treated previously in literature. It also acts as a benchmark for the linking of the GA code to the FE package ABAQUS responsible for the function evaluation.

Having validated the GA and its linking to ABAQUS, it was used in the optimization of the I-stiffened panel first seen in Chapter 4 so as to increase its damage resistance in postbuckling. Chapter 10 discusses how this was done by introducing how the optimization problem was formulated and then discussing how the various FE models presented in the previous chapters were linked together in an autonomous fashion so as to optimise the stacking sequence of various parts of the I-stiffened panel to minimize the level of debonding at its skin-stiffener interface when it is loaded deep into its postbuckling regime.

Chapter 11 concludes the thesis emphasizing how all the various aspects relating to FE modelling of the buckling and postbuckling behaviour of composite structures, modelling of their failure mechanisms, and application of a genetic optimization achieved the goal of successfully constructing an FE based optimization procedure for composite structures that takes into account out-of-plane damage mechanisms which may occur prior to overall bucking collapse. Having done this, various areas of future work are discussed particularly relating to how the optimization procedure could be improved as well as how it may be applied to different problems involving different optimization goals and design variables.

Chapter 2

Postbuckling stiffened composite structures – a literature review

This chapter gives a literature review focused on experimental investigations which have been undertaken in order to assess the buckling and postbuckling behaviour of stiffened composite structures and the numerical methods developed to try and model this behaviour. Tests on buckling and postbuckling, with its associated mode-jumping can be dated back to the 1950's with the work conducted by Stein on an aluminium plate. Stein's work formed the basis for future investigations, and in the 1970's research on this buckling and postbuckling behaviour was extended to plate structures made of advanced composite materials. Stiffened composite panels were then considered, where panels composed of a skin stiffened by longitudinal stiffeners either co-cured or adhesively bonded onto the skin were tested, typically but not uniquely, in uniaxial compression. Such tests involved loading the panels and observing their structural behaviour before, during, and after buckling. Experimental results showed the same fundamental principles as were first observed by Stein in the aluminium plate, namely that of sudden mode-jumps in the buckle configuration of the structure as the compressive loading is increased past the buckling load. Experimental works on plate structures were often coupled with analytical models to capture the postbuckling behaviour of the plates. Such accurate analytical analyses are not possible on the case of stiffened composite panels, and hence the current philosophy is to construct FE models of the panels tested to try and capture their behaviour. With the increase in computational resources in modern times, such models have become more and more detailed.

This chapter is divided into two sections, the first dealing with a selection of experimental work ranging from buckling of simple plates to full compression tests until collapse of stiffened composite panels. In the second section, the numerical work related to these experiments is described. This includes the analytical solutions proposed for the buckling and postbuckling of plates, FE models of the stiffened composite panels, and more recent modified non-linear solution procedures which combine quasi-static and dynamic solution strategies to better capture the dynamic mode-jumps which occur in the postbuckling regime of stiffened composite panels.

2.1 Experimental tests

2.1.1 Stein's aluminium plate

One of the first research efforts dealing with secondary instabilities associated with mode-jumping was the work conducted by Stein [12]. Stein derived a linear set of equations to replace the non-linear large deflection equations for plates. Theoretical results were compared to experimental data from a test conducted on an aluminium plate. The plate was supported by a multiple-bay fixture so as to replicate the theoretical boundary conditions of simply supported straight edges free of in-plane shear, and had dimensions of 52.32 in. by 25.36 in. with thickness 0.072 in.. Lateral support was provided by knife edges in a fixture forming eleven panels of dimension 4.71 x 25.36 inches. A hydraulic testing machine was used for the compression applying load through the use of a hydraulic ram. Testing of the plate revealed a buckle pattern of a five half-wave configuration, soon followed by mode-jumps to different configurations. These changes in the buckled mode-shape "occurred in a violent manner and were observed to go from 5 to 6 to 7 to 8 buckles".

2.1.2 Experimental testing of aluminium plates

Stein's work on the mode-jumping observed in metallic plates was later extended to composite structures. Initially many researchers focused on analytical solutions to classical un-stiffened orthotropic plate problems. Harris [13] considered the buckling behaviour of rectangular, simply supported, orthotropic, composite plates subject to biaxial loads. Similarly, Banks [14] investigated the buckling and post-buckling behaviour of orthotropic plates under in-plane loading with simple supports at the loaded ends and elastically restrained boundary conditions on the unloaded edges. Postbuckling test results for un-stiffened graphite-epoxy plates loaded in compression were also compared with analytical predictions by Starnes [15] who additionally discussed their failure characteristics and the effect of low-speed impact damage on their behaviour in postbuckling. Plates with a cut-out have also been considered, due to the necessity of such cutouts to exist on specific components for practical reasons such as in wing spars and cover panels to provide access for hydraulic lines and maintenance in aircraft. Nemeth [16] compiled an extensive review of work conducted since the early 1970's dealing with the effects of cutouts on the postbuckling behaviour of composite rectangular plates. Effects such as cut-out size, eccentricity, shape, orientation, plate orthotropy or anisotropy, loading and boundary conditions, and plate aspect and slenderness ratio were discussed.

2.1.3 Buckling and postbuckling of stiffened composite panels

A lot of research has also focused on the buckling and postbuckling characteristics of stiffened composite panels. Much of these works bear their fruits in the understanding obtained for the buckling and postbuckling characteristics of plates as pioneered by Stein. Starnes Jr. et al. [17] conducted an experimental investigation in which they studied the postbuckling behaviour of sixteen different graphite-epoxy panels loaded in compression. Skin thickness, stiffener spacing, and stiffener cap thickness were varied to determine both the effect of skin postbuckling response and lighter stiffeners on the performance of the panel. Eight specimens were undamaged, while the remaining eight were damaged prior to testing to assess the effect of impact on their performance. All of the undamaged panels buckled into a configuration consisting of one half-wave across the width of each skin-bay, and either four or five half-waves across the skin-bay length. Some of the specimens were able to sustain more than three times their initial buckling load before failure. This highlights the importance of understanding the behaviour of such panels in their postbuckling regime so as to exploit their ability to carry load well past buckling.

Romeo [18] tested hat and blade-stiffened graphite/epoxy panels in uniaxial compression as well as wing-box beams under pure bending. Results were compared to a variety of theoretical methods based on wide column and simply supported plate theory, orthotropic buckling equations, and torsional instability theory. After the experimental tests, Romeo highlighted how "in some cases, the structures tested showed a remarkable postbuckled strength", reinforcing observations made by Starnes Jr. et al. relating to the load carrying ability of such composite stiffened panels beyond local buckling.

More recent work dealing with the experimental testing of stiffened composite panels includes that of Falzon et al. [19] who tested two blade stiffened composite panel in uniaxial compression. The panels were made from T800/924C unidirectional prepreg and contained four stiffeners secondary bonded onto the skin using a film adhesive. The panels were tested in uniaxial compression to collapse to investigate their buckling and postbuckling behaviour. Both panels buckled into the four half-wave shape visible in the experimental Moiré fringe patterns in Figure 2.1 (a). Buckle patterns developed earlier in the central skin-bay due to the fact that the central stiffeners had double the spacing of the edge stiffeners. Buckling occurred at 110 kN for the first panel and 105 kN for the second panel. This was confirmed by out-of-plane displacements measured by Linear Voltage Differential Transducers (LVDTs) and back-to-back stain gauge readings. The second panel exhibited a mode-jump to the five half-wave configuration shown in Figure 2.1 (b) at a loading of 570 kN. Evidence of this mode-jump was found in strain reversals and sudden changes in out-of-plane displacements as the location of buckle crests changed on the panel as a result of the mode-jump.

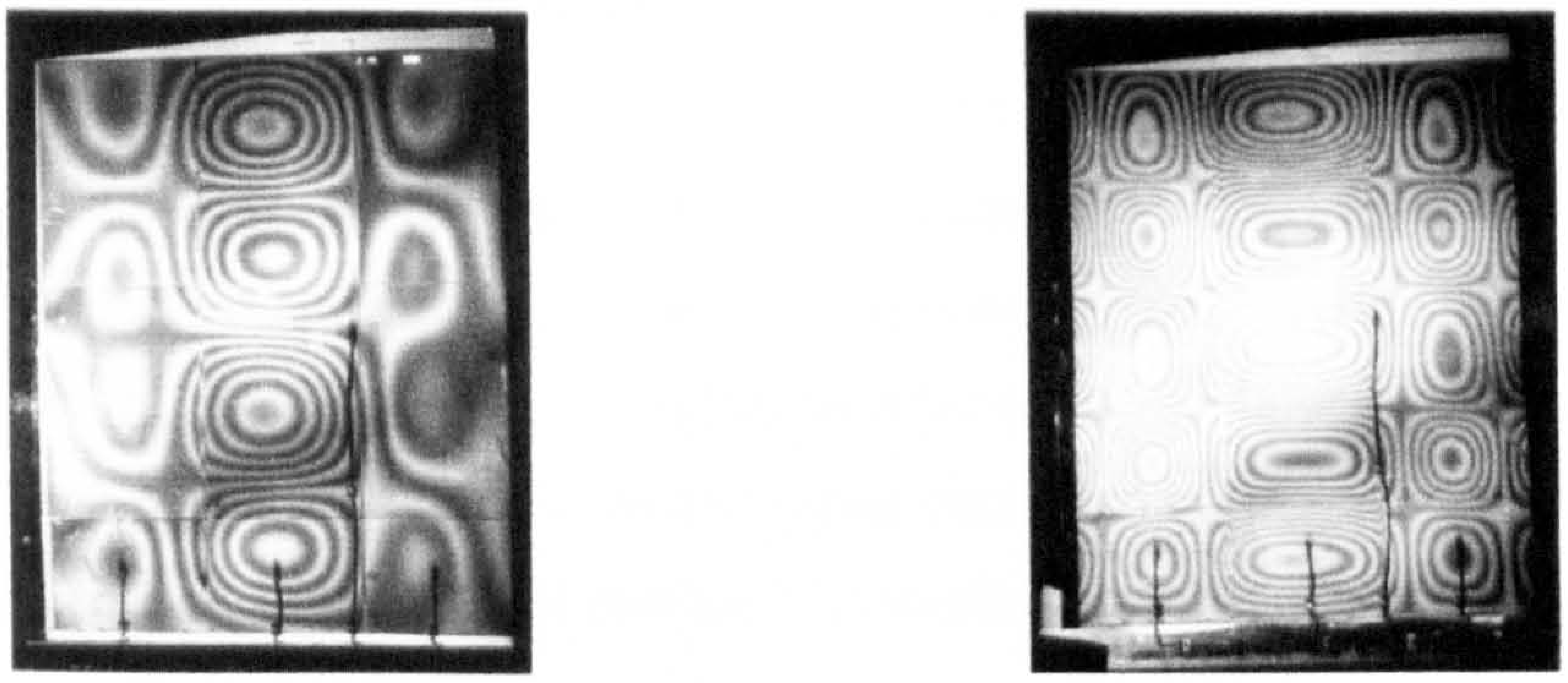
(a) (b)

Figure 2.1: Blade-stiffened panel Moiré fringe patterns at loading: (a) 300 kN, (b) 570 kN.

The testing of the blade-stiffened panel was part of a large experimental programme conducted at Imperial College London to investigate the behaviour and postbuckling failure of carbon-fibre composite stiffened panels with different stiffener configurations. Stevens et al. [8] investigated a set of I-stiffened panels stiffened by four I-shaped stiffeners equally spaced across the panel width. A total of four panels were manufactured, two with co-cured stiffeners and two with secondary bonded stiffeners where a layer of adhesive was placed between the panel skin and the tapered stiffener flanges. All panels had a length of 865 mm and a width of 610 mm. The shadow Moiré technique allowed the qualitative observation of the panels' buckle pattern, and out-of-plane displacements as well as strains were monitored using LVDTs and back-to-back strain gauges. All panels buckled into a six half-wave configuration. The lowest recorded buckling load was 110 kN, and the highest 115 kN. A mode-jump was observed at about 430 kN where the central skin-bay suddenly jumped from the six half-wave configuration to a seven half-wave configuration before panel failure occurred at loadings between 460 kN and 480 kN for each of the four panels. Stevens et al. [20] also reported tests on similar panels with J rather than I-shaped stiffeners. In this case buckling occurred at about 30 kN and panel collapse at 80 kN.

A hat-stiffened panel was tested by Falzon and Steven [21]. The panel had two co-cured stiffeners and was manufactured using T300/934 unidirectional prepreg. The panel and its experimental results are discussed in detail in Chapter 4.1, where ABAQUS FE models for the buckling and postbuckling response of the panel are discussed. A similar panel, with the same two hat-stiffeners but containing a circular cut-out in the skin bay was analyzed by Falzon [22]. Chapter 4.2 contains the experimental results and their comparison with numerical FE analysis relating to another panel, this time I-stiffened, originally manufactured by BAE systems [23]. The panel contained four equally spaced I-stiffeners which, unlike in the hat-stiffened panel, were secondary bonded to the skin using an adhesive rather than being co-cured.

Tests comparing panels with different shaped stiffeners were also conducted by Kong et al. [24]. Here panels had a length of 280 mm and width 160 mm, and two stiffeners manufactured by a continuous lay-up of the skin. Experimental investigations were carried out on both I and blade-stiffened panels. The panels buckled into a two half-wave configuration and did not exhibit any mode-jumps prior to failure, which in the case of blade-stiffeners occurred at a load about five times higher than the buckling load. Two I-stiffened panels were considered, with different stiffener cap widths. The panel with the wider stiffener caps failed at a loading almost seven times its buckling load, whilst the panel with the smaller stiffener caps was able to carry a load just over five times its buckling load. These experiments once again highlighted the potential in exploiting the postbuckling regime of stiffened composite panels.

2.2 Numerical methods

2.2.1 Analytical solutions

The experimental investigations discussed relating to simple plates, from Stein's aluminium plate to the other works on the buckling and postbuckling of composite plates, coupled the experimental observations with analytical analyses. In order to fully appreciate such analytical solutions, a full introduction to plate theory, the buckling of plates, and the behaviour of plates in their post-critical reserve would have to be given. It is not the purpose of this thesis to present such a detailed description of the analytical solution to plate structural stability. Thorough discussion of thin-plate theory and structural stability theory in general may be found in the monographs by Timoshenko and Gere [25], Timoshenko and Woinowsky-Krieger [26], and Bazant and Cedolin [27]. The understanding of such theory is imperative as it forms the basis for numerical analysis conducted on stiffened composite panels, since the skin bays of such panels may be approximated as plates whose boundary conditions reflect the presence of stiffeners.

In his discussion of the various studies on the effects of cutouts on the buckling and postbuckling behaviour of plates with cut-outs, Nemeth [16] pointed out how "special purpose" analytical analyses are typically more limited in scope than FE analyses, but a lot of the analytical research such as the one discussed has highlighted how such analyses may be used to conduct parametric studies on factors such as buckling behaviour. FE analyses on the other hand are more accurate and better suited to more complex problems such as the buckling and postbuckling behaviour of complete panels. In the next section the FE analyses conducted on the experimentally tested panels of Section 2.1.3 are discussed.

2.2.2 Finite element analyses

In his study of the graphite-epoxy panels, Starnes [17] compared experimental findings with the buckling predictions obtained by the PASCO computer code [28], which was based on an orthotropic prismatic plate formulation. Postbuckling analyses were conducted using the STAGS non-linear general shell finite element analysis computer code [29]. The final STAGS model contained six plate elements across the skin between stiffeners, and seven plate elements per longitudinal half-wave of the buckling mode. The stiffener web was modelled with two plate elements between the skin and stiffener cap, and a matching longitudinal mesh density as the skin, whilst the stiffener cap was modelled as a discrete beam. Analytical results obtained using STAGS compared well with the experimental postbuckling results.

In the investigation of I-stiffened carbon fibre panels, Stevens et al. [8] compared experimental results with those obtained by modelling the panels using an in-house finite element program, FE77 [30]. Nine-noded, quadrilateral, Mindlin shell elements, able to model laminate properties and which included shear deformation were used throughout the model. Figure 2.2 (a) shows the undeformed mesh corresponding to half of the panel modelled and Figure 2.2 (b) shows the numerically predicted deformed shape corresponding to a typical six-half wave buckle mode-shape of the panel. Non-linear modules were developed to conduct the postbuckling analysis. Imperfections in the form of the first eigenvector of a linear eigenvalue analysis were used to assist the non-linear solver onto the appropriate postbuckling path.

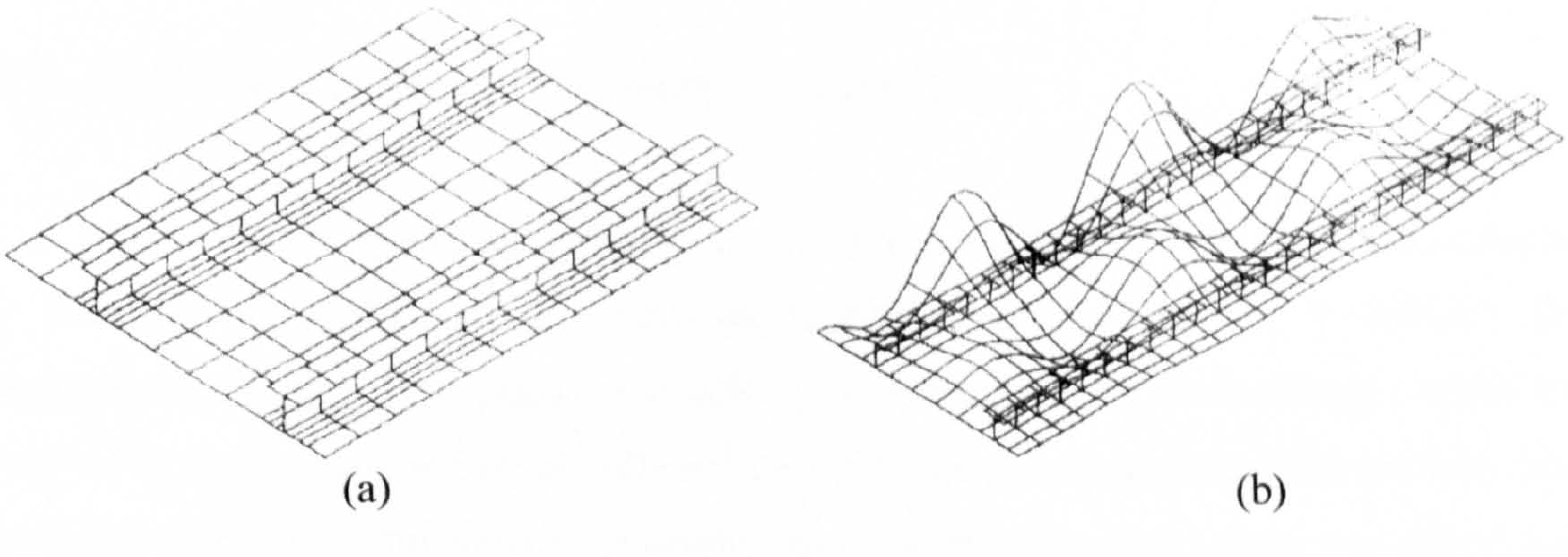
(a) (b)

Figure 2.2: Undeformed (a) and deformed (b) buckle shape of I-stiffened panel model analyzed by Stevens et al. [8]

The FE model showed correct evaluation of stress resultants on the buckled panel at a specific loading state. In particular, it is unknown whether the FE model was able to capture the mode-jump from six to seven half-waves that was observed experimentally in all of the panels tested.

Falzon et al. [19] also compared the experimentally observed buckling mode-shape with that predicted using FE77 for the blade stiffened panel tested. A linear eigenvalue analysis on the blade-stiffened panel model revealed a first eigenvalue of 113.84 kN which agreed well with the experimental buckling load, and the second eigenvalue was calculated at 115.96 kN. It was argued that the close proximity of this second eigenvalue with the buckling load of the panel helped to explain the mode-switch observed in the second panel.

Kong et al. [24] compared their experimental results on blade and I-stiffened panels with those obtained via FE analyses. FE models with 8-noded degenerated shell elements were created to model both the I-stiffened and blade-stiffened panels, and additionally models were made to represent panels of the same dimensions but with hat-shaped stiffeners. When comparing analytical and experimental buckling loads, differences of 15% or less were reported. Numerically predicted strains in the postbuckling range were compared to experimental values and a good correlation was found. None of the panels tested experimentally showed any mode-jumping in the postbuckling regime, hence it is not known whether the non-linear solution techniques used would be able to capture such secondary instabilities should they occur in a different panel.

As mentioned earlier, in Chapter 4 it will be discussed how FE models were created to model a co-cured hat-stiffened panel and a secondary bonded I-stiffened panel. Full details of the models created in ABAQUS are discussed and the results obtained fromm the numerical analyses compared to those obtained experimentally [21,23].

2.2.3 Modified non-linear finite element procedures

A lot of the mentioned numerical studies in which FE models were created to replicate the buckling and postbuckling behaviours highlight the fact that it is difficult for computational models of the panels to steadily capture the dynamic mode-changes which are observed in compressive testing of stiffened panels as the panels are loaded deeper into their postbuckling regime. This introduces another area where a literature survey was conducted, that of how standard path-following non-linear FE procedures may be modified so as to more reliably capture the mode-jumping phenomenon.

Numerical techniques for non-linear quasi-static analysis bear their roots to the arc-length methods, which are intended to enable solution algorithms to pass limit points without convergence problems. The arc length method was originally proposed by Riks [31] and Wempner [32]. Several modifications, such as the cylindrical arc-length methods were later introduced by Crisfield [33]. The effectiveness of the arc-length method in capturing mode-switching phenomena is however limited due its difficulty in dealing with bifurcation points. Cerini and Falzon [34] emphasized this problem and discussed some of the arc-length method's limitations. De Souza Neto and Feng [35] discussed a criterion to produce reliable path direction prediction in the presence of such snap-backs, but unless an initial imperfection is added to the model, the method fails.

More advanced solution strategies were investigated to deal with bifurcation points. Riks et al. [36] presented a combined static-dynamic analysis to attempt to tackle this problem. This required using the arc-length method in the static part of the solution procedure, and then using restart schemes to switch to a dynamic procedure. Falzon and Cerini [37] presented an automated solution procedure that did not require such restart schemes. The arc-length method was again used in the quasi-static part of the solution, but then a modified explicit dynamic routine was implemented when a mode-jump was about to occur. This proved more efficient computationally than standard implicit and explicit schemes. The method also contained eigen-mode injection allowing the algorithm to switch to a secondary path without the need to introduce initial geometric imperfections into the model so as to reduce bifurcation points to limit points.

Chapter 3

Buckling and postbuckling in finite elements

The scope of this chapter is to give a theoretical foundation to the FE analysis tools that will be used in the FE modelling of the various structures considered in this thesis, specifically eigenvalue buckling analyses and non-linear quasi-static analyses used to trace buckling and postbuckling response. In Chapter 2 it was seen how different non-linear solution schemes exist to model the postbuckling behaviour of structures such as a stiffened composite panel and to try and capture their mode-jumping that is observed experimentally. The modified non-linear solution schemes mentioned all required the user-edited subroutines to be coded and are not available "ready for use" in standard commercial FE packages. In Chapter 1 it was highlighted how the ultimate aim of this research work was to establish an analysis methodology for the optimization of stiffened composite structures using the tools available in the FE package ABAQUS. Another important consideration is how diverging from standard quasi-static methods in the analysis of buckling and postbuckling analysis of, for example, a stiffened composite panel increases computational time and cost considerably due to the dynamic analyses requiring very small time steps to guarantee stability of the algorithm coupled with result accuracy. Because of this, the implementation of a modified scheme involving both static and dynamic analysis was not considered. Instead, it was sought to make the most efficient possible use of the "stand-alone" resources and algorithms available within the ABAQUS quasi-static framework so as to minimize computational time and cost, a factor of paramount importance when dealing with optimization which traditionally requires a lot of iterations.

This chapter starts with a very brief introduction to buckling and conducting linear eigenvalue buckling analyses. Discussion then follows on to how the postbuckling regime of a structure may be investigated using non-linear algorithms. The need for non-linear analysis is justified, and then the theory behind the Newton-Raphson scheme used in ABAQUS quasi-static non-linear analysis is considered and several of its modifications discussed. Pitfalls of this algorithm are identified, and analysis techniques able to circumvent such problems such as energy dissipation schemes are explained.

3.1 Linear buckling analysis

3.1.1 The buckling phenomenon

The buckling phenomenon is best understood in its simplest form, by considering a simple plate or beam subject to a compressive end load. As this loading is increased, the beam and plate will undergo purely axial compression until a certain critical load, the buckling load, is reached. For a perfect structure then the beam or plate will have no preferred direction of buckling and hence a bifurcation will exist at the buckling load. For a perfect beam, the lateral deflection would simply go to infinity, whilst for a plate a secondary stable path exists as first discussed in Chapter 1 and illustrated in Figure 1.4. This form of buckling is known as stable symmetric buckling since the secondary path, like the primary, is stable and the plate has no preferred direction for out-of-plane displacements.

In reality a perfect structure will not exist due to the presence of imperfections. Imperfections in the material, geometry, or boundary conditions will exist, termed initial imperfections. Due to the presence of such imperfections, the structure will have a "preferred" direction of buckling and the bifurcation at the buckling load will not exist, but rather a smooth transition occurs from the primary to secondary paths representing the buckling and postbuckling regimes of the structure. The magnitude of the imperfection will influence both the buckling load and initial prebuckling stiffness, where a bigger imperfection will lower the buckling load. This reduction is usually minimal, and hence the structure is termed imperfection insensitive. Nonetheless, in analysis of the buckling and postbuckling behaviour of structures, it is important to be aware of the possible imperfection sensitivity

3.1.2 Linear eigenvalue buckling analysis

In an FE model a linear eigenvalue analysis is typically used to determine the buckling load of a structure. The theory behind such an analysis is widely documented in literature [38,39] and results in the eigenvalue problem given below:

$$(\mathbf{K}^n + \lambda_i \mathbf{K}_\sigma^n)\varphi_i^n = 0 \qquad (3.1)$$

where $\mathbf{K}^n$ is the tangent stiffness matrix of the structure and $\mathbf{K}_\sigma^n$ the geometric stiffness matrix computed from the internal stresses. The superscript *n* refers to an *n* degree of freedom structure. φ_i is the *i*'th eigenvector corresponding to the *i*'th eigenvalue λ_i ,and gives the mode shape of the structure's *i*'th buckling mode. These mode shapes correspond to the shape of the deformed configuration and are typically normalised so that their maximum displacement is 1.0. When conducting FE linear eigenvalue analyses, both the eigenvalues λ_i and the eigenvectors φ_i are usually required. The first eigenvalue will correspond to the buckling load of the structure, and eigenvectors are typically used in nonlinear analyses as initial geometric imperfections for a structure in which the actual imperfections are unknown.

The classical mathematical eigenvalue problem has received a lot of attention in literature [40,41], but the classical methods that exist for the extraction of eigenvalues are not well suited to the FE method. Most structures contain a large number of degrees of freedom and this precludes the use of classical methods due to the necessity to manipulate very large and fully populated matrices. In fact, the tangent stiffness and geometric stiffness matrices are sparse and symmetric, but the need to invert them when solving for eigenvalues results in fully populated matrices. Methods have been developed to extract eigenvalues particularly suited to the sparse matrices arising from the FE method. In particular such methods are useful as often only the first few eigenvalues are required, or in fact only the first one in the case of a buckling load. ABAQUS provides eigenvalue extraction via the Lanczos and subspace iteration methods. The subspace iteration method was first introduced into FE applications by Bathe and Wilson [42] for solving the eigenvalue equation for dynamic problems rather than buckling, and the Lanczos method has been discussed by a variety of authors and various modifications have been proposed [43,44,45,46,47]. A mathematical description of both the subspace iteration and Lanczos methods as available in ABAQUS may be found in the ABAQUS Theory Manual [39].

3.2 Non-linear analysis

3.2.1 The need for non-linear analysis

Eigenvalue linear buckling analysis is of limited scope when analysing a structure. The analysis assumes a linear relationship between the applied loading and the displacement response of the structure. This is in general a good approximation in a stiffened structure such as a composite panel up to the buckling load, and hence in the FE analysis of such a structure an eigenvalue buckling analysis is conducted to obtain the numerical buckling load. An eigenvalue buckling analysis does not however yield any information on the postbuckling behaviour of the structure. After buckling the buckled state of the structure means that displacements will, in general, be large and the linear assumption will no longer hold. In this case, a non-linear analysis is required, and with the advent of computers and the increase of computational power, non-linear analyses are now standard, especially using the FE method.

In general there are three instances which warrant the need for a non-linear analysis. These are geometric non-linearity, material non-linearity, and non-linearity due to contact. Geometric non-linearity occurs when the load-displacement relationship of a structure is no longer linear within the elastic limit of the material. As mentioned earlier an example of this is a stiffened composite panel in its postbuckling regime where the buckled skin has large out-of-plane displacements. Material non-linearity occurs when plasticity effects become important or a material with a non-linear stress-strain curve, such as a rubber, is being modelled. Non-linearity due to contact occurs when two surfaces come together and the effect of one on the other needs to be considered. For the modelling of buckling and collapse, only the first two types of non-linearity are significant. However, contact may be important when considering fracture, as fracture surfaces will develop and these may come into contact with one another.

3.2.2 The standard incremental algorithm

In a non-linear analysis, to predict the response of a structure, an incremental solution is adopted where the external load is applied as a series of load increments. These load increments are small enough so that the structure can be assumed to behave linearly within each increment. The general equilibrium equation for the structure is that the externally applied loads **f** are equal to the internal resisting forces **p**:

$$\mathbf{f} - \mathbf{p} = \mathbf{0} \tag{3.2}$$

For a specific load increment *n*, Equation (3.2) may be written as:

$$\Delta\mathbf{f}^{n} - \Delta\mathbf{p}^{n}(\mathbf{u}^{n}) = \mathbf{0} \tag{3.3}$$

$\Delta\mathbf{f}^{n}$ is the external load increment at increment *n*, whilst $\Delta\mathbf{p}^{n}$ is the incremental internal force vector for the unknown displacement configuration $\mathbf{u}^{n}$ at increment *n*.

Since the behaviour within each increment is assumed linear, then:

$$\Delta\mathbf{p}^{n}(\mathbf{u}^{n}) = \left[\frac{\partial\mathbf{p}}{\partial\mathbf{u}}\right]_{\mathbf{u}^{n-1}} \Delta\mathbf{u}^{n} \tag{3.4}$$

This becomes:

$$\Delta\mathbf{p}^{n}(\mathbf{u}^{n}) = -\mathbf{K}_{T}^{n-1}\Delta\mathbf{u}^{n} \tag{3.5}$$

Where $\mathbf{K}_{T}$ is the tangent stiffness matrix. Equation (3.5) can be substituted back into Equation (3.3) to yield:

$$\Delta\mathbf{f}^{n} = \mathbf{K}_{T}^{n-1}\Delta\mathbf{u}^{n} \tag{3.6}$$

By inverting the stiffness matrix the incremental $\Delta\mathbf{u}^n$ is found, and since the solution at the previous increment *n*-1 is known, the updated solution is:

$$\mathbf{u}^n = \mathbf{u}^{n-1} + \Delta\mathbf{u}^n \tag{3.7}$$

3.2.3 The Newton-Raphson algorithm and its modifications

The incremental method described is highly inefficient and also not reliable. The reason for this is that no check for global equilibrium is made during the process and hence the solution can move away from the actual load-displacement of the structure which is being investigated. To prevent this from happening, the incremental method can be coupled with an iterative procedure so as to dissipate the residual forces. One such algorithm is the Newton-Raphson algorithm.

Equation (3.2) is an exact equilibrium equation which will never be exactly satisfied in numerical solutions. Hence a converged state is sought after in which the equilibrium error is sufficiently small. A measure of this error is given by the vector of residual forces **r**:

$$\mathbf{r} = \mathbf{f} - \mathbf{p} \tag{3.8}$$

If an approximate displacement solution $\mathbf{u}_i^n$ has been found, where the exact solution is $\mathbf{u}^n$, then a Taylor series expansion truncated after the first two terms may be used to obtain an improved solution $\mathbf{u}_{i+1}^n$. The residual force vector for this improved solution is given by:

$$\mathbf{r}(\mathbf{u}_{i+1}^n) = \mathbf{r}(\mathbf{u}_i^n) + \left[\frac{\partial\mathbf{r}}{\partial\mathbf{u}}\right]_{d_i^n} \delta\mathbf{u}_i^n \tag{3.9}$$

Recalling the exact equilibrium equation (3.2) and using the new approximation $\mathbf{u}_{i+1}^n$ then:

$$\mathbf{r}(\mathbf{u}_i^n) - \mathbf{K}_{Ti}^n \delta\mathbf{u}_i^n = 0 \tag{3.10}$$

Equation (3.10) is solved for the iterative displacement $\delta\mathbf{u}_i^n = 0$ and the improved solution obtained as:

$$\mathbf{u}_{i+1}^n = \mathbf{u}_i^n + \delta\mathbf{u}_i^n \tag{3.11}$$

The iterative solution process of the Newton-Raphson technique is best understood graphically as shown in Figure 3.1.

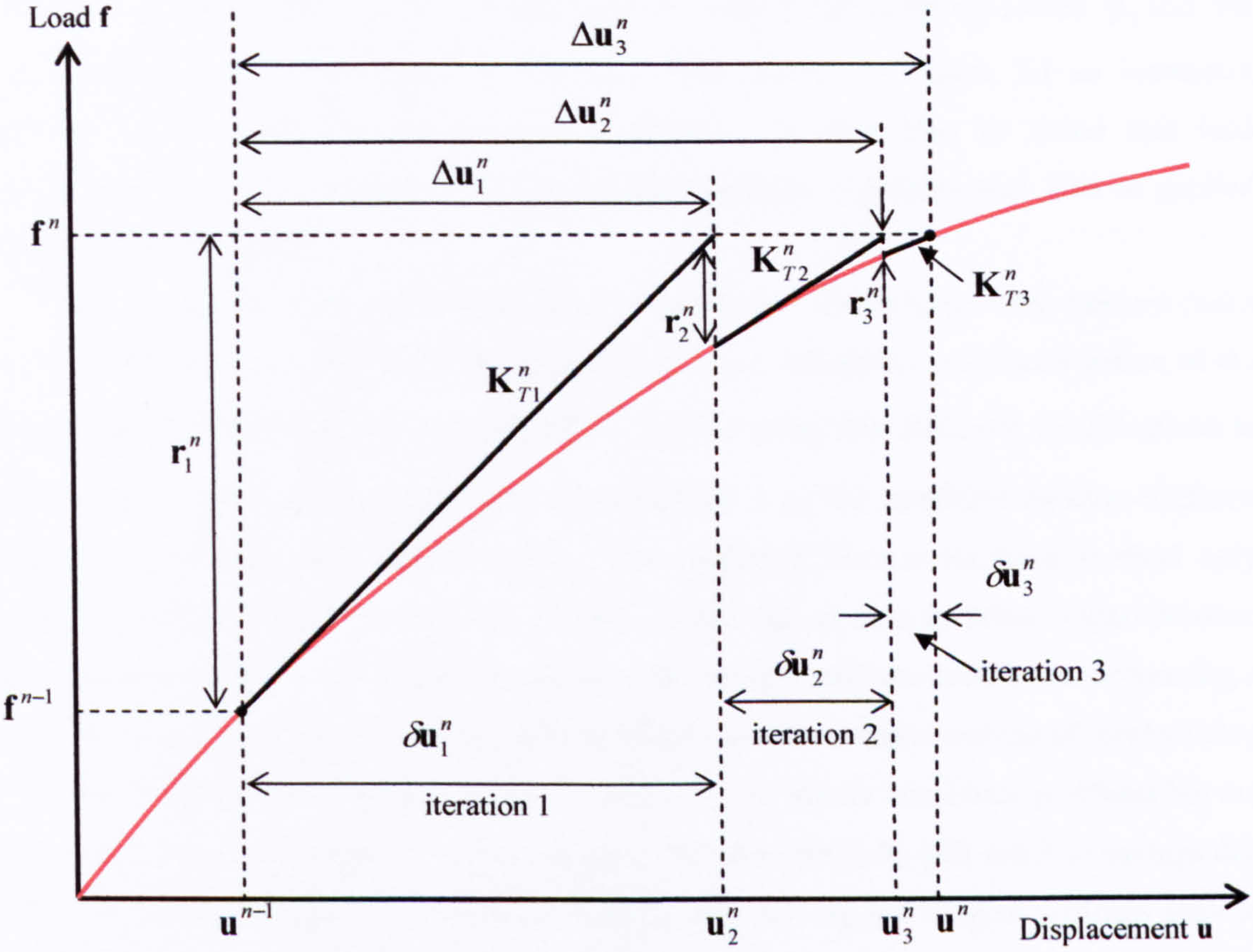

Figure 3.1: Newton-Raphson algorithm under load control.

Suppose a converged solution has been found for increment *n*-1, corresponding to displacements $\mathbf{u}^{n-1}$ and applied loads $\mathbf{f}^{n-1}$, and the solution for increment *n* is required. The first step is to predict the displacements $\mathbf{u}_0^n$ and use these displacements to predict the internal resisting forces $\mathbf{p}_1^n$. The subscript refers to i=1, namely the first iteration. The residual force vector, visible in Figure 3.5, is found as:

$$\mathbf{r}_1^n = \mathbf{f}_1^n - \mathbf{p}_1^n \tag{3.12}$$

A convergence check is then made to see whether $\mathbf{r}_1^n$ is within a pre-specified convergence tolerance. If it is, then the solution has been evaluated and the analysis continues to the next increment, *n+1*. If convergence has not occurred, then the tangential stiffness matrix $\mathbf{K}_{T1}^n$ is re-evaluated and factorised. This then allows the corrective displacement to be calculated as:

$$\delta\mathbf{u}_1^n = \left[\mathbf{K}_{T1}^n\right]^{-1}\mathbf{r}_i^n \tag{3.13}$$

The estimated displacement for $i = 2$ is then:

$$\mathbf{u}_2^n = \mathbf{u}_1^n + \delta\mathbf{u}_1^n \tag{3.14}$$

This new estimated displacement is then used to predict the resisting forces $\mathbf{p}_2^n$ and the process repeats until a convergent solution has been found. In Figure 3.1 an increment requiring three iterations to convergence is shown. It must also be noted that load incrementation has been explained, but the Newton-Raphson algorithm may also be applied using displacement control.

The Newton-Raphson method presented is usually avoided in large finite element codes since considerable computational effort is required in the calculation and factorization of the tangent stiffness matrix $\mathbf{K}_{Ti}^n$ at each iteration. To overcome this difficulty modifications to the Newton-Raphson method have been proposed, such as the modified Newton-Raphson method and quasi-Newton methods [38]. The modified Newton-Raphson method only updates the tangent stiffness matrix occasionally, rather than at each iteration. Quasi-Newton methods aim to obtain a good approximation to the tangent stiffness matrix by performing a simple modification to a previously calculated tangent stiffness matrix instead of recalculating it. The modified Newton-Raphson method is attractive for mildly non-linear problems but not for severely non-linear cases. It, as well as quasi-Newton methods, will result in savings due to the reduced computations required in forming and solving the tangent stiffness matrix. However these might be offset by the increased number of iterations required for convergence and hence larger number of force residual calculations. For this reason, in most non-linear analyses ABAQUS by default utilizes the standard Newton-Raphson technique, but a quasi-Newton method is available should the user wish to use it.

3.2.4 Limitations of Newton-Raphson methods

The Newton-Raphson algorithm described, as well as related iterative incremental schemes suffer from a severe limitation, that of failing in the presence of highly non-linear behaviour. An example of this is the case of buckling or collapse. At the bifurcation point (in the case of no imperfections) the diagonal matrix D of the factored stiffness matrix will have a negative entry. Matrix inversion is done using an LDL^T decomposition, where L is a lower triangular matrix and D is a diagonal matrix with all entries greater than zero for a tangential stiffness matrix which is positive definite. A negative entry in D corresponds to a negative eigenvalue of the tangent stiffness matrix $\mathbf{K}_t$, which becomes indefinite. If this is the case, the postbuckling response will not be captured and the algorithm will predict the structure to proceed on its unstable primary path even after the bifurcation point. The introduction of an imperfection into the model effectively removes the bifurcation and transforms the bifurcation point into a limit point. The Newton-Raphson method often still fails even in this instance, which may be associated with snap-through and snap-back behaviour in the load-displacement equilibrium curve. Figure 3.2 (a) shows snap-through behaviour and Figure 3.2 (b) snap-back behaviour. In Figure 3.2 (a), under load control the Newton-Raphson scheme is likely to fail upon reaching the point labelled A as it is unable to converge past this limit point. In reality, the structure would snap-through to point B. A similar argument applies for displacement control, where in Figure 3.2 (b) a displacement controlled incremental scheme would encounter difficulties in dealing with the snap-back that occurs at point A. In general, this problem can be identified as having two aspects, that of identifying the proximity of the local limit point A, and the subsequent negotiation of this limit point by "jumping" to the equilibrium configuration at point B.

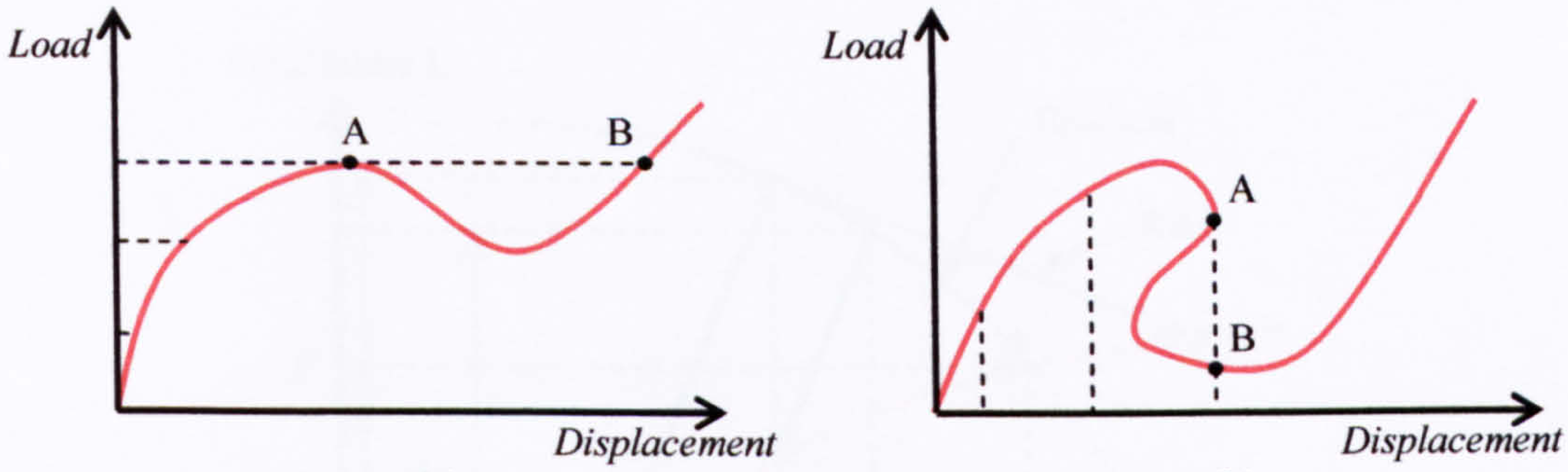

(a) (b)

Figure 3.2: Examples of snap-through (a) and snap-back (b) behaviour.

Several approaches exist to deal with limit points without having to revert to a full dynamic analysis. Two such approaches, which are readily available in ABAQUS, are the arc-length method and the use of an energy dissipation scheme. Other schemes also available are discussed in detail by Ramm [48].

3.2.5 The arc-length method

The arc-length method was originally established by Riks [31] and Wempner [32]. It is also known as a constrained method, where the load level at each iteration is varied rather than keeping the applied load level constant during a specific load increment. Doing this adds an auxiliary equation to the set of equations solved to advance the solution, so that the arc-length method effectively requires the solution of $N+1$ equations for an N degree of freedom problem. The auxiliary equation constrains the iterative displacements to follow a specific path aimed towards a converged solution. For a load step increment n, the constraint equation for the i'th iteration is:

$$\left(\Delta \mathbf{u}_i^n\right)^T \left(\Delta \mathbf{u}_i^n\right) + \left(\Delta \lambda_i^n\right)^2 = \left(l^n\right)^2 \tag{3.15}$$

where $\Delta\mathbf{u}_i^n$ and $\Delta\lambda_i^n$ are the total incremental displacement vector and load factor respectively, and l^n is the arc length. The arc-length method, as originally proposed by Riks, iterates along a hyperplane which is perpendicular to the tangent of a previously converged increment solution. As shown in Figure 3.3, the distance of the hyperplane to the previous converged solution is given by the arc-length l^n. A modification proposed by Crisfield [33] iterates along a hypersphere to improve the speed of convergence. The arc-length constraint is in this case also used at the correction stage. The correction stage refers to the iterations aimed at reducing the residual force vector, while the predictor is the first iteration within each increment.

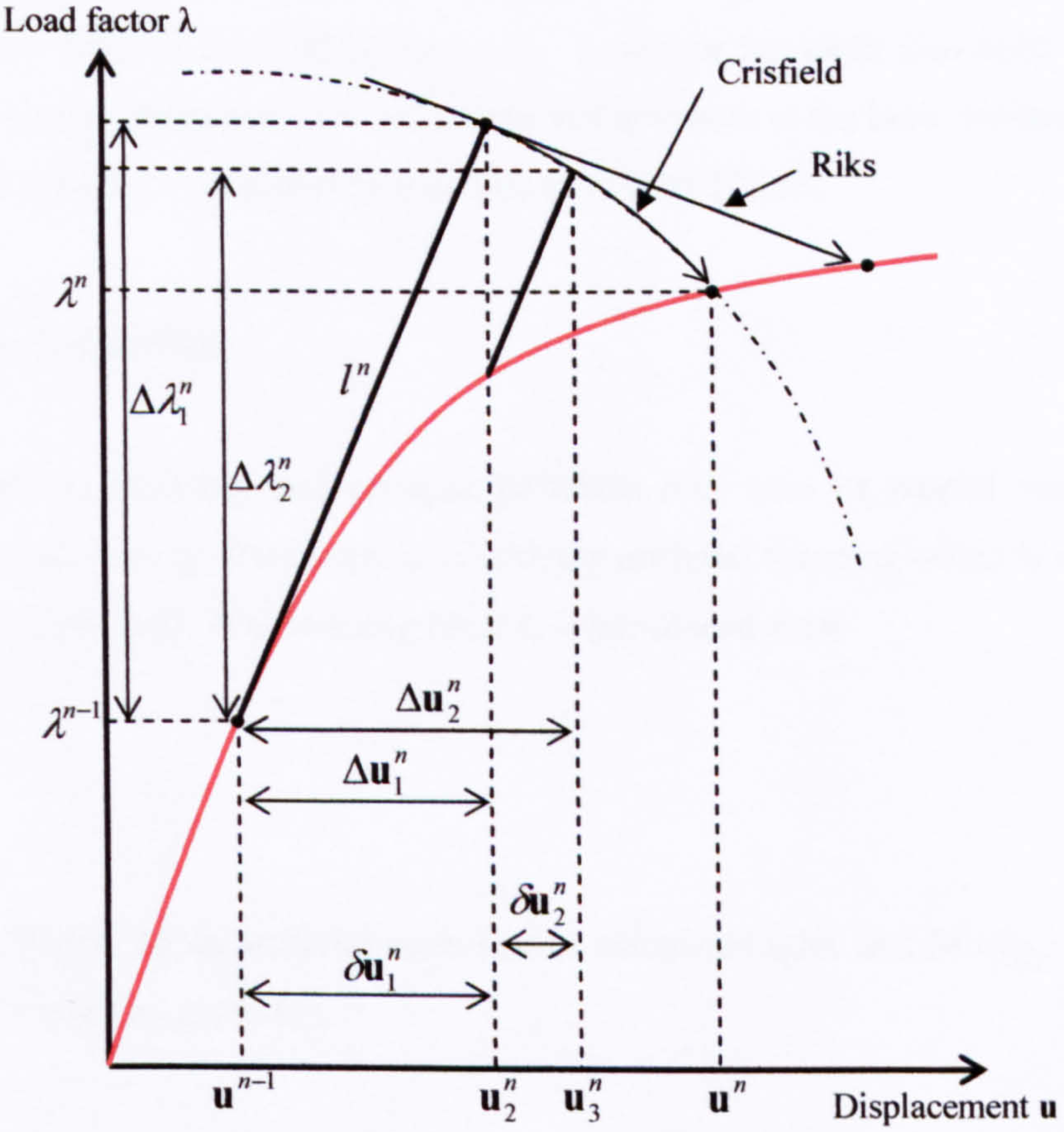

Figure 3.3: The arc-length method for Riks and Crisfield formulations.

The arc-length constraint Equation (3.15) is to be solved together with the equilibrium Equation (3.2). This is not appropriate in FE analysis since the augmented stiffness matrix will not be symmetric or banded. Batoz and Dhatt [49] showed that for the case of displacement control the system of equations reduces to a quadratic equation in the total incremental displacement $\Delta\lambda_i^n$:

$$a_1\left(\Delta\lambda_i^n\right)^2 + a_2\Delta\lambda_i^n + a_3 = 0 \tag{3.16}$$

Two possible solutions exist for the load increment, and it is very important to choose the sign of $\Delta\lambda_i^n$ at the predictor stage correctly to successfully trace the response of the structure. One way to do this is to choose the $\Delta\lambda_i^n$ with the same sign as the determinant of the stiffness matrix. If a positive definite stiffness matrix exists, a positive load increment is applied, whereas a negative diagonal term implies a negative eigenvalue and hence either a limit or bifurcation point has been reached. The arc-length method is effective in dealing with limit points, but this is not the case for bifurcation points. Matching the predictor with the sign of the stiffness matrix at a bifurcation would result in a negative load increment. This negative load increment could then take the response back below buckling, and hence the next load increment would be positive. Once more the analysis would go beyond the bifurcation point, and an oscillatory behaviour would be observed. Corrector iterations also need appropriate choice of iterative load increment. Modifications and advances to the basic arc-length method here described have been considered by a variety of authors [33,35].

3.2.6 Energy dissipation

Instabilities in buckling and collapse problems may also be treated via an energy dissipation scheme. Energy dissipation is effectively artificial damping which is added to the equilibrium Equation (3.2). If a damping force $\mathbf{f}_d$ is introduced then:

$$\mathbf{f}-\mathbf{p}-\mathbf{f}_d=0 \tag{3.17}$$

where:

$$\mathbf{f}_d=c\mathbf{M}\mathbf{v} \tag{3.18}$$

c is a damping factor, **M** an artificial mass matrix calculated with unit density, and **v** is the vector of nodal velocities given by:

$$\mathbf{v}=\frac{\Delta\mathbf{u}}{\Delta t} \tag{3.19}$$

u are the nodal displacements and Δt the time increment. While the structure is stable, the viscous forces and hence the energy dissipated will be very small. Once an instability develops, such as at buckling or a mode-jump in a stiffened panel, then the local velocities increase and part of the strain energy released is dissipated by the applied damping.

The value of the damping parameter c is central to this scheme. Too small a value will still lead to the non-linear analysis being unable to control the instability and hence not converging, whist too high a value can lead to erroneous results. The scheme presented here is the one that is available in ABAQUS. ABAQUS calculates a default value of c at the first increment of a step. The first increment is usually stable, and hence the damping factor is calculated such that the extrapolated dissipated energy is a small fraction of the extrapolated strain energy. Care must be taken by the user to ascertain that this default damping value is small enough so as to not affect results adversely.

3.2.7 Dynamic analysis

Another solution strategy for modelling the buckling and postbuckling behaviour of structures such as stiffened composite panels is the use of a full dynamic analysis. Dynamic analyses become particularly attractive when instabilities associated with mode jumping occur. When a composite stiffened panel suddenly mode-jumps form one buckle configuration to the next, dynamic effects in the structure lead to a release in the stored strain energy. As parts of the structure accelerate due to these dynamic effects, inertial forces occur which are not included in the Newton-Raphson scheme presented previously. It is these inertial forces that effectively stabilize the structure meaning that a unique convergent solution may be found.

Solving of a dynamic non-linear problem relates to solving the dynamic equation of motion:

$$\mathbf{M}\ddot{\mathbf{u}} + \mathbf{C}\dot{\mathbf{u}} + \mathbf{K}\mathbf{u} = \mathbf{f} \tag{3.20}$$

In Equation (3.20) $\mathbf{u}$, $\dot{\mathbf{u}}$, and $\ddot{\mathbf{u}}$ are the displacement, velocity, and acceleration vectors respectively. **K**, **C**, and **M** are the stiffness, damping, and mass matrices respectively while **f** is the vector of externally applied loads. If the static solution is required, the velocities and accelerations are effectively zero since the structure is not moving and Equation (3.20) reduces to:

$$\mathbf{K}\mathbf{u} = \mathbf{f} \tag{3.21}$$

From Equation (3.21) it is easily noted that the mass and damping matrices are not involved, and therefore any suitable representations may be used, and it is such representations that affect the numerical efficiency of dynamic analyses.

In general, dynamic analyses are very computationally expensive relative to quasi-static methods when the dynamic events are of a short duration compared to the whole quasi-static response. This is the case when a mode jump occurs, and hence form a computational point of view the use of quasi-static analyses are presented previously in this chapter coupled with, for example, energy dissipation schemes to overcome the convergence difficulties associated with mode jumping are more attractive. This is particularly true in an optimization procedure when repetitive FE runs are required, in which case the use of dynamic analyses is often prohibitive, and it is for this reason that quasi-static solution methods throughout this research work. A more detailed discussion of dynamic analyses may by found in the textbooks by Cook et al. [50] and Bathe [51].

3.3 Concluding remarks

This chapter has given a brief background to the phenomenon of buckling, and then discussed the various methods available to model a structure's buckling behaviour as well as its response when subject to loads past its critical buckling load. All the methods discussed form the basis of FE buckling and collapse analyses central to the work conducted in this thesis. In Chapter 4, two stiffened composite panels are modelled using the FE package ABAQUS and the analysis tools described in this chapter. It must again be mentioned how the need for efficient computations is central to the methods chosen, since the ultimate aim is to integrate the FE analyses with an optimization procedure. The latter will require repetitive FE runs, and hence the reduction of computational cost is a must. Also, all the techniques used are available in ABAQUS without the need for special user subroutines.

The approach taken for conducting buckling and collapse analysis in ABAQUS as detailed in Chapter 4 can be generalized as a four way process. First an FE model is created of the structure to be analyzed. This is done using a pre-processor such as ABAQUS/CAE. Following this a linear eigenvalue buckling analysis (using the Lanczos extraction method) is conducted to obtain the buckling load of the structure as well as typically the first few eigenvalues and associated mode-shapes. Since an eigenvalue analysis yields no information about postbuckling behaviour, a full non-linear analysis is conducted. It was seen how such analyses pose the problem of instabilities resulting in the non-linear solution algorithms such as the Newton-Raphson method being unable to converge. To prevent this, geometric imperfections corresponding to a linear superposition of the first few eigenmodes are introduced into the FE model. These effectively remove bifurcations, but still the analysis may fail due to the presence of limit points at the secondary instabilities associated with mode-jumping. To deal with these instabilities, the energy dissipation scheme discussed is used, introducing viscous damping into the analysis and allowing the ABAQUS non-linear solution algorithms to trace the full postbuckling of the structure. Alternatively, an arc-length method may be used. The fourth and final step is to extract the results from the bucking and non-linear analyses via a postprocessor such as ABAQUS/Viewer.

Chapter 4

Finite element modelling of stiffened composite panels

This chapter shows how the techniques described in Chapter 3 relating to the FE modelling of stiffened composite structures are applied in an FE framework using the FE package ABAQUS to model the buckling and postbuckling characteristics of two stiffened composite panels. The main aim of the investigations is to create FE models which are able to predict the buckling characteristics of the panels as well as trace their postbuckling behaviour by capturing the panels' secondary instabilities. A further aim of this chapter is to examine how initial geometric imperfections on a stiffened panel may influence its buckling and postbuckling response. To do this, different imperfections are incorporated into the FE models and their effects discussed. The viscosity parameter associated with an energy dissipation scheme introduced in Chapter 3, essential for non-linear quasi-static analyses of this kind, is also varied to assess its effect on the accuracy of the FE solutions.

The first panel considered is a hat-stiffened panel, while the second panel has I-shaped stiffeners. The two panels were chosen for their different stiffener geometry, skin thickness, and lay-up. This chapter is divided into two sections, one dealing with each panel. Within each panel section, experimental setup and results are presented first, followed by details of the FE models created to replicate the panels and the subsequent analysis solutions. Following this, the FE results are discussed and compared to the experimental findings.

It is important to note that the FE models presented in this chapter have no failure capability and, in fact, simulations were run past the experimental failure loads of the panels. It is discussed how the inability to model failure influences the numerical results when compared to experiment. Chapter 5 introduces failure and the various techniques used in modelling it, and Chapters 6 and 7 will show how failure modelling can be incorporated into FE analyses such as the ones presented in this chapter.

4.1 Hat-stiffened panel

4.1.1 Experimental procedure

The hat-stiffened panel was previously experimentally tested by Falzon and Steven [21]. It was manufactured using T300/934 unidirectional prepreg. The nominal material properties for the material, where values for only tension were quoted, are shown in Table 4.1. Figure 4.1 shows the stiffener locations and overall dimensions of the panel. The loaded edges were potted in epoxy resin and machined parallel in order to ensure uniform loading and prevent brooming. This resulted in the panel having a 425 mm long and 335 mm wide effective test section. The panel was reinforced by two stiffeners, spaced 186 mm apart and was co-cured, meaning that the hat-stiffener design was fully incorporated as detailed in Figure 4.2 consisting of a $[\pm45,0,90]_S$ quasi-isotropic lay-up with a thickness of 1.344 mm.

Figure 4.1 shows the location of back-to-back strain gauges and LVDTs used to measure strains and out-of-plane displacements respectively. As can be seen, five sets of back-to-back strain gauges were present on the panel. The use of back-to-back strain gauges allows for the bending and membrane components of strain to be measured. Two LVDTs were used, LVDT A at a position 113 mm from the panel centre, and LVDT B 25 mm in the other direction on the panel's longitudinal centreline. Positive readings indicated out-of-plane displacements towards the stiffener side. Divergence of the strain readings in back-to-back strain gauges as well as sudden changes in out-of-plane displacements as measured by the LVDTs should be an indication of buckling and of any mode shape changes associated with secondary instabilities. The Shadow Moiré technique was used to observe qualitatively the out-of-plane displacements of the buckled skin, and a video recorder captured the dynamic mode changes. A compression test fixture allowed the panel to be tested under uniaxial compression in a 250 kN Instron Universal Testing Machine with a crosshead displacement of 0.02 mm/min.

Table 4.1: Nominal material data for T300/934 Unidirectional Prepreg.

Property	Value
Longitudinal tensile modulus	124 GPa
Transverse tensile modulus	11.7 GPa
In-plane shear modulus	5.5 GPa
Poisson's ration	0.3
Ply thickness	0.168 mm

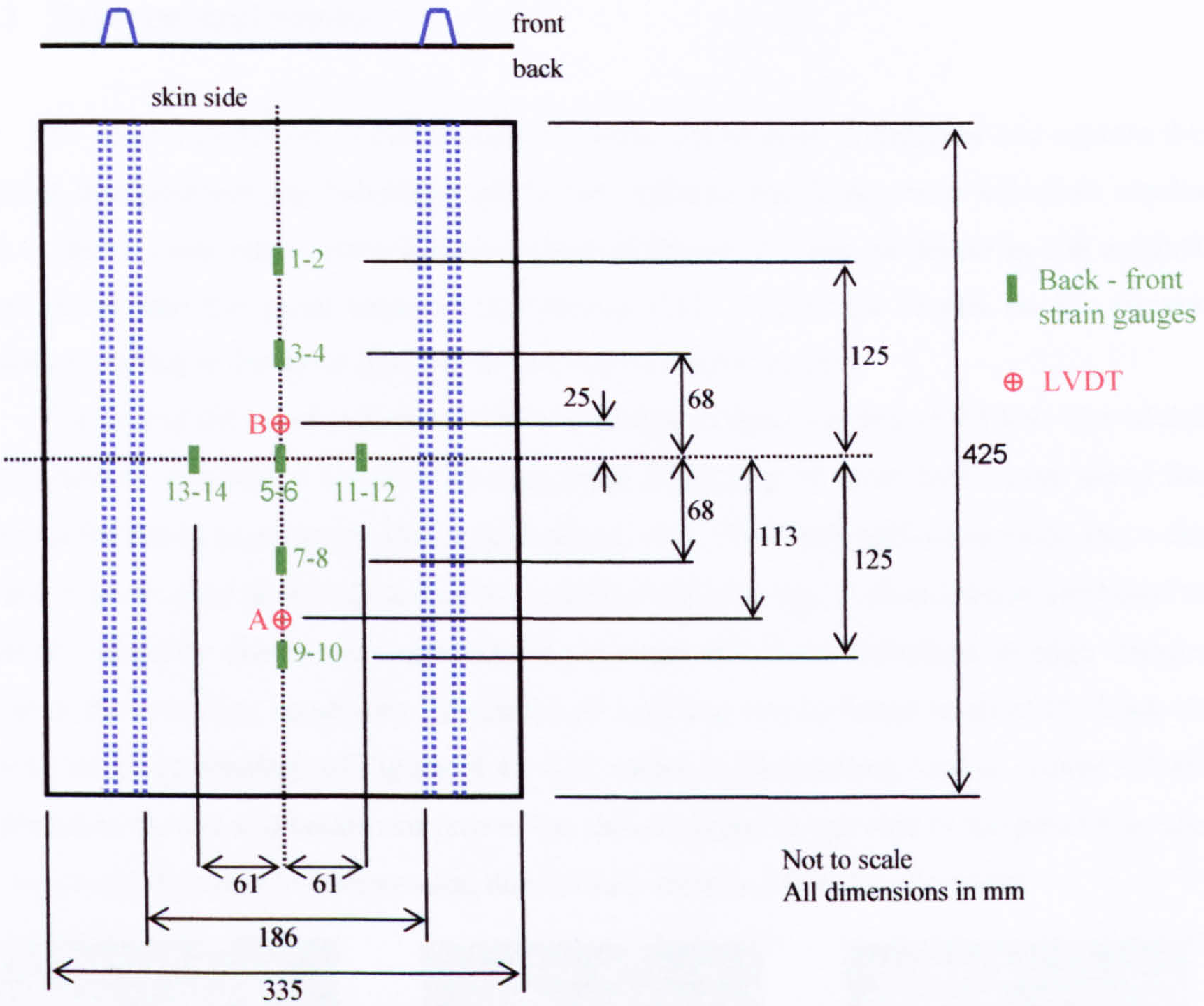

Figure 4.1: Hat-stiffened panel effective test section dimensions with strain gauge and LVDT locations.

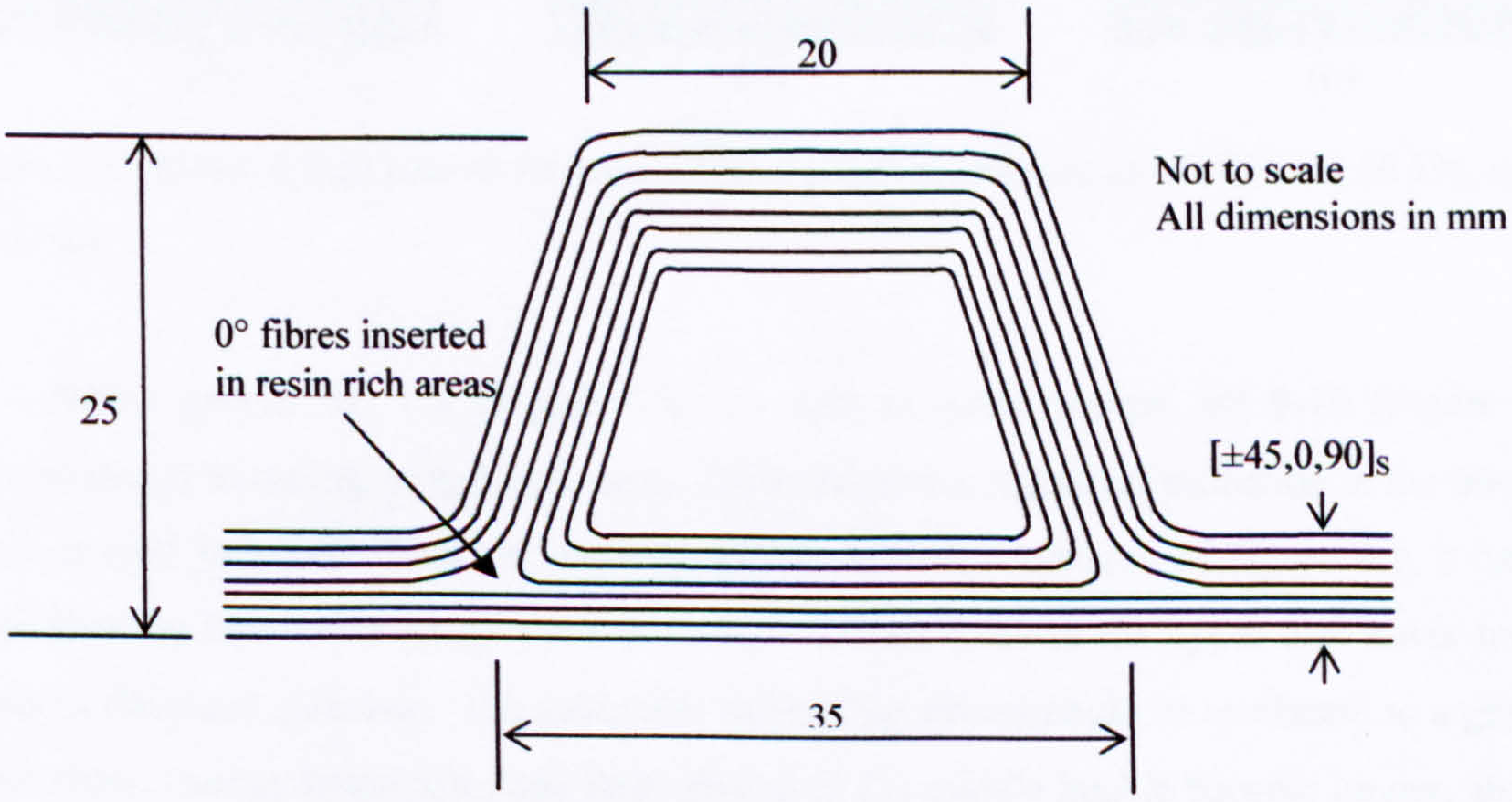

Figure 4.2: Detail of integrated hat-stiffener design.

4.1.2 Experimental results

The results presented in this section are sufficient to fully understand and capture the buckling and postbuckling behaviour of the hat-stiffened panel, but more complete results such as those from other strain gauges shown in Figure 4.1 can be found in the original investigation into the panel experimental testing [21]. Numerical results on the figures presented relating to the developed FE model will be discussed later.

The skin of the panel started to buckle at an approximate loading of 9.4 kN. The Moiré fringe patterns revealed a buckling configuration consisting of three half-waves along the length of the panel, as is clearly visible in Figure 4.3 (a). The three half-wave mode shape did not however develop uniformly across the length of the skin-bay, a phenomenon attributed to material variability due to the manufacturing process and slight variations in edge stresses owing to the boundary conditions. Evidence of buckling can be found in all of the back-to-back strain gauge readings of Figures 4.4 – 4.6, where at the buckling load of around 9.4 kN the strains in the top and bottom surface of the skin diverged as one side of the panel skin was in tension and the other in compression due to the formation of the buckle crests.

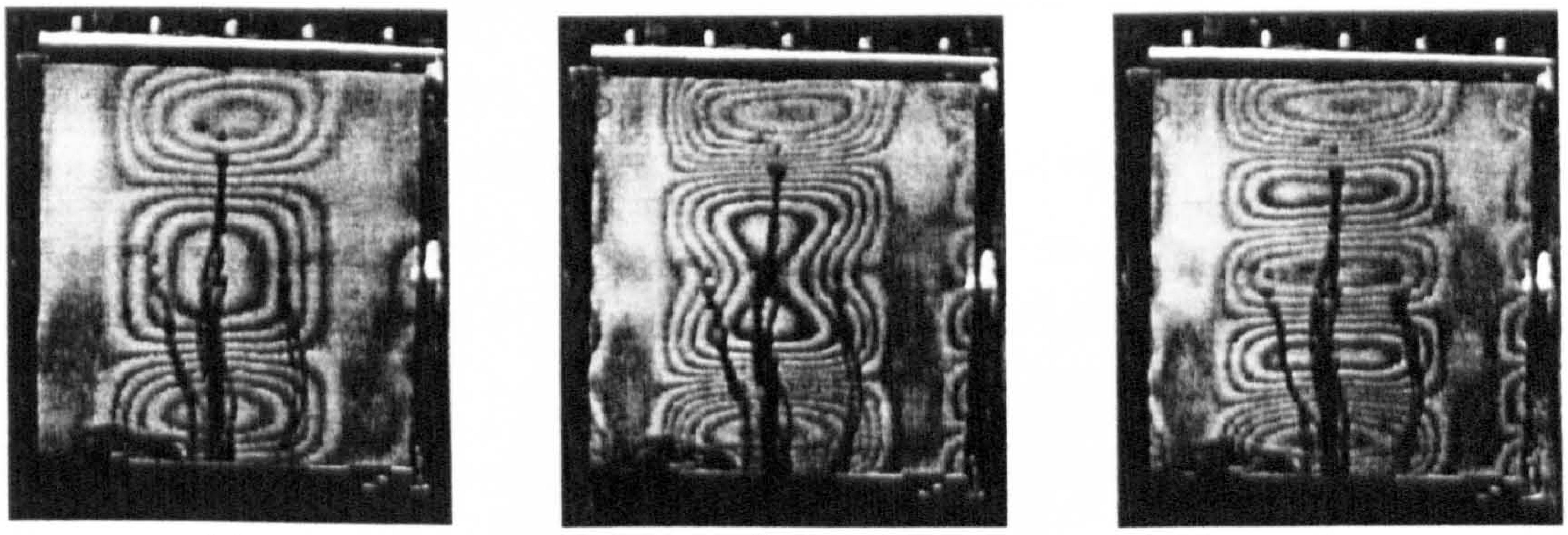
(a) (b) (c)

Figure 4.3: Moiré fringe patters for hat-stiffened panel at loading: (a) 40 kN, (b) 66 kN, and (c) 67 kN.

Strain gauges SG 1-2 (Figure 4.4), as well as strain gauges SG 9-10 (Figure 4.6) showed that at a loading of approximately 40 kN there was a gradual reduction in the bending strain at their location. With reference to the Moiré fringe patterns of Figure 4.3, it can be noted that the two strain gauge pairs were at locations close to the upper and lower buckle crests of the panel skin-bay. The reduction in bending strains could be attributed to a gradual mode shape change where the node lines shifted as the middle buckle became longer, and the top and bottom buckles shorter. This is clearly visible in Figure 4.3 (b), where as a result of the change in local curvature the central buckle peak formed a "waist".

At a load of 66 kN, a dynamic mode-jump to a five half-wave configuration was observed, shown in Figure 4.3 (c). At this loading, strain gauges SG 1-2 and SG 9-10 showed reductions in readings, evidence of this mode-jump, as was visible in Figure 4.4 and Figure 4.6. The reductions in strains occurred as the position of the strain gauges after the mode-jump was closer to a node line rather than a buckle crest as before the mode-jump. Such dramatic changes in curvature were not measured by strain gauges SG 3-4 at the dynamic mode-jump, but still some increase in strains were detected as can be seen in Figure 4.5 as a buckle crest moved closer to this position. The out-of-plane displacements as measured by LVDT A and LVDT B are further evidence of buckling and of the dynamic mode shape change. A rapid increase of out-of-plane displacement was visible in both Figure 4.7 and Figure 4.8 at the buckling load of 9.4 kN, and then a rapid change in recorded readings was also detectable at the mode-jump of the panel to the five half-wave configuration at a loading of 66 kN. This is particularly appreciable in Figure 4.7 relating to LVDT A as the recorded out-of-plane displacement was seen to change from 4.3 mm to -1.4 mm as a result of the mode-jump.

The first audible acoustic emission was detected at a loading of 26 kN, followed by further emissions at 29 kN and 33 kN. No damage was visible at this point, and hence the emission was attributed to matrix cracking. Prior to the mode-jump to five half-waves another cracking sound, again with no visible damage, was heard at 49 kN. The first visible damage occurred at 79 kN, and was observed at the node-lines of the unloaded edges in the upper left-hand region of the panel, shortly followed by failure in the bottom-right region. This damage was associated with transverse shear stress failure at the free edges, and it remained localized without propagating unstably. The panel failure at 103 kN occurred due to the local buckling of the hat-stiffeners.

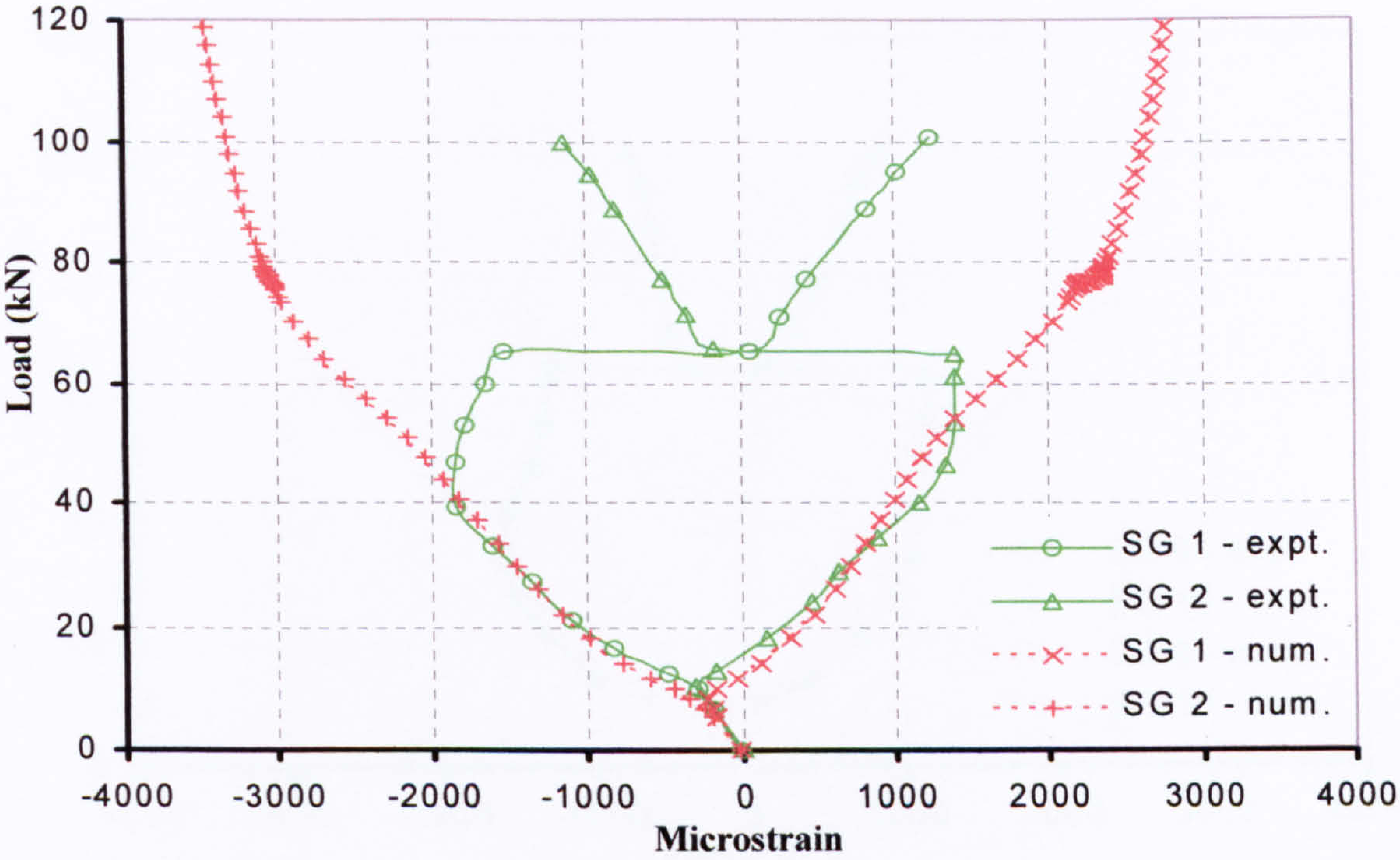

Figure 4.4: Hat-stiffened panel: experimental and numerical results for back-to-back strain gauge pair SG 1-2.

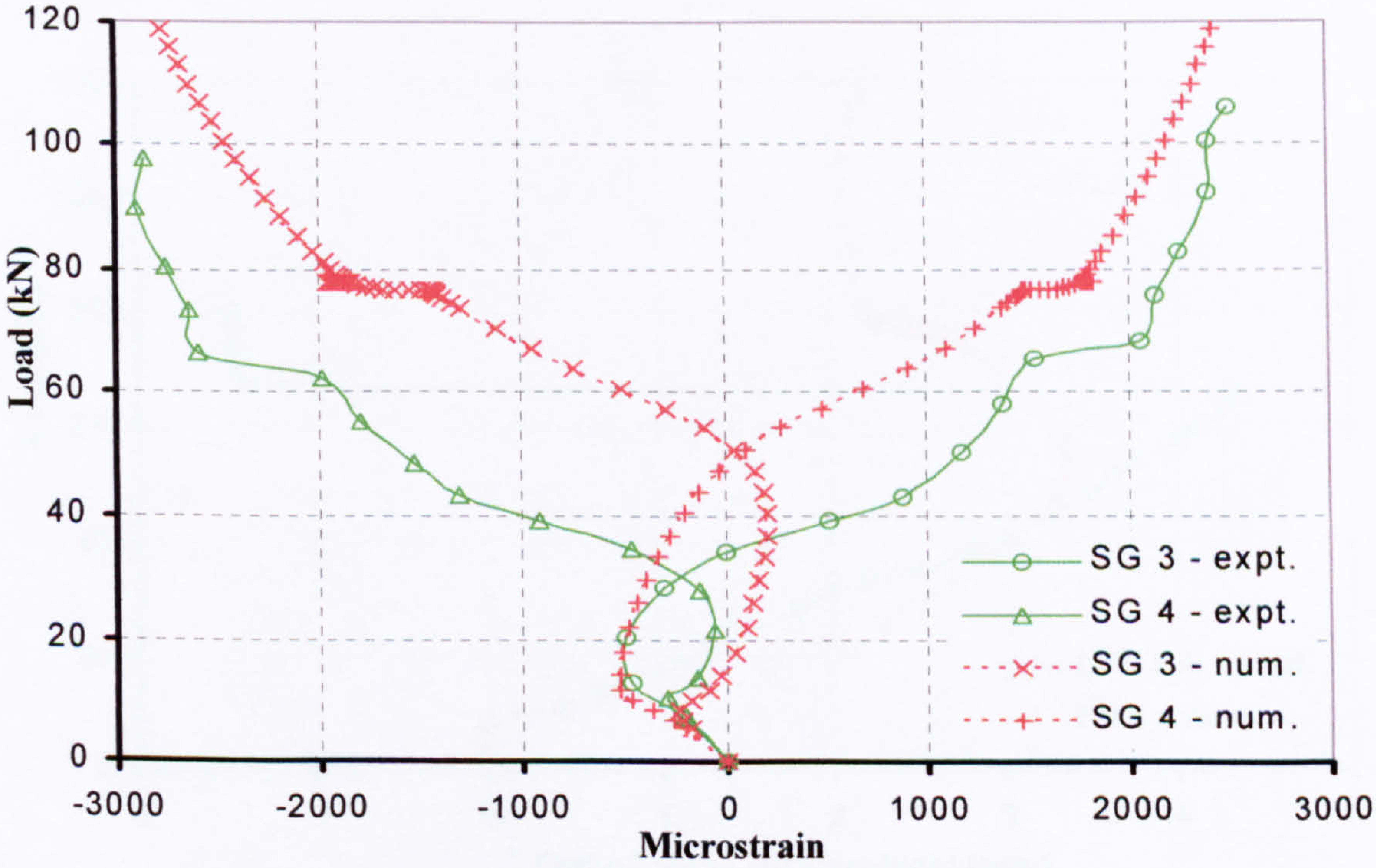

Figure 4.5: Hat-stiffened panel: experimental and numerical results for back-to-back strain gauge pair SG 3-4.

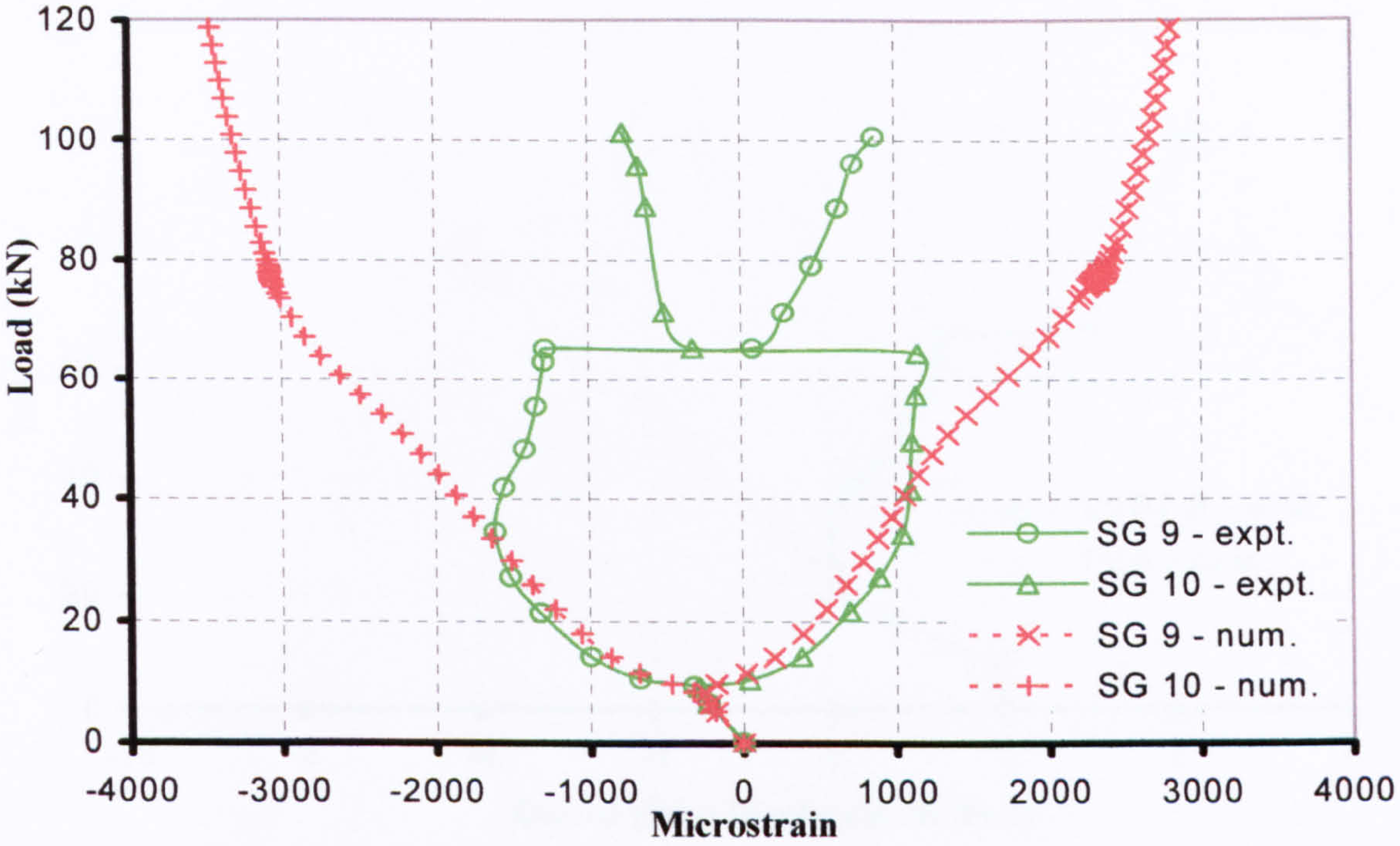

Figure 4.6: Hat-stiffened panel: experimental and numerical results for back-to-back strain gauge pair SG 9-10.

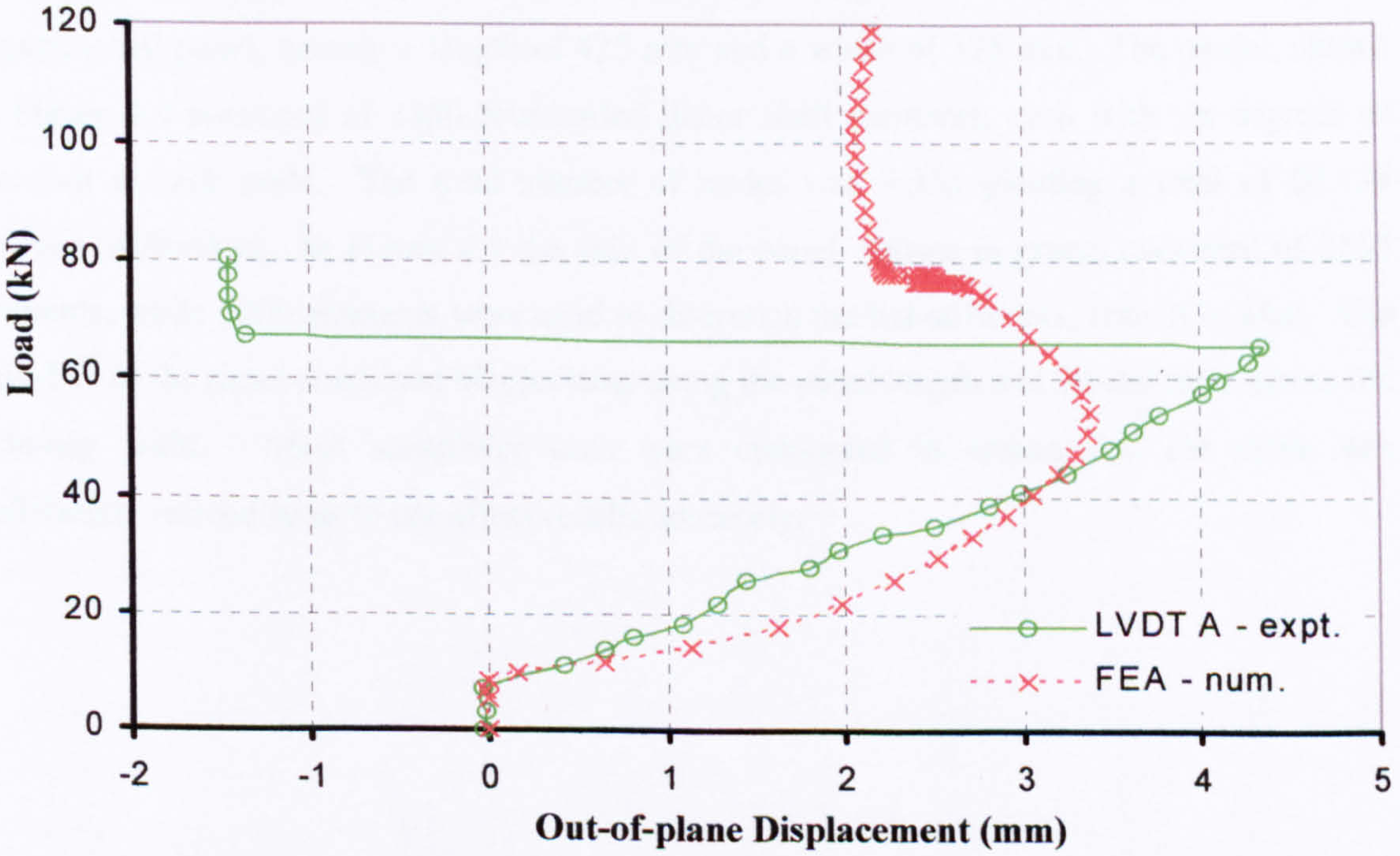

Figure 4.7: Hat-stiffened panel: experimental and numerical out-of-plane displacements at location A.

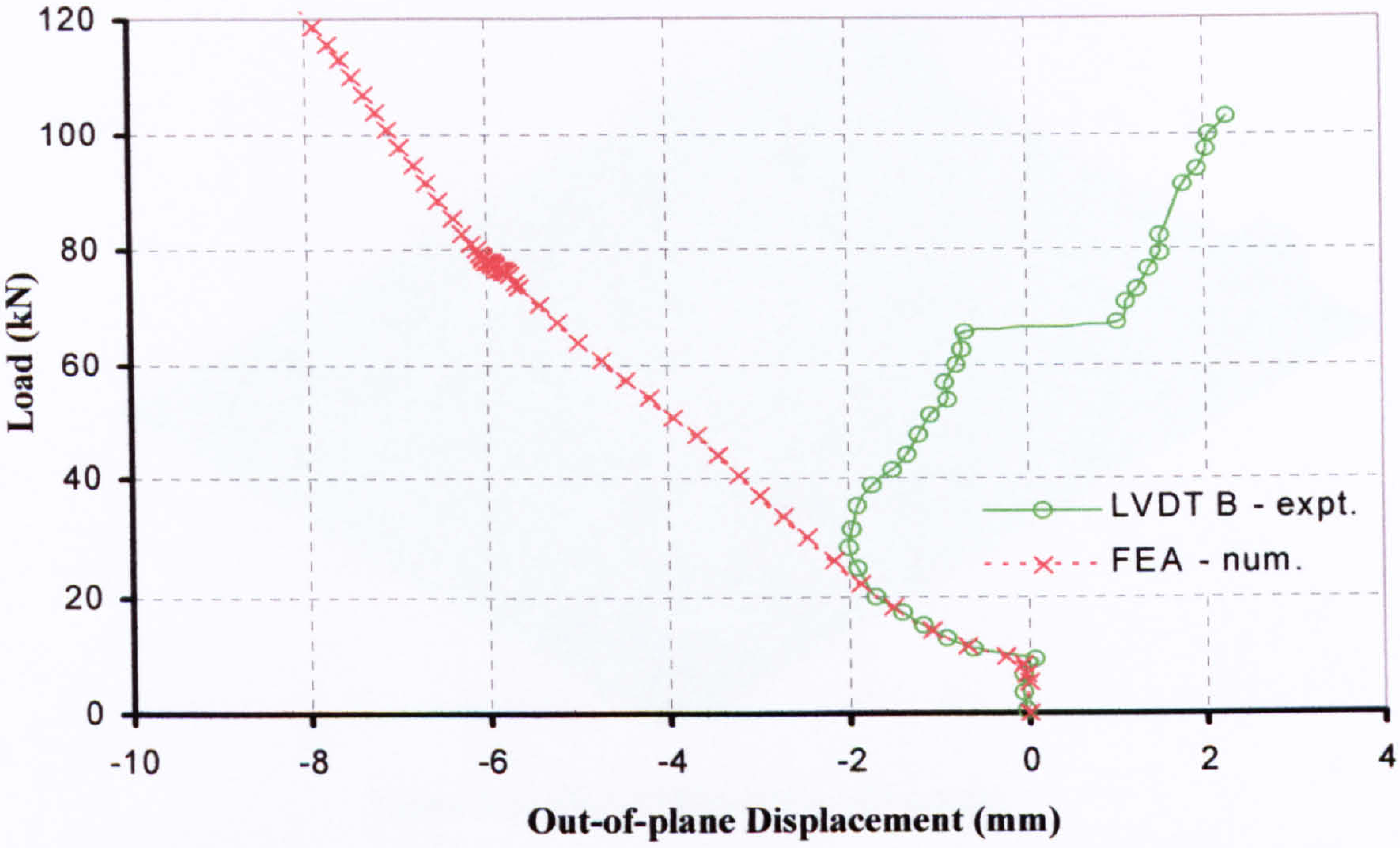

Figure 4.8: Hat-stiffened panel: experimental and numerical out-of-plane displacements at location B.

4.1.3 Finite element model

An FE model to replicate the hat-stiffened panel was created using the FE package ABAQUS. The panel model had dimension corresponding to the effective test section of the experimental panel, namely a length of 425 mm and a width of 335 mm. The model, shown in Figure 4.9 consisted of 3360 four-noded linear shell elements, each with six degrees of freedom at each node. The total number of nodes was 3,355 yielding a total of 20,130 degrees of freedom. In Figure 4.9 the skin of the panel, shown in green, consisted of 2160 elements, while 1200 elements were used to discretize the hat-stiffeners, shown in blue. The skin-bay of the panel contained 60 elements along the panel length and 20 elements across the skin-bay width. Mesh sensitivity tests were conducted to ensure that the mesh was sufficiently refined so as to not affect results adversely.

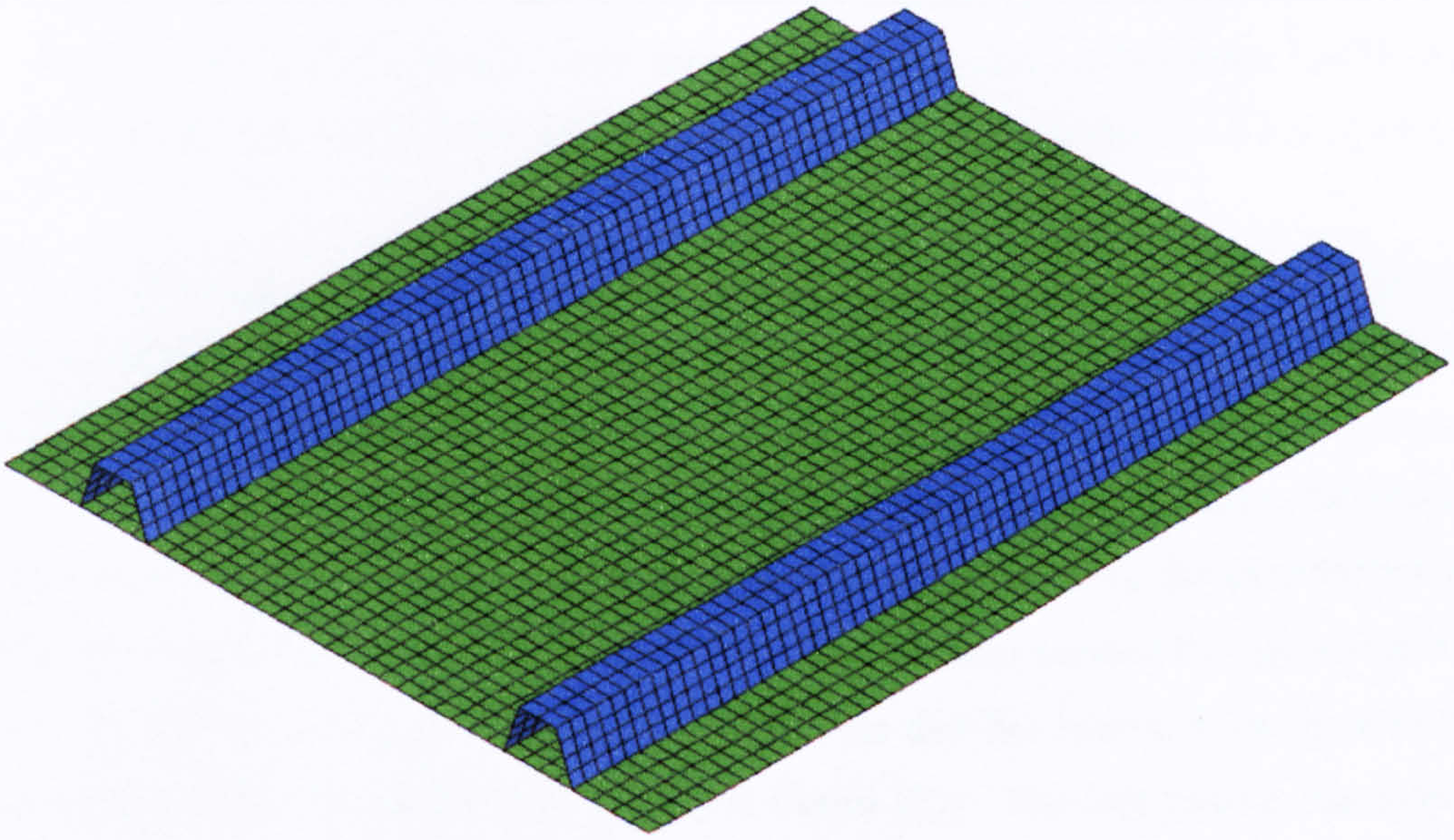

Figure 4.9: Hat-stiffened panel FE model.

Composite sections were used to define the appropriate lay-up of $[\pm45,0,90]_S$ for the skin and hat-stiffeners. Local coordinate systems were set-up so as to ensure correct material orientations as the plies "wrapped" around the hat stiffeners and elements were assigned the material properties of Table 4.1. The loading on the panel was modelled by initially restraining both panel ends in all degrees of freedom, hence replicating a clamped boundary condition. Following this, the longitudinal translational degree of freedom at one end was released and prescribed a displacement to model the displacement-controlled loading on the experimental panel.

4.1.4 Linear eigenvalue buckling analysis results

The FE analysis conducted on the panel model to trace its buckling and postbuckling response consisted of two steps, as discussed in Chapter 3. The first was a linear eigenvalue buckling analysis to find the eigenvalues and associated mode shapes of the panel. This was then followed by a non-linear quasi-static analysis to trace the panel's response deep into its postbuckling regime. To account for initial geometric imperfections, the initial buckling mode shape was scaled such that the maximum out-of-plane displacement imperfection corresponded to a small percentage of the skin thickness. The magnitude of the imperfection as well as mode shapes to which it corresponds was altered in a parametric study to assess the imperfection sensitivity of the hat-stiffened panel FE model. The imperfections were introduced into the model prior to running of the non-linear analyses, which also included viscous damping to cope with the potential mode-jumps in the solution. A parametric study was also conducted to see how the amount of viscous damping affects the non-linear FE solution. The final FE analysis results were then compared to the experimental LVDT and strain gauge readings, and out-of-plane displacement contours with the observed Moiré fringe patterns.

The linear eigenvalue analyses revealed an overestimation of the prebuckling stiffness and initial buckling load of the hat-stiffened panel when using the nominal material properties of Table 4.1. It must also be noted that these properties are tensile values which, as expected, will yield an overestimation in prebuckling stiffness and buckling load. To account for this, the elastic moduli used in the FE analyses were adjusted using the experimentally observed prebuckling stiffness and reduced by 9.3%. This can also account for any variability arising form the manufacturing process and is a technique that has been previously used by Stanley and Felippa [52], Nagendra et al. [53], and Cerini [23]. The first three mode shapes predicted by the linear eigenvalue buckling analysis are shown in Figure 4.10.

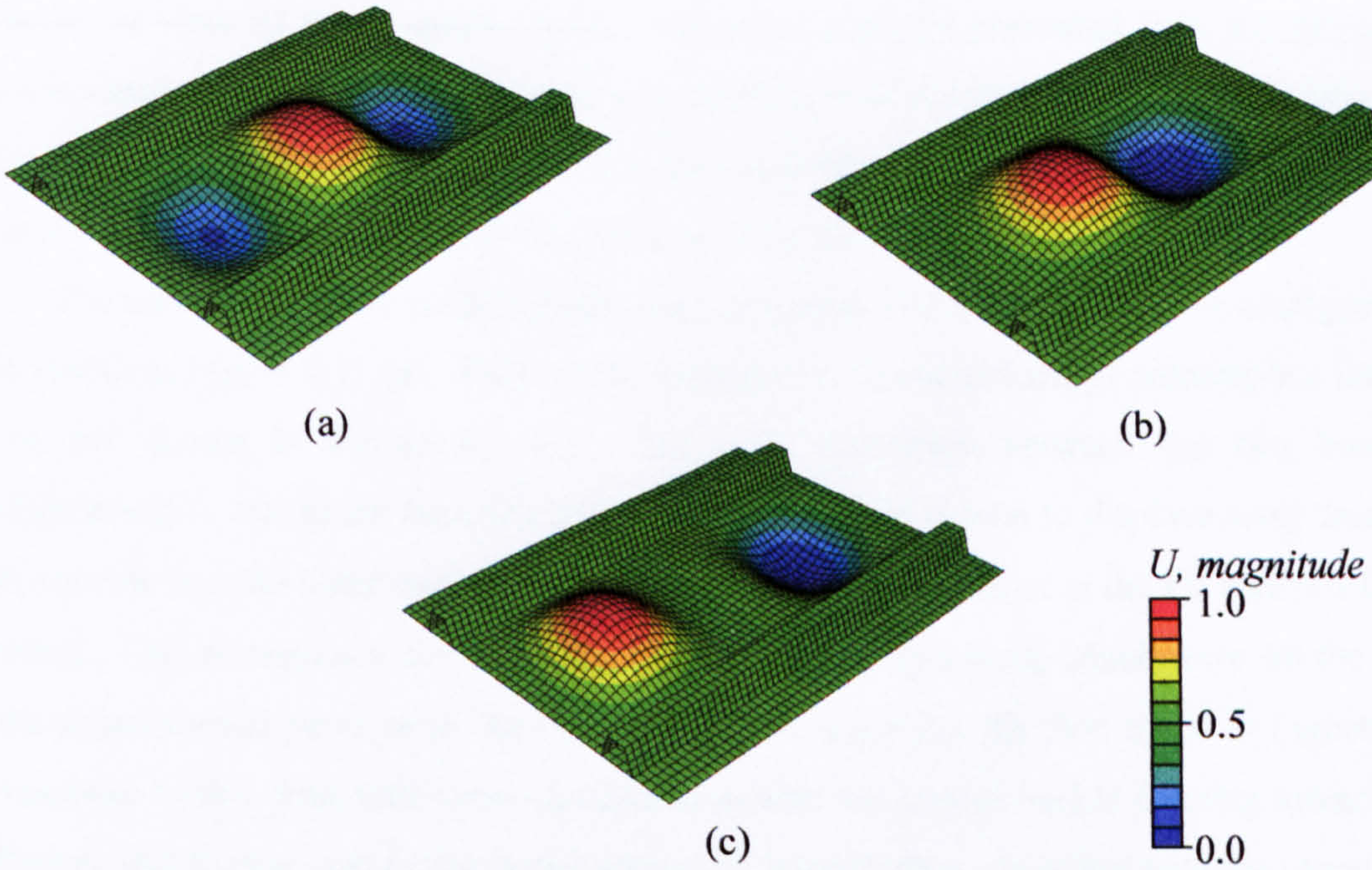
(a)

(b)

(c)

Figure 4.10: Hat-stiffened panel: linear buckling analysis mode shapes. First mode (a), second mode (b), and third mode (c).

It can be seen how the first mode shape associated with the hat-stiffened panel corresponds to a three half-wave configuration, whilst the second and third mode-shapes correspond to different two half-wave configurations. Table 4.2 shows the results of the linear eigenvalue analysis. The buckling load, corresponding to the first eigenvalue, was 9.46 kN, in close agreement with the experimentally observed buckling load of 9.4 kN.

Table 4.2: Results of linear eigenvalue analysis on hat-stiffened panel.

Eigenvalue	Load
1 – Buckling load	9.46 kN
2	9.73 kN
3	11.44 kN

4.1.5 Non-linear analysis results

Before comparing the numerical non-linear FE analysis results with the experimental results, a parametric study was conducted in order to assess the sensitivity of the hat-stiffened panel model to the geometric imperfection introduced, as well as the effect that viscous damping may have on the accuracy of the solution. Results of these parametric studies are presented after the comparison of the experimental results with the final numerical solution. However in view of these results, in the numerical analysis presented here the geometric imperfection introduced to the panel was a superposition of the first three buckling modes and had a maximum out-of-plane displacement corresponding to 6% of the skin thickness. The viscosity parameter took a value of 2% of the default ABAQUS value.

The non-linear solver predicted the panel to buckle into a three half-wave configuration as is visible in Figure 4.11 (a). This can be compared to the Moiré fringe patterns at a loading of 40 kN shown in Figure 4.3 (a). The only difference between the two buckling configurations is that in the experiment the central buckle was seen to displace away from the stiffener side and the outer buckles towards the stiffener side, whilst in the FE analysis this is reversed. This discrepancy can be attributed to initial imperfections, which were not the same in the experimental panel as in the FE mode. The shape for the first mode in Figure 4.10 corresponds to this three half-wave configuration with the central buckle forming towards the stiffeners, and formed part of the initial geometric imperfection - together with the second and third modes - to the FE panel model.

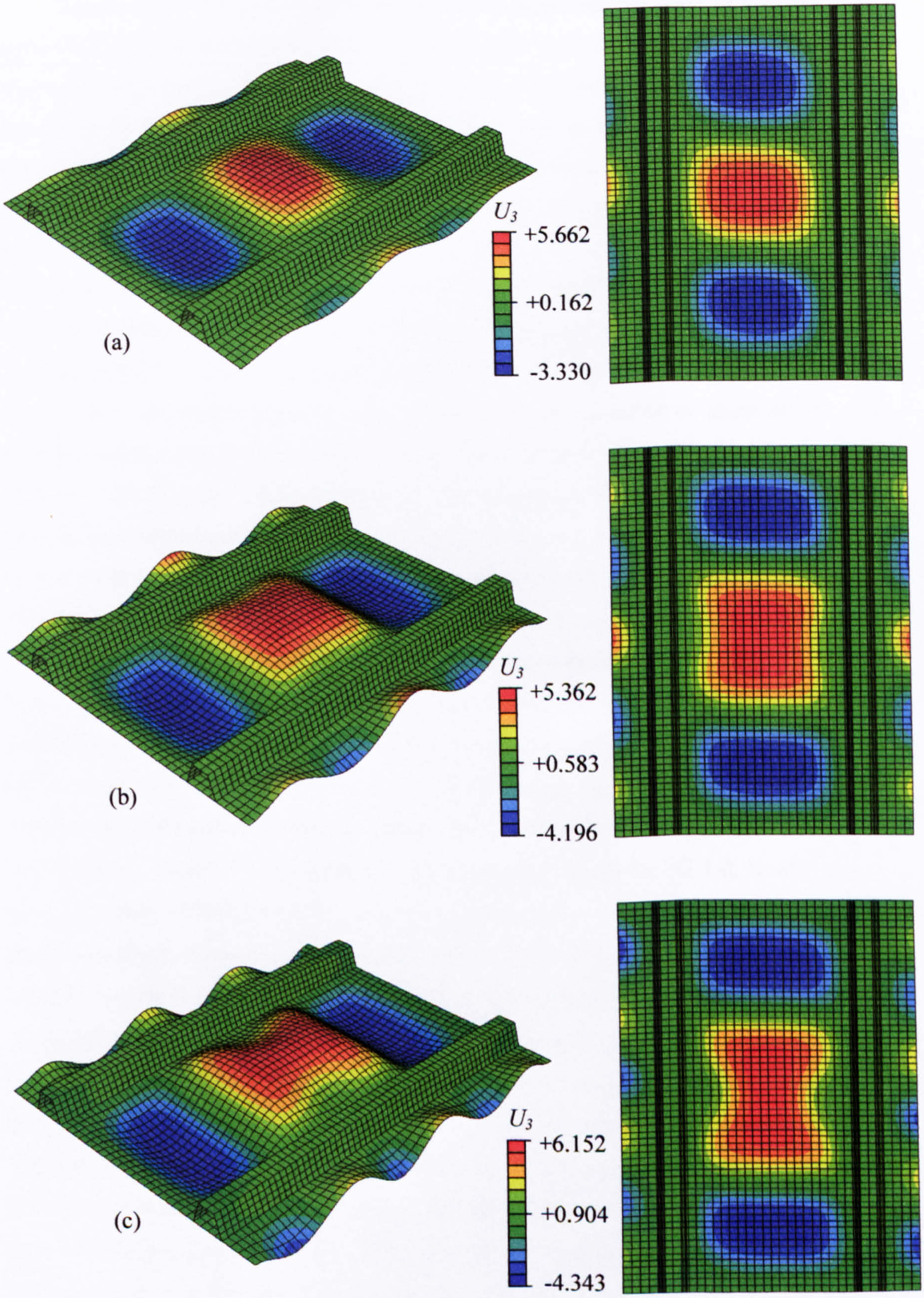

Figure 4.11: Numerical analysis: deformed shape (scale factor five) and out-of-plane displacement contour plots for hat-stiffened panel at loading: (a) 40 kN, (b) 66 kN, (c) 80 kN.

Figures 4.4 – 4.6 show that in all the strain gauge readings there is generally good agreement between the experimental and numerically predicted load at which the strains begin to diverge for each strain gauge pair, evidence of the initial buckling of the panel. At a loading of 40 kN a reduction in the bending strains was recorded experimentally by strain gauges SG 1-2 and SG 9-10 as can be seen in Figure 4.4 and Figure 4.6 respectively. This was associated with the formation of a "waist" in the middle buckle peak and increase in aspect ratio of the top and bottom buckle peaks. This was predicted by the non-linear analysis as well, as the out-of-plane displacement contours of Figure 4.11 (b) for a 66 kN load show. However the formation of this waist occurred more gradually in the FE model, evidenced by the lesser reduction in the strain gauge readings SG 1-2 and SG 9-10 of Figure 4.4 and Figure 4.6. In fact, the strains began to reduce substantially at a loading of about 80 kN. The experimental dynamic mode-jump to six half-waves could not be captured by the numerical analysis. The FE panel continued to remain in the three half-wave configuration, with the waist in the middle buckle crest becoming more pronounced as shown in Figure 4.11 (c). A sudden mode-jump did however occur in the portions of skin to the outside of the two hat-stiffeners. This was a jump from the initial five half-waves to a six-half-wave configuration.

The inability of the FE analysis to capture the dynamic mode-jump could be attributed to the microcracking that occurred in the experimental panel at 26 kN, 29 kN, and 33 kN as evidenced by the acoustic emissions. Microcracking and delamination within the panel are not accounted for in the FE model, and in reality change the stiffness of the structure and therefore could be responsible for the panel skin-bay suddenly jumping to the five half-wave configuration. Figure 4.4 illustrates how strain gauge readings for SG 1-2, located near the top buckle crest of the initial half-wave configuration showed very good correlation between experimental and numerical results in the initial postbuckling region. As the central half-wave formed the waist, then as mentioned earlier the strains observed experimentally reduced faster than those predicted numerically. The same comments can be made regarding SG 9-10, positioned on the lower buckle crest of the initial buckling configuration. The reversal in curvature visible in Figure 4.5 relating to SG 3-4 was also predicted numerically, albeit in a more gradual fashion. This reversal was due to the waist formation in the central buckle crest and increase in aspect ratio of the top and bottom buckle crests. Figure 4.5 also shows how the numerical analysis predicted a sudden increase in the strains at about 76 kN. This is at a loading just prior to the outer skin portions changing form a five half-wave configuration to a six half-wave configuration as mentioned earlier. The experimental increase in the strains at 66 kN was due to the jump of the skin-bay to the five half-wave configuration.

The observations made relating to the strain gauge results are confirmed by those of the out-of-plane displacements. Figure 4.7 shows the correlation of the numerically predicted out-of-plane displacement with the measured out-of-plane displacement of LVDT A. The experimental displacement is slightly higher than the numerical one up to a load of around 44 kN, at which point the rate of increase in the numerically predicted displacement starts reducing. At 66 kN the experimental displacement reverses due to the dynamic mode-jump. Figure 4.8 shows the correlation in out-of-plane displacement at point B, whose agreement between experimental and numerical values is very good in the initial postbuckling regime. This cannot be said at higher loads, where due to the more rapid waist formation of the middle buckle crest the experimental out-of-plane displacement reduces before reversing sign at the mode-jump. Note that in Figure 4.7 and Figure 4.8 the numerical out-of-plane displacements were reversed for comparison with the numerically predicted values, in view of the different direction of buckling between the panel model and the experiment.

The static path-following FE methods used in this section showed that good quantitative agreement in the results was obtained for buckling as well as in the initial post-buckling regime of the hat-stiffened panel. Deeper in the postbuckling regime, correlation between experiment and numerical analysis was fair at best. To improve this and obtain a better prediction of the hat-stiffened panel's behaviour, more efficient methods combining static and dynamic solutions may be implemented [23,36,37]. However, the use of such methods will increase computational cost, and are hence not suited to FE based optimization algorithms. Furthermore, it was seen how some of the discrepancy between experimental and numerical results later in the postbuckling regime of the hat-stiffened panel could be attributed to the matrix cracking observed experimentally as well as out-of-plane damage mechanisms which was not captured by FE analyses. Out-of-plane failure and its modelling will be investigated in Chapter 5.

4.1.6 Imperfection sensitivity

As discussed in Chapter 3, geometric imperfections were introduced into the FE model prior to conduction the non-linear analysis so as to remove bifurcations. In fact, the introduction of an imperfection means that a bifurcation becomes a limit point. The initial imperfection magnitude was altered and its effect investigated. The imperfection corresponded to a linear superposition of the first three buckle mode shapes of the panel. The amount of viscous damping introduced into the analysis was kept at 1% of the default value so as to not affect results, as discussed in the next section.

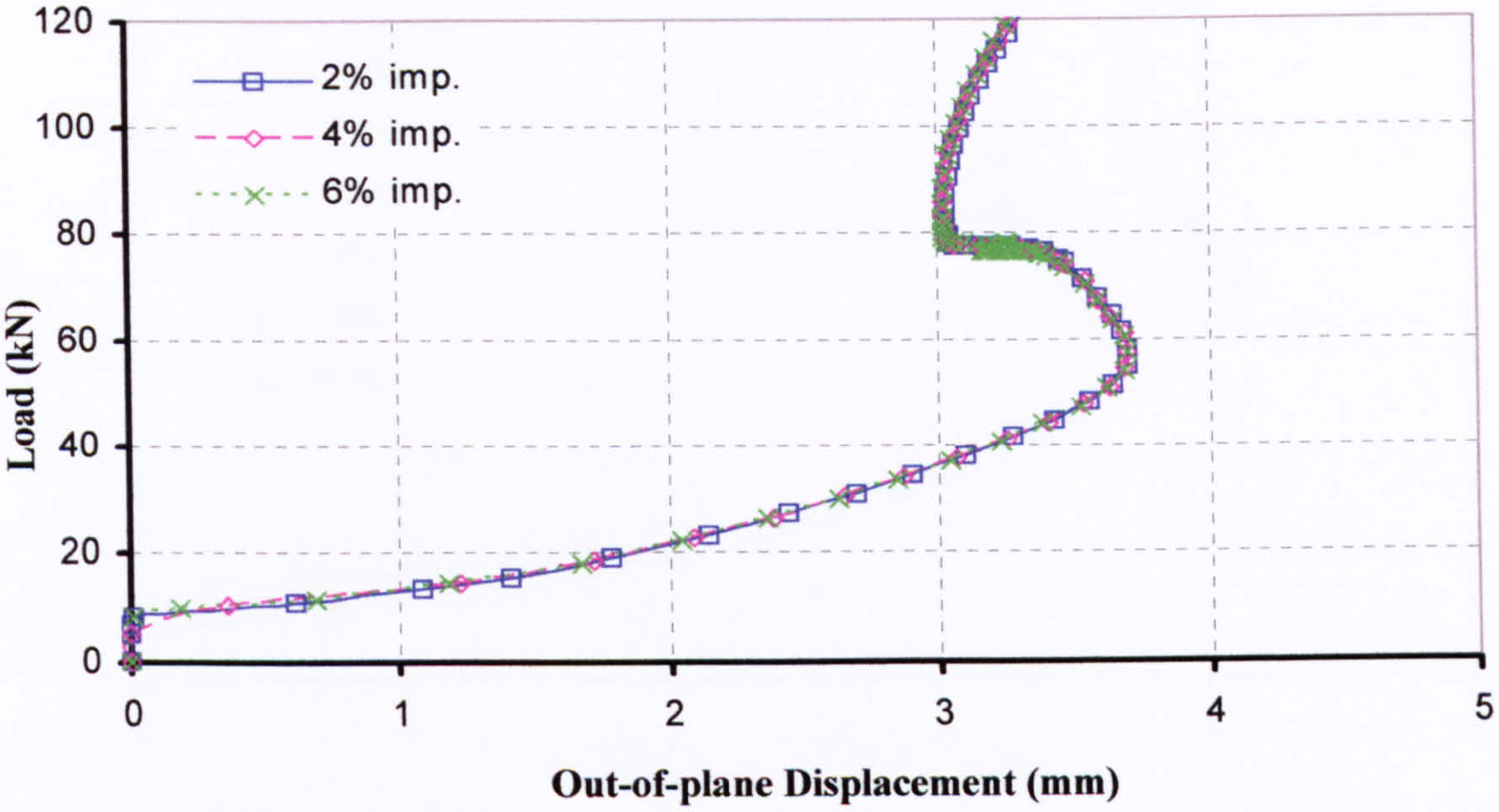

Figure 4.12: Effect of imperfection type and magnitude on numerically predicted out-of-plane displacements at location A.

Figure 4.12 shows the effect that changing the imperfection amplitude and type has on the numerically predicted postbuckling behaviour of the hat-stiffened panel. The out-of-plane displacements are compared at the experimental position of LVDT A. Changing the imperfection magnitude has no effect on the predicted panel behaviour as can be seen by the dark blue, pink, and green curves being practically identical. In view of the results shown in Figure 4.12, it can be said that the hat-stiffened panel FE model is imperfection insensitive.

4.1.7 Effect of viscous damping

Like in the case of geometric imperfections, a parametric study was conducted to assess the effect that modifying the amount of viscous damping introduced into the analysis has on the FE solution. In the absence of any viscous damping, the analysis aborts prematurely. This is due to the inability of the non-linear solver in traversing the limit point in the load-displacement curve at the point of the secondary instability. The introduction of initial imperfections means that a bifurcation point is transformed into a limit point, but still the convergence difficulties prevent the solver in converging without the introduction of viscous damping.

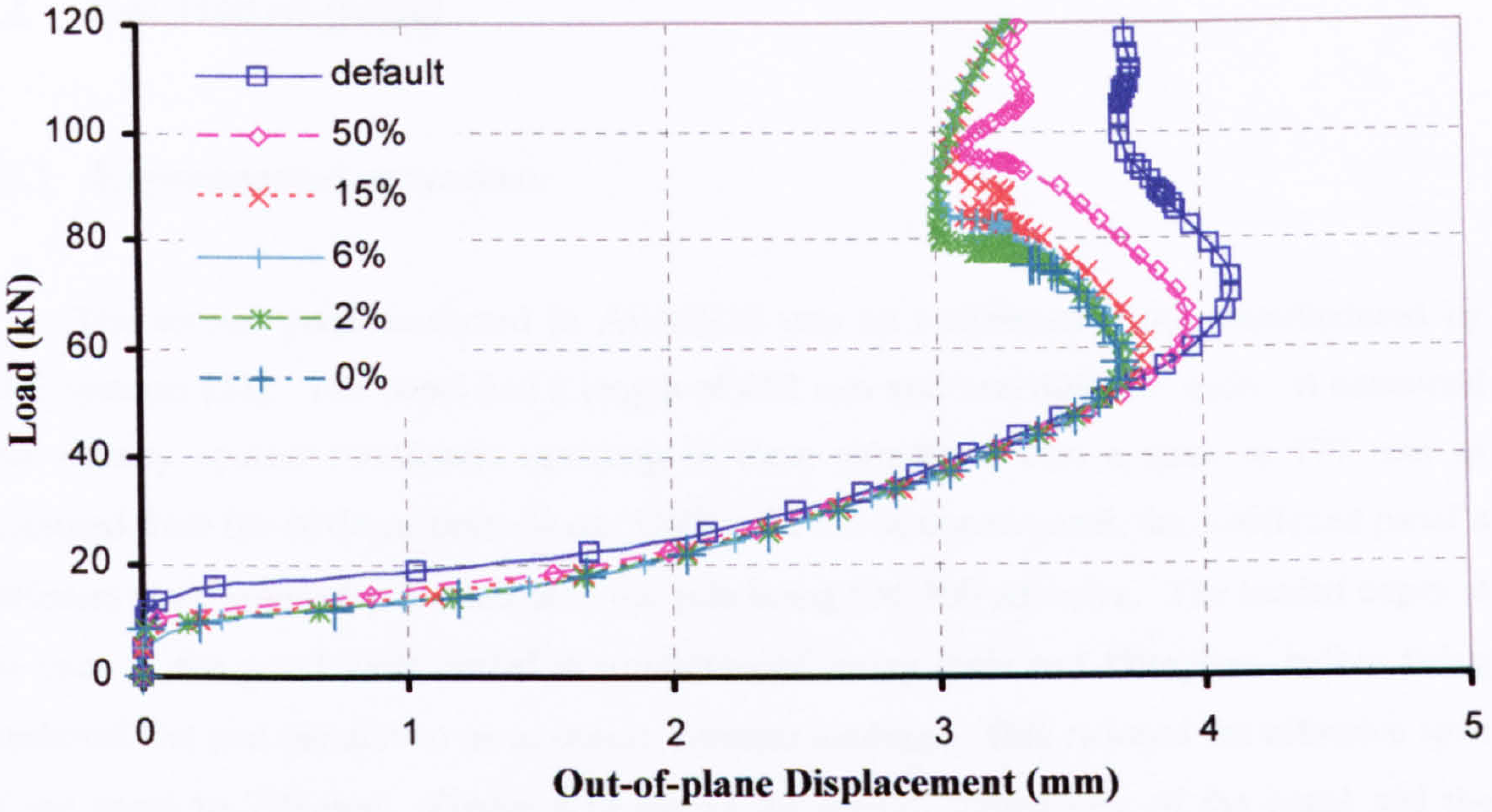

Figure 4.13: Effect of viscosity parameter on numerically predicted out-of-plane displacements at location A.

Figure 4.13 shows the out-of-plane displacement predicted by the FE non-linear analysis at the location of LVDT A in Figure 4.1. The results with five values of viscous damping as well as without the energy dissipation scheme are shown. The dark blue line refers to the default amount of damping when the stabilize option discussed in Chapter 3 is added to the analysis. The other lines refer to percentages of this default damping value. Intermediate damping values such as 20% and 6% indicate how as the damping value is reduced from the default value, then the solution "moves" towards convergent values. It is clear how convergence in the solution occurs for a low damping value, as the light blue and green lines indicate for 2% and 6% of the default damping value respectively. These values for the out-of-plane displacements are practically identical to those predicted by the non-linear solver with no viscous damping prior to premature analysis termination. This termination in the analysis with no damping occurs at the point of the mode-jump that was observed in the skin portions on either side of the hat-stiffeners. Figure 4.13 also shows that an insufficient reduction in the viscous damping value leads to an inaccurate solution. The buckling load is seen to be higher, as can be seen by the point at which the out-of-plane displacement starts increasing rapidly (about 11.69 kN for the default damping parameter against 9.46 kN for convergent solutions corresponding to lower damping values). For the remainder of the solution history, the out-of-plane displacements are inaccurate too, although following the same general trend. This highlights the importance of conducting such a parametric analysis on the amount of viscous damping used to ensure that the results are not affected adversely.

4.2 I-stiffened panel

4.2.1 Experimental procedure

The second panel analyzed in ABAQUS was an I-stiffened panel manufactured by BAE systems [23]. The panel had a length of 850 mm and was 604 mm wide. It contained four equally spaced I-stiffeners resulting in three skin-bays with a span of 177 mm as measured from the stiffener centrelines. Unlike the hat-stiffened panel, the I-stiffened panel's stiffeners were secondary bonded onto the skin using FM-300 adhesive. The loaded edges at the ends of the panel were potted in a mixture of epoxy resin and fibreglass, before being machined flat and parallel so as to ensure uniform loading. This reduced the effective span of the panel to 790 mm. Figure 4.14 shows the overall dimensions of the panel and the location of the stiffeners. The skin had a lay-up of $[45,-45,0_2,-45,45,90_2]_S$ corresponding to a skin thickness of 2.0 mm. The stiffeners had a height of 31.6 mm, and a cap measuring 31.0 mm in width as illustrated in Figure 4.15 (a). The stiffener flanges had a lay-up of $[45,-45,-45,45,0_4]$ with a drop-off scheme as shown in Figure 4.15 (b), and plies "continued" into the web and cap. Figure 4.16 (a) is a C-scan image of the stiffener flange near the web of the stiffener, whilst Figure 4.16 (b) is a C-scan image of the stiffener web itself, both illustrating how some plies terminated in the vicinity of the stiffener web and in the web itself. The panel was manufactured using T300/914 unidirectional prepreg. Table 4.3 shows the unidirectional properties of the material as determined by BAE systems.

Table 4.3: Nominal material data for T300/914 Unidirectional Prepreg.

Property	Value
Longitudinal tensile modulus	135 GPa
Longitudinal compressive modulus	120 GPa
Transverse tensile modulus	9 GPa
Transverse compressive modulus	9 GPa
In-plane shear modulus	4.9 GPa
Poisson's ratio	0.28
Ply thickness	0.125 mm

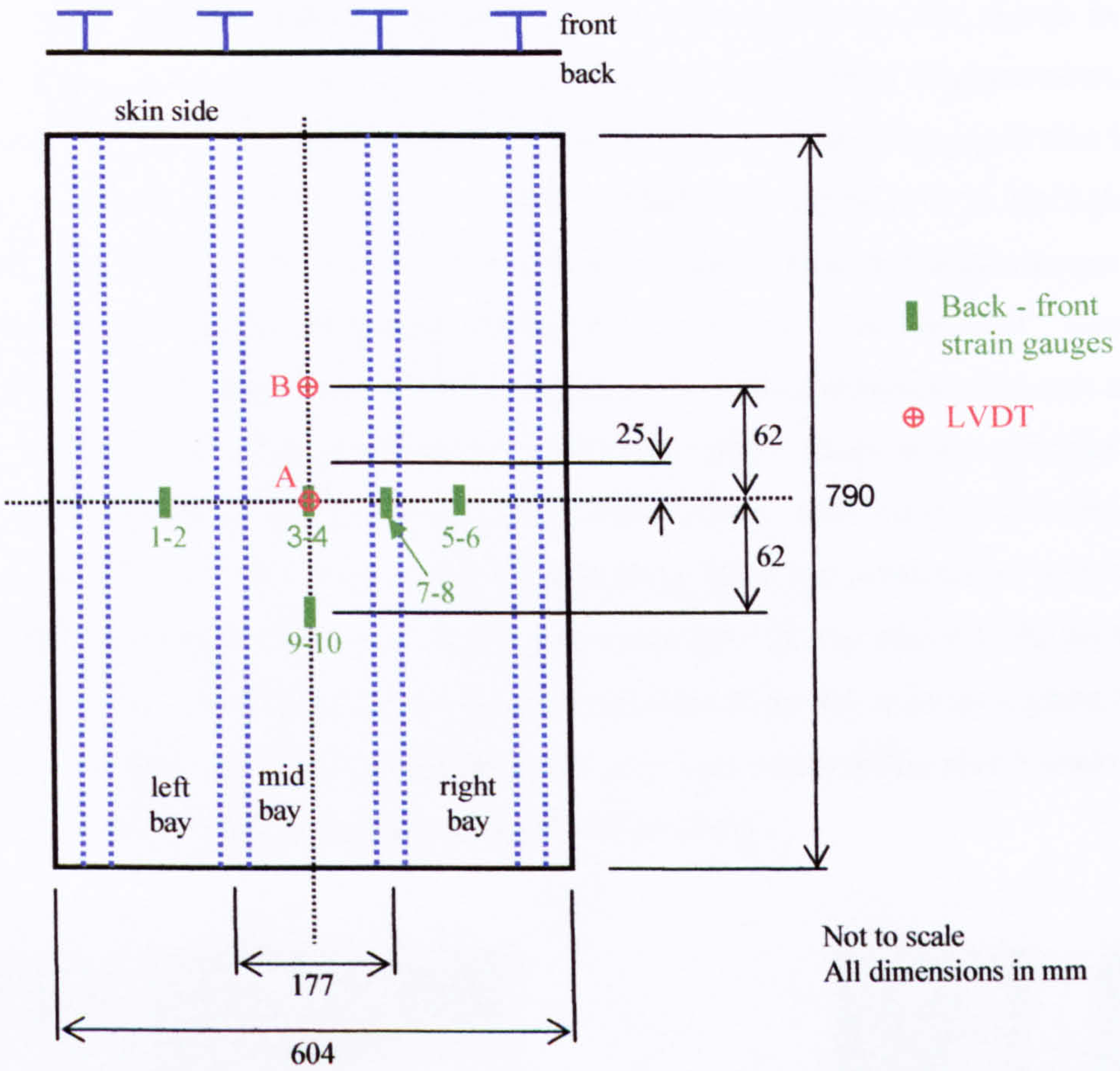

Figure 4.14: I-stiffened panel: effective test section dimensions with strain gauge and LVDT locations.

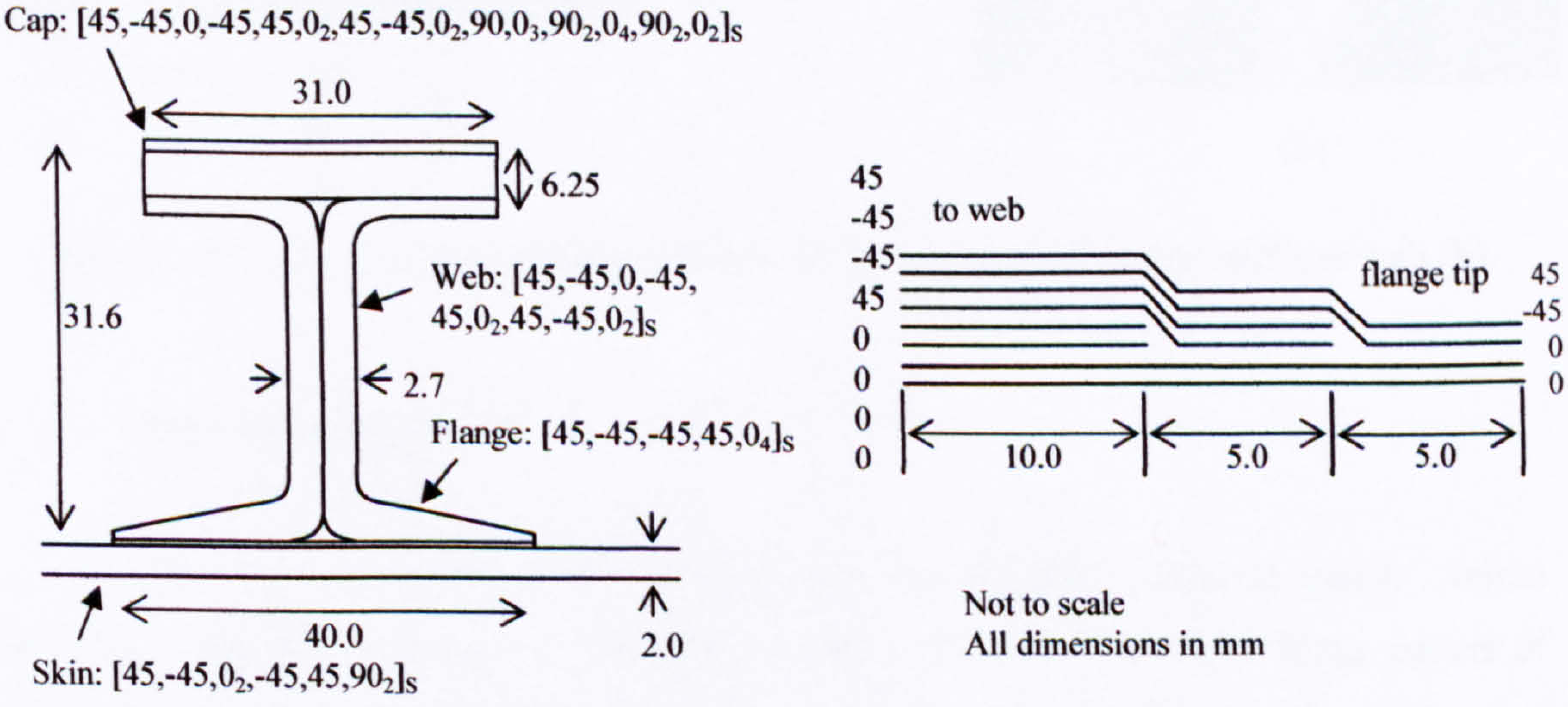

(a) (b)

Figure 4.15: I-stiffeners: dimension and lay-up (a) with ply drop-off detail (b).

Back-to-back strain gauges and LVDTs, whose locations are shown in Figure 4.14, were mounted on the panel to monitor strains and out-of-plane displacements. A back-to-back strain gauge pair was placed at the centre of each of the three panel skin bays. SG 1-2 were located in the left bay, SG 3-4 in the middle bay, and SG 5-6 in the right bay. These locations were selected so that in the case of an odd number of buckles across the length of the panel, then the strain gauges would be located near a buckle crest. Correspondingly, another set of strain gauges, SG 9-10 was placed a vertical distance of 62 mm away from the panel centre as illustrated in Figure 4.14 so as to capture strains near a potential buckle node-line. By similar reasoning out-of-plane displacements were measured at the centre of the panel by LVDT A and at a position 62 mm away from the panel centre by LVDT B (in the opposite direction to SG 9-10). Strain gauge pair SG 7-8 was placed at the location of one of the stiffeners. Shadow Moiré fringe patterns were observed so as to capture the qualitative buckling behaviour of the I-stiffened panel as it was compression tested under displacement control with a crosshead displacement of 0.04 mm/min.

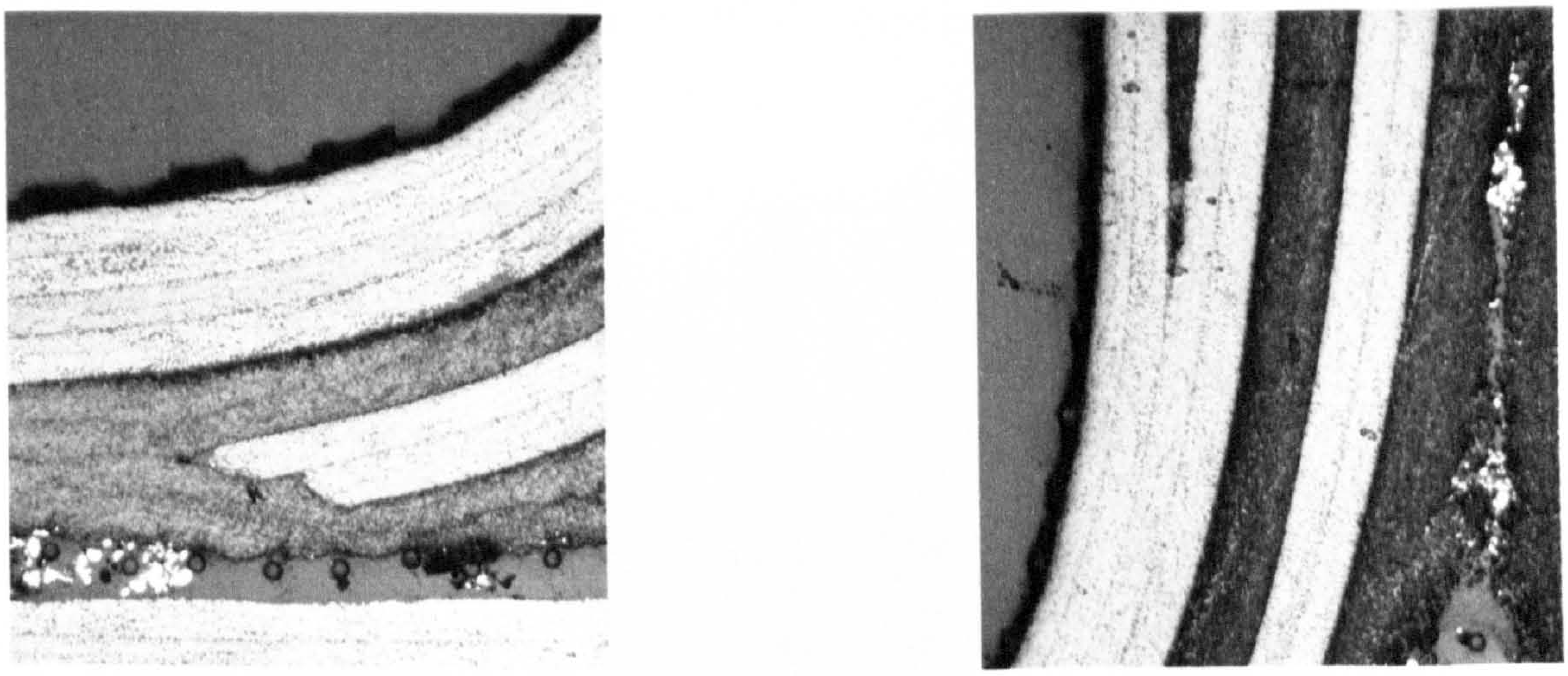
(a) (b)

Figure 4.16: C-scan image of stiffener flange at the web end (a) and of stiffener web (b).

4.2.2 Experimental results

Figure 4.18 shows the load-displacement curve for the I-stiffened panel. Initial buckling of the panel occurred at a loading of about 120 kN. The Moiré fringe patters of Figure 4.17 (a) show how at 160 kN the buckle pattern was fully developed and constituted of a five half-wave configuration in all three of the skin bays. Adjacent skin bays interacted with each other so that buckles either side of a stiffener had opposite magnitude out-of-plane displacements. Evidence of buckling was seen in all strain gauge readings. At the buckling load of 120 kN back-to-back strain readings in Figures 4.19 – 4.21 began to diverge significantly due to the curvature in the skin caused by the buckle crests. Buckling was also clear in both LVDT A and LVDT B readings as out-of-plane displacements quickly increased as a result of buckling in Figure 4.22 and Figure 4.23 respectively. The higher readings at LVDT A than LVDT B indicated how the former was close to a buckle crest location whilst the latter was adjacent to a buckle node line. Numerical results on the figures presented relating to the developed FE model will be discussed later.

At a 241 kN the I-stiffened panel exhibited a sudden mode-jump to a six half-wave configuration. Figure 4.17 (b) shows how this occurred in all three of the skin bays. Because of the new configuration in the buckle shape of the panel, LVDT A was now close to a buckle node-line and the out-of-plane displacements recorded at this location reduced significantly as is clear in Figure 4.22. Conversely point B recorded a sudden increase in out-of-plane displacements as a buckle crest relocated to its vicinity. The strains in Figure 4.18 and Figure 4.19, as expected, recorded a reduction in the strains due to their location at the centre of the skin bays, whilst Figure 4.21 shows how SG 9-10 recorded a decrease in readings for the same reasoning just discussed relating to the out-of-plane displacements. An audible snap was heard when the sudden mode-jump occurred.

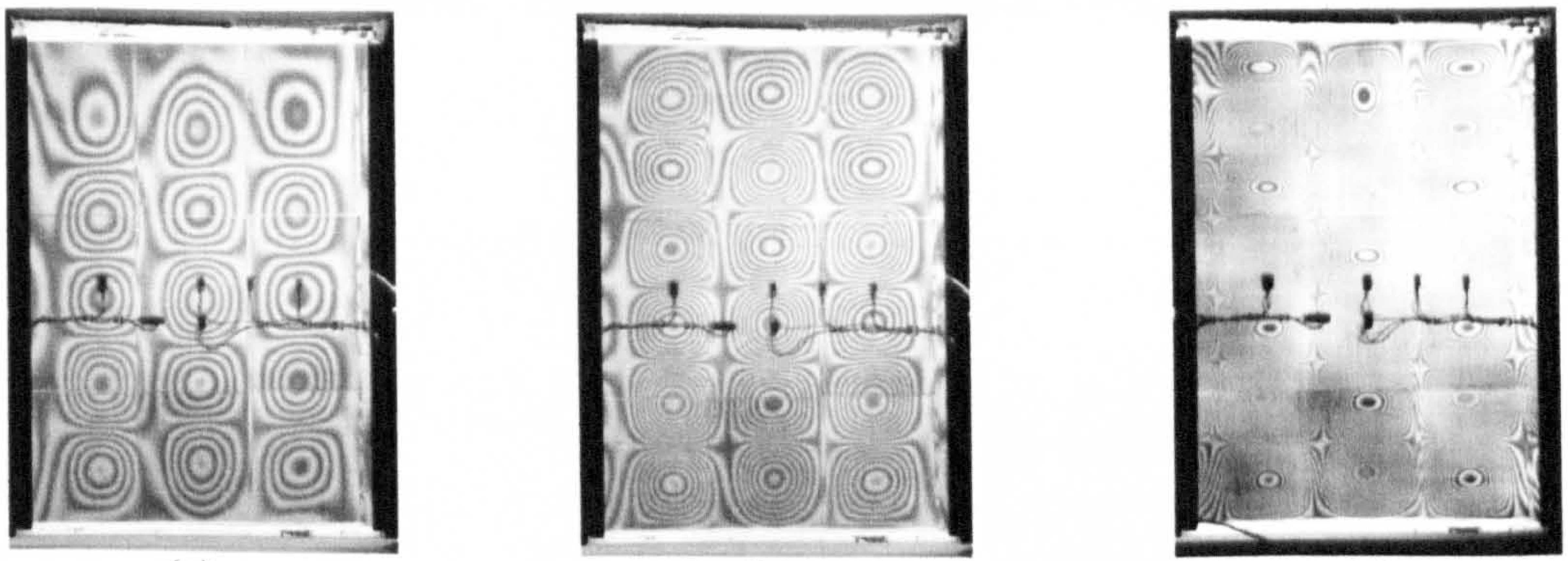
(a) (b) (c)

Figure 4.17: Moiré fringe patters for I-stiffened panel at loading: (a) 160 kN, (b) 242 kN, (c) 487 kN.

Further sudden mode-jumps were observed first in the left bay at 473 kN and then in the right bay at 486 kN. These corresponded to a change into a seven half-wave configuration. Figure 4.17 (c) shows how the middle bay remained in the six half-wave configuration, but the top buckle crest appeared elongated highlighting the interaction of skin-bays with one another across the stiffeners. This was evidenced by the top buckle in the left and right bays being squeezed. Strains in the right and left bays again showed a sudden change at the loadings corresponding to the mode-jumps to seven half-waves, and SG 3-4 as well as SG 7-8 located in the middle bay recorded similar sudden changes even if no "complete" mode-jump occurred in this skin bay. This was also true of recorded out-of-plane displacement readings in Figure 4.22 and Figure 4.23.

Panel collapse occurred at 525 kN following audible acoustic emission occurring on several occasions between loadings of 518 kN and 524 kN. At failure interlaminar delamination was observed in the skin at the left hand-side of the panel, cracks were observed in the skin and stiffeners, and debonding at the skin-stiffener interface was also noted.

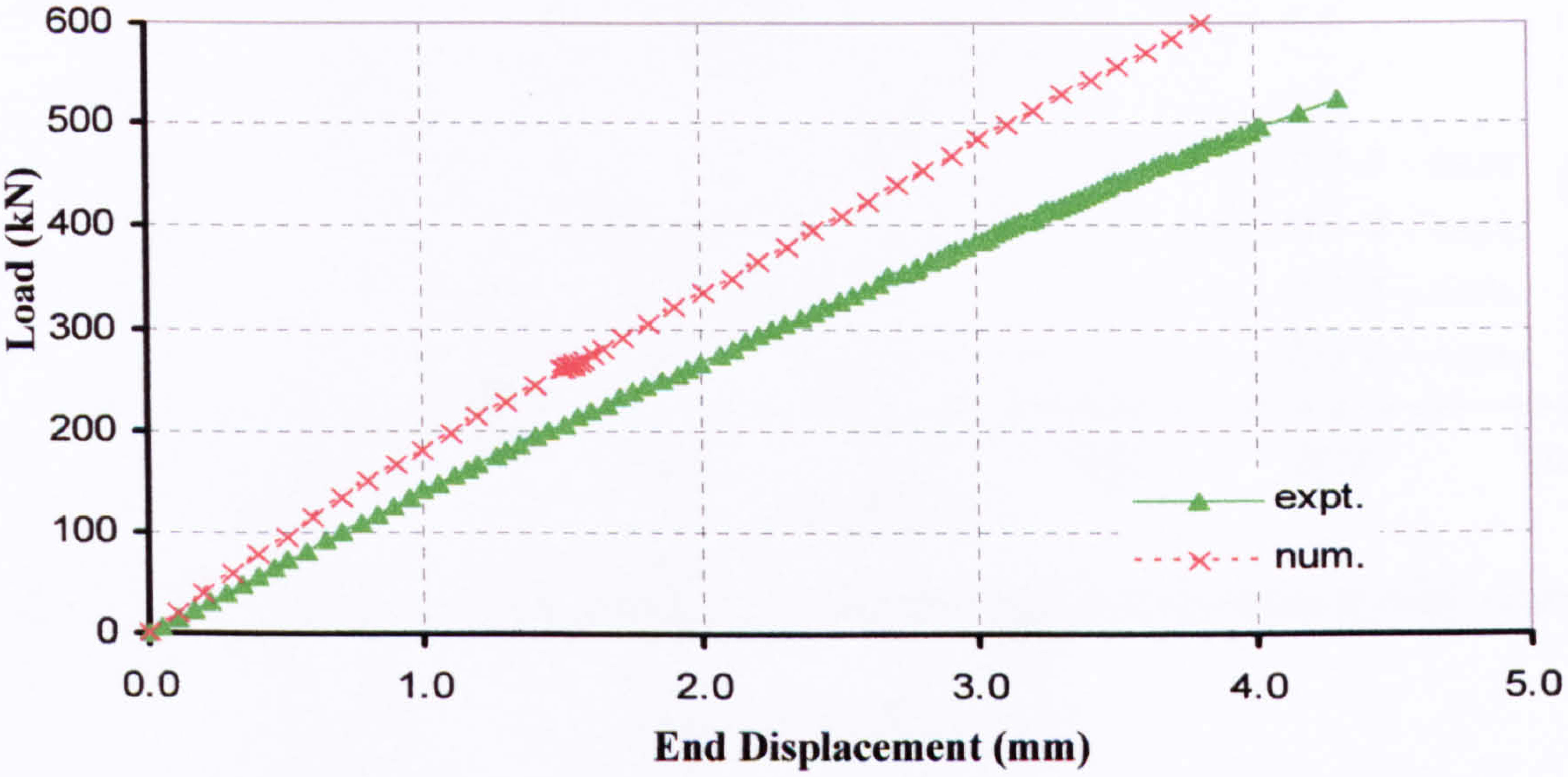

Figure 4.18: I-stiffened panel: experimental and numerical compressive load against end displacement curve.

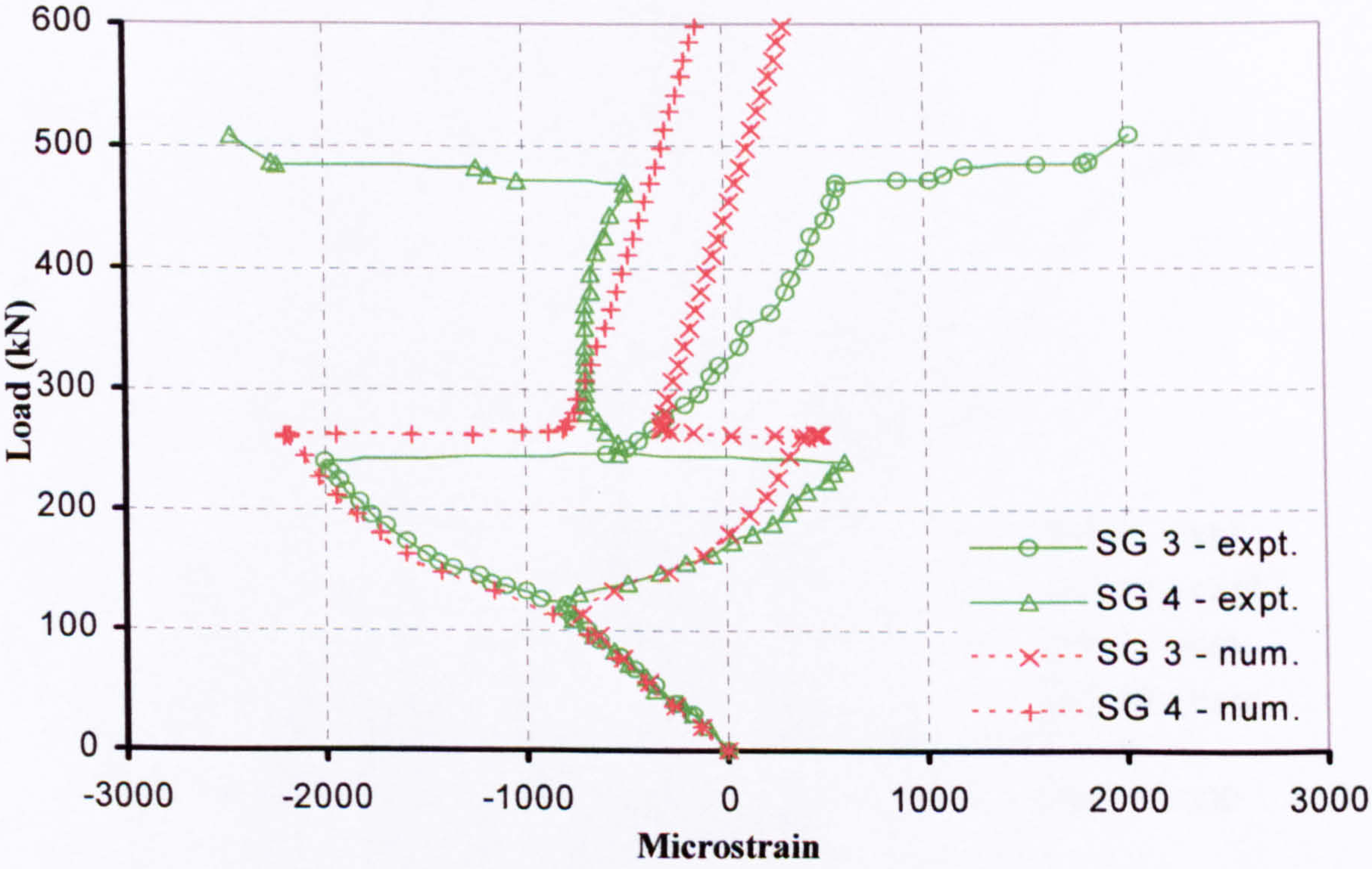

Figure 4.19: I-stiffened panel: experimental and numerical results for back-to-back strain gauge pair SG 3-4.

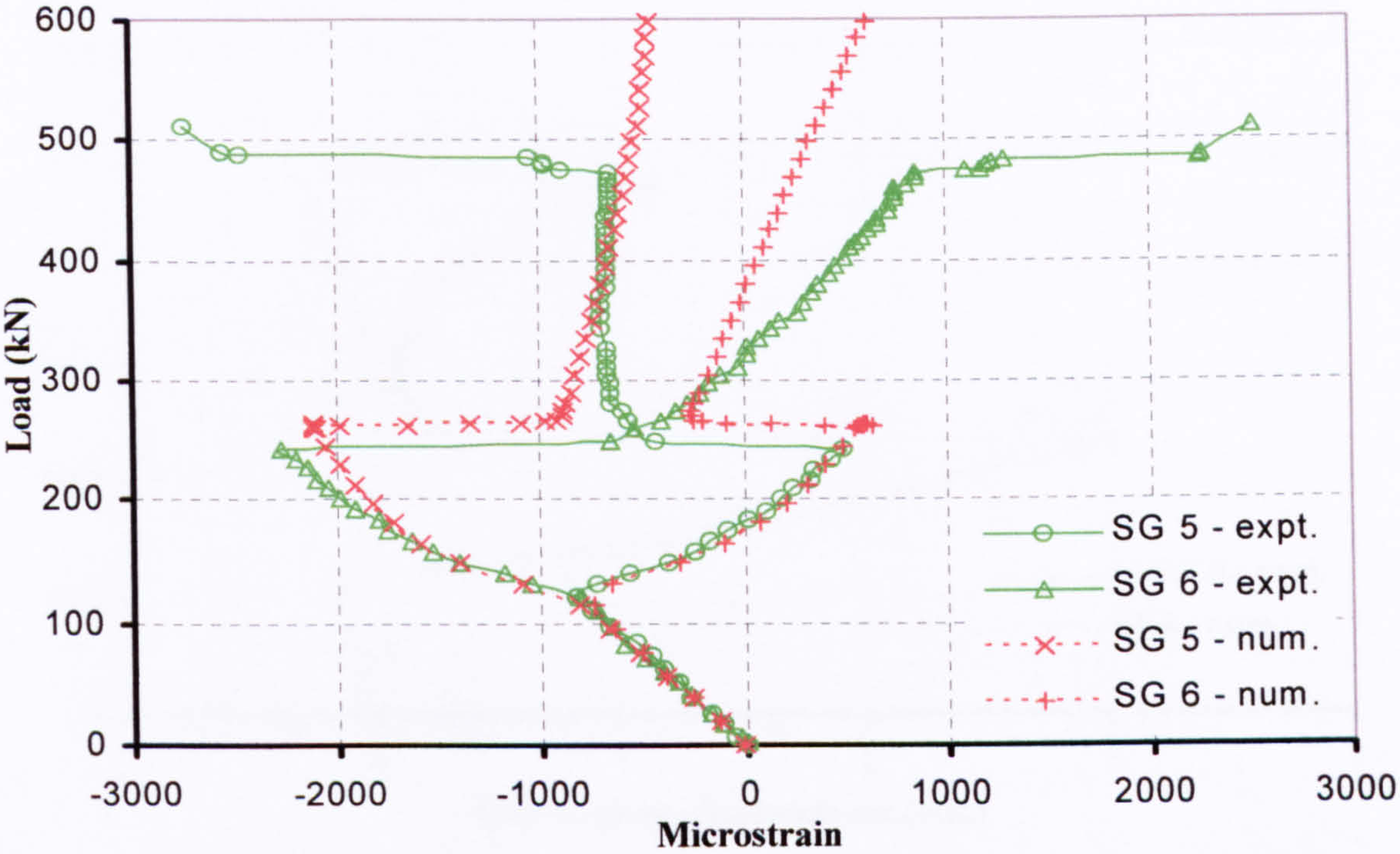

Figure 4.20: I-stiffened panel: experimental and numerical results for back-to-back strain gauge pair SG 5-6.

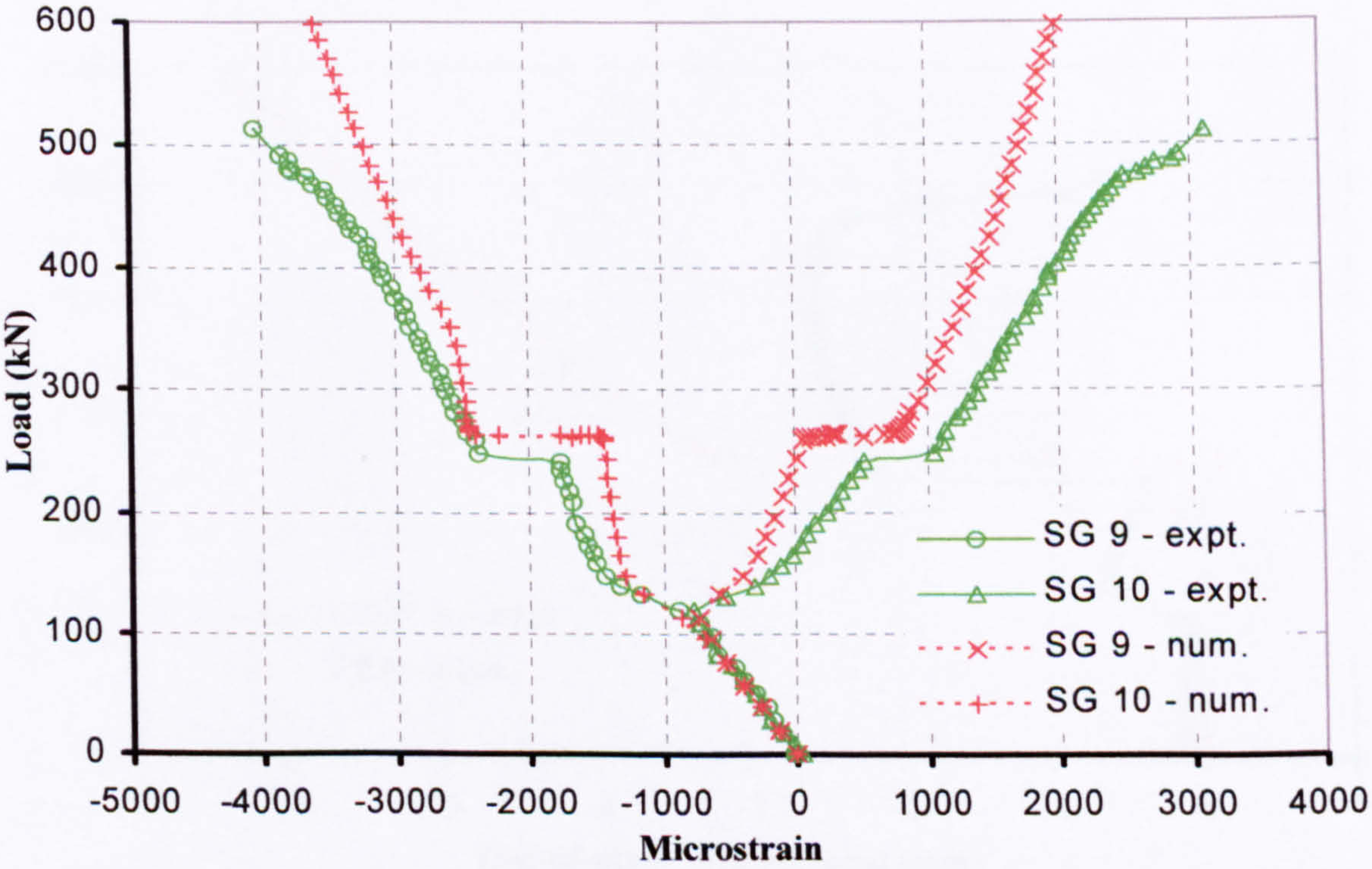

Figure 4.21: I-stiffened panel: experimental and numerical results for back-to-back strain gauge pair SG 9-10.

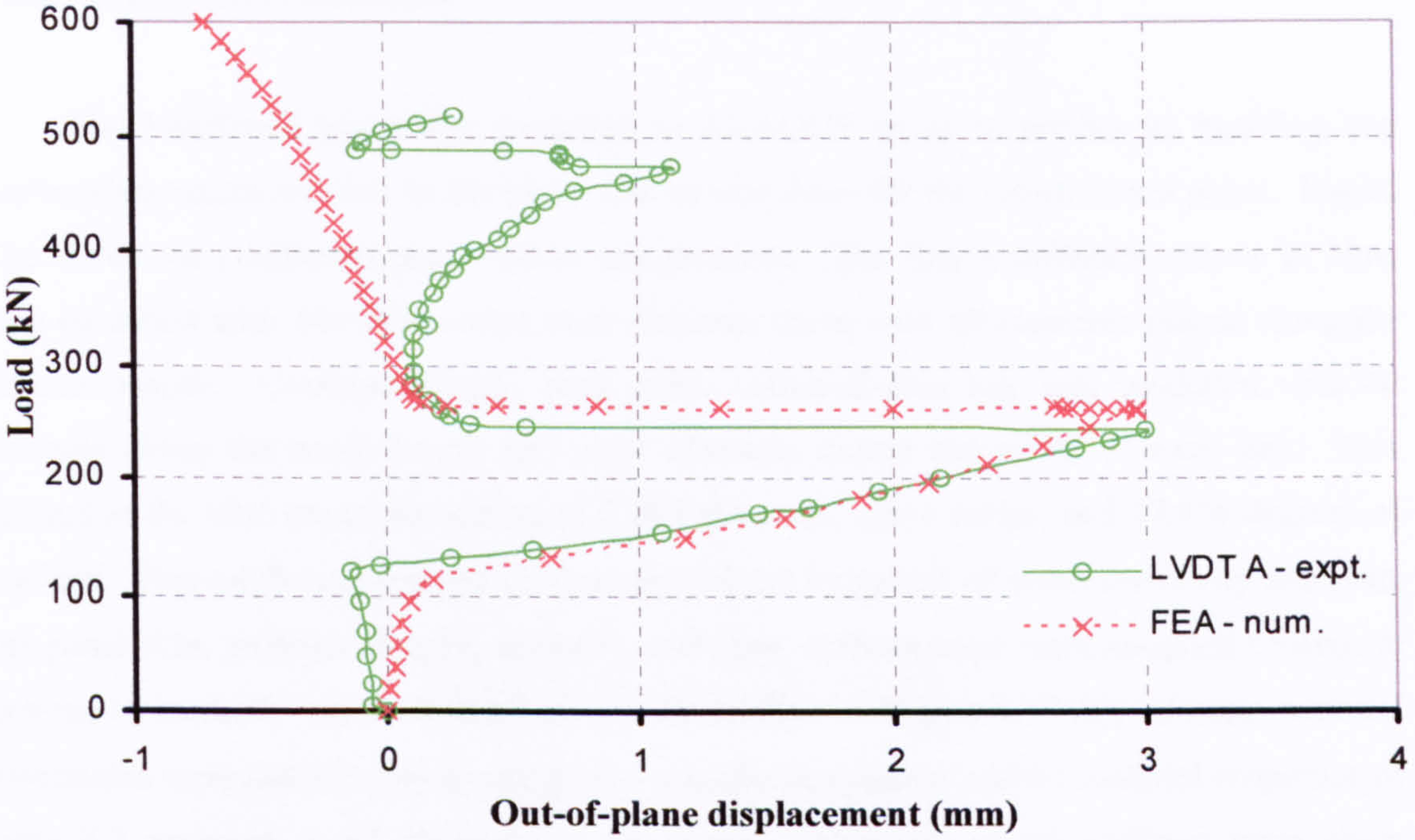

Figure 4.22: I-stiffened panel: experimental and numerical out-of-plane displacements at location A.

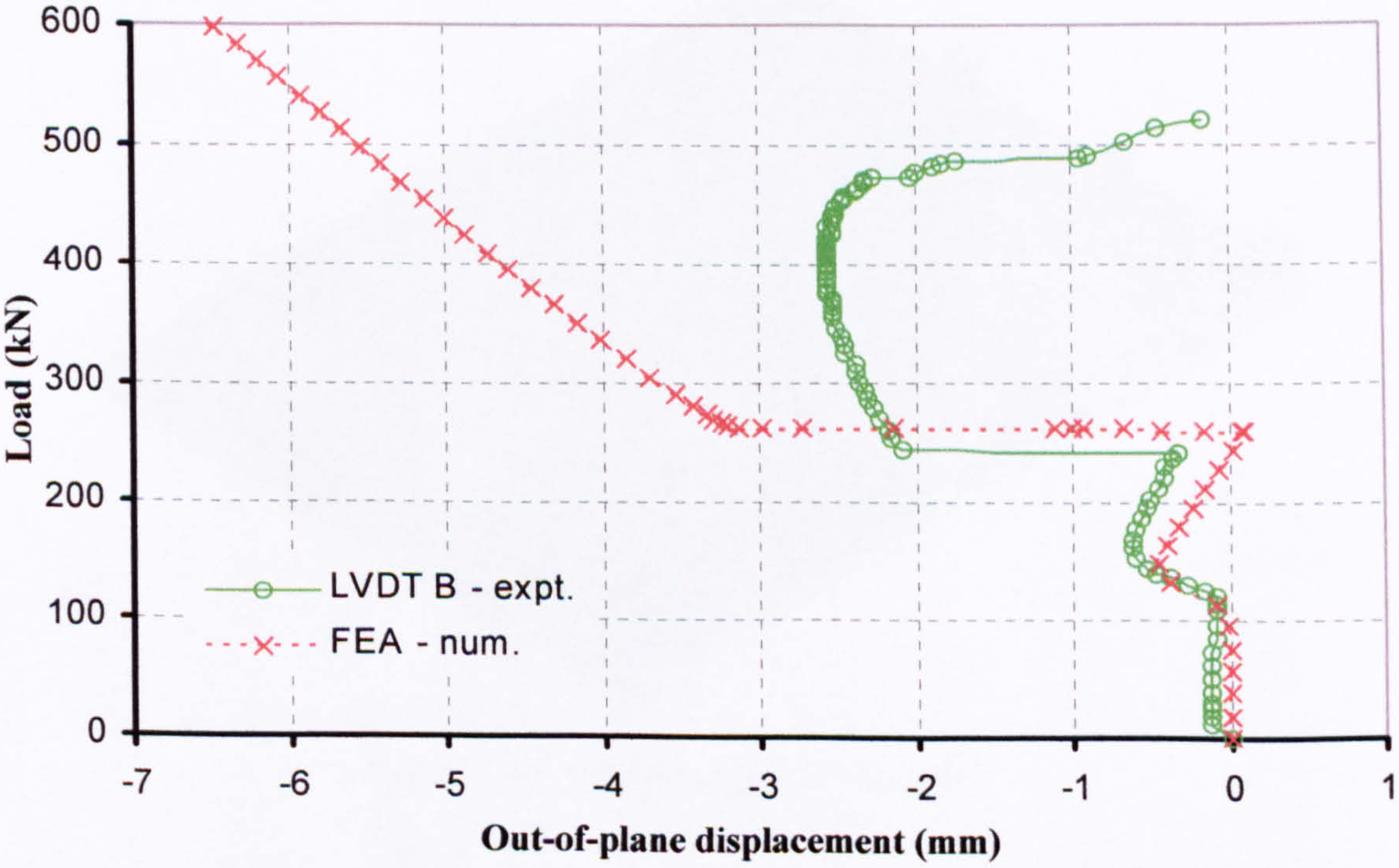

Figure 4.23: I-stiffened panel: experimental and numerical out-of-plane displacements at location B.

4.2.3 Finite element model

The I-stiffened panel was modelled in ABAQUS so as to predict its buckling and postbuckling characteristics in the same was as was done for the hat-stiffened panel. Figure 4.24 shows the I-stiffened panel model and its mesh. The four I-stiffeners, shown in blue, were modelled with 440 four-noded shell elements each, with 40 elements placed along the stiffener length. Correspondingly, each green coloured skin bay was modelled with 40 elements along the panel length and eight elements across the width of each bay. This resulted in the total model consisting of 2,800 elements, 2,911 nodes, and 17,466 degrees of freedom. This mesh was deemed sufficiently refined by means of mesh sensitivity analyses. The panel skin, stiffener flanges, stiffener, web, and stiffener caps were assigned composite sections to correctly represent their lay-up ad detailed in Figure 4.15 (a). Correct material orientations were specified by creating local coordinate systems and the material properties of Table 4.3 assigned to all elements in the model. Elements in the stiffener were given compressive properties, whilst skin elements were given properties corresponding to an average of the tensile and compressive values of Table 4.3. Additionally, the flange drop-offs in Figure 4.15 (b) were modelled by specifying shell offsets in those elements constituting the panel flanges. Both panel ends were set clamped boundary conditions, and then the loaded end was given a displacement controlled boundary condition to replicate the experimental compression test of the panel. As in the experiment, side edges were kept free.

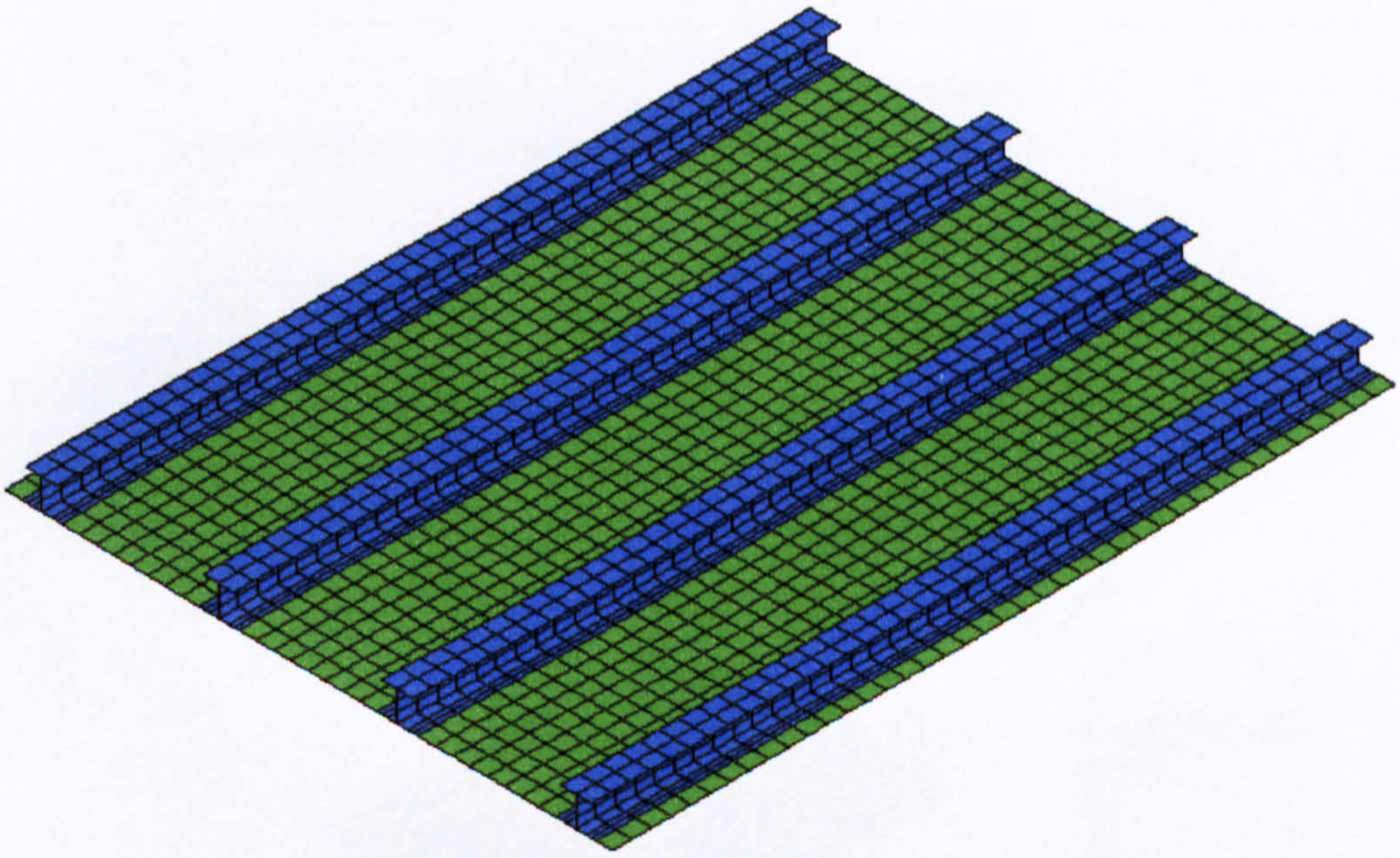

Figure 4.24: I-stiffened panel: FE model.

4.2.4 Linear eigenvalue buckling analysis results

As for the hat-stiffened panel, the first step in predicting the buckling and postbuckling characteristics of the I-stiffened panel was to conduct a linear eigenvalue analysis on the FE model. This determined the buckling load of the structure, and the mode shapes to be used as initial geometric imperfections in the subsequent nonlinear analyses.

The material properties as quoted by BAE in Table 4.3 included compressive values, and hence the technique of reducing the nominal moduli was not used in the case of the hat-stiffened panel. Table 4.4 shows the results of the eigenvalue analysis, the first eigenvalue yielding a buckling load for the panel of 125.2 kN, very close to the experimentally observed 120 kN. Figure 4.25 shows the mode shapes corresponding to the first three eigenvalues. The first mode shape corresponds to the panel having a five half-wave configuration in all three of its skin bays. The second mode shape, whose eigenvalue is very close to the first, corresponds to a four half-wave configuration in all skin bays. The third mode shape is again a three half-wave configuration, but the top two buckles and bottom two buckles seem separated by a flatter region towards the centre of each skin bay.

Table 4.4: Results of linear eigenvalue analysis on I-stiffened panel.

Eigenvalue	Value
1 – Buckling load	125.2 kN
2	127.3 kN
3	132.3 kN

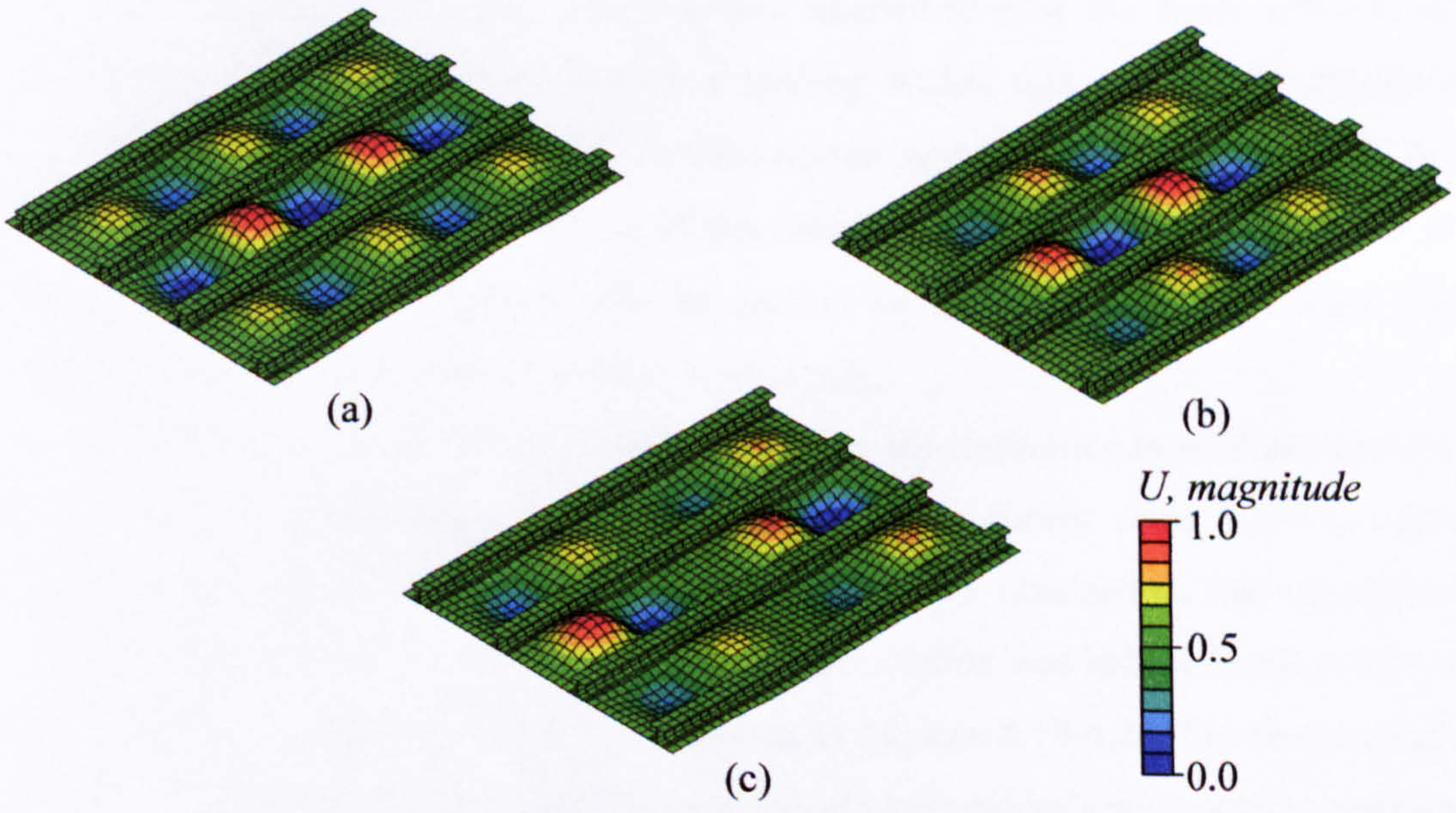

Figure 4.25: I-stiffened panel: linear buckling analysis mode shapes. First mode (a), second mode (b), and third mode (c).

4.2.5 Non-linear analysis results

The numerical results of the nonlinear analysis were compared to the experimental results after an investigation was conducted on the imperfection sensitivity of the FE panel model. Following this, the effect of the amount of viscous damping introduced into the analysis was also investigated. For clarity purposes, the results of these parametric sensitivity studies are presented after the discussion of the numerical results. The results presented related to an initial geometric imperfection of 3% of the skin thickness corresponding to a linear superposition of the first three buckle mode shapes. The amount of viscous damping introduced was 2% of the default value determined by ABAQUS.

In Figure 4.18 the numerically obtained compressive end load against displacement curve is compared with its experimental counterpart. It is quite clear how the FE model shows an overly stiff response when compared to the experimental values. As mentioned earlier, the technique of reducing the nominal moduli for the material properties as was done in the case of the hat-stiffened panel was not adopted since compressive values were available as shown in Table 4.3. A number of reasons exist to explain the discrepancy between the experimental and numerical curves. The first is that in the experiment the ends of the panel were potted in epoxy resin, and then the displacement-controlled loading was applied on one of the potted ends. This could have contributed to the experimentally measured response being less stiff than the actual one. Another possible factor explaining this discrepancy is the compliance of the testing machine used to apply the displacement controlled loading, which could further soften the experimental load-displacement curve seen in Figure 4.18. This aspect was also seen in the testing of various thick-skinned stiffener runout specimens conducted by Falzon et al. [54], where it was mentioned how the finite stiffness of the compression testing machine resulted in a loading which was not strictly displacement controlled as assumed in the FE model. A third reason relates to the FE model itself. At high loading and in the postbuckling regime of the panel, as the number of buckle crests in the panel increases, higher curvatures will be present in the panel skin, and these will be effectively represented by a fewer number of elements.

The possibility of the above reasons explaining the difference in stiffness between the experimental and numerically obtained load-displacement curves seem justified when the strain gauge results as well as out-of-plane displacements obtained in the experiment are compared to those of the FE model. A very good correlation was indeed found in both strain values and out-of-plane displacements as shown in Figures 4.19-4.23, the characteristics of which are discussed next together with the numerical panel model's postbuckling response.

The FE panel model buckled into a five half-wave configuration as shown in Figure 4.26 (a). This can be compared to the Moiré fringe patterns of Figure 4.17 (a) corresponding to a loading of 160 kN. The occurrence of buckling occurring at the numerically predicted loading of 125.2 kN is confirmed by all the numerical strain and out-of-plane displacement results in Figures 4.19 - 4.23. Back-to-back strains and strain gauge pairs exhibited diverging strains due to the sudden changes in curvature at buckling as one side of the panel skin went into tension and the other into compression in the vicinity of buckle crests. All three skin-bays showed the same five-half wave configuration as is clear in Figure 4.26 (a), and this was evidenced by the numerical – and experimental – strains in Figure 4.19 and Figure 4.20 for strain gauges SG 3-4 and SG 5-6 taking very similar values. Numerical strains at the position of SG 9-10, located at a position 62 mm away from the centre of the panel in the middle skin bay also appeared to be relatively near a buckle crest as their readings in Figure 4.21 indicate. Numerical and experimental strains were in very close agreement in the initial postbuckling regime of the panel, as were the out-of-plane displacements at positions A and B in Figure 4.22 and Figure 4.23.

The nonlinear solver predicted the panel to mode-jump at a load of 262 kN, in good agreement with the experimental 241 kN. As in the experiment, this consisted in a sudden jump of all three skin bays from the five half-wave configuration to a six half-wave configuration. The deformed shape of the panel model in this configuration just after the mode-jump at a loading of 262 kN is shown in Figure 4.26 (b). Strains in the middle of the central and right skin-bay at positions SG3-4 (Figure 4.20) and SG 5-6 (Figure 4.21) showed sudden reductions in values. This was due to the relocation of buckle crests on the panel resulting in these locations to be close to a buckle node line. Similarly, numerical strains at SG 9-10 abruptly increased as this position became even closer to a buckle crest. Similar observations can be made relating to out-of-plane displacements at locations A and B.

After the mode-jump, the correlation between numerical and experimental values was not as accurate as in the initial postbuckling regime. Figure 4.26 (c) shows how the FE panel remained in the six half-wave configuration, whilst in the experiment the right and left skin-bays were seen to jump to a seven half-wave configuration with the middle skin bay showing an elongated top buckle as it interacted with the side bays despite remaining in the six-half-wave configuration. All numerical strain and out-of-plane displacements indicate how numerical values showed no more sudden changes in values as the panel remained in the same configuration with buckle crests growing in size.

There are several reasons to why the FE model was not able to capture the mode-jumps that occurred in the right and left skin-bays shortly prior to the experimental panel collapse. There is inevitable microcracking in the actual panel that occurs at high loadings as was evidenced by acoustic emission being reported prior to complete failure, and such Microcracking may modify the actual stiffness of the panel. One such acoustic emission corresponded to a loud bang as the panel jumped form the five to the six half-wave configuration. Some local damage may have occurred at this point and influenced how the panel behaved at higher loadings. Another very important factor is how evidence of skin-stiffener debonding and other delaminations were observed to have occurred in the panel at failure. The FE model had no capability to model such phenomena which may be very influential precursors to the eventual overall collapse of the panel. Chapter 5 looks at further experimental evidence highlighting the importance of delamination and its influence on the collapse load and failure mechanism of composite structures such as stiffened panels, and at how failure can be incorporated into FE models. The I-stiffened panel discussed here is revisited in Chapter 7 to show how the ABAQUS submodelling capability can be used to model out-of-plane damage in the panel due to skin-stiffener debonding.

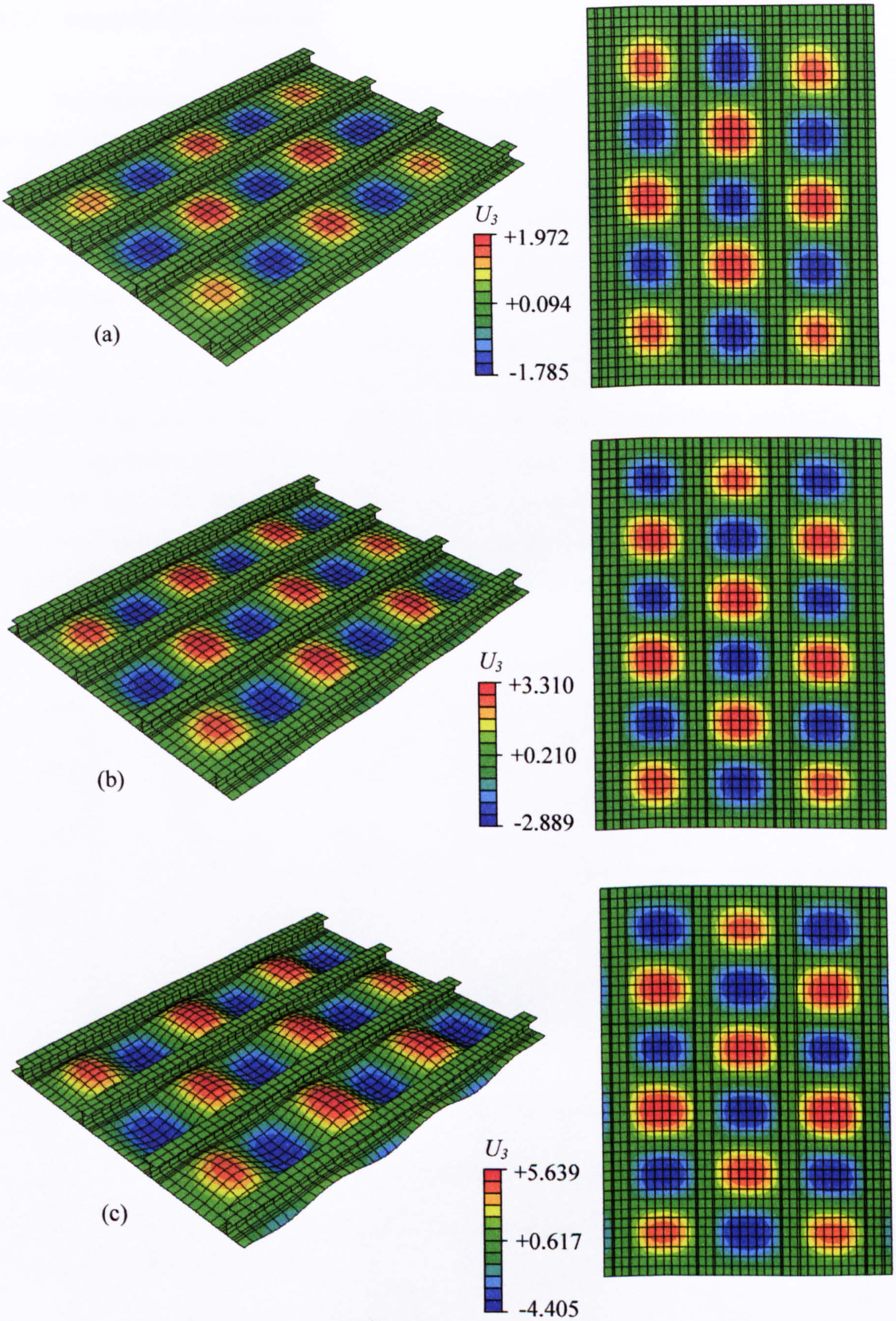

Figure 4.26: Numerical analysis deformed shape (scale factor five) and out-of-plane displacement contour plots for I-stiffened panel at loading: (a) 160 kN, (b) 265 kN, (c) 487 kN.

4.2.6 Imperfection sensitivity

An imperfections sensitivity analysis was run on the FE model of the I-stiffened panel to asses what the effect of changing the imperfection magnitude has on the predicted numerical postbuckling behaviour. Figure 4.27 shows the out-of-plane displacements at position A corresponding to the panel centre. Three different initial imperfections in the panel were considered, all corresponding to a linear superposition of the first three buckle mode shapes of the panel. It is clear from Figure 4.27 that for an imperfection of increasing amplitude, the panel's postbuckling behaviour changes. In all cased the I-stiffened panel buckles into a five half-wave configuration and then jumps to a six half-wave configuration, but the loading at which this jump occurs is affected by the magnitude of the imperfection. For an imperfection of 1% of the skin thickness, the mode-jump occurs at a load of about 359.1 kN, for a 3% imperfection at 262 kN, and for a 5% imperfection at 190.1 kN. Therefore it seems that unlike the hat-stiffened panel, the I-stiffened panel is imperfection sensitive, and increasing the magnitude of the imperfection decreases the load at which the mode-jump occurs.

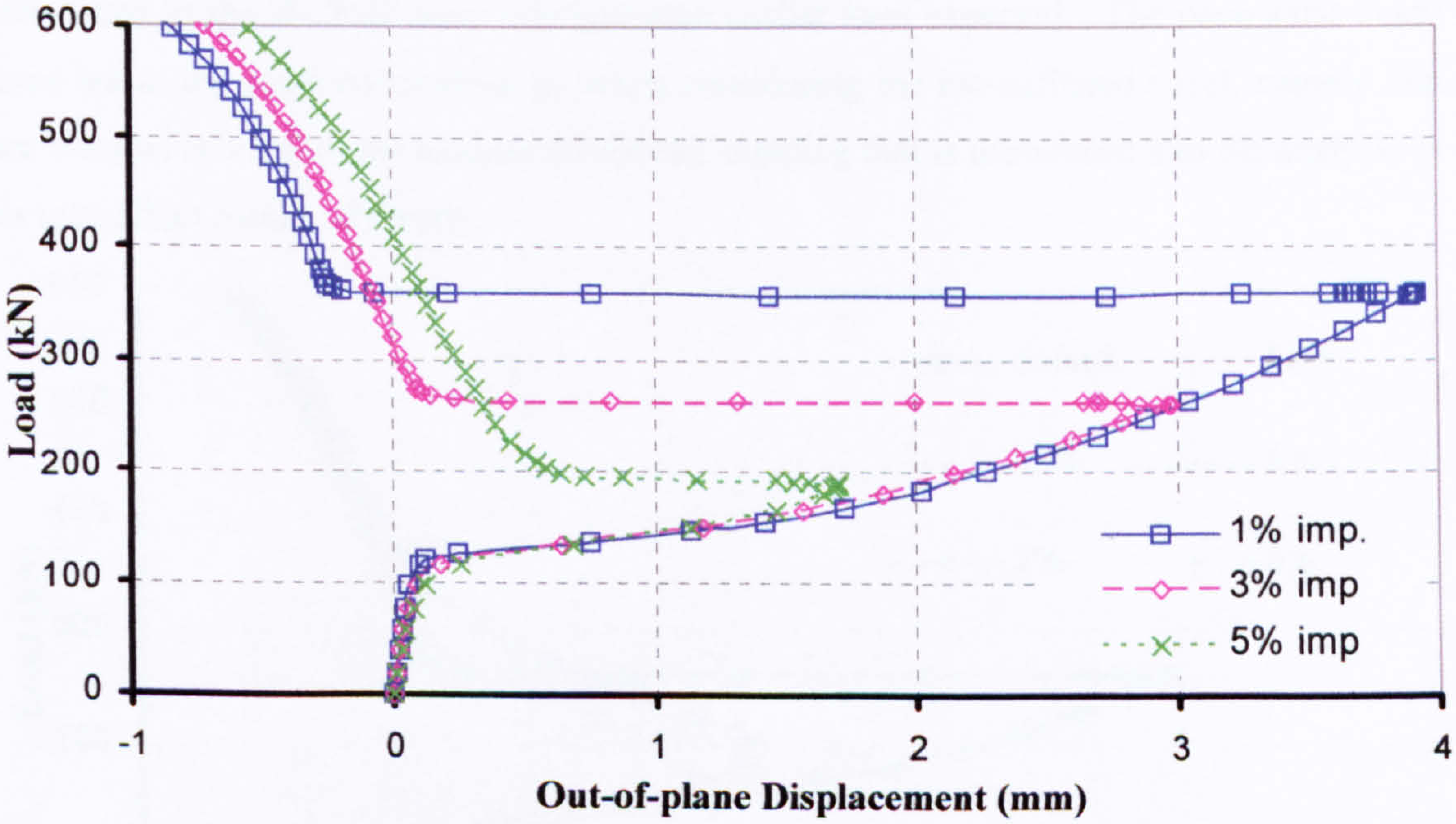

Figure 4.27: Effect of imperfection type and magnitude on numerically predicted out-of-plane displacements at location A.

4.2.7 Effect of viscous damping

As was observed in the analysis of the hat-stiffened panel, changing the amount of viscous damping introduced into the nonlinear analysis affects the results obtained. Figure 4.28 shows the results of a parametric study conducted by altering the viscosity parameter, and all analyses were run with an imperfection of magnitude 3% of the skin thickness and corresponding to a superposition of the first three mode shapes. The line corresponding to no viscous damping, labelled 0%, shows how the nonlinear ABAQUS solver was unable to trace the I-stiffened panel's postbuckling response past the mode-jump from five to six half-waves. This was due to the instability that this mode-jump presents and the associated convergence difficulties. By adding viscous damping the analysis was able to proceed. Large damping values however yield erroneous results. The dark blue, red, and pink lines, corresponding do default damping, 50%, and 15% of the default value respectively show how the out-of-plane displacements at the panel centre changed with decreasing damping. For the low damping values of 6% and 2%, shown in light blue and green, the out-of-plane displacements corresponded to those in the absence of damping except that the solver was now able to capture the dynamic mode-jump. For larger viscosity parameters the panel exhibited the mode-jump to the six half-wave configuration earlier than expected. The parametric study hence led to the same conclusions as when considering the hat-stiffened panel, namely that care must be taken with the amount of viscous damping that is introduced into the analysis as this may affect results adversely.

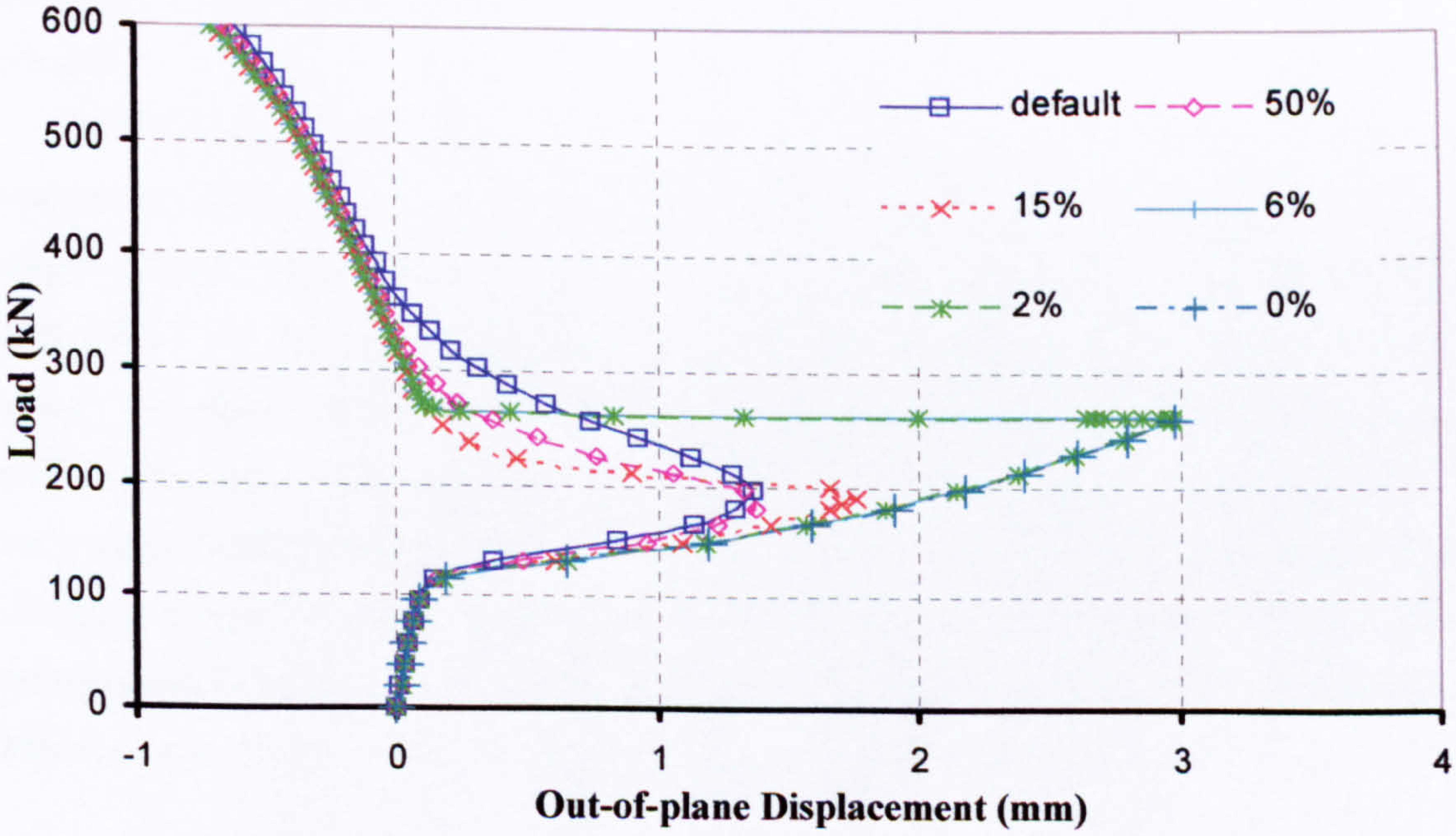

Figure 4.28: Effect of viscosity parameter on numerically predicted out-of-plane displacements at location A.

Chapter 5

Failure mechanisms and their modelling

This chapter begins with a discussion of why failure modelling is required, giving specific reference to the FE models created for the two stiffened composite panels of Chapter 4 and their inability to model damage such as skin-stiffener debonding. Subsequently the experimental investigations discussed in Chapter 2, relating to compressive testing of stiffened composite panels are revisited, this time focussing on the failure mechanisms of the panels. This highlights the need to model the potential separation of the stiffeners from the skin in an FE model, as it this phenomenon rather than in-plane material failure that leads to panel collapse. Discussion then moves on to previous work looking at failure of other composite structures such as stiffener runout regions. Some fractographic analyses work and research relating to impact damage is also considered as these give valuable insight into the damage mechanisms of composite structures. Subsequently a brief introduction is given to fracture mechanics with specific reference to how out-of plane damage such as skin-stiffener debonding may be modelled in an FE framework. This leads to the two major available approaches – the Virtual Crack Closure Technique (VCCT) and the use of the interface elements.

VCCT is discussed briefly before the interface elements available in ABAQUS are examined and their full theoretical formulation given, relating to how they are able to model damage initiation as well as propagation. Having done this, a simple Double Cantilever Beam (DCB) problem is considered to validate the elements under a pure opening Mode I loading. The results of this investigation are shown in Appendix A. The sensitivity of the interface elements to various analysis parameters required by ABAQUS is also discussed. Finally means of interface element validation under mixed mode loading are considered. This provides a foundation for Chapter 6 and Chapter 7 where it will be seen how interface elements may be used to model debonding in more complex composite structures such as stiffener runouts and the I-stiffened panel first considered in Chapter 4.

5.1 The need for failure modelling

In Chapter 4 it was seen how the buckling and postbuckling behaviour of stiffened composite structures may be modelled in the FE package ABAQUS. This was demonstrated by constructing FE models for two stiffened composite panels and then conducting linear eigenvalue buckling analyses followed by nonlinear analyses. It was shown how good correlation between experimental results was obtained of the buckling load as well as strains and out-of-plane displacements for both panels. Mode-jumping in the panels was observed as secondary instabilities developed leading to a sudden change in the buckle pattern. For the hat-stiffened panel this corresponded first to a gradual elongation of the central buckle crest in the three half-wave buckled configuration followed by a jump to a five half-wave configuration at a higher load. The FE non-linear analysis was able to capture the gradual change but not the sudden jump to the five half-wave configuration. For the I-stiffened panel, which buckled into a five half-wave configuration, ABAQUS was able to fully capture the dynamic mode-jump in all skin-bays to the six half-wave configuration as was observed in the experiment. Another mode-jump was observed experimentally just prior to collapse, where the panel side-bays jumped to a seven half-wave configuration. This was not captured by the FE analyses. In both cases it was argued that the inability of the FE model to capture the mode-jumps occurring at high loads was due to the presence of microcracking and other damage mechanisms present in the panel, which altered the panel's stiffness and ultimately its behaviour in the upper postbuckling regime. Microcracking was observed via acoustic emission in the experimental tests, and investigation of the failed panels also showed other damage mechanisms such as debonding between the skin and stiffener. It is the inability of the FE model to capture such failure mechanisms, which may initiate prior to overall collapse of the panel which is addressed in this chapter, focusing on how out-of-plane failure may be modelled in an FE framework.

5.2 Experimental failure investigations

5.2.1 Stiffened composite panels

Earlier works dealing with the experimental testing of stiffened composite panels generally did not deal with trying to understand the exact failure characteristics of the panels. This is due to the fact that failure mostly occurred in a very sudden fashion, and hence its explosive and destructive nature did not allow for specific failure mechanisms to be identified. Such was the case in Romeo's [18] testing of graphite/epoxy hat and blade-stiffened panels under uniaxial compression. Starnes et al. [17] did comment, albeit briefly, on the failure characteristics of the graphite-epoxy panels that they tested. For the specimens tested in their undamaged state, failure was seen to occur when the skin and stiffeners separated from one another. When this happened the skin invariably buckled across the panel and global collapse was observed. The investigation also showed that the highest membrane strains occurred at the location of the stiffener flanges, and it is these localized strains that acted as precursors to the local failure in the skin-stiffener interface region which eventually promoted the panel collapse. Testing of pre-damaged panels (delamination-type defects in the skin directly under the stiffeners) revealed that damage in the skin-stiffener interface region could further reduce the postbuckling strength of panels as it allowed skin-stiffener debonding to occur at lower loads than for undamaged specimens. Knight Jr. et al. [55] also looked at the postbuckling behaviour of some curved stiffened-epoxy panels loaded in uniaxial compression. These were not discussed in Chapter 2 as they formed a continuation and basis for comparison with the similar but flat panels just mentioned. Failure in the curved panels was akin to that of the flat panels, initiated by local skin-stiffener separation. The authors also commented that "the high membrane strains in the vicinity of the stiffeners coupled with the large out-of-plane displacements are apparently sufficient to cause separation of the skin and the stiffeners".

The last statement about the out-of-plane displacements caused by the buckled skin configuration of the stiffened panels in their postbuckling regime was looked at in more detail by Stevens et al. [8] in the testing of I-stiffened panels. Three types of failure modes were seen to occur over the failed panels. The first was separation of the stiffener cap, the second was the stiffener detaching and pulling away the first ply of the skin with it, and finally the stiffener detaching but with the skin remaining intact. In order to understand these failure mechanisms, Stevens and co-workers looked at the nature and magnitude of the stresses that develop in the interface between the skin and stiffeners as the panel buckled. These were generated by the load transfer between the skin and stiffeners. Buckling and postbuckling of the I-stiffened panels – and in fact all stiffened panels – showed periodically varying displacements due to the formation of the buckle crests. This meant that the stress resultants and therefore interface stresses would also be of a periodic nature, and hence only needed to be examined at positions corresponding to buckle node and buckle anti-node lines. These positions were where the stress resultants have their maximum values. At an anti-node line, there are two possibilities which can lead to skin-stiffener debonding. With reference to Figure 5.1, the stiffener flange acts as a step change in bending stiffness to the skin moment M_F. Because of this, the skin moment has a tendency to pull the skin and stiffener flange apart, generating interface peel stresses. Secondly, there is a moment transfer M_W between the stiffener web and the stiffener flange/panel skin at the foot of the web. The moment acts so as to pull the flange on the tension side away from the panel skin hence contributing towards stiffener debonding. Flange tapering acts to help in alleviating this effect.

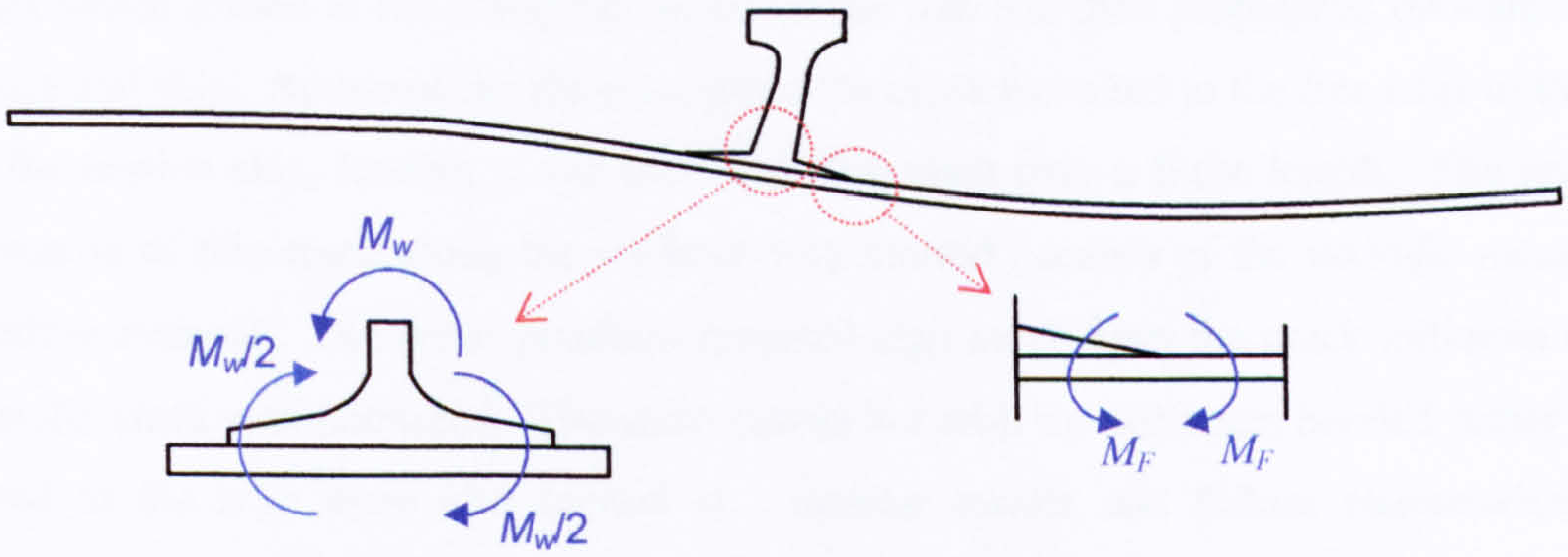

Figure 5.1: Mechanisms promoting skin-stiffener debonding at the location of a buckle anti-node line.

Node lines on the other hand have no deformation in the panel cross section. This means that the bending moments in both the stiffener and skin are close to zero, but it is at these points that twisting moments M_{XY} reach a maximum. For compatibility conditions between the skin and the flange to be enforced, interface shear stresses develop as illustrated in Figure 5.2. Once these reach a critical value, then delamination between the skin and stiffener flange occurs. Once again, flange tapering eases this effect.

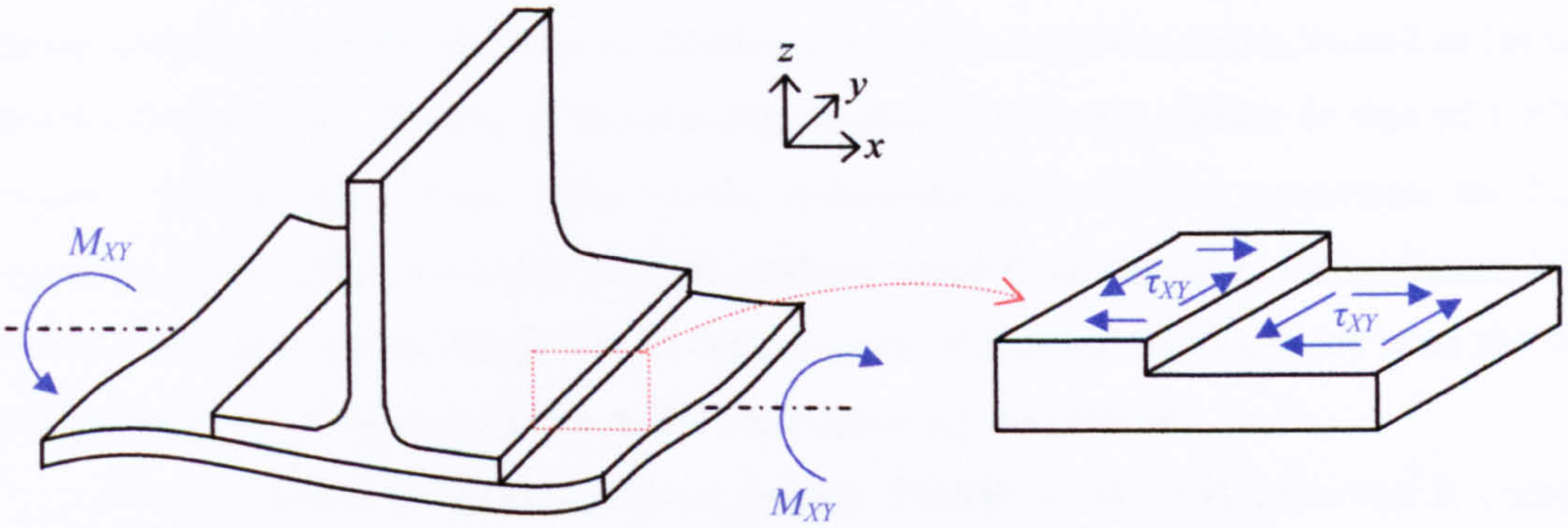

Figure 5.2: Conditions at a node line leading to interface stresses promoting debonding.

Three separate locations in the panel showed a specific failure mode. The base of the stiffener web at anti-node lines, where the bending moments were at the maximum, showed a crack which started in the triangular region of the web and then propagated outwards into the flange and skin. At two of the three locations the crack travelled to the free edge of the flange on the tension side, leading to the latter splitting open over a finite length. The lengthwise extension of this crack along the stiffener was limited because of the periodic nature of the bending moment. The stress resultant reversed sign away from the crack initiation site, and thus the crack was stabilized. The same panels but with the stiffeners bonded rather than co-cured to the skin were also looked at. Similar results and failure characteristics were observed, but a slightly higher compressive load was supported by the panel, and crack propagation tended to remain in the flange rather than the first ply of the skin.

Kong et al. [24] also tested I-stiffened panels and compared them with panels containing hat and blade stiffeners. Not much attention was paid to the failure modes, but since the stiffeners were fabricated by the continuous plies of the skin and then co-cured, skin-stiffener debonding was not observed. It was however noted how I stiffeners rotated less in the postbuckled regime than blade stiffeners due to their higher torsional stiffness and hence I-stiffened panels were able to withstand a higher load than their blade-stiffened counterparts.

The observations regarding skin-stiffener debonding initiating at node and anti-node lines were confirmed by Stevens et al. [20] in the comparative discussion of the failure modes visible in various carbon/epoxy compression panels featuring I, J, and two types of hat-stiffeners. In the hat-stiffened panels failure was observed to occur at buckle node lines. At this location the twisting moment was a maximum and the load was diffused into the stiffener via interfacial shear stresses. The skin-stiffener debonding propagated from the flange edge towards the stiffener web. Tapering of the stiffener flanges was expected to relocate the failure location to the buckle crests since the diffusion stresses at the interface would be alleviated by the tapering. However, testing revealed that for the only panel whose failure mode could be identified, a shear debonding opposite a nodal line still occurred as for the un-tapered flange case. Failure of the J-stiffened panels was very similar to that of I-stiffened panels. At anti-node lines, were buckle deformations were at a maximum, the bending moments in the stiffener acted to pull the stiffener away from the skin. Failure hence initiated either at the edge of the flange due to the presence of a stress concentration or at the base of the stiffener web as shown in Figure 5.2 and Figure 5.1 respectively.

In the testing of blade-stiffened panels, Falzon et al. [19] observed a completely different failure mode. This occurred because unlike I, J, and hat-stiffened panels which have a high torsional stiffness arising from the torsion/bending stiffness of the stiffener caps (in the case of I and J-stiffeners) or the closed section hat-stiffeners, blade stiffeners have a low St. Venant torsional stiffness. Failure therefore occurred at a location away from the stress concentrations at the base of the blade stiffeners. The blade stiffeners remained mainly attached to the skin, but mid-plane delamination of the web was visible at failure locations. Falzon et al. suggested that a critical value of the shear stress τ_{XZ} was reached near the mid-plane of the web on a nodal line and at the free edge. Figure 5.3 shows how there are two contributions to this shear stress arising from the transverse shear loading N_{XZ} and the twisting moment M_{XY}, both of which attain maximum values at node-lines.

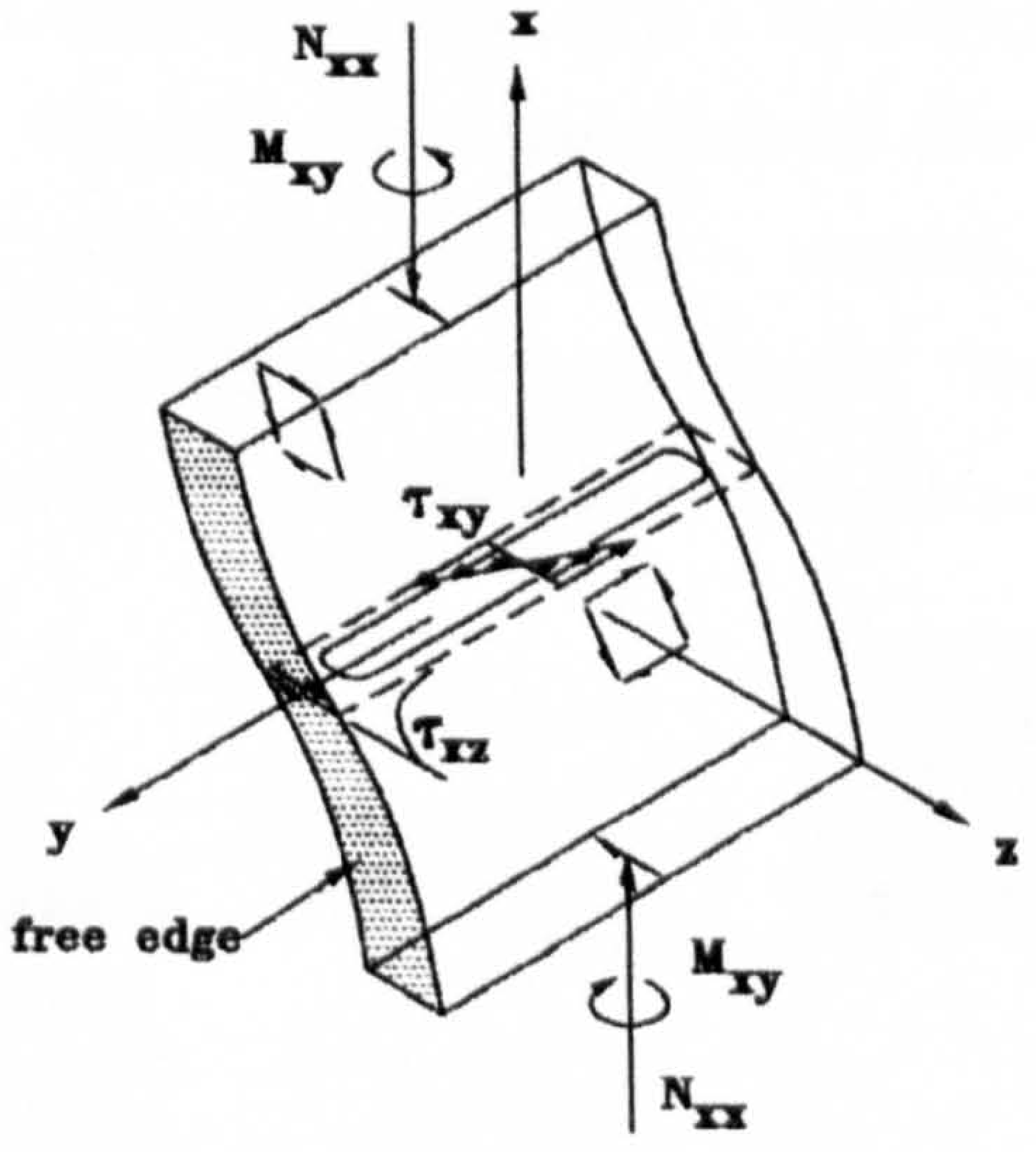

Figure 5.3: Failure mechanism consisting of web mid-plane delamination in blade stiffened panels. Figure by Falzon et al. [19].

The experimental investigations discussed often mentioned the alleviating effect of flange tapering on skin-stiffener debonding. This was investigated by Vijayaraju et al. [56] who tested representative carbon/epoxy T-pull specimens under peel load conditions to study the failure behaviour of the skin-stiffener interface. It was found that by using capping strips on the stiffener flanges, the increase in failure load was significant. Capping strips refer to additional plies placed between the skin and stiffener to increase the longitudinal bending stiffness of the structure. Overlay plies, additional plies set over the top of the stiffener flanges "covering" the ply drops were also considered, but the increase in failure load was only marginal. All specimens showed failure which initiated by debonding occurring either at the flange end or in the corner of the stiffener noodle region where the flange meets the web. In the case of failure initiating in this noodle region, it progressed to the skin-stiffener interface eventually leading to complete debonding. Failure initiating at the flange end progressed inwards and also eventually led to complete debonding.

5.2.2 Stiffener runout regions

When used in structural components, stiffeners in stiffened panels must terminate at structural features such as cut-outs and ribs. This interrupts the load path, and hence specific research efforts have been made to look at the vulnerability of stiffener runout regions to suffer damage and hence potentially lead to failure of whole panels. Falzon et al. [57] tested three different blade stiffener runout configurations subject to a uniaxial compressive loading. These are shown in Figure 5.4, with the skin coloured in blue and the stiffener in grey. The first configuration (a) had the blade tapered linearly to a finite height at the edge of the runout. In the second (b) the skin thickness was tapered linearly over the tapered length of the stiffener, while the third configuration (c) had a constant but thicker skin with a correspondingly thicker stiffener with a greater taper length. The three configurations were tested and their behaviour and failure characteristics identified and compared.

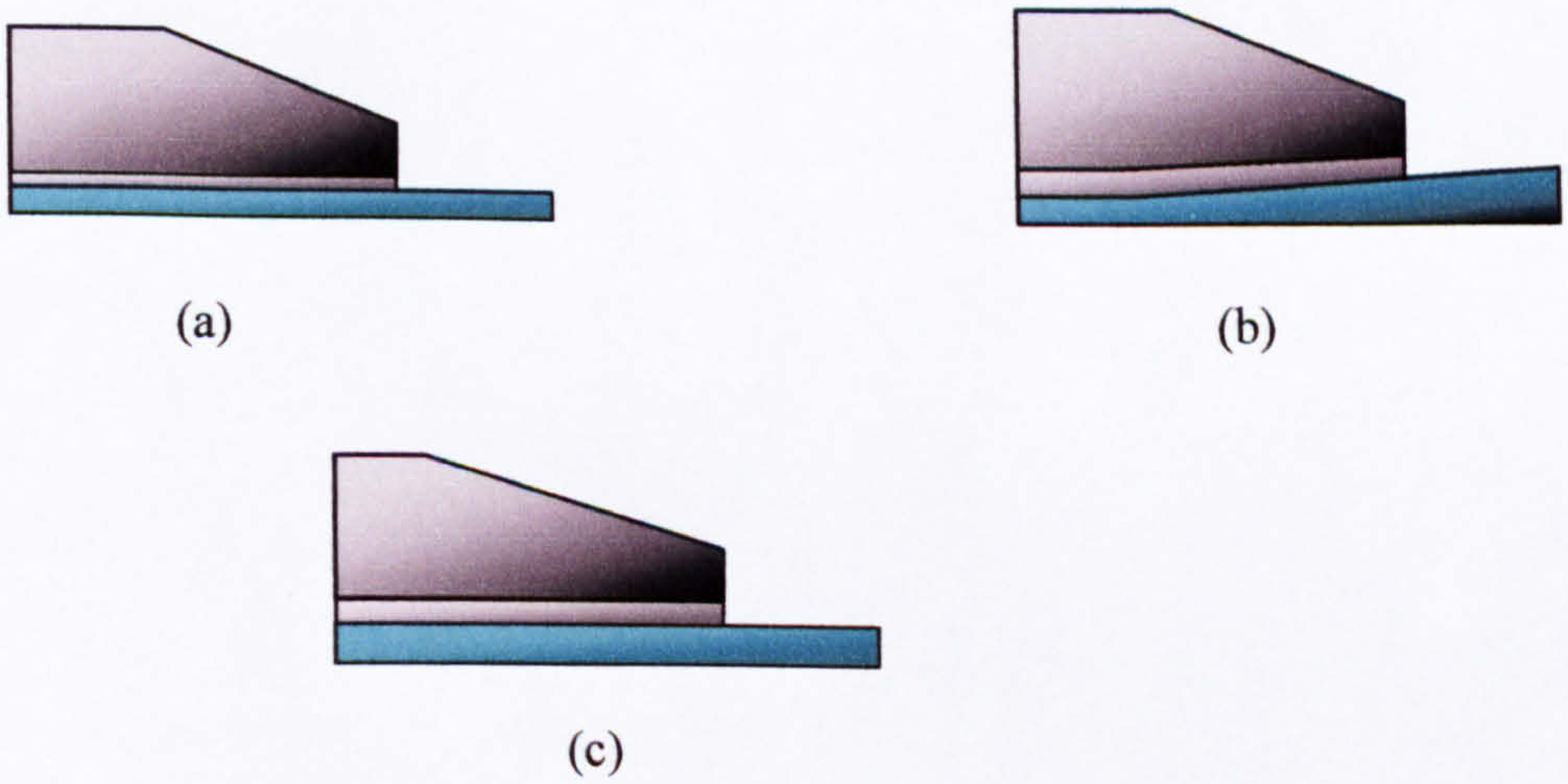

(a)

(b)

(c)

Figure 5.4: Side-on views of stiffener runout configurations considered by Falzon et al. [57].

The first configuration showed little strain at the end of the runout region, and this was identified as being due to the fact that the compressive strains are counteracted by the tensile bending strains which exist in this region. The geometric discontinuity in the form of the stiffener runout introduced high bending deformation in the unsupported skin region after the runout. Failure of the specimen occurred as highly unstable crack growth which initiated in the 0°/90° ply interface between the skin and stiffener flange and then propagated throughout the whole specimen in a sudden fashion. The second configuration, with the increasing skin thickness, showed much lower compressive strains in the runout region than the first as the thicker skin reduced the bending deformation. Despite the reduced bending energy available for crack propagation, failure still occurred in a similar fashion to the first configuration, via unstable crack growth. The third, thicker, configuration showed different behaviour. There was little bending measured on the stiffener flange in the runout region, and the top of the stiffener flange went into tension suggesting a change in curvature at the end of the flange. Failure occurred through crack initiation and initially unstable propagation, but this became stable as the crack travelled further. Thick shell elements, with a refined mesh in the runout region, were employed to model the skin and stiffener, and the Virtual Crack Closure Technique (VCCT) used to model crack propagation. The FE models captured the qualitative behaviour of the real specimens rather well. Strain energy release rates indicated unstable crack growth for the first two configurations, but eventually stable crack growth for the third configuration as was seen in the experiments.

Falzon et al. [58] then extended the above work by modifying some of the specimens so as to taper the stiffener down to the skin, as this was thought to alleviate the stress concentration due to the geometric discontinuity. Surprisingly, these were found to fail at lower loads than the non-tapered configuration, both for thin and thicker skins. Additionally, thicker skin specimens with a tapering skin thickness were also tested, and these unexpectedly showed a different failure mode to the non-tapering skin thick specimens. Interlaminar shear occurred as the stiffener web split at its centreline. This was due to a crack propagating along one skin-stiffener flange interface flange and around the noodle region. On the other hand, as already seen, the non-tapering thick skin specimens failed by initially unstable, but then stabilized, crack growth in the skin-stiffener flange interface. FE models aimed at capturing the behaviour of the stiffener runout sections were also constructed [54]. The formulation behind the thick shell composite finite element used in the analyses was described, and the resulting FE simulations, able to capture the qualitative experimental behaviour of the runout specimens were commented upon in detail.

5.2.3 Fractographic analyses and impact damage

Fractographic analyses are experimental studies aimed at understanding the progression of failure by analyzing the fracture surface after collapse. This is often difficult in composite panels since failure can be rather sudden, and hence it is complicated to track the exact sequence of events. Greenhalgh and Garcia [59] performed testing and a fractographic analysis of stiffener runout specimens, investigating different geometric features of the runouts and their effect on failure. Three different configurations were looked at and are shown in Figure 5.5.

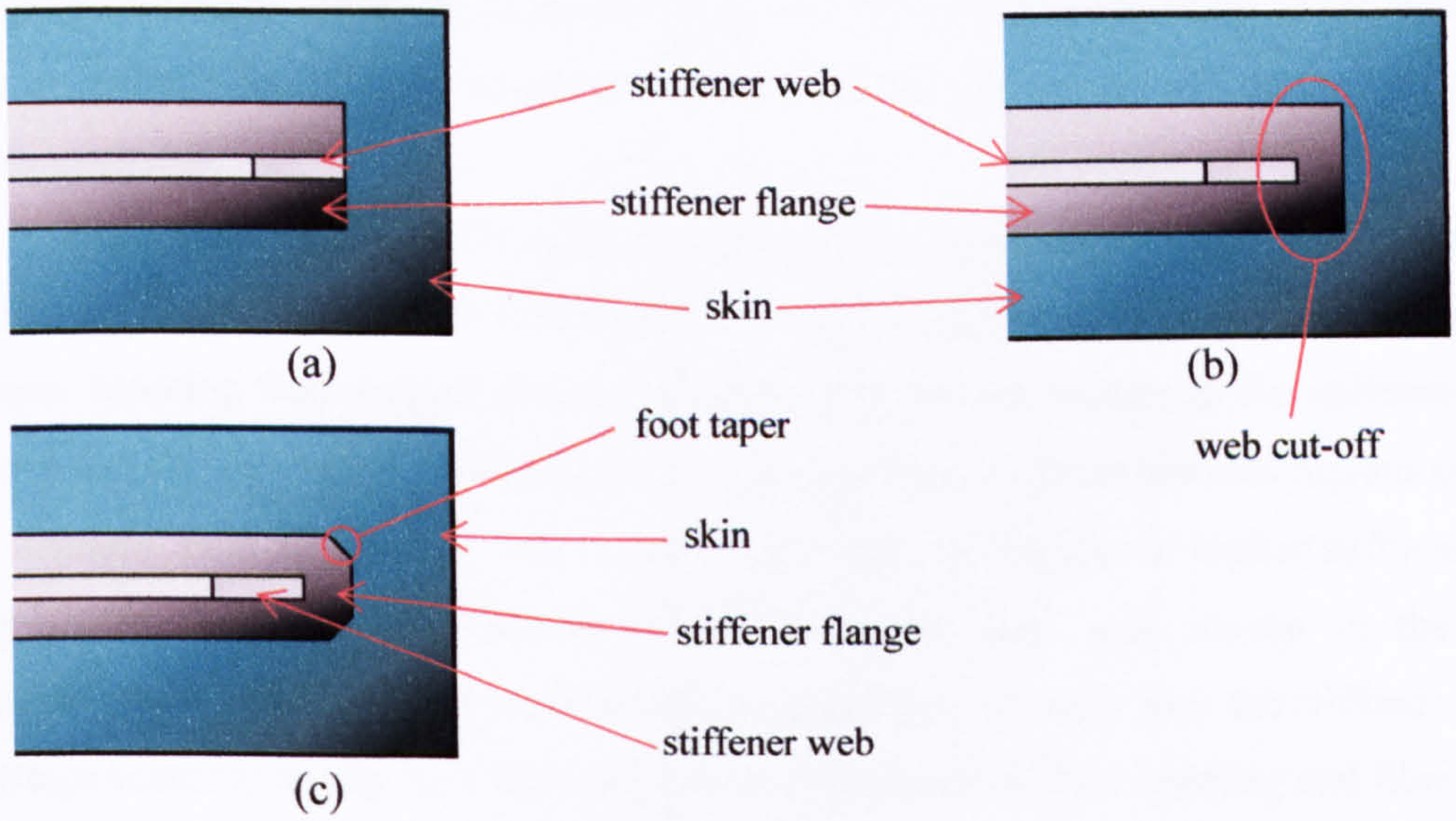

Figure 5.5: Top down views of stiffener runout configurations investigated by Greenhalgh and Garcia [59].

The first configuration, in Figure 5.5 (a) was just a regular runout, with no tapering of the stiffener foot and no web cut-off. The second configuration – Figure 5.5 (b) - introduced a web cut-off, while the third had both a web cut-off and foot taper as shown in Figure 5.5 (c). All three configurations included a tapered web. The three runout types were found to show similar failure characteristics, and a fractographic analysis for each configuration was conducted in great detail and the findings portrayed. Extension of the stringer foot, combined with its tapering, as in the third configuration, increased the strength of the runouts since it somewhat prevented the rise of in-plane tensile stresses in the skin. Cracking noises where heard during the testing long before final failure, and were attributed to the development of skin-stiffener delamination at the stringer tip.

A similar fractographic analysis was conducted by Meeks et al. [60]. Here however, complete composite stiffened panels rather than just runout specimens were tested in compression and their failure mechanisms induced via a fractographic analysis. Five panels were tested in uniaxial compression to failure; one undamaged panel, a panel with a bay impact defect, a panel with a foot impact defect, a panel with an embedded bay defect, and finally a panel with an embedded foot defect. The primary cause of failure for all of the five panels was found to be debonding of the stiffeners from the skin. Twisting and bending moments were generated as the panels buckled, in much the same way as described earlier when discussing the various experimental tests that have been conducted on stiffened panels. The defects in the panels acted as initiation sites for skin-stiffener debonding. FE analyses were conducted to model the panel buckling and changes in mode shape in the postbuckling regime using two different iterative methods, but no damage growth or fracture processes were modelled.

Impact damage on stiffened composite panels was also investigated by Greenhalgh et al. [61]. These studies were conducted so as to attempt to identify delamination sizes and shapes resulting from impact damage at different locations relative to the stiffeners. It was found that during impact delaminations had a propensity to grow towards regions of changes in stiffness, such as ply-drop offs in the stringer foot, or regions of higher stiffness, such as parallel to the stiffener direction. Damage in the bays was mostly in the form of delaminations which grew in size towards the back face, whereas over the stiffener centreline damage occurred mostly near the front face and consisted of fibre crushing and fibre fracture.

Wiggenraad and co-workers [62,63] conducted experiments to look at damage tolerance on a variety of damaged composite structures. These included sandwich structures, stiffened flat and curved panels, stiffened cylinders, and on a variety of simplified specimens. Two different blade-stiffened composite panel designs were investigated and compared to two other panels with a lower axial stiffness skin. The failure mode was found to consist of a load eccentricity being present since the beginning of the loading history, subsequently causing local bending near the area where the damage is present. Sub-laminates delaminated mainly in the lateral direction along 90° ply interfaces and bent out of plane, leading to unstable propagation of the delaminations causing global bending and eventually panel collapse.

A variety of other research efforts have been made to look at the effect of damage in composite structures. Yap et al. [64] devised a comprehensive automated FE modelling tool to look at the effect of skin-stiffener debonds in composite stiffened panels. Modelling of the damaged region was simplified to a 2D case, with a crack being able to grow only along the interface between the skin and stiffener, without crossing plies. Experiments were conducted so as to try and validate this modelling. Artificial skin-stiffener debonds were introduced in a stiffened composite panel by insertion of a folded Teflon foil so as to prevent adhesion between the stiffener and the skin. The panel was compressively loaded to investigate the debond growth behaviour up to the limit load and also its residual strength up until failure. The results showed that the simulation was able to predict the global buckling mode as well as the local buckling mode near the de-bonded region rather well. Discrepancies were identified and the limitations of the model possibly causing them identified. Local buckling initiated the skin-stiffener separation, and then global buckling caused the instability of the stringer flange as the loading was increased. This high deformation resulted in high peel stresses at the crack front and hence subsequent crack growth. Parametric studies were also conducted to see the effect of debond size and type, and details of the findings relating to local and global buckling commented upon. Fleshner and Herakovich [65] took a slightly different approach and introduced a new Component Damage Indicator into a finite element code so as to predict both the initiation and evolution of damage, as well as final failure, of composite structures. Details of the Component Damage Indicator were fully discussed, and it was then implemented in ABAQUS to look at a stiffened composite panel subject to a variety of load combinations. As expected the model showed that stiffener delamination was the dominant mode of failure of the panel, and the Component Damage Indicator proved to be a practical predictor for the failure of the panel.

5.3 Fracture mechanics

5.3.1 Basic concepts

The various works reviewed relating to the failure of composite structures have almost always highlighted how failure occurs due to mechanisms such as skin-stiffener debonding or the initiation and propagation of a crack. Such failure mechanisms in composites can be related to the brittle fracture of welded low-strength steel structures, where little plastic deformation is involved. Conventional design concepts based on tensile strength, yield strength and buckling stress are insufficient where cracks occur. Fracture is likely to initiate in regions where a stress concentration exists, and the initiation of a crack further increases the effect of this stress concentration. Fracture mechanics provides a means of analysis for structures with pre-existing cracks or with crack related failure mechanisms as is the case in composite materials. Fracture mechanics as a design tool helps to answer questions such as what the residual strength of a structure should be as a function of crack size, what the critical crack size before complete collapse is, or how long it may take for an initial crack to grow to this critical size.

One of the basic equations of fracture mechanics was established by Griffith [66]. As shown in Figure 5.6 (a), Griffith considered an infinite plate of unit thickness with a central transverse crack of length 2a. The plate is fixed at its ends and subject to a stress σ. Figure 5.6 (b) shows the load-displacement plot for the plate, with the area OAB representing the elastic energy in the plate for a specific loading. Assuming the crack to extend by an additional distance ∂a, then the stiffness of the plate will be reduced as some of the load is relaxed since the ends of the plate are fixed. The elastic energy is subsequently reduced to the area OCB, and the energy released by the crack growth from length a to new length $a + \partial a$ is represented by the shaded triangle OAC.

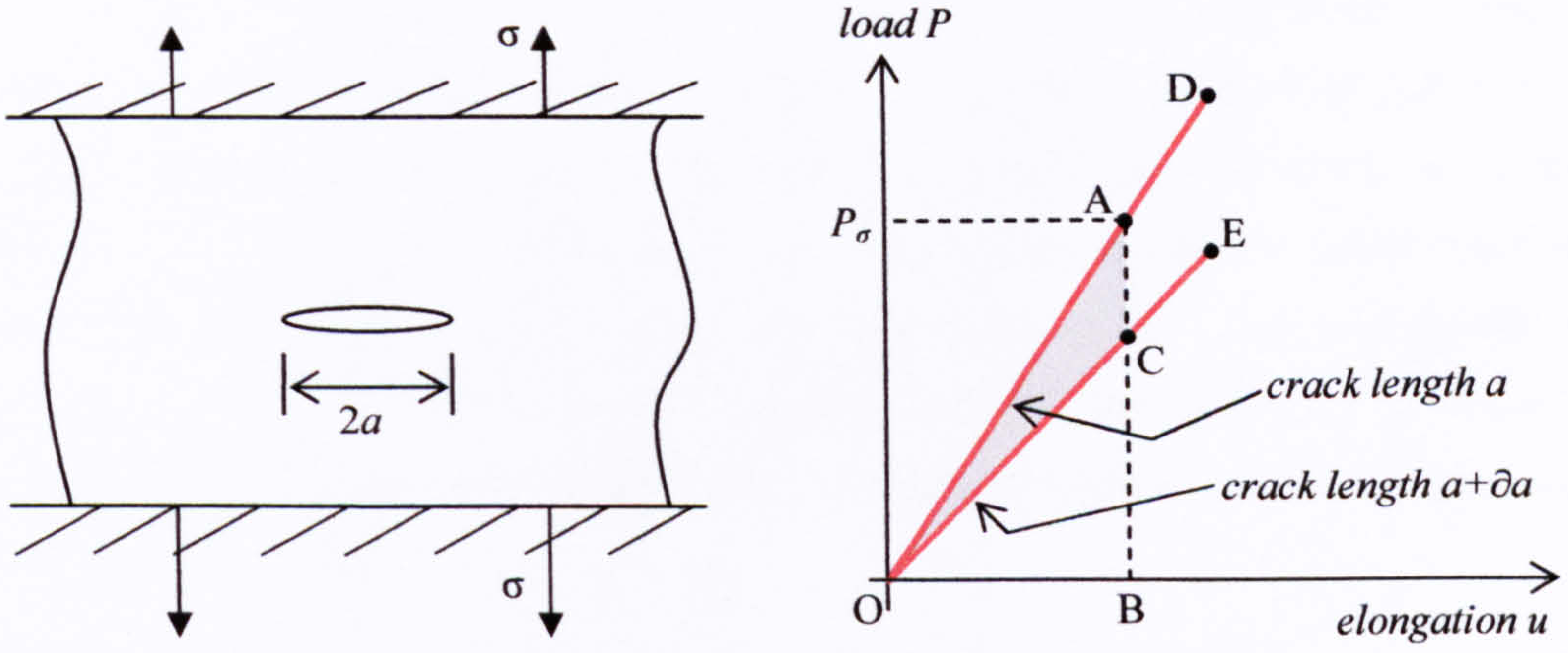

Figure 5.6: Griffith theory showing (a) cracked plate with fixed ends and (b) elastic energy released by crack growth.

Griffith stated that crack growth will occur if the energy released within the structure is sufficient to create the new crack surfaces. In Figure 5.6 (b), the triangle ODE is the amount of energy available for further crack growth. Stated mathematically, the condition for crack growth is:

$$\frac{\partial U}{\partial a} \geq \frac{\partial W}{\partial a} \tag{5.1}$$

where U is the strain energy and W is the energy required for crack growth. $\frac{\partial W}{\partial a}$ is the crack resistance more commonly denoted by G. For crack growth to occur, then this value G must exceed a critical value G_C. A crack may, in general, be stressed in three different modes as illustrated in Figure 5.7.

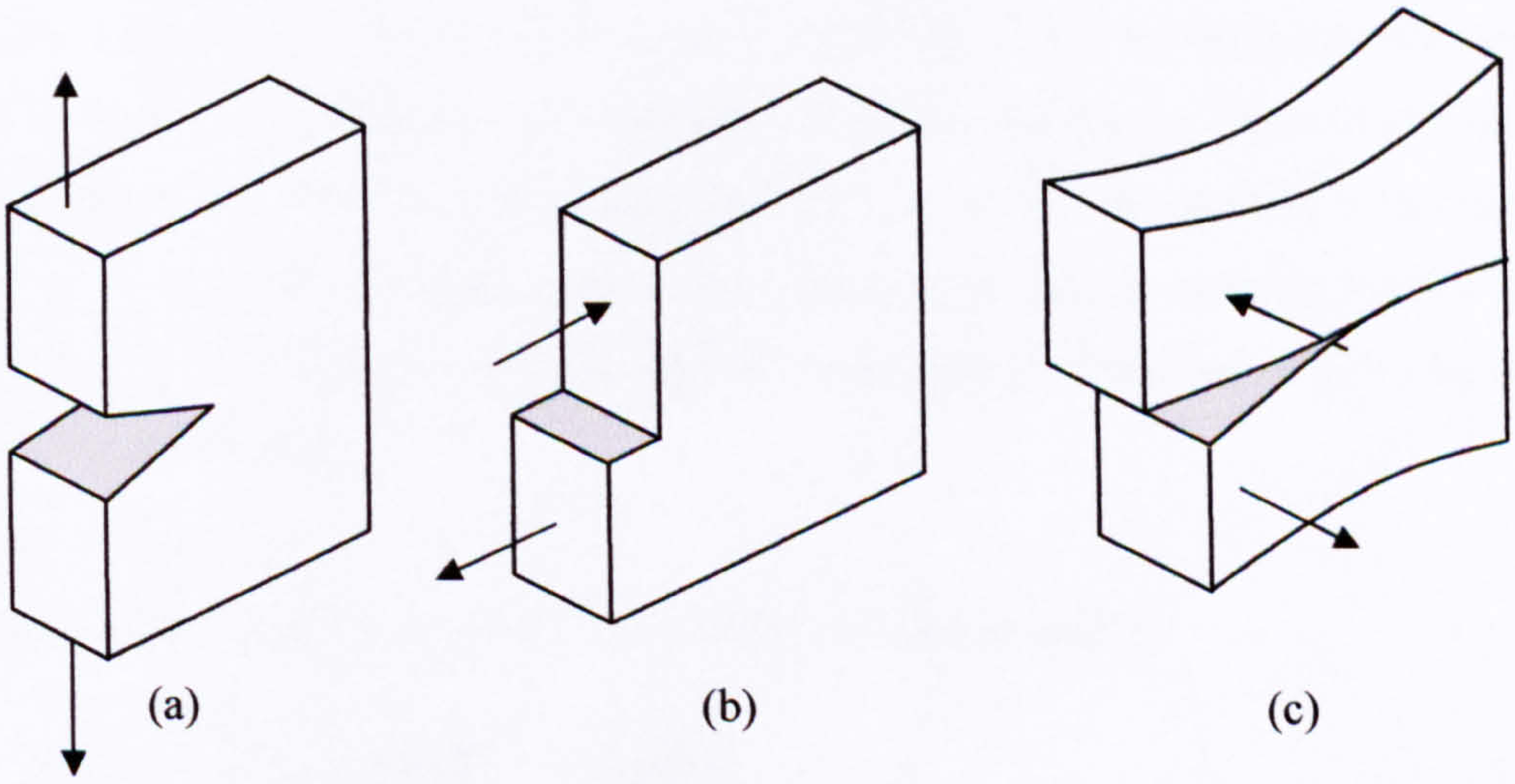

(a) (b) (c)

Figure 5.7: The three crack extension modes: (a) Mode I, (b) Mode II, (c) Mode III.

Mode I loading is an opening mode which occurs as a result of opening stresses. The crack surfaces displace in a direction normal to the plane of the crack. Mode II is a sliding mode, where the displacement of the crack surfaces is in the same plane of the crack, perpendicular to the latter's leading edge. Mode III is a tearing mode caused by out-of-plane shear. Displacements on the crack surface are in the same plane as the crack and parallel to its leading edge. Each of the three modes is associated with its own strain energy release rate; G_I, G_{II}, and G_{III}. The total strain energy release rate G_T can then be expressed as the sum of the individual components:

$$G_T = G_I + G_{II} + G_{III} \tag{5.2}$$

5.3.2 The virtual crack closure technique

The implementation of fracture mechanics to model the phenomenon of crack initiation and propagation in an FE analysis is now a widespread modelling methodology. Two major approaches can be identified to model the propagation of a crack in for example a composite material undergoing delamination. The first is the use of VCCT and the second the development and application of interface elements. This section will briefly discuss the major principles behind VCCT and how it is applied to model crack propagation in an FE model. A plethora of research work has been undertaken in this field, and the reader is referred to an extensive review compiled by Krueger [9] which deals with both the theoretical approach and applications of VCCT.

The VCCT technique bears its roots to the Crack Closure Method, which in turn is based on Irwin's [67] crack closure integral. The principle is based on the central assumption that when calculating the strain energy release rate, the amount of energy released by opening a crack is the same as the amount of work done in closing the crack. Figure 5.8 shows a 2D crack configuration. The crack has an existing length a and is to be extended by an additional length Δa. Two modes for crack extension are possible in 2D, the opening Mode I and the sliding Mode II. When this is the case, the total strain energy release rate is given by the sum of the two components:

$$G_T = G_I + G_{II} \tag{5.3}$$

The crack closure integrals proposed by Irwin are then the following:

$$G_I = \lim_{\Delta a \to 0} \left[\frac{-1}{2\Delta a} \int_0^{\Delta a} \sigma_{ZZ}(x,0) w(x - \Delta a, 0) dx \right] \tag{5.4}$$

$$G_{II} = \lim_{\Delta a \to 0}\left[\frac{-1}{2\Delta a}\int_0^{\Delta a}\sigma_{XZ}(x,0)u(x-\Delta a,0)dx\right] \tag{5.5}$$

where *x* and *z* refer to coordinates of a coordinate system at the crack front as shown in Figure 5.8. *u* and *w* are the displacements in the *x* and *z* directions respectively.

The application of the Crack Closure Method with the FE method is performed using two finite element analyses. In the first analysis the crack is closed at a length *a* in Figure 5.8. The forces at the crack tip are obtained by summing the nodal forces at common nodes for each element above or below the crack plane. The crack is then opened by the additional distance Δa and the displacements obtained by this second FE solution.

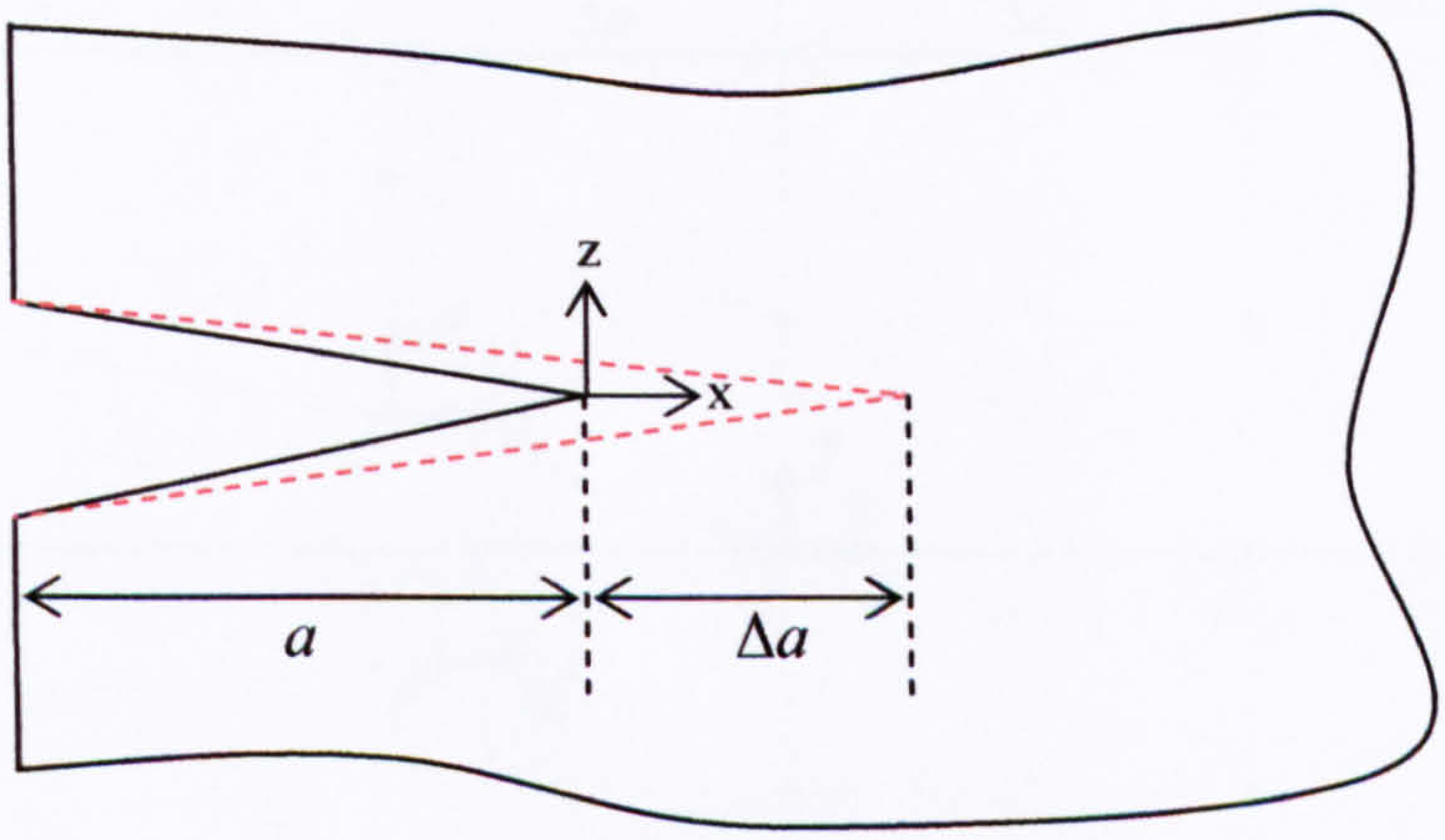

Figure 5.8: 2D crack configuration for Clack Closure Method.

VCCT was first proposed by Rybicki and Kanninen [10] and its application with four noded elements is shown in Figure 5.9. The same assumptions as for the Crack Closure Method apply, but it is additionally assumed that, with reference to Figure 5.9, a crack extension Δa from a + Δa at node *j* to $a + 2\Delta a$ at node *k* does not significantly alter the state at the crack tip. What this means is that when the crack tip is at node *k*, the displacements behind it are approximately equal to those behind the crack tip at node *i* when the crack tip is located at node *j*. Also, the energy ΔE released in extending the crack from $a + \Delta a$ to $a + 2\Delta a$ is the same as the energy required to close the crack between nodes *j* and *k*. The strain energy release rates G_I and G_{II} are then calculated as:

$$G_I = \frac{-1}{2\Delta a}Z_j\left(w_i^t - w_i^b\right) \tag{5.6}$$

$$G_{II} = \frac{-1}{2\Delta a}X_j\left(u_i^t - u_i^b\right) \tag{5.7}$$

where Δa is the element length at the crack front and X_j and Z_j are the forces at the crack tip located at node j. The relative displacements behind the crack tip are then determined by the nodal displacements on the top crack face (u^t and w^t) and those at the bottom crack face (u^b and w^b). The equations discussed are easily modified for different element types such eight-noded elements. Furthermore a 3D crack may also be considered where the additional strain energy term G_{III} is taken into account, as explained by Krueger [9] together with VCCT procedures for arbitrarily shaped delamination fronts and necessary corrections for elements with different length or width at the crack tip, as well as combining VCCT with geometrically nonlinear FE analyses.

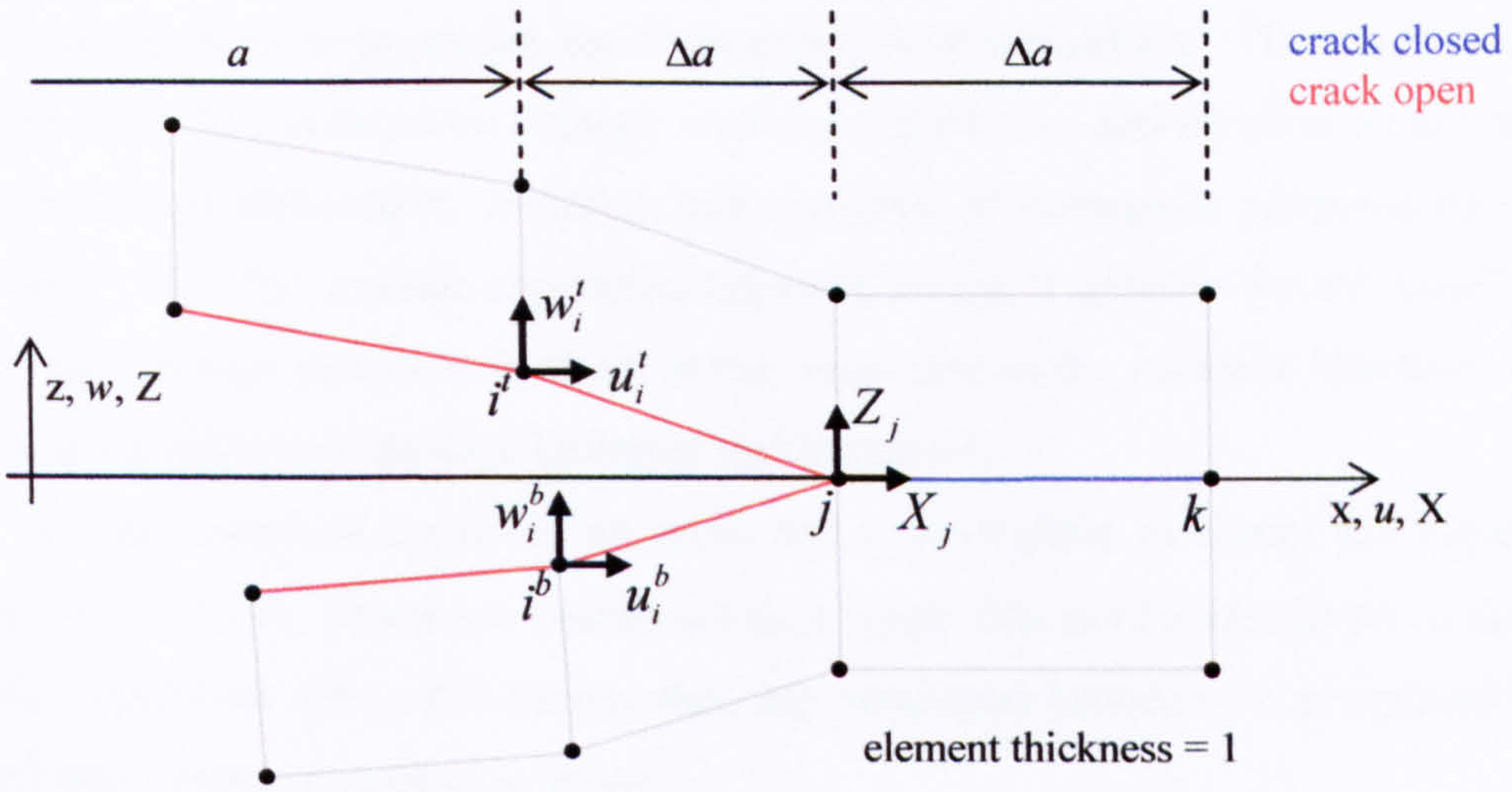

Figure 5.9: Application of the VCCT technique to four-noded elements.

VCCT allows a single FE run to determine whether a crack will continue to propagate. This will happen when the strain energy release rates are compared with their critical values. If they are in excess of these critical values, then crack propagation will occur. Under mixed-mode loading several expressions have been proposed relating the different modes to a failure criterion. These are discussed next together with interface elements as the latter also use the same criteria when dealing with mixed-mode crack propagation. VCCT is easily implementable in an FE code and has proven to successfully model crack propagation. However it is only capable of modelling crack propagation, in the sense that a pre-existing crack must exist in the model. For certain geometries and load conditions, it may be extremely difficult to determine the exact location of this initial crack or delamination and hence implement it into an FE model. Furthermore, complicated moving mesh techniques may be required when the crack front is advanced during delamination growth. Interface elements on the other hand do not pose some of the above problems, and can model both crack initiation and propagation. Their formulation and implementation into the FE package ABAQUS is discussed next.

5.4 Interface elements

5.4.1 Introduction

Interface elements are interfacial decohesion elements placed between solid finite elements to model the initiation and progression of delamination. In FE analyses of composite materials, interface elements can be placed between the various composite layers or at adhesive interfaces. They use failure criteria combining aspects from both strength-based analysis to predict the onset of softening at the interface where the elements are placed, and fracture mechanics to predict the propagation of delamination. The traction-separation model in ABAQUS is based on damage mechanics principles and involves an initially linear elastic behaviour followed by initiation and evolution of damage as proposed by Camanho and Davila [11]. The traction-separation approach makes it possible for the combination of one or more damage mechanisms to act at the same time on the cohesive interface, with each mechanism consisting of damage initiation and evolution.

Interface elements consist of an upper and a lower plane as shown and highlighted in grey in Figure 5.10. These two planes act as a single one until a certain prescribed failure criterion is satisfied. Once this occurs, then the connection between the two planes is broken and discrete damage is created or grown.

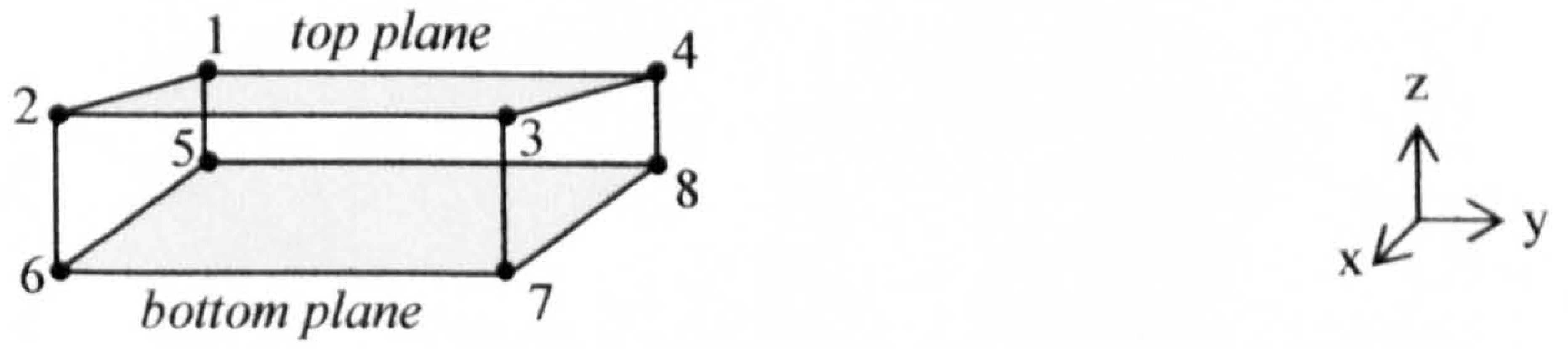

Figure 5.10: Interface element geometry with top and bottom planes.

Interface elements are governed by the stresses and relative displacements of the interface surfaces, rather than stress-strain relations as in continuum elements, and hence their constitutive equation is defined in terms of relative displacements and tractions across the interface. Each point on the top and bottom surface has a corresponding, or homologous, point on the opposite surface. An example of homologous points are points 1 and 5, or 3 and 7 in Figure 5.10. When the interface is closed, then homologous points are in contact with one another. When the interface is loaded then the two surfaces will move relative to one another. The relative displacements between homologous points are defined in terms of two displacement components, corresponding to an opening and a sliding mode. The opening mode corresponds to Mode I loading on a crack as was illustrated in Figure 5.7, while sliding is due to Mode II. The tearing Mode III may also be considered as a sliding mode, since it is often difficult to determine which direction the crack front is oriented.

To correctly model the delamination process, a suitable constitutive equation relating the tractions and relative displacements of the cohesive interface is required. This involves the use of a cohesive zone to remove the singularity at the crack tip as first proposed by Dudgale [68] and Barenblatt [69]. Physically the cohesive zone represents the coalescence of crazes in the resin rich layer at the crack tip and the way in which the material loses its ability to carry load. This principle can be related to Griffith's theory of fracture if the area under the traction - relative displacement curve of the interface element constitutive law is equal to the corresponding fracture toughness.

5.4.2 Constitutive law for single mode delamination

For pure Mode I and pure Mode II or Mode III loading a softening constitutive behaviour as shown in Figure 5.11 is used. This is a bilinear law as is available in the FE package ABAQUS. Various other modifications to this law have been proposed and may be implemented, such as an exponential constitutive law or a third-order polynomial constitutive law [70].

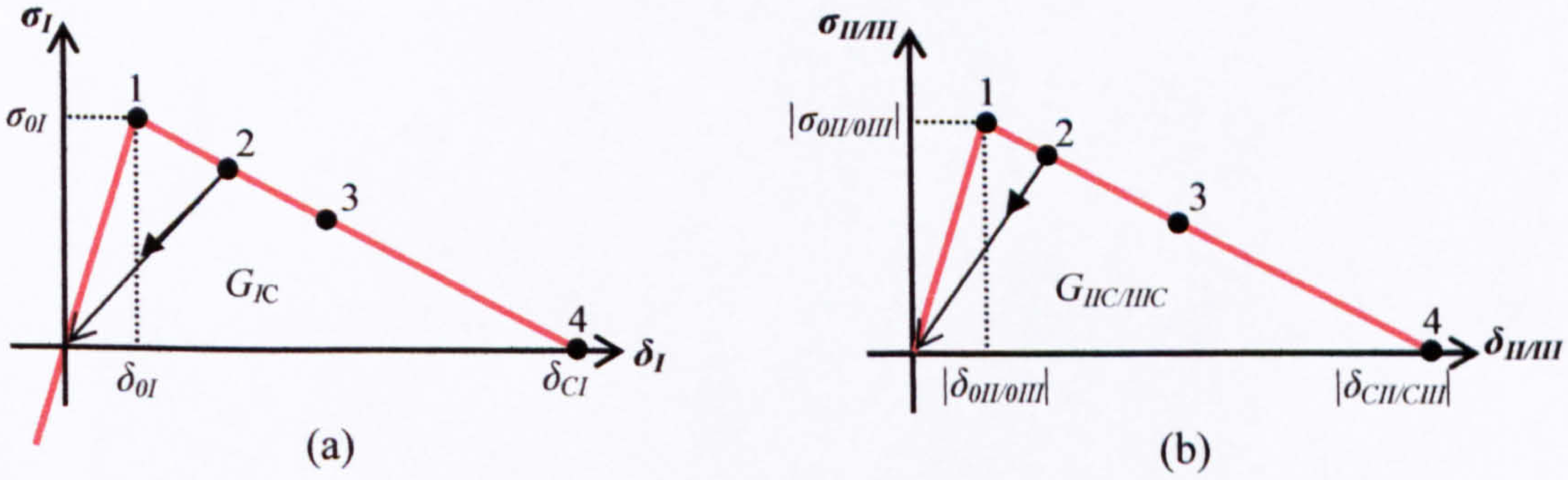

Figure 5.11: Bi-linear traction-separation laws for interface elements in (a) Mode I and (b) Mode II/ Mode III delamination.

Initially, when a point is loaded, the traction - relative displacement behaviour is elastic, with a high initial stiffness holding the top and bottom surfaces of the interface elements together. For pure Mode I, Mode II, or Mode III loading, damage initiates once the interfacial normal or shear tractions reach their respective interlaminar tensile or shear strengths, σ_{0I} and $\sigma_{0II/0III}$. At this point, labelled 1 in Figure 2 (a) and (b), the relative opening displacements are δ_{0I} and

$\delta_{0II/0III}$ respectively. The subscript '*0*' refers to the onset of damage as it is at this threshold that damage initiates and starts propagating. The onset tractions and relative displacements are related as:

$$\delta_{0I} = \frac{\sigma_{0I}}{k}, \ \delta_{0II/0III} = \frac{\sigma_{0II/0III}}{k} \tag{5.8}$$

where k is the high initial stiffness holding the top and bottom surfaces together. After damage initiation has occurred, the stiffnesses are gradually reduced to zero via points 2 and 3 to point 4 in Figure 2 (a) and (b). At point 4, when the traction reaches zero, the energy absorbed must equal the critical energy release rate for the respective mode. Hence the area under the traction-relative displacement curve of Figure 5.11 is the respective Mode I, II, or III fracture toughness G_{IC}, G_{IIC}, or G_{IIIC}. These define the final relative displacements of the interface once complete failure has occurred, which are labelled δ_{CI} for the opening Mode I and $\delta_{CII/CIII}$ for the sliding Mode II and Mode III. Once again it must be stressed that the term sliding is used here for both Mode II and Mode III because the distinction between the latter two modes is dependent on the direction of the relative displacement of the homologous points on the cohesive interface, which in turn depends on the orientation of the crack propagation. When the crack propagation direction is unknown, or in a generic situation with more than one crack growth direction, then it is extremely difficult to distinguish between Modes II and III. The final displacements are hence obtained as:

$$\delta_{CI} = \frac{2G_{IC}}{\sigma_{0I}}, \ \delta_{CII/CIII} = \frac{2G_{IIC/IIIC}}{\sigma_{0II/0III}} \tag{5.9}$$

5.4.3 Damage irreversibility and interpenetration

The unloading behaviour of the interface must also be considered and damage irreversibility accounted for. To do this, a new state variable δ^{max} is introduced. This is the maximum relative displacement suffered by the point of interest on the interface over time and is defined as:

$$\delta_I^{\max} = \max\{\delta_I^{\max}, \delta_I\} \text{ with } \delta_I^{\max} \geq 0 \text{ for Mode I} \tag{5.10}$$

$$\delta_{II/III}^{\max} = \max\{\delta_{II/III}^{\max}, |\delta_{II/III}|\} \text{ for Mode II/ III} \tag{5.11}$$

Using δ^{max} in the constitutive equation allows for the irreversibility of damage to be taken into account. This is shown in Figure 5.11 by a point unloading from point 2 elastically towards the origin with a reduced secant stiffness. Once irreversibility has been addressed, the whole irreversible, bi-linear, softening constitutive law may be expressed as follows:

$$\sigma_i = \begin{cases} k\delta_i \Leftarrow \delta_i^{\max} \leq \delta_{0i} \\ (1-D_i)k\delta_i \Leftarrow \delta_{0i} < \delta_i^{\max} < \delta_{Ci} \\ 0 \Leftarrow \delta_i^{\max} \geq \delta_{Ci} \end{cases} \tag{5.12}$$

$$D_i = \frac{\delta_{Ci}\left(\delta_i^{\max} - \delta_{0i}\right)}{\delta_i^{\max}\left(\delta_{CI} - \delta_{0i}\right)}, D_i \in [0,1] \tag{5.13}$$

where the subscript i refers to the pure loading mode, i = I, II/III, and D is a damage variable which ranges from 0 when damage is about to initiate (point 1 in Figure 5.11) to 1 when complete failure has occurred (point 4 in Figure 5.11).

As stated earlier, once point 4 in Figure 5.11 is reached, the interface is completely broken and all penalty stiffnesses are reduced to zero. It is however required to avoid the two surfaces interpenetrating. This is done by re-applying the normal penalty stiffness once interpenetration is detected by adding the following condition:

$$\sigma_I = k\delta_I \Leftarrow \delta_I \leq 0 \tag{5.14}$$

Hence the interface behaviour defined by the traction-separation constitutive law described can be fully expressed once the properties relating to the fracture toughness values G_{IC}, $G_{IIC/IIIC}$, interlaminar normal and shear strengths σ_{0I}, $\sigma_{0II/0III}$, and penalty stiffness k are defined.

5.4.4 Mixed mode delamination

Delamination growth under a pure single mode loading is the simplest of cases, but in a general situation is unlikely to occur. When more than one mode acts simultaneously, a delamination may start propagating prior to one of the single mode limit tractions (σ_{0I} or $\sigma_{0I/0II}$) being reached. In this case a general formulation for interface elements is required, which can handle mixed-mode damage initiation and progression. Two quantities are first defined, a shear relative displacement δ_{shear}, and a total mixed mode relative displacement δ_m:

$$\delta_{shear} = \sqrt{(\delta_{II})^2 + (\delta_{III})^2} \tag{5.15}$$

$$\delta_m = \sqrt{\langle\delta_I\rangle^2 + (\delta_{II})^2 + (\delta_{III})^2} = \sqrt{\langle\delta_I\rangle^2 + (\delta_{shear})^2} \tag{5.16}$$

where Mc-Cauley brackets $\langle x\rangle$ are used and defined as

$$\langle x\rangle = \begin{cases} 0 \Leftarrow x \leq 0 \\ x \Leftarrow x > 0 \end{cases} \tag{5.17}$$

Similarly the shear traction is given by

$$\sigma_{shear} = \sqrt{(\sigma_{II})^2 + (\sigma_{III})^2} \tag{5.18}$$

A mode mixity ratio β can also be defined as:

$$\beta = \max\left\{0, \frac{\delta_{shear}}{\delta_I}\right\} \tag{5.19}$$

Using the above parameters, a certain displacement δ_m at the interface will result in a specific mixed mode damage state. As for pure single mode loading, a damage initiation and a damage propagation criterion are required. This is shown graphically in Figure 5.12, which is similar to Figure 5.11 but applies for mixed mode loading rather than for a single mode.

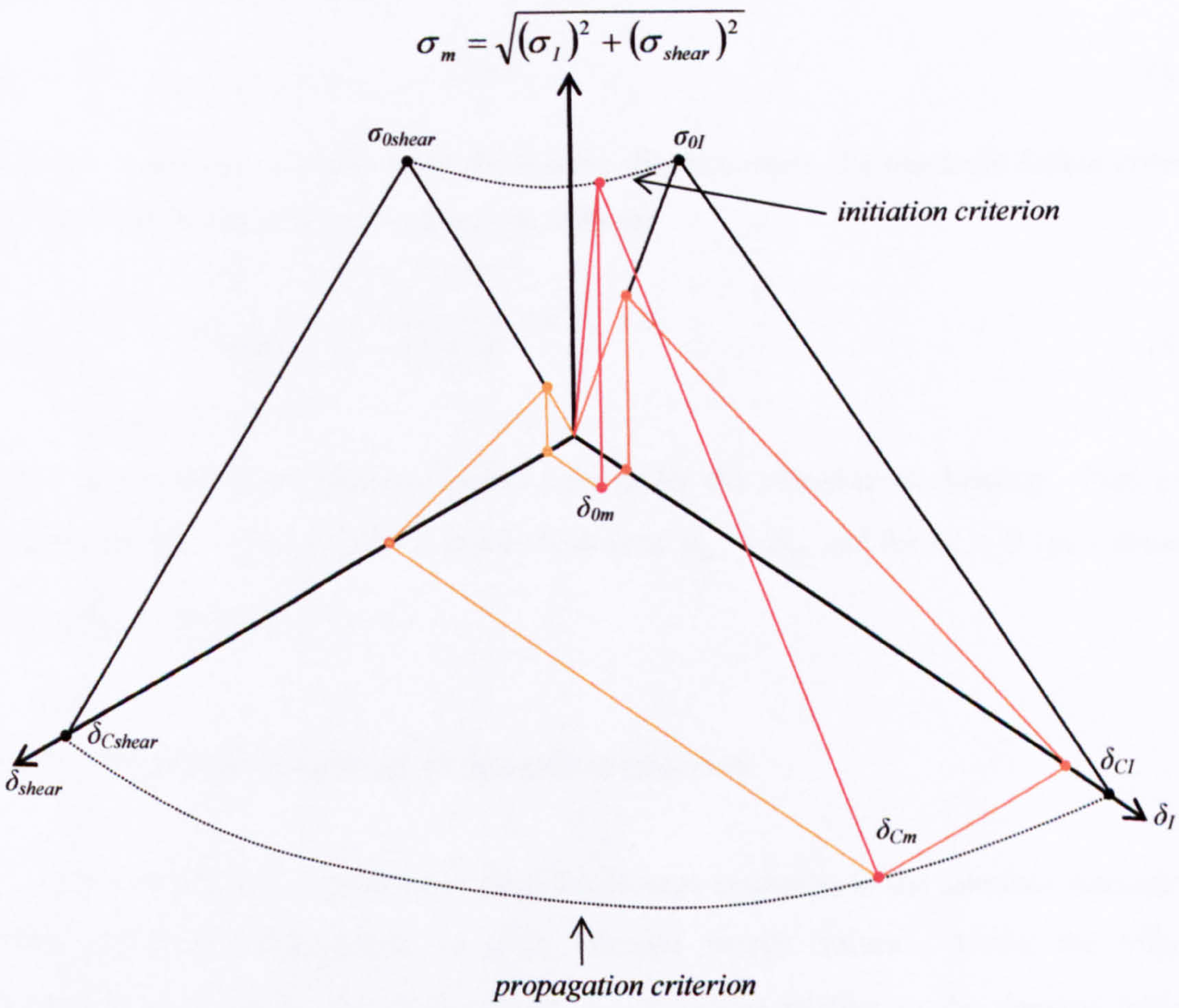

Figure 5.12: Mixed mode behaviour for bi-linear traction-separation law.

5.4.5 Mixed mode damage initiation criterion

Under pure single mode loading, damage initiation occurs when the traction components exceed their respective maximum values. Cui et al. [71] stressed that under mixed mode loading, interactions exist between the interlaminar stress components which mean that a mixed mode damage initiation criterion taking such interactions into account is necessary. The quadratic stress criterion is widely used in this sense, although ABAQUS offers the user the possibility of also using the maximum nominal stress, maximum nominal strain, and maximum quadratic strain criteria for damage initiation.

The quadratic stress criterion can be stated as follows:

$$\left(\frac{\langle\sigma_I\rangle}{\sigma_{0I}}\right)^2+\left(\frac{\sigma_{shear}}{\sigma_{0shear}}\right)^2=1 \tag{5.20}$$

σ_{0I} and σ_{0shear} are the interlaminar normal and shear strengths as shown in Figure 5.12. Assuming $\sigma_{0II}=\sigma_{0III}$ then $\sigma_{0shear}=\sigma_{0II}=\sigma_{0III}$ and the single mode relative displacements at softening onset are given by:

$$\delta_{0I}=\frac{\sigma_{0I}}{k},\ \delta_{0II}=\delta_{0III}=\delta_{0shear}=\frac{\sigma_{0shear}}{k} \tag{5.21}$$

Since the tractions are functions of the relative displacements, the quadratic failure criterion may be stated in terms of tractions only as follows:

$$\delta_{0m}=\begin{cases}\delta_{0I}\delta_{0shear}\sqrt{\dfrac{1+\beta^2}{(\delta_{0shear})^2+(\beta\delta_{0I})^2}} \Leftarrow \delta_I>0\\ \delta_{0shear}\Leftarrow\delta_I\le 0\end{cases} \tag{5.22}$$

where δ_{0m} is the onset relative displacement under the mixed-mode loading. Pure mode loading is recovered when $\beta=0$ (pure Mode I) as $\delta_{0m}=\delta_{0I}$ and for $\delta_I=0$ (pure shear) as $\delta_{0m}=\delta_{0shear}$ (or when $\beta\rightarrow\infty$).

5.4.6 Mixed mode damage propagation criterion

In ABAQUS it is possible to describe damage evolution in the interface elements via either effective displacements or using fracture energy values. Using the effective displacement approach, the displacement δ_{Cm} at failure relative to the damage initiation displacement δ_{0m} is specified. This softening law may be either linear, exponential, or expressed in tabular fashion. As was discussed for single mode loading, damage evolution is best described using energy arguments based on the energy dissipated during the damage process. Hence fracture toughness values are usually used to predict propagation under mixed mode loading. The specific criterion used determines the state of complete decohesion. Several criteria are available in ABAQUS for damage propagation in interface elements. Here the Benzeggagh-Kenane (BK) [72] criteria is discussed as it will be subsequently used in the models presented throughout this thesis. Other damage evolution criteria are available for use, such as using a power interaction of the fracture energies, as discussed in the ABAQUS documentation [39].

The BK criterion is expressed in terms of Mode I and Mode II fracture toughness values and a parameter η obtained from Mixed Mode Bending (MMB) experimental tests:

$$G_{IC} + (G_{IIC} - G_{IC})\left(\frac{G_{II}}{G_T}\right)^{\eta} = G_C, G_T = G_I + G_{II} \tag{5.23}$$

If Mode III loading is also acting on the interface then:

$$G_{IC} + (G_{IIC} - G_{IC})\left(\frac{G_{shear}}{G_T}\right)^{\eta} = G_C, G_T = G_I + G_{shear} \tag{5.24}$$

The value of the parameter η is material dependent. For example, for a composite with a thermoplastic resin) a value of 0.63 is typically used, for tough epoxy resin a value of 1.3, and for a brittle epoxy resin a value of 1.75 [11]. At total decohesion, the energies absorbed by each mode in mixed mode loading are:

$$G_I = \int_0^{\delta_I^{Cm}} \sigma_I d\delta_I \tag{5.25}$$

$$G_{II} = \int_0^{\delta_{II}^{Cm}} \sigma_{II} d\delta_{II} \tag{5.26}$$

$$G_{III} = \int_0^{\delta_{III}^{Cm}} \sigma_{III} d\delta_{III} \tag{5.27}$$

The upper limits to the integrals relate to the relative displacements at total decohesion for each mode. Substituting Equation (5.12), Equation (5.16), Equation (5.19) into Equations (5.25-5.27) and using the latter into the BK criterion Equation (5.24) allows the mixed mode displacements at complete decohesion, δ_{Cm}, to be expressed as:

$$\delta_{Cm} = \begin{cases} \dfrac{2}{k\delta_{0m}}\left[G_{IC} + (G_{IIC} - G_{IC})\left(\dfrac{\beta^2}{1+\beta^2}\right)^{\eta}\right] \Leftarrow \delta_I > 0 \\ \delta_{Cshear} \Leftarrow \delta_I < 0 \end{cases} \tag{5.28}$$

5.4.7 Constitutive law

For mixed mode loading, the constitutive law is defined by the penalty stiffness k, the mixed mode relative displacements for damage initiation and total decohesion δ_{0m} and δ_{Cm} respectively, and the damage variable D. As in the case of a pure single mode loading damage irreversibility is taken into account by considering a maximum relative displacement:

$$\delta_m^{\max} = \max\{\delta_m^{\max}, \delta_m\} \tag{5.29}$$

The damage variable under mixed mode loading is then defined as:

$$D = \begin{cases} 0 \Leftarrow \delta_m^{\max} \leq \delta_{Om} \\ \dfrac{\delta_{Cm}\left(\delta_m^{\max} - \delta_{0m}\right)}{\delta_m^{\max}\left(\delta_{Cm} - \delta_{0m}\right)} \Leftarrow \delta_{0m} < \delta_m^{\max} < \delta_{Cm} \\ 1 \Leftarrow \delta_m^{\max} \geq \delta_{Cm} \end{cases} \tag{5.30}$$

and it follows that $D \in [0,1]$.

The constitutive equation is then simply:

$$\sigma_t = (1 - D)k\delta_t \tag{5.31}$$

The condition to avoid interpenetration for compression conditions as discussed for pure single mode loading is used:

$$\sigma_I = k\delta_I \Leftarrow \delta_I \leq 0 \tag{5.32}$$

The only state variable used to track the damage at the interface is the maximum relative displacement variable $\delta_m^{\max}$. The relative displacements for initiation and ultimate failure of the interface are then dependent of the mode mixity ratio β, penalty stiffness k, and material properties. For a complete definition of the interface which will be subject to mixed mode loading conditions, the parameters required for definition are then the penalty stiffness k, interlaminar strengths σ_{0I} and $\sigma_{0II/0III}$ and the fracture toughness values G_{IC} and $G_{IIC/IIIC}$.

5.5 Interface element validation

Appendix A shows the interface element discussed validated using a DCB problem. The DCB problem investigated is widely regarded as the first benchmark when considering the modelling of crack propagation. This is because it represents the simplest case, that of a near pure Mode I crack growth. Further validation of interface elements is required, but this has already been tackled by a wide variety of authors and is hence not reported here. Furthermore, the interface elements used are the ones directly available in ABAQUS and a wide variety of validation tests are included in the ABAQUS documentation [39]. Traditionally the next step after consideration of a DCB problem would be that of an ENF test so as to see how the interface elements behave under predominantly Mode II loading [73]. Once this is done, then validation moves towards mixed mode loading. In the ABAQUS documentation, the problem considered is that of mixed mode multi-delamination of a composite specimen with two initial cracks. This problem was first proposed by Alfano and Crisfield [74] and has been widely used in the validation of crack propagation modelling techniques.

In the remainder of this thesis the interface elements presented here are used to model advanced composite structures so as to "incorporate" the out-of-plane failure capability that is necessary to capture the failure and collapse characteristics of structures such as stiffened composite panels. In general such structures will undergo complex failure processes, and hence the mixed mode loading formulation presented is essential. In the next chapter it will be seen how two different stiffener runout specimens can be modelled in ABAQUS with the potential failure of the skin-stiffener interface modelled using interface elements. Chapter 7 will then reconsider the I-stiffened panel seen in Chapter 4. As was discussed in the literature review of this chapter, such stiffened panels exhibit skin-stiffener debonding which may act as a precursor to final collapse, and hence inclusion of this phenomenon in a credible FE model is vital.

Chapter 6

Finite element modelling of stiffener runout sections

In Chapter 5 the many experimental investigations first introduced in Chapter 2 were reconsidered, this time focusing on the failure mechanisms of the various composite structures tested. Most of the experimental work highlighted how out-of-plane failure associated with skin-stiffener debonding acted as a precursor to final global collapse. This was especially true in composite stiffened panels where the periodically changing out-of-plane displacements due to buckle deformations gave rise to maximum twisting and bending moments at positions corresponding to buckle node and anti-node lines respectively, resulting in through-thickness stresses which led to the debonding. Chapter 5 introduced the main concepts of fracture mechanics, and how interface elements may be incorporated into an FE model so as to predict failure modes such as delamination or skin-stiffener debonding.

This chapter takes the concepts explained in Chapter 5, particularly pertaining to interface elements, and applies them to the modelling of two stiffener runout specimens. These specimens were previously manufactured and tested experimentally, and some FE analyses were conducted so as to capture their qualitative behaviour using VCCT. Here the FE models attempt to capture the behaviour of the specimens and model the potential skin-stiffener debonding with the introduction of interface elements at the skin-stiffener interface. Numerical results pertaining to strains are compared to strain gauge results obtained experimentally, and observations made relating to how the numerical results correlate to the experimental findings. The predicted collapse loads for the specimens are compared to the collapse loads observed experimentally, giving an insight into how well the interface elements are able to capture the failure modes of the stiffener runout specimens.

6.1 Introduction

The problem of through-thickness stresses promoting skin-stiffener debonding is even more critical in regions such as stiffener runouts. Such runouts must exist as it is necessary to terminate stiffeners at specific structural features such as cutouts or ribs in an airframe construction. Such a termination of the stiffener interrupts the stiffener load path, and hence in this region high interlaminar and shear stresses may develop. This has become ever more important due to the recent trend of using thicker-skinned stiffened composite structures in heavily loaded regions of, for example, an airframe structure. Hence the design of a runout region is vital in how the load is transferred to the unsupported part of the skin. A common design practice is to taper the height of the stiffener web towards the runout edge, as this has been deemed to have an alleviating effect on the significant interface and peel stresses present in this region.

Stiffener runout regions have received a lot of attention with regards to their experimental testing. For example, when NASA tested the composite C130 wing box section which was developed as part of their Advanced Composites Technology (ACT) program [75,76], failure of the stiffener runout region was identified as the critical failure mode for the whole structure. Due to the presence of a transverse rib, the hat-stiffener on the structure was manufactured to taper to a runout. This resulted in the unsupported skin section to be subjected to high bending strains due to the load path eccentricity at this location. Failure initiation was sited at this unsupported skin region, and then propagated across the panel and down the spars leading to eventual catastrophic global collapse of the wing box. Similar observations were made by Brooks [77] during the compressive testing of a co-bonded hat-stiffened runout panel. High bending and shear stresses at the edge of the runout resulted in unstable crack propagation at the skin-stiffener interface promoting final failure. Extensive testing of stiffener runouts was also conducted in the Department of Aeronautics at Imperial College London as was discussed in Chapter 5. Three different blade-stiffened runout configurations were tested by Falzon et al. [57] who then went on to modify some of the specimens [58] so as to try and alleviate the stress concentration due to the presence of the discontinuity at the runout end. Greenhalgh and Garcia [59] conducted fractographic analyses on failed runout specimens, looking at how geometric modifications such as the introduction of web cut-offs and foot tapering affected the failure characteristics of the runout specimens.

FE models of the various stiffener runout configurations tested by Falzon et al. were constructed by the same authors [54]. Such models aimed at qualitatively capturing the behaviour of the specimens and sought to measure strain energy release rates by the use of VCCT. As was discussed in Chapter 5, VCCT has a major limitation in the sense that an initial crack is required and hence the method is only able to simulate crack propagation.

Furthermore the FE models discussed did not seek to try and model the failure behaviour of the runout specimens. This is necessary in the ultimate goal of reducing costs associated with experimental testing. High fidelity FE models able to replicate the behaviour of a structure such as a stiffener runout and also give valuable insight into its failure characteristics are essential so as to reduce the amount of experimental testing necessary to validate a particular structure. Two stiffener configurations are modelled in this chapter, both of which were part of a large experimental program investigating the failure of stiffener runout specimens [78]. Both specimens consisted of a blade stiffener co-cured onto a skin. The stiffener was tapered down towards the runout end, and the specimens were sized so that interlaminar shear stress failure occurred in the skin-stiffener interfaces at a loading lower than the Euler buckling loads. Each of the two specimens – referred as specimen A and specimen B – is discussed next, relating to its experimental testing and results obtained, FE model, and comparison of the experimental and numerical results. Differences in behaviour between the two specimens are also investigated and explained.

6.2 Stiffener runout specimen A

6.2.1 Specimen geometry and experimental setup

Specimen A was a thinner skinned specimen having an overall length of 440 mm and a width of 120 mm. At the runout end, the unsupported length of skin section was 40 mm. The blade stiffener tapered linearly over a length of 200 mm to a final height of 10 mm above the skin. Such tapering where the stiffener does not go all the way down to the skin is done for more practical manufacturing purposes, but results in a step discontinuity in the cross-sectional area giving rise to a stress concentration at the edge of the stiffener. The skin thickness was 8.0 mm, and all relevant dimensions for the specimen are shown in Figure 6.1. The ends of the specimen were first potted in epoxy resin and then machined parallel so as to ensure uniform loading during the uniaxial compression tests. Such tests were undertaken using a hyperstiff 250-T compression-testing machine. Due to the relatively high stiffness of the specimens, a high machine stiffness was required and it was desirable that the specimens were not destroyed after failure initiation due the machine energy. Figure 6.1 also shows the location of various strain gauges mounted on Specimen A so as to measure in-plane and bending strains. LVDTs were used to measure displacements. Additionally, an acoustic emission recorder was utilized so as to try and detect any damage activity before final catastrophic failure.

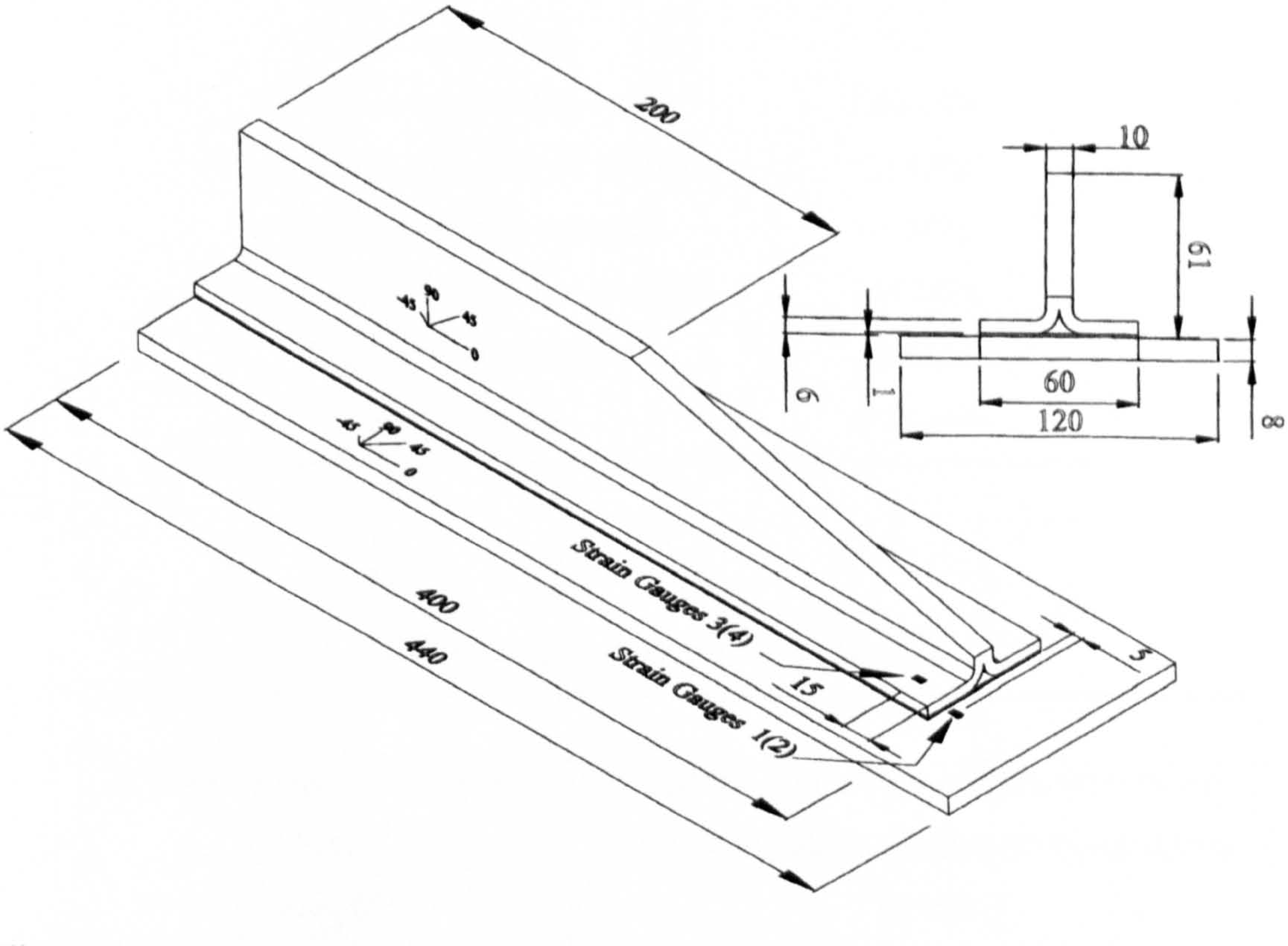

Figure 6.1: Specimen A dimensions with strain gauge locations, figure by Falzon et al. [78].

The material used in the manufacturing was AS4-8552 unidirectional carbon-fire composite, the nominal material properties of which are summarized in Table 6.1 The lay-up of the stiffener, skin, and closing plies are shown in Table 6.2. The closing plies were located between the skin and the bottom surface of the stiffener flanges, and spanned the whole width of the stiffener, which was co-cured onto the skin. It must be noted that in Table 6.2 the lay-up of the skin and closing plies are given from the outer to the inner surface of the specimen with the outer layer defined as the smooth surface which would form part of the aerodynamic surface in a wing structure and the inner surface defines as the surface on which the stiffener is mounted. The lay-up for the half-section of the stiffener is referred from the bottom flange surface, at the stiffener/closing plies interface and moving up towards the free surface. Similarly, in Figure 6.1 back-to-back strain gauge pairs are quoted such that the bracketed strain gauge label refers to the gauges which were mounted on the outer smooth surface of the specimen directly under the un-bracketed label gauges which are visible in the figure.

Table 6.1: Nominal material data for AS4-8552 unidirectional composite @ 60 V_f, dry.

Property	Value
Longitudinal tensile modulus	135 GPa
Longitudinal compressive modulus	128 GPa
Transverse tensile modulus	9.5 GPa
Transverse compressive modulus	10.3 GPa
In-plane shear modulus	4.9 GPa
Poisson's ratio	0.3
Longitudinal tensile strength	1.68 GPa
Longitudinal compressive strength	1.1 GPa
Transverse tensile strength	61 MPa
Transverse compressive strength	244 MPa
In-plane shear strength	90 MPa
Ply thickness	0.25 mm

Table 6.2: Lay-up details for specimen A.

Part	Lay-up
Stiffener (per half section)	$[0/90/0_2/-45/45/0_4/-45/45/0_2/90/0_3/90/0]$
Skin	$[45/-45/0/90/0_2/-45/45/0_2/90/0_2/45/-45/0]_S$
Closing plies	$[0/90/0_2]$

6.2.2 Experimental results

The strains as recorded by the four strain gauges of Figure 6.1 are shown in Figure 6.2. The highest compressive strains were recorded by SG1, the strain gauge located on the stiffener side of the unsupported skin at the end of the runout. SG2 was located at the same position on the unsupported skin but on the outside surface. Here the readings were much lower, and in fact very little strain was recorded by the strain gauge at this location. This is due to the fact that at this position the compressive strains arising from the uniaxial compression of the specimen are counteracted by tensile bending strains. These arose as the unsupported region of the skin bent away from the stiffener side, so that the inner surface was in a state of higher compression than the outer surface. In fact the curvature may be measured by the difference in the back-to-back strain gauge readings of strain gauges SG1 and SG2. It is clear from the large difference in the recorded values that the section of unsupported skin underwent a large amount of bending deformation caused by the geometric eccentricity of the stiffener runout. SG3 and SG4, corresponding to the other strain gauge pair mounted on the stiffener region recorded the opposite trend, that of a slightly higher compressive strain on the outer surface than on the inner surface on the stiffener flange. Comparing SG3 and SG1, both located on the inner surface, it may also be stated that the strain measured on the inner surface at the centre of the stiffener flange and close to the stiffener edge was much lower than that on the inner surface of the unsupported skin. At failure of the specimen, the maximum recorded strain was recorded by SG1 as approximately 8000 μs.

Failure of specimen A occurred at a compressive load of 245 kN. A marked increase in displacement (0.39 mm) was clear at the failure point as recorded by the LVDT, and occurred due to the testing machine's finite stiffness which may have acted to provide additional energy into the specimen to propagate the crack. Crack initiation and propagation was sudden and highly unstable, and the crack propagated across the whole interface in an almost instantaneous fashion. This inevitably led to catastrophic failure at the 90°/0° interface in the closing plies between the bottom of the stiffener flange and the skin top surface. Additionally a noticeable increase in acoustic emission was present just prior to failure, but because of the unstable nature of the crack growth leading to collapse it was not possible to unload the specimen quickly enough to arrest crack propagation.

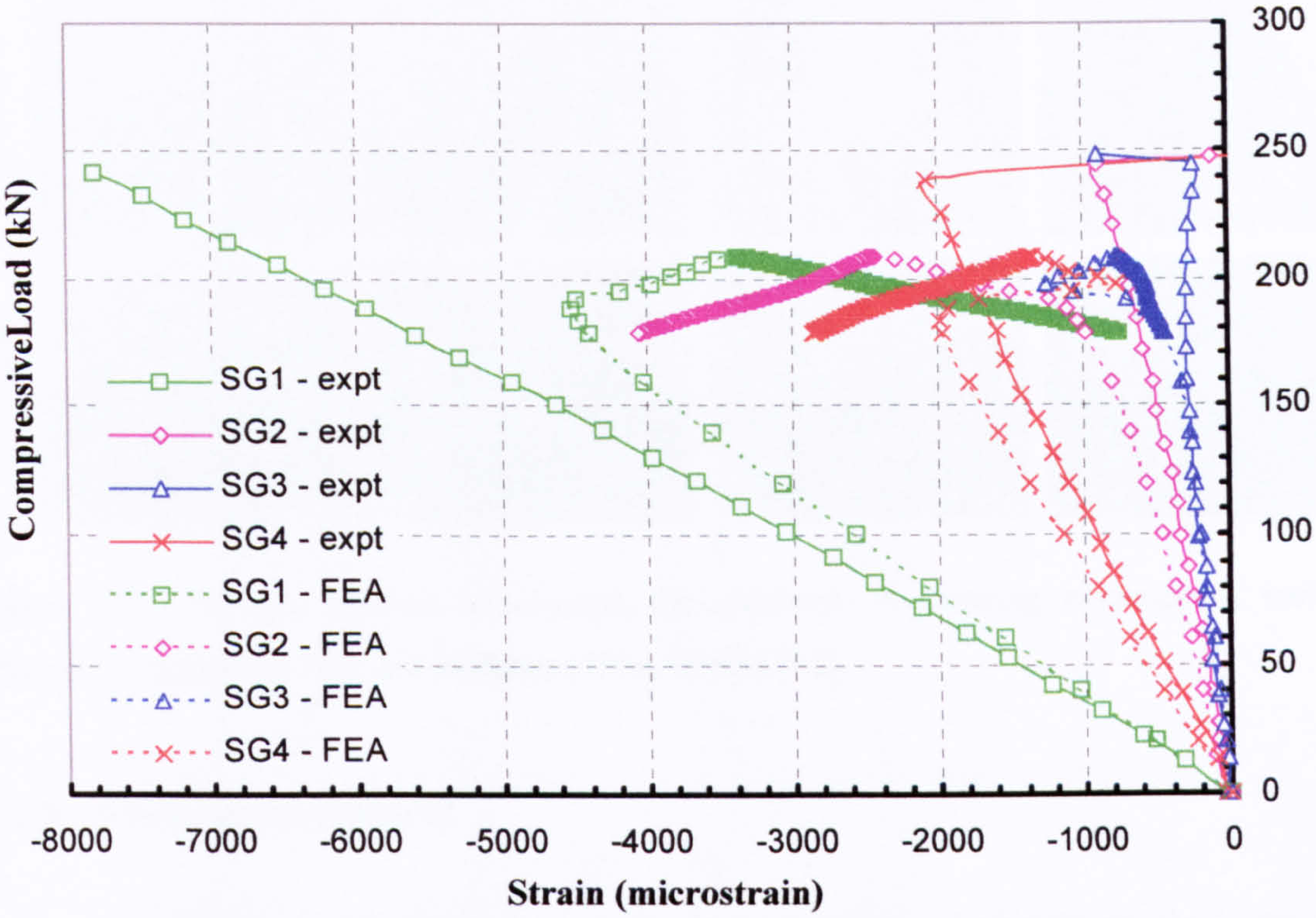

Figure 6.2: Experimental and numerical strain gauge results for specimen A.

After final collapse of specimen A, a fractographic analysis of the fracture surface was undertaken so as to better understand the failure processes. The micrographs used are shown in Figure 6.3. These only show half of the specimen width, since the fracture surface morphology displayed symmetry. Close to the end of the runout (0.5 mm), widespread crushing and fretting across the whole width of the crack front was observed, indicating the presence of high out-of-plane compressive forces which were deemed to arise from the loading offset in the stiffener. At a position 10 mm away from the edge, crushing was more pronounced towards the edges and rather negligible towards the stiffener centreline position. It was hypothesised that these compressive forces may have delayed the onset of crack initiation, and the failure morphology suggested a Mode II dominated fracture surface, in a direction parallel to the stiffener length. Additionally, some crack growth inwards from the edges at the corners of the stiffener was also observed.

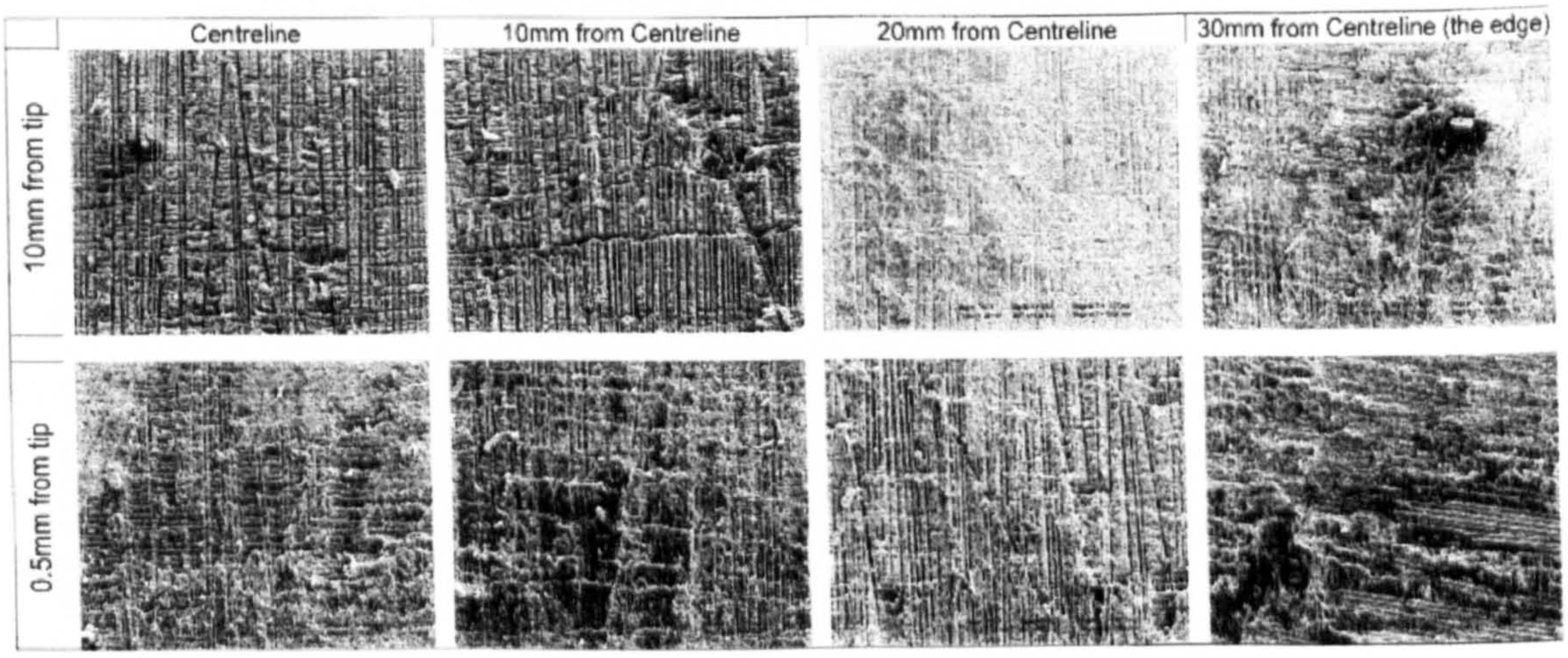

Figure 6.3: Fracture surface micrograph for specimen A showing evidence of surface crushing between the skin and stiffener (750x, 0° tilt) [58].

6.2.3 Finite element model

A detailed finite element model was developed for specimen A with the aim to not only capture the qualitative behaviour of the specimen during its compression test, but also model its failure characteristics and evaluate how credible an FE model can be in revealing the entire failure process of such a runout specimen. This was particularly important in view of how failure of the experimental specimen occurred in the skin-stiffener interface region. When dealing with a composite material made up of various components with different lay-ups, such as the skin and stiffener in the runout specimen, complex 3D stress states arise at the crack tip and these are difficult to predict using FE models. To overcome this difficulty, a possible approach is to use standard brick elements throughout the model, but in order to capture the through-thickness stresses which are critical to the failure process as was discussed previously, typically one element per ply is required in the thickness direction. When structures containing a substantial number of plies in their lay-up are considered, this soon becomes prohibitively expensive form a computational point of view. A second approach is that of using the shape functions of brick elements whilst setting up various planes of Gauss integration points, coinciding with each ply in the component. This is still expensive due to the large number of integration points required to achieve acceptable accuracy. A third approach is that of using thick shell, or continuum shell, elements and gives a very good compromise between accuracy and computational cost of the FE analysis. Continuum shell elements only have translational degrees of freedom, just like standard brick elements, however strains are defined in the local directions of the mid-surface plane as for the case of conventional shell elements. The thickness of continuum shell elements is determined solely by their nodal connectivity, and when used in ABAQUS such elements look just like brick elements from a modelling perspective. Their constitutive and kinematic behaviour however is similar to that of conventional shell elements. The formulation of continuum shell elements is discussed in the ABAQUS documentation [39], as well as by Falzon et al. [79] who presented the formulation of a similar element to improve the computational efficiency associated with the calculation of strain energy release rates in laminated structures.

Due to symmetry considerations, only half of the runout specimen was considered. The FE model consisted of three separate parts – the skin, stiffener, and interface layer – connected together using tie constraints. Eight-node continuum shell elements were used throughout the stiffener and skin parts, with one element used through the thickness of the skin. In the case of the stiffener, one element was used through the thickness of the stiffener half section, and another element through the thickness of the closing plies. Six-node wedge elements were also used in the corner region of the stiffener at the tapered runout end. Figure 6.4 shows the final mesh of the model with an expanded view of the runout region, in which a finer mesh was used as this was the location where crack initiation was expected to occur. Likewise a finer width wise mesh was used in the stiffener and that portion of the skin directly under the stiffener so that the interface elements placed at the skin-stiffener interface would be sufficiently small to correctly model crack initiation and propagation. A coarser mesh was used at the end of the specimen away from the runout region as it was expected that final collapse would have occurred prior to the crack propagation reaching this location. Mesh sensitivity tests were carried out to assure that the final mesh in both the length wise and width wise directions was fine enough to guarantee convergent results. Table 6.3 gives a summary of the mesh used.

Table 6.3: Specimen A mesh details.

Element type	Number of elements - location
eight-node continuum shell	891 – skin
	1,651 – stiffener
six-node continuum shell	5 – stiffener
eight-node interface	876 – interface layer

Continuum shell elements require the definition of local coordinate systems to guarantee that the 0° and 90° directions for ply orientations as well as ply stacking direction are defined. In the model separate coordinate systems were defined to guarantee correct material orientations, following which the lay-up of the skin and stiffener were defined as in Table 6.2. Figure 6.5 shows the ply orientations for the first, or bottom ply of each component. For the skin this is a 45° ply, whilst for the stiffener it is a 0° ply. It can be seen how the local *1* direction (blue) corresponds to the fibre direction and the local *2* direction (yellow) is the direction orthogonal to a fibre. The local *3* direction (red) corresponds to the stacking – or thickness – direction of the composite.

Three different boundary conditions were applied on the model to correctly replicate the experimental setup. A clamped boundary condition was set to all nodes at the end of the model opposite the runout. The skin nodes at the other extremity of the model were also initially clamped and then the axial displacement degree of freedom was released by prescribing a compressive displacement so as to establish a displacement controlled uniaxial compression of the specimen which was done in a quasi-static non-linear analysis. Finally, all nodes on the symmetry plane were assigned symmetric boundary conditions.

Interface elements were placed at the interface between the skin and stiffener under the closing plies. This was done so as to model the mixed-mode crack initiation and propagation in the specimen. The interface elements followed the formulation detailed in Chapter 5, with a traction-separation law describing their behaviour. A high initial stiffness held the skin-stiffener interface together up until damage initiation, which was established using the quadratic stress criterion of Equation (5.20). Following initiation of damage, damage propagation was expressed using the BK criterion of Equation (5.24). The interface properties used relating to the interlaminar tensile and shear strengths a well as fracture toughness values for Mode I, Mode II, and Mode III loading are shown in Table 6.4 and were taken from experimental values [80]. Viscous regularization as discussed in Appendix A was used in the analysis, and parametric studies were conducted to ensure that a small enough value for the viscosity parameter μ. This was given a value of 1.0^{-4} which aided in speeding up convergence whilst not affecting results adversely.

Table 6.4: Skin-stiffener interface properties [80].

Property	Value
Interlaminar tensile strength σ_{0I}	61 MPa
Interlaminar shear strength $\sigma_{0II}/\ \sigma_{0III}$	49.8 MPa
Mode I fracture toughness G_{IC}	532 J/m^2
Mode II/III fracture toughness $G_{IIC}/\ G_{IIIC}$	2,358 J/m^2
Poisson's ratio ν_{12}	0.28

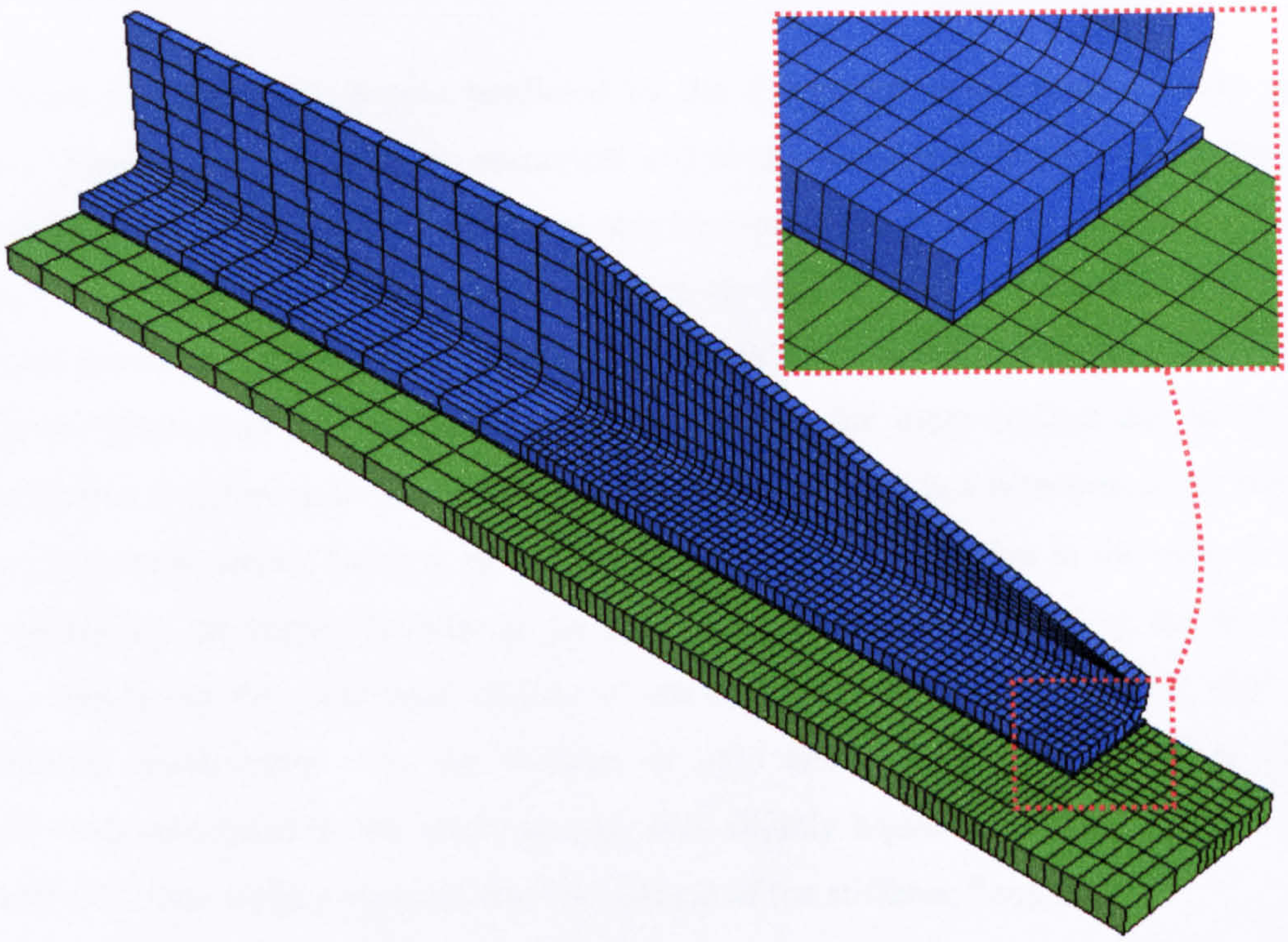

Figure 6.4: ABAQUS FE mesh for specimen A, with expanded view of runout region.

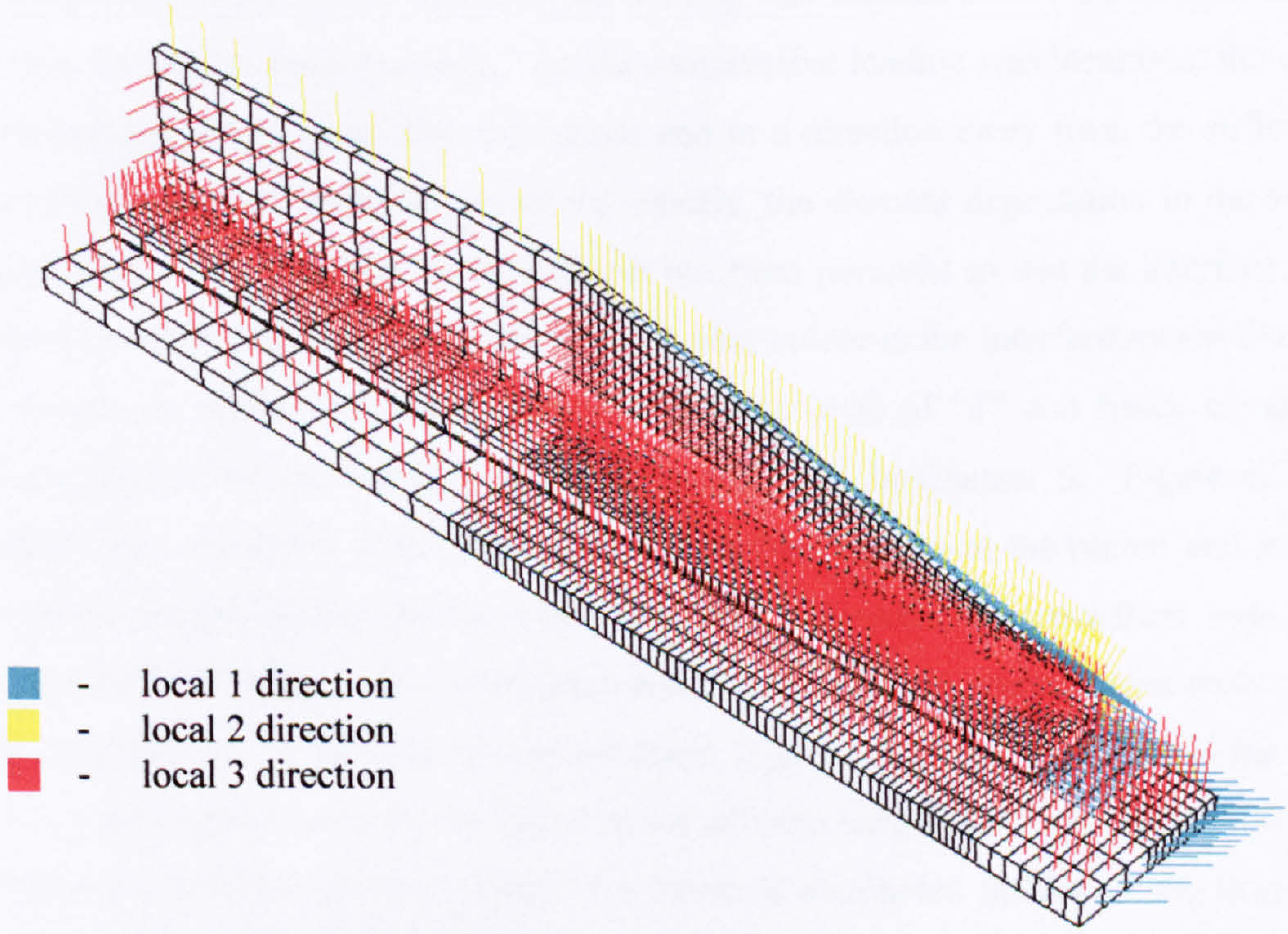

Figure 6.5: ABAQUS material directions for correct lay-up of specimen A model. Orientations shown for bottom plies of skin and stiffener.

6.2.4 Finite element results

Figure 6.2 shows the strains predicted by the FE model at the various strain gauge locations. Good agreement between numerical and experimental strains can be seen for all of the strain gauge results. The FE model was able to capture the difference in recorded strains between SG1 and SG2. As was mentioned when discussing the experimental results, SG2 located on the outer smooth surface of the unsupported skin near the runout end recorded a much lower strain than SG1 at the same location but on the inner surface due to the high bending strains developing in this region. As the skin deformed in a direction away from the stiffener, the inner surface became in much higher compression relative to the outer surface, hence explaining the higher stresses at the position of SG1 as confirmed by the numerical results. Strains on the supported section of the specimen also compared well with their experimental counterparts. At the location of SG3 and SG4, numerical strains closely matched those measured by the strain gauges with slightly higher compressive strains being present on the outer surface compared to the surface of the stiffener flange.

The FE model confirmed the observations made during the experiment that the unsupported skin region underwent large bending deformations and local changes in curvature occurred due to the geometric discontinuity imposed by the termination of the stiffener. This was evident in the difference in strains at locations SG1 and SG2, but is also apparent when viewing the deformed configuration of the specimen FE model. Figure 6.7 shows the deformed shape of the model as the loading was increased with a deformed scale factor of five for visualization purposes. As the compressive loading was increased, the skin underwent bending deformation bear the runout end in a direction away from the stiffener. Adjacent to the deformed configuration of the models, the element degradation in the skin-stiffener interface is shown. Part of the stiffener has been removed so that the interface and its associated level of degradation may be seen. A blue colour at the interface means that no damage is present, whilst red corresponds to a damage level of "1" and hence complete stiffness degradation of the interface elements as discussed in Chapter 5. Figure 6.7 (a) clearly shows how the crack at the skin-stiffener interface initiates at the runout end and is spread rather uniformly across the interface, with a slight tendency to grow from under the corner of the stiffener flange. This observation was also made in the fractographic analysis of the failed specimen A. As the loading was increased, Figure 6.7 (b) and (c) illustrate how the crack quickly propagated along the specimen in the stiffener length direction. Inspection also revealed that the interface elements failed in a Mode II dominated fashion as the skin was compressed. However at a certain point the skin suddenly buckled away form the stiffener opening the interface in Mode I as the specimen failed. Figure 6.7 (c) is a snapshot just after this begins to happen. Further compression just opens the interface more and more along the stiffener length as the runout is unable to carry any more load.

The interface elements captured the failure characteristics of specimen A very well, and crack propagation occurred in a very sudden fashion in the FE model. The initially Mode II dominated fracture followed by Mode I opening correlates with the fractographic findings of a Mode II dominated fracture surface with extensive crushing and fretting. Crack growth occurred along the stiffener direction, just as in the experiment. The FE analysis predicted collapse of runout specimen A at a loading of 208 kN, compared with the experimentally observed 245 kN. Figure 6.6 shows the final collapsed FE model of the specimen, where the interface elements have been removed for clarity. This further confirms the good agreement between numerical and experimental results, not only in view of strain values at the various panel locations but also of the failure characteristics observed.

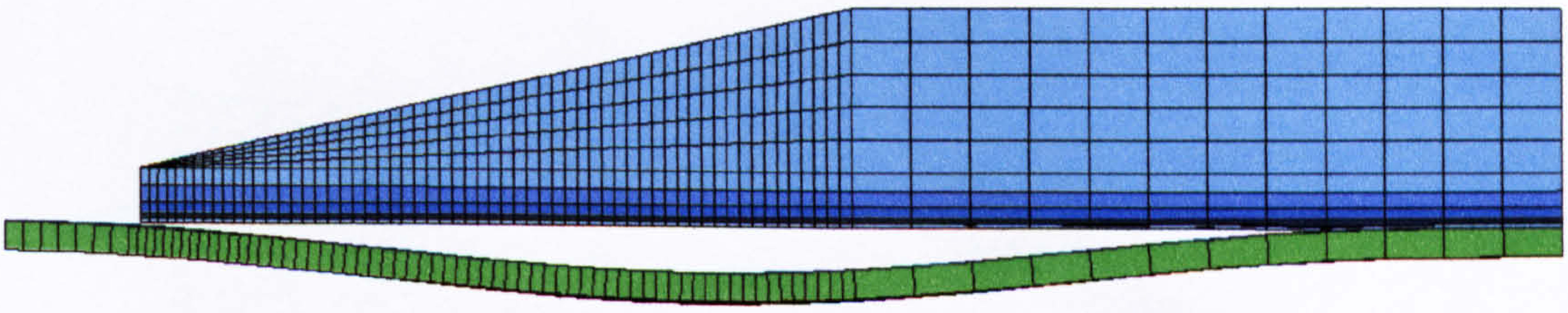

Figure 6.6: Side on view of deformed FE specimen A model after collapse. Deformation scale factor 1.

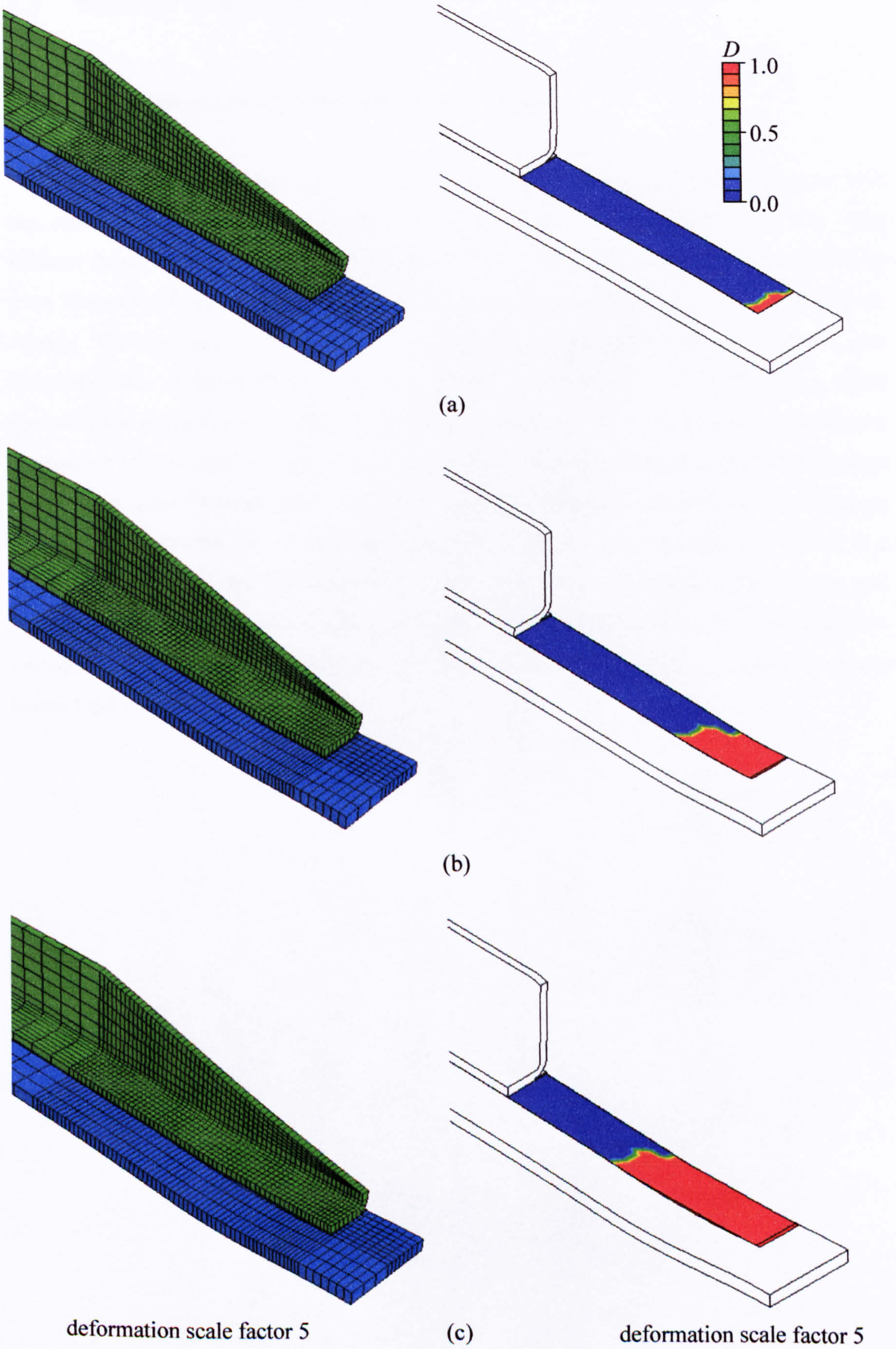

Figure 6.7: FE deformed shape and interface damage for specimen A at loading of (a) 160 kN, (b) 208 kN, (c) just after collapse.

6.3 Stiffener runout specimen B

6.3.1 Specimen geometry and experimental setup

Specimen B was a scaled-up version of Specimen A. It had a skin thickness of 13.0 mm and hence a corresponding increase in length to 540 mm and width 200 mm. The stiffener flange width was increased from 120 mm to 200 mm, and the stiffener web thickness from 10 mm to 14 mm, but the unsupported section of skin at the runout end was still kept at 40 mm. The tapering of the stiffener web was done over a greater length, now 200 mm, and the termination of the stiffener taper at a height above the skin still meant that a stress concentration existed at the stiffener edge at the runout end. Figure 6.8 shows the complete dimensions of the runout specimen B together with the locations of back-to-back strain gauge pairs. Once again the same convention as for specimen A applies, where the bracketed gauge is that gauge positioned on the smooth surface that would form the aerodynamic surface in a wing structure. Like for the thinner specimen, the ends were potted in epoxy resin and machined parallel to ensure uniform loading during the testing in the 250-T compression-testing machine and an acoustic emission recorder was used to detect any damage activity before final collapse.

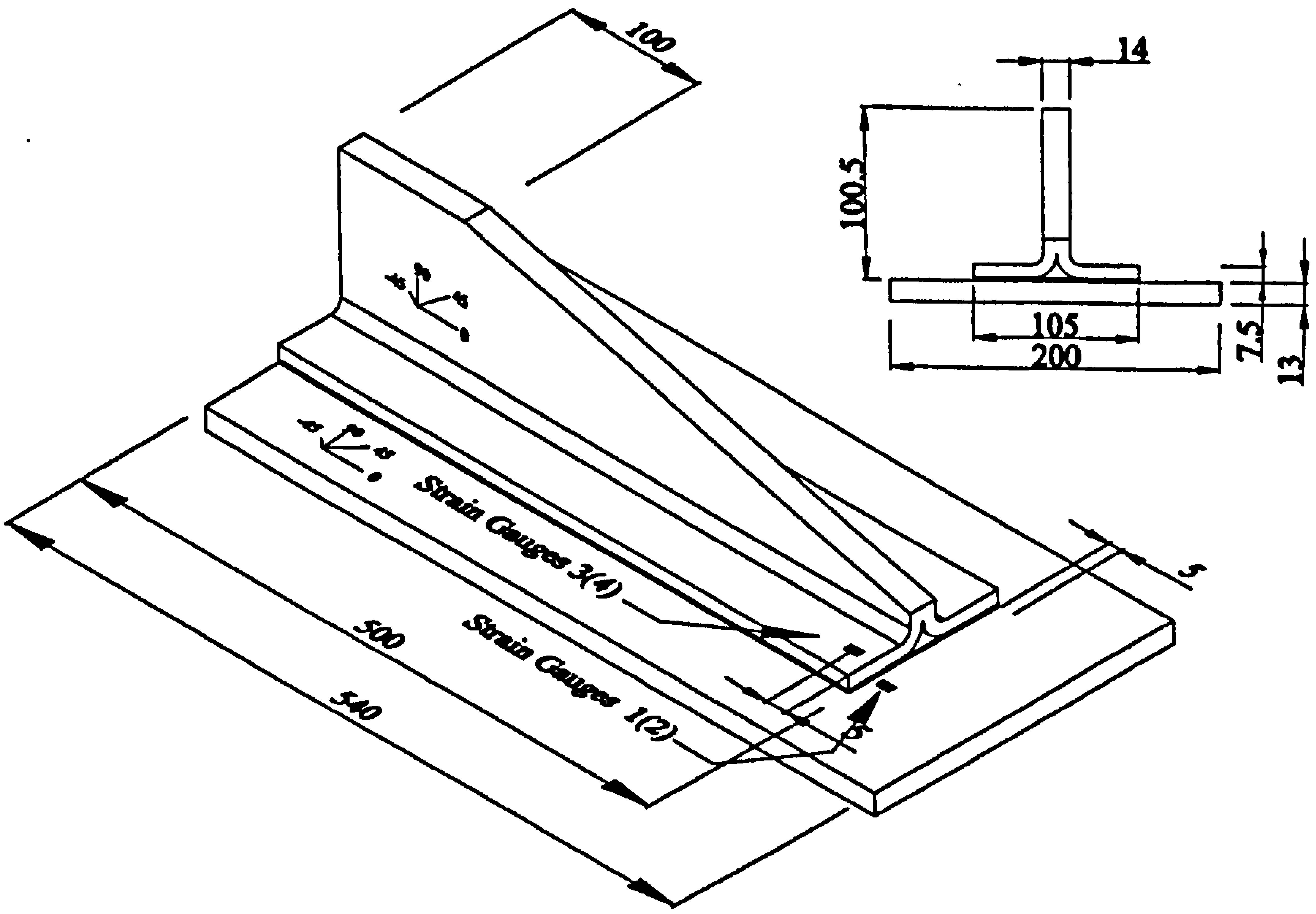

Figure 6.8: Specimen B dimensions with strain gauge locations, figure by Falzon et al. [78].

The same unidirectional carbon-fibre AS4-8552 material, whose nominal properties are listed in Table 6.1, was used in the manufacturing of Specimen B. Table 6.5 shows the lay-up for the skin, stiffer and closing plies, again given form the outer, smooth surface inwards to the stiffener side.

Table 6.5: Lay-up details for specimen B.

Part	Lay-up
Stiffener (per half section)	$[-45/0_2/45/0_2/90/0_2/45/0/90/0_2/90/$ $0/-45/0_2/90/0_2/45/0_2/-45_2/45]$
Skin	$[45/-45/0_2/90/0_2/45/-45/0_3/45/-45/$ $0/90/0_2/45/-45/0/90/0_2/45/-45]_S$
Closing plies	[-45/45]

6.3.2 Experimental Results

As stated before, specimen B was basically a scaled up version of specimen A with a skin thickness increased to 13.0 mm and a stiffener which tapered for a length of 400 mm, over a longer distance than for specimen A. The strain gauge locations are shown in Figure 6.8. SG1 and SG2 were located at a distance 5.0 mm away form the runout end on the unsupported skin section, with SG2 being on the outside smooth surface. Both were at a distance of 15 mm from the stiffener centreline. Figure 6.9 shows the strain gauge readings recorded by the various strain gauges. As for specimen A the highest readings were recorded by the SG1 mounted on the inside of the specimen on the supported skin. SG2 showed much lower readings, again due to the compressive axial strains on the outside of the skin being counteracted by the tensile bending strains which arise due to the change in curvature at this location. SG3 was located 5 mm from the runout edge but on the stiffener flange surface, with SG4 directly below it on the supported skin section, and again both 15 mm form the stiffener centreline. Little bending strains were recorded by the latter strain gauges, as visible in Figure 6.9, meaning that only slight bending occurred in the supported region just before the runout. The inner surface even went into slight tension, as evidenced by positive readings of the red line corresponding to SG3.

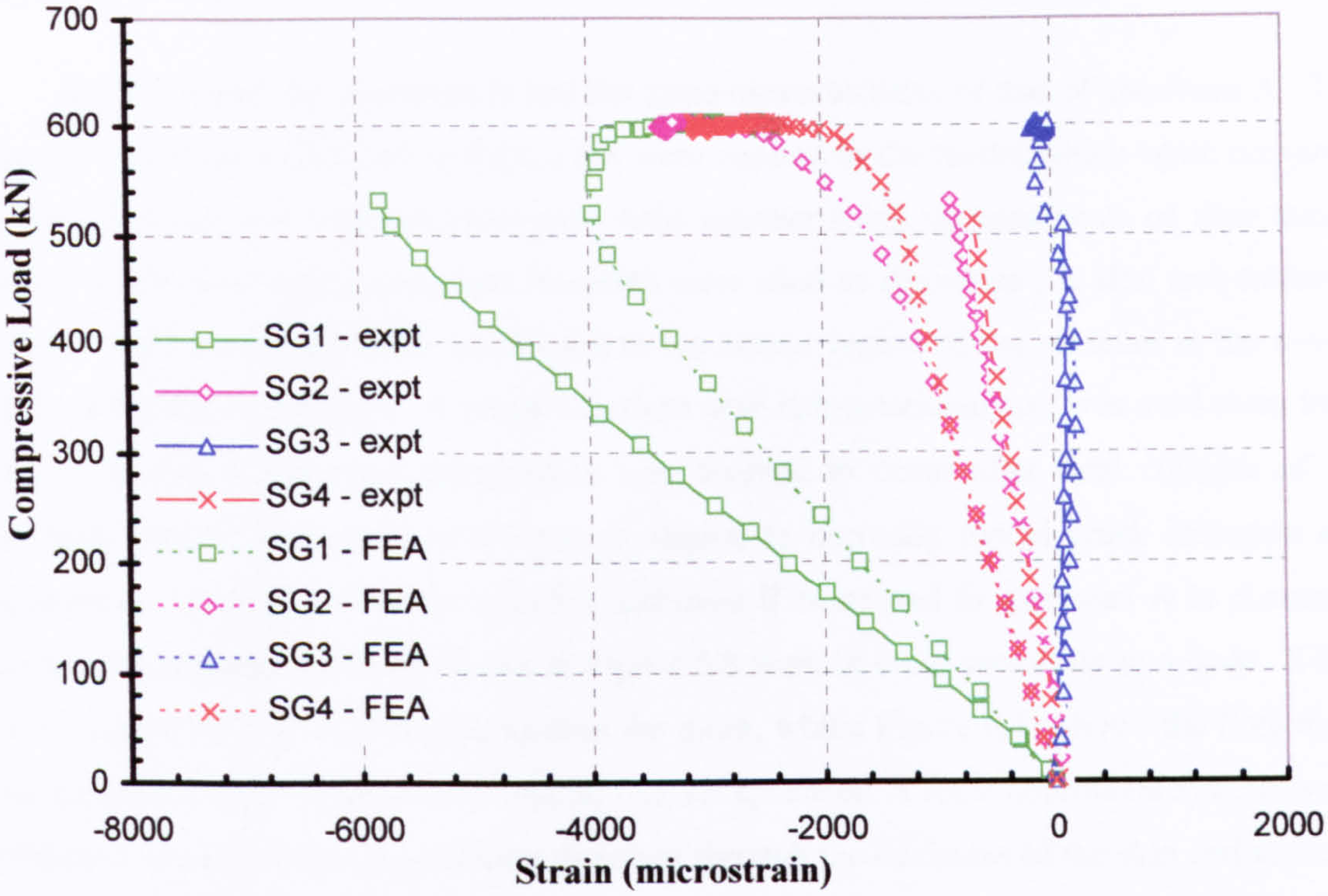

Figure 6.9: Experimental and numerical strain gauge results for specimen B.

Specimen B failed at a loading of 538 kN, higher than specimen A as expected due to its bigger dimensions. The maximum compressive strain at failure was close to 6000 μs as recorded by SG1, and the observed failure mode was very different to that of the thinner specimen A. Crack initiation was followed by initially unstable crack propagation, but this soon changed as crack growth became stable. This meant that it was possible to stop the test at the loading of 538 kN before the crack propagated throughout the whole length of the specimen. This was in contrast to the abrupt and unstable crack propagation observed in specimen A. The failure surface of specimen B was symmetric, and Figure 6.10 shows the crack through the sectioned specimen.

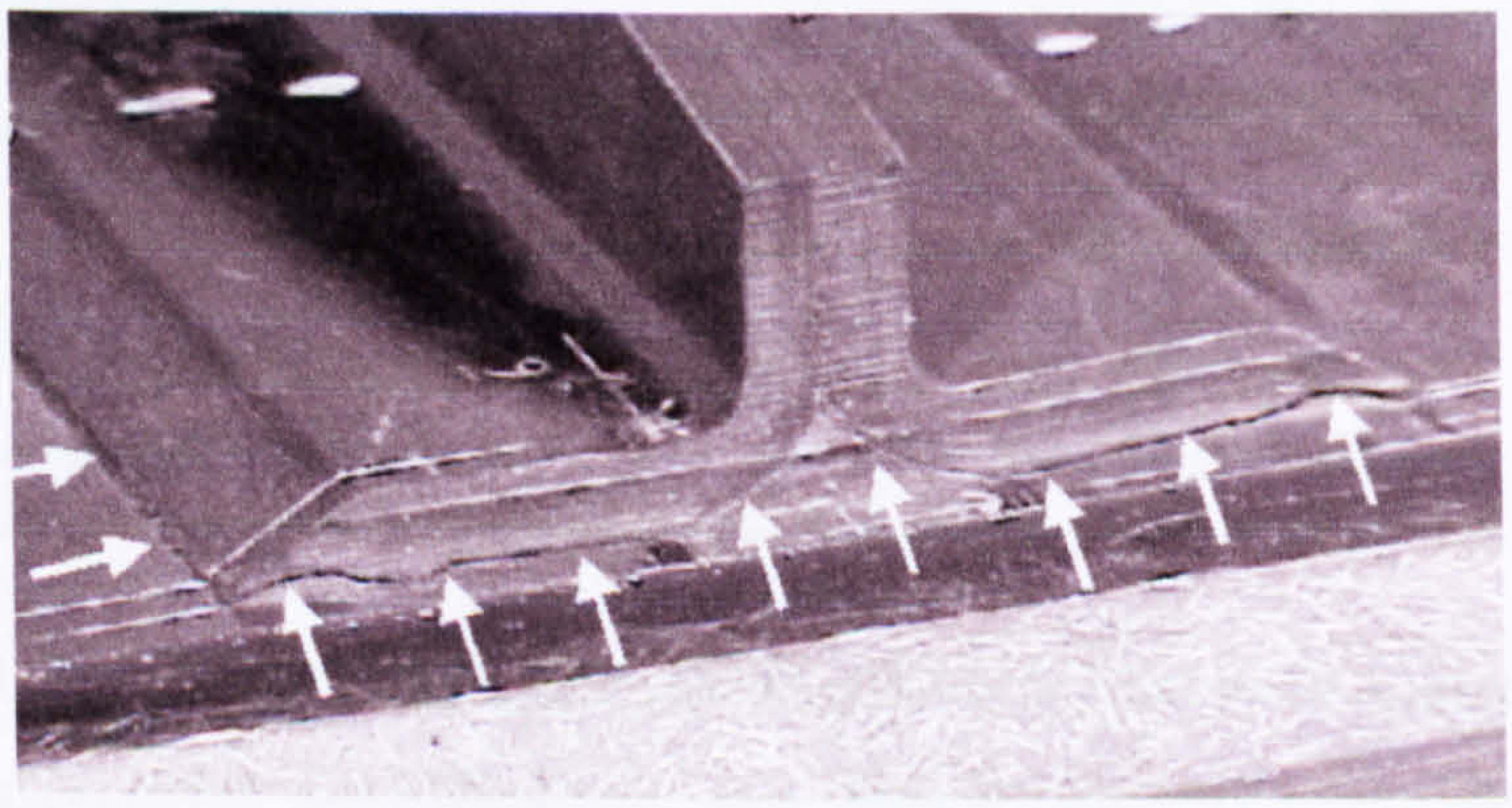

Figure 6.10: Section showing the crack across the skin-stiffener interface width of failed specimen B [58].

6.3.3 Finite element model

The FE model for specimen B had the same characteristics of that of specimen A. The bigger dimensions as detailed in Figure 6.8 were applied to the model which again consisted of skin, stiffener, and interface layer parts held together using tie constraints on their shared nodes. Eight-node continuum shell elements were used to discretize the skin and stiffener, with six-node wedge elements again used at the corner region of the stiffener at the runout end near the end of the taper. A coarser mesh to save computational cost was used away from the runout end where crack propagation was deemed to occur after final collapse of the specimen, and a finer mesh at the runout region to correctly model crack initiation and propagation. A finer mesh was used for specimen B compared to specimen A to guarantee that the strain gauge locations shown in Figure 6.8 were in close proximity to a node. Table 6.6 shows the number of elements used in the mesh, whilst Figure 6.11 shows the final mesh with a detailed view of the runout region. As for specimen A local coordinate systems were developed so as to define the stacking direction through the thickness of the skin and stiffener parts and then composite layers were defined corresponding to the lay-ups of Table 6.5. Similar boundary conditions were applied as in the case of specimen A, holding the end opposite the runout clamped throughout the displacement controlled compression which was applied via a displacement boundary condition on the nodes at the end of the skin at the runout end. Since only half of the specimen was modelled, appropriate boundary conditions were applied on all nodes on the symmetry plane. Interface elements were placed at the skin-stiffener interface in exactly the same fashion as described previously for specimen A, with the interface being defined by the same traction separation law as detailed in Table 6.4. Again, a non-linear quasi-static analysis was run so as to include the effects of large displacement deformations.

Table 6.6: Specimen B mesh details.

Element type	Number of elements - location
8-node continuum shell	1,666 – skin
	2,966 – stiffener
6-node continuum shell	4 – stiffener
8-node interface	1,170 – interface layer

It should be noted that a mesh sensitivity analysis was carried out so as to ascertain that the mesh described in Table 6.6 was sufficiently fine. This is discussed in Section 6.5

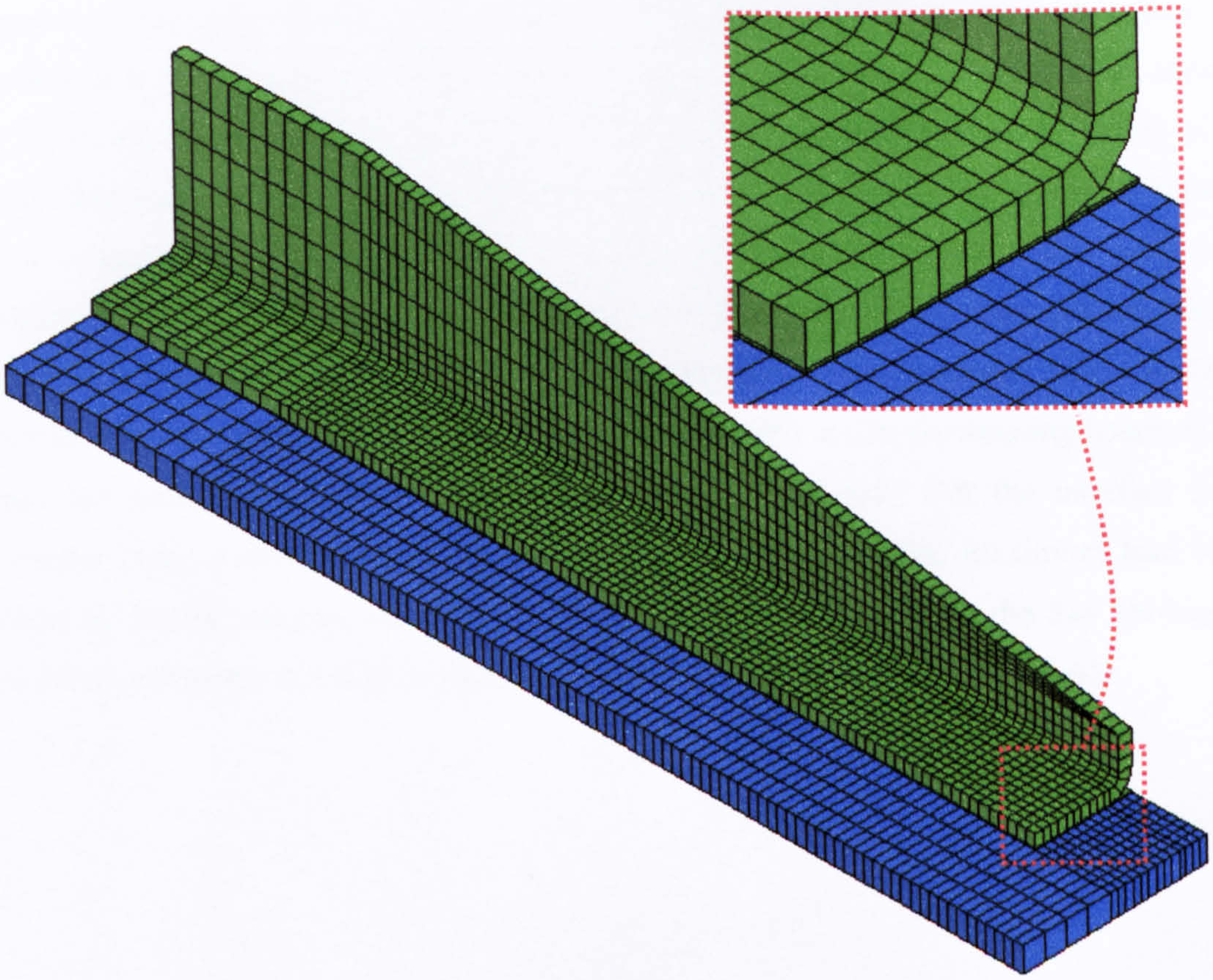

Figure 6.11: ABAQUS FE mesh for specimen B, with expanded view of runout region.

6.3.4 Finite element results

The numerically predicted strains are shown together with the measured strain gauge results in Figure 6.9. Good agreement can be seen between numerical and experimental values. At the location of SG1, numerical strains were lower than in the experiment, but the difference between SG1 and SG2 values still shows how the FE model was able to capture the bending that is present away from the stiffener, leading to the outer smooth surface of the unsupported skin having lower strains compared to the inner surface. SG2 and SG4 measured very similar values, also seen in the FE results meaning that on the outside surface of the unsupported skin comparable strain levels occurred as on the outside of the supported skin region near the runout. The FE analysis also captured the slightly tensile strains at the location of SG3 on the surface of the stiffener flange. This is seen by the dotted blue line in Figure 6.9 which closely matches the experimental solid blue line.

Figure 6.12 shows the deformed shape of the FE model for different load levels and the corresponding damage at the skin stiffener interface. The observation made when looking at the strain results that the skin is bending away form the stiffener side is confirmed, but due to the greater thickness of the stiffener this effect was not as pronounced as for specimen A. A deformation scale factor of ten is used in Figure 6.12 and close inspection shows how bending of the skin is in fact occurring. Again the crack initiated at the runout end as can be seen in Figure 6.12 (a) relating to a loading of 520 kN. The crack front moved down the length of the stiffener, but crack propagation was different to that of specimen A. Specimen B showed initially unstable crack growth, but this became stable as the loading was continued, correlating very well with the experimental findings discussed earlier. Figure 6.12 (b) shows how at an applied load of 600 kN the crack has propagated into the specimen, and at failure it has advanced so that almost all the interface elements directly under the tapering length of the stiffener are completely degraded as visible in Figure 6.12 (c). For the interface layer degradation plots, a deformation scale factor of one was used. The maximum load level predicted by the FE analysis was 602 kN, which can be compared with the 538 kN load at which the experimental test was stopped as the crack growth was found to be stable.

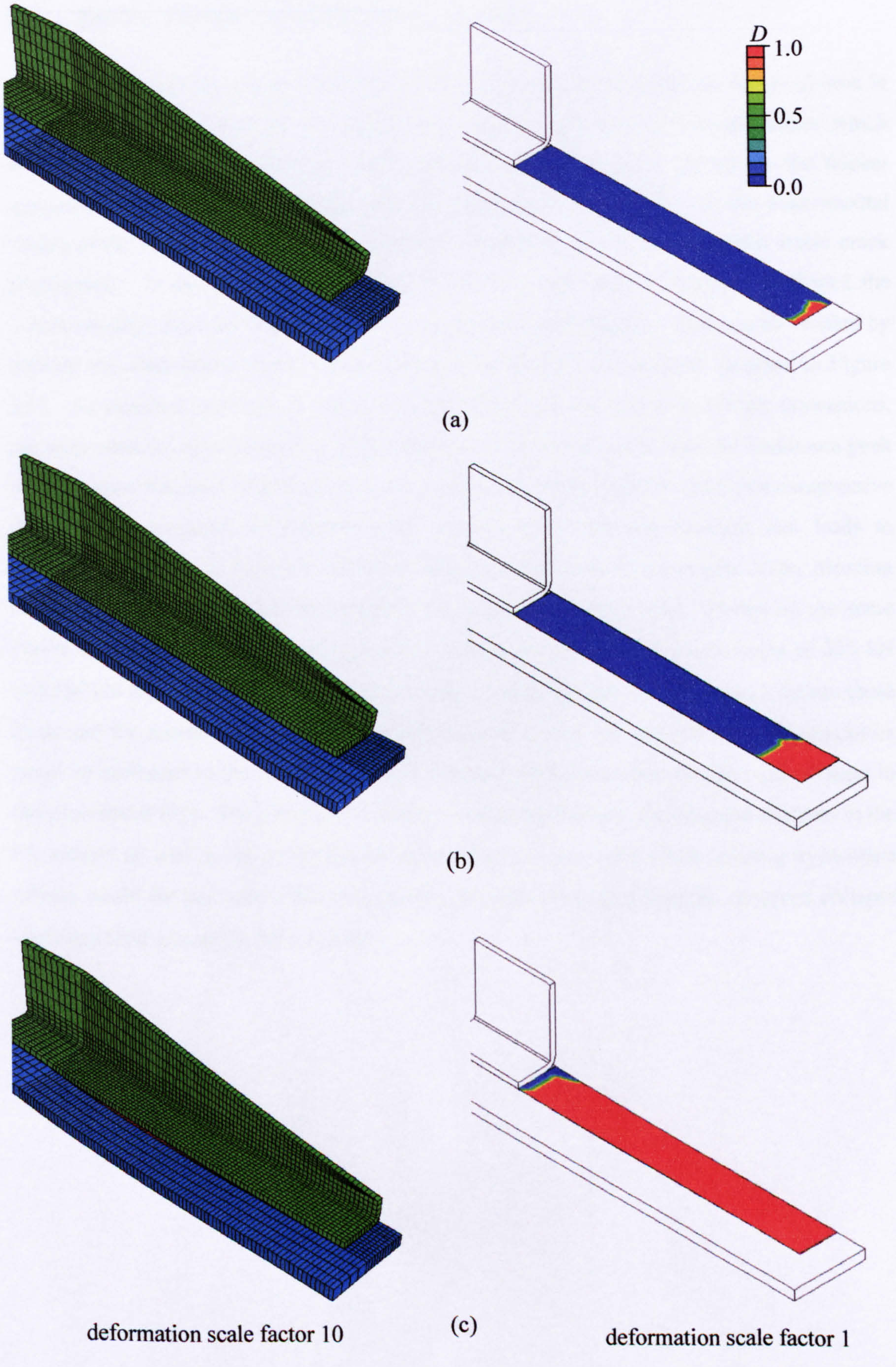

Figure 6.12: FE deformed shape (deformed scale factor 10) and interface damage for specimen B at loading of (a) 520 kN, (b) 600 kN, (c) after collapse.

6.4 Stable versus unstable crack growth

In discussing the results of the two stiffener runout specimens it was observed how in both the experiment and the FE analysis the thinner specimen A showed failure which occurred due to sudden unstable crack propagation, whilst crack growth in the thicker specimen B was seen to be initially unstable but then became stable. In the experimental testing of the latter specimen it was possible to unload the specimen during this stable crack propagation. In discussing the FE results it was said how the FE analyses confirmed the experimentally observed behaviour relating to the crack propagation. This can be verified by plotting the load-displacement curves produced by the two FE analyses as done in Figure 6.13. As expected specimen B shows a much higher stiffness due to its thicker dimensions, however what is important to note is the difference in the two curves after the maximum peak load has been reached. Specimen A shows a reduction in the load for additional compressive displacement, evidence of unstable crack growth as further displacement just leads to collapse. Specimen B however shows a flattening of its load-displacement curve, meaning that as the crack propagated the specimen was still able to carry load. Plotted on the same Figure 6.13 are the experimentally recorded failure loads for the two specimens of 245 kN and 538 kN for specimens A and B respectively. Good agreement can be seen between these loads and the numerically predicted maximum loads of 208 kN and 602 kN. Discrepancies could be attributed to the existence of high frictional forces between the skin and stiffener in the experiment [81]. The inclusion of contact modelling between the skin and stiffener in the FE models as well as the modelling of other failure modes, particularly relating to in-plane failure, could further reduce this discrepancy between the experimentally observed collapse loads and their numerical counterparts.

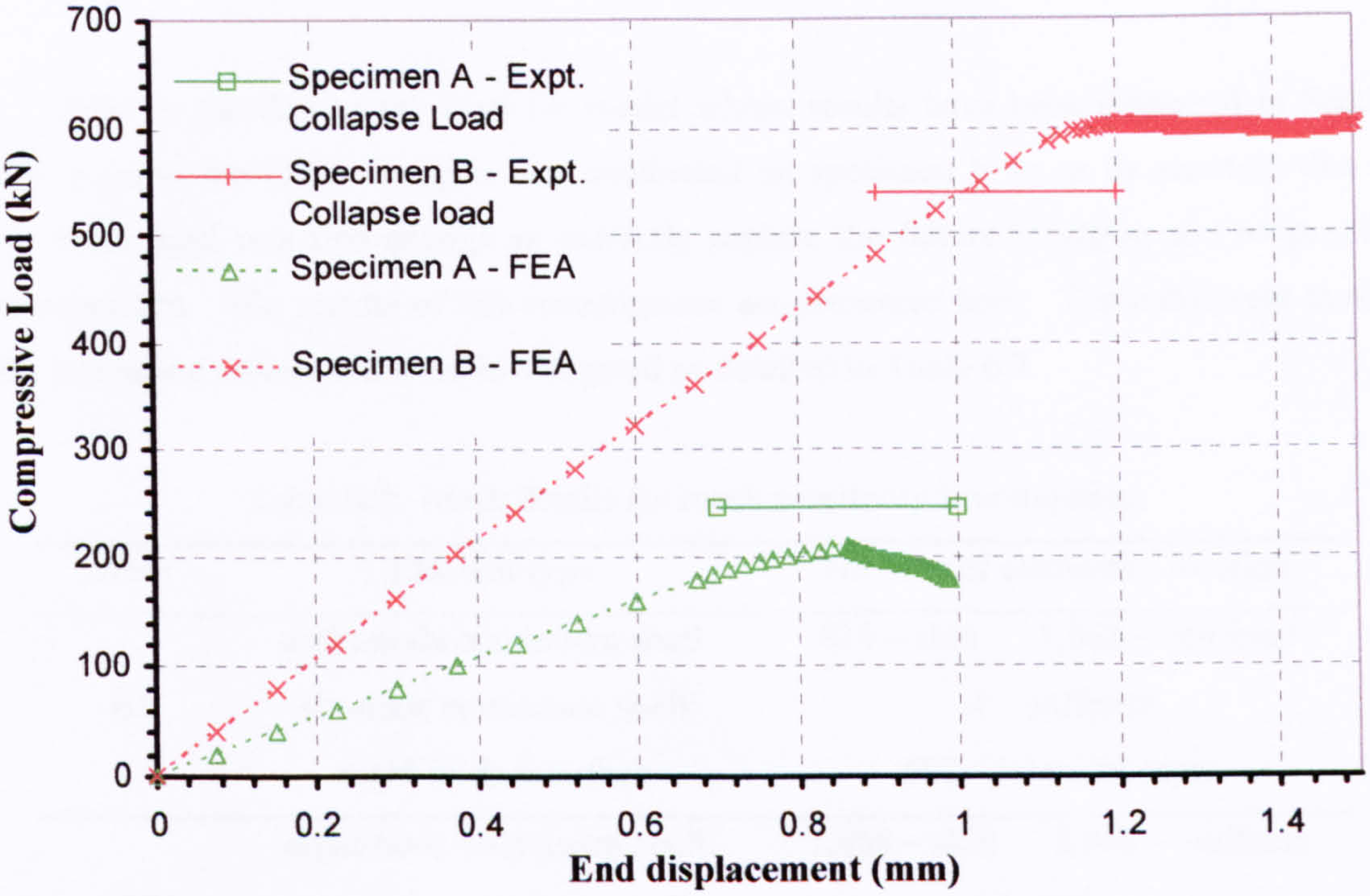

Figure 6.13: FE load-displacement curves and experimental collapse loads for specimens A and B.

Both of the FE analyses conducted on the two specimens were run using the interface parameters shown in Table 6.4 describing the interface element constitutive law of the interface elements. The fracture toughness values stated relate to secondary-bonded specimens [80] rather than co-cured specimens as the stiffener runout specimens tested. A re-run of both analyses was done using fracture toughness values taken from standard DCB/ENF tests, but this resulted in failure being predicted to occur at a far earlier load level than observed experimentally. An explanation of this could be the existence of large compressive stresses in the runout specimens resulting in the onset of fracture being delayed in the experiments. Furthermore, fracture toughness values may have been augmented by the high frictional forces which were present in the Mode II dominated fracture surface, a possibility proposed by Cui et al. [81].

6.5 Mesh sensitivity

Prior to running of the final FE model whose results have been discussed in Section 6.3.4, a mesh sensitivity analysis was conducted on specimen B so as to ascertain that the final mesh used was fine enough to correctly capture the failure initiation and propagation characteristics. The results of this investigation are presented here. Three different meshes with increasing refinement were investigated as detailed in Table 6.7.

Table 6.7: Mesh details for mesh sensitivity investigation.

Mesh	Element type	Number of elements - location
B1	eight-node continuum shell	819 – skin 1,562 – stiffener
	six-node continuum shell	4 – stiffener
	eight-node interface	580 – interface layer
B2	eight-node continuum shell	1,666 – skin 2,966 – stiffener
	six-node continuum shell	4 – stiffener
	eight-node interface	1,170 – interface layer
B3	eight-node continuum shell	6,664 – skin 11,335 – stiffener
	six-node continuum shell	5 – stiffener
	eight-node interface	4,680 – interface layer

Details of the FE models corresponding to each of the meshes are the same as those described in Section 6.3.3 relating to the composite layup, boundary conditions, and interface layer properties. The mesh sensitivity was assessed by comparing both the deformed shape of the FE model as the loading was increased and the corresponding damage at the skin stiffener interface. Figure 6.14 shows the interface element damage at the skin stiffener interface for the three meshes B1, B2, and B3 for three different load levels, corresponding to (a) 520 kN, (b) 600 kN, and (c) just after collapse of the runout. It should be noted that for the coarser mesh B1, Figure 6.14 shows the contours for a slightly lower loading of about 577 kN rather than 600 kN, as discussed shortly when comparing the numerical load-displacement curves. It is noted how the damage contours are very similar for all three meshes, with the only difference being that the coarser B1 mesh showed a slightly larger cohesive zone ahead of the crack front because of the coarser interface element size. Figure 6.14 (d) shows the deformed shape for the three meshes just after collapse using a deformation scale factor of 10, and it can be seen how the deformed shapes were very similar. Such deformed shapes at the other lower levels were also investigated but not included in Figure 6.14 as they were practically identical for all the meshes.

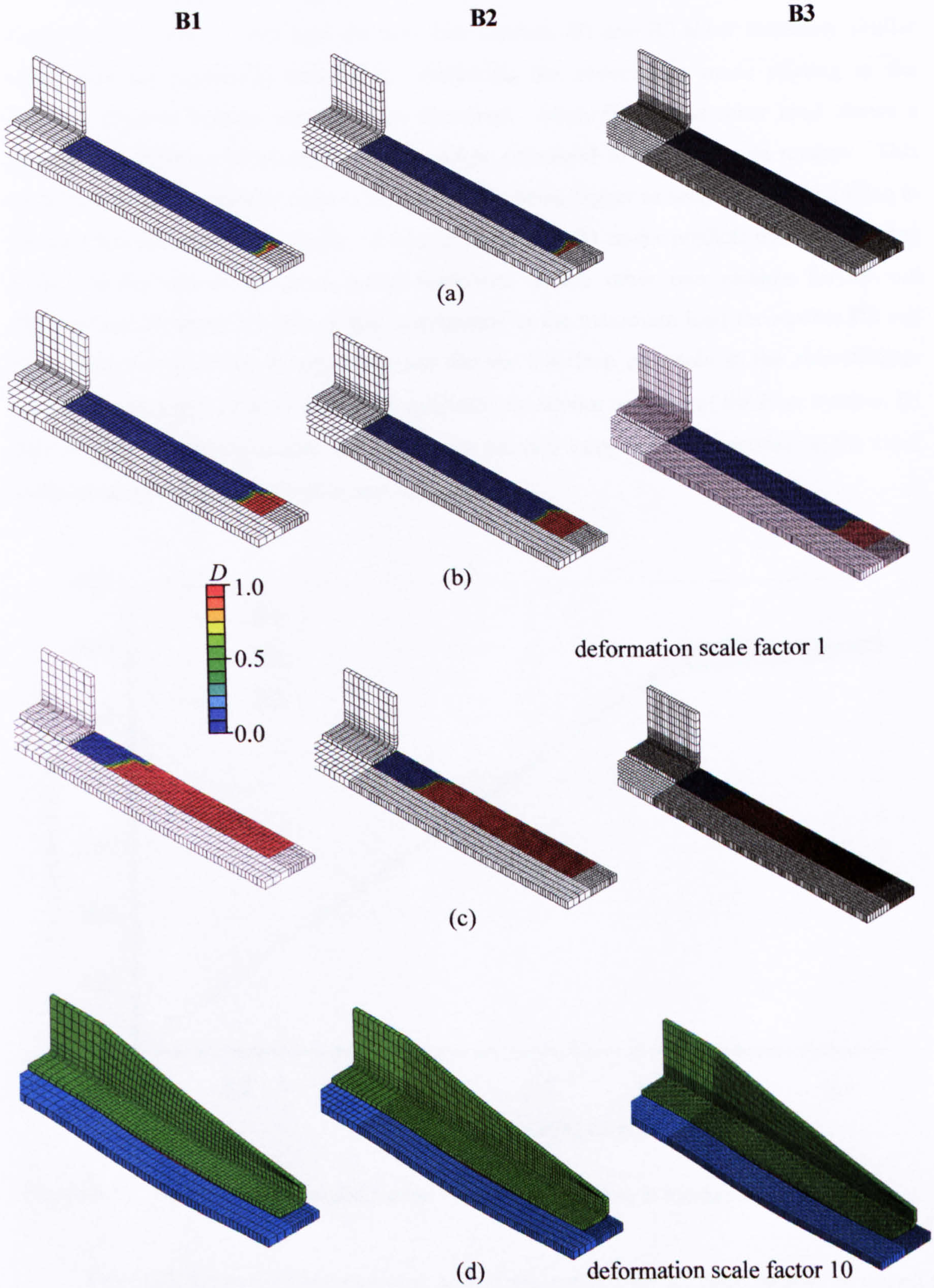

Figure 6.14: FE interface damage for meshes B1, B2, and B3 at loading of (a) 520 kN, (b) 600 kN, (c) just after collapse. FE deformed shape deformed scale factor 10 for meshes B1, B2, B3 (d) just after collapse.

The load-displacement curves obtained from the three different meshes are shown in Figure 6.15. It can be seen how the two finer meshes, B2 and B3 show extremely similar values and are practically coincident, reinforcing the observation made relating to the interface element damage contours just discussed. Mesh B1 on the other hand shows a reduction in stiffness which occurs earlier when compared to the other two meshes. This could be due to the cohesive zone at the crack front being bigger as seen in Figure 6.14 due to the interface elements being larger. It is seen how mesh B1 under predicts the load carrying ability of the runout specimen when compared to the other two meshes for an end displacement of about 1.2 mm which corresponds to the maximum load for meshes B2 and B3. Hence even if the damage contours for the interface elements at the skin-stiffener interface in Figure 6.14 were seen to be qualitatively similar to those of the finer meshes, B1 did not yield convergent results and hence was deemed inappropriate in modelling the crack initiation and propagation in the runout specimen.

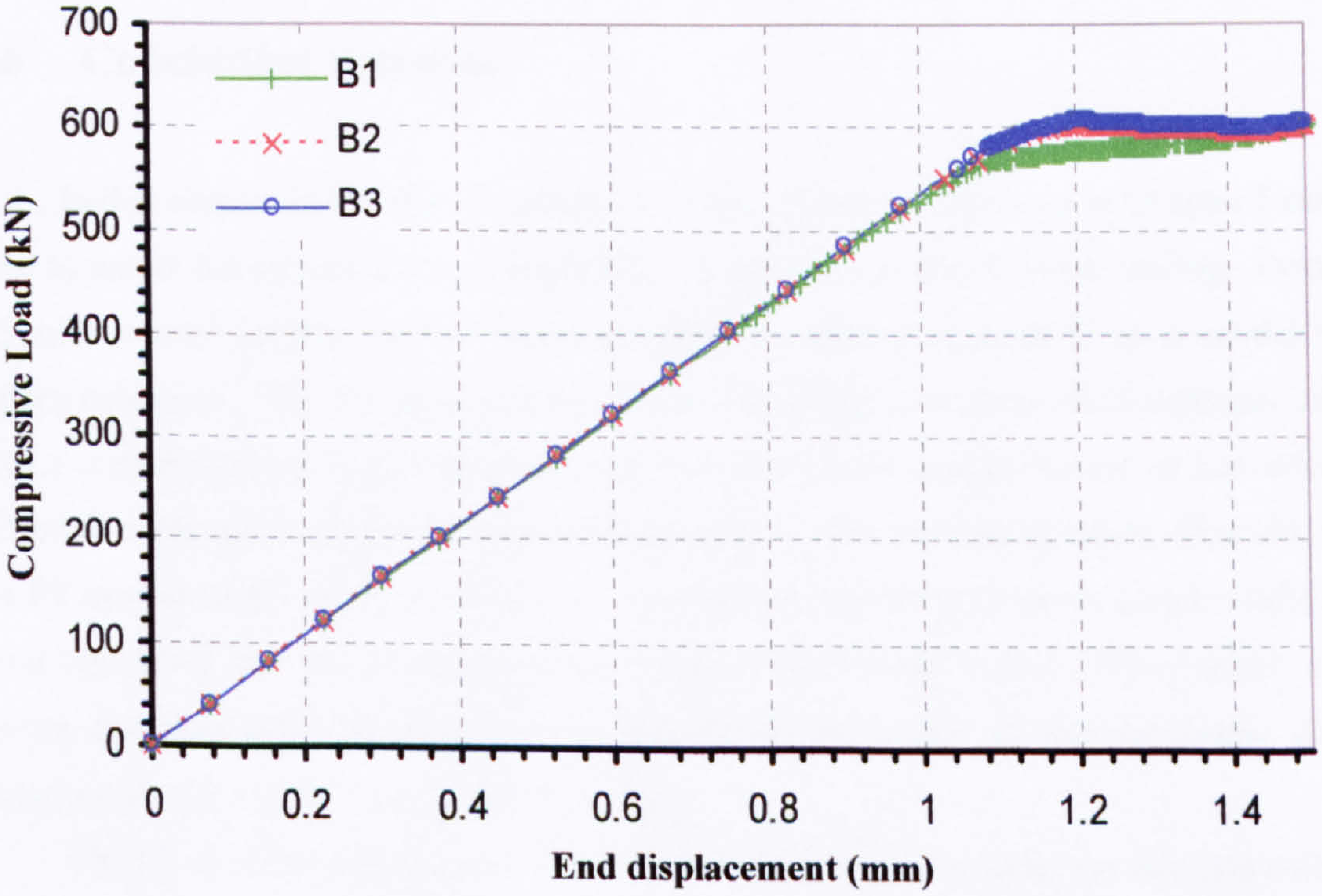

Figure 6.15: FE load displacement curves for runout specimen B meshes B1, B2, and B3.

Table 6.8 shows the computational cost of the analysis for all three meshes as run on a dual core 1.66 GHz PC. It is clear how refinement of the mesh drastically increases computational cost, and this is largely attributed to the increased number of interface elements that are undergoing stiffness degradation at the skin-stiffener interface.

Table 6.8: Computational cost for meshes B1, B2, and B3.

Mesh	Computational time (hours)
B1	3.1
B2	12.2
B3	56.1

From the mesh sensitivity analysis it is quite clear how mesh B2 was sufficiently fine to capture both the qualitative behaviour of the runout specimen relating to its deformed configuration as the loading is increased and the crack initiation and propagation characteristics as obtained from the interface element damage at the skin-stiffener interface and load-displacement curve. It is for this reason that mesh B2 was chosen and its results presented in Section 6.3.4.

6.6 Concluding remarks

In this chapter it was shown how the interface elements introduced in Chapter 5 can be used to model the initiation and propagation of a crack under mixed mode loading. Detailed FE models were created for two different stiffener runout specimens so as to model their failure behaviour. The FE models were constructed using continuum shell elements, which give a considerable saving in computational cost when compared to the use of conventional 3D brick elements in modelling composite structures. The numerical results obtained from the FE models of the two specimens were compared to experimental strain gauge results, and good agreement was seen between numerical and experimental values. Observations made during the experiment relating to the deformation behaviour of the specimens during compression were confirmed by the FE analyses.

The FE models, with the inclusion of interface elements between the skin and stiffener interface of the runout specimens were able to give valuable insight into the failure characteristics of both specimens. In particular, the models were able to capture the unstable crack growth that occurred in the thinner skinned specimen, as well as the initially unstable but then stable crack growth in the thicker skinned specimen. FE models such as the ones presented highlight the possibility in the reduction in experimental testing, particular coupon and specimen tests. Such reduction in testing, achieved via credible numerical analyses able to capture both qualitative and quantitative behaviour of the structure being modelled, can result in a great savings during component validation.

Chapter 7

Finite element modelling of skin-stiffener debonding in an I-stiffened panel

In Chapter 6 it was seen how interface elements were successfully used to model the failure mode of two different stiffener runout specimens. The two specimens exhibited different failure characteristics, namely unstable crack growth for the thinner specimen and initially unstable followed by stable crack growth for the thicker specimen. In both cases good correlation was found not only in the comparison of numerical and experimental strain results, but the numerical FE models were also able to capture the deformation characteristics of both specimens during the compressive testing as well as the initiation and propagation of the crack at the skin-stiffener interface which led to eventual collapse. Crack initiation and propagation was modelled under mixed-mode conditions, using the interface element traction-separation law introduced in Chapter 5.

The focus of this chapter is to look at another structure and use interface elements to model out-of-plane damage mechanisms. The I-stiffened panel first modelled in Chapter 4 is re-visited, in an attempt to model skin-stiffener debonding which, as evidenced by the experimental tests discussed in detail in Chapter 5, acts as a significant precursor to final collapse of the panel structure. Chapter 4 highlighted how at higher load levels damage mechanisms not modelled by the shell element FE model of the I-stiffened panel could explain the discrepancies between experimental and numerical results. Nonetheless, for the prebuckling, buckling, and a most of the postbuckling regime of the panel a very good correlation was found between the experimental behaviour of the panel and the numerical prediction, in particular relating to the mode-jump that was seen to occur when the panel jumped from a five half-wave configuration to a six half-wave configuration. Experimental investigations also highlighted how such a mode-jump may act as an instigator to damage mechanisms such as skin-stiffener debonding, and this chapter aims to try and model this phenomenon. First the approach taken, which is the use of a global-local model, is introduced, before discussing details of the FE model constructed to attempt to capture the skin-stiffener debonding in the I-stiffened panel. Numerical results are compared to experimental observations made during the failure testing of the I-stiffened panel.

7.1 Choosing a modelling approach

7.1.1 Available modelling strategies

In the modelling of the stiffener runout specimens of Chapter 6 it was discussed how continuum shell elements were used throughout the models. Continuum shell elements discretize a 3D body in much the same way as 3D brick elements, meaning that they have three translational degrees of freedom at each of their eight nodes (in the case of linear elements) and no rotational degrees of freedom. Furthermore, their thickness is solely determined by their nodal connectivity. Similarly to conventional shell elements however, strains are defined on the mid-surface plane and the kinematic and constitutive behaviour is very much like that of conventional shells. The great advantage in using continuum shells is that they offer a very good compromise between computational time and accuracy of results when compared to using 3D brick elements where to capture the through-thickness stresses correctly in a composite structure, typically an element per ply must be used – something prohibitively expensive when a structure with many plies in its lay-up is being modelled. The formulation for continuum shell elements may be found in the ABAQUS documentation [39] as well as being presented by Falzon et al. [79].

It was also highlighted in Chapter 6 how another approach is to set up planes of Gauss integration points corresponding to the plies in the composites. This allows the use of 3D brick elements without having to revert to using one element per ply in the thickness direction. This is still however rather inefficient due to the fact that a large number of such planes need to be considered for composites containing a substantial number of plies in their lay-up. The I-stiffened panel FE model of Chapter 4 was computationally cheap as it was solely composed of conventional shell elements. Nonetheless as was seen in the discussion of the results, good agreement was found between numerical and experimental results relating to the prebuckling, buckling, and postbuckling regimes of the panel. The five half-wave buckle configuration of the panel was predicted by the FE model, as was the sudden mode-jump to a six half-wave configuration. However the model contained no failure modelling capability and Chapter 5 gave extensive experimental evidence of how important out-of-plane failure such as skin-stiffener debonding is to structures like the I-stiffened panel. To add this failure capability to the FE panel model, an approach similar to the modelling of the stiffener runouts may be used. This involves using continuum shell elements to discretize the panel model, with interface elements being placed at the skin stiffener interface in order to model the skin-stiffener debonding which potentially occurs as the panel is compressed deep into its postbuckling regime. The use of interface elements in a conventional shell model is illadvised due to the fact that appropriate connectivity between the interface and the components on either side can not be established due to the mid-surface geometric reference surface of conventional shell elements.

7.1.2 Reducing computational cost

Figure 7.1 shows an FE model of the I-stiffened panel of Chapter 4 constructed with continuum shell elements, with an expanded view of the skin-stiffener interface region. The skin and stiffeners were created and meshed as separate parts, as was the interface layer under each stiffener which is composed of the interface elements discussed in Chapter 5. Tie constrains were then used between the skin and bottom nodes of the interface layer and the stiffener and top nodes of the interface layer. Local material orientations were defined as for the stiffener runout models so as to guarantee the correct modelling of the various composite lay-ups. The model construction and definition was very similar to that of the runout specimens detailed in Chapter 6.

Figure 7.1: Continuum shell element model of I-stiffened panel.

The computational cost of running such a model is acceptable, but only up until a secondary instability is reached. In the case of the I-stiffened panel, it was seen in Chapter 4 how the conventional shell model was able to capture the mode-jump that occurred from a five half-wave configuration to a six half-wave configuration in the postbuckling regime of the panel. This was also initially captured by the continuum shell model of Figure 7.1. However, at the point of the secondary instability corresponding to the mode-jump, time increments in the non-linear analysis become extremely small as the solver sought to find the new equilibrium configuration. This was acceptable for the conventional shell model, as the computational time required for each increment is small. For a much more complex model such as the one in Figure 7.1 the analysis becomes prohibitively expensive. This computational problem did not occur in the modelling of the stiffener runouts, as secondary instabilities were not present. Due to the complexity of the I-stiffened panel model, each increment takes longer to convergence, and when convergence does occur it is only for a very small incremental step in the loading. Hence when a secondary instability is reached, the time increments required are so small that it is impossible to run such an FE model to trace the full postbuckling response of the panel without reverting to extensive parallel computing or the use of a supercomputer. For the model shown in figure 7.1, it was possible to run the analysis past buckling and into its post-buckling regime, and the solution confirmed the five half-wave configuration. However time increments became extremely small at the point where the panel was mode-jumping to the six half-wave configuration and the analysis was aborted.

The size of time increments required for convergence may be increased by the use of energy dissipation schemes as was discussed in Chapter 3, but great care must be taken when using such schemes to ensure that results are not affected adversely. Parametric analyses such as the ones in Chapter 4 on the amount of damping used may not be conducted due to the sheer size of the model, and even with the introduction of some energy dissipation schemes analysis times are still far too great.

In view of the reasons discussed above, namely of the prohibitive computational cost of creating a full model of the I-stiffened panel containing interface elements at the skin-stiffener interface to model debonding, a different approach was taken. This approach consisted of keeping the conventional shell model of the I-stiffened panel seen in Chapter 4 to capture the behaviour of the panel, and linking this to a detailed local model containing interface elements able to predict skin-stiffener debonding. Such an approach – known as submodelling – is extremely efficient from a computational point of view, something of paramount importance when considering the ultimate aim of this research effort – that of developing and FE optimization strategy which takes into account damage mechanisms. Optimization requires repetitive runs of a model to be made, and hence the need for each model to be as computationally cheap as possible is apparent. The main principles behind using this global-local modelling approach in ABAQUS are discussed in Appendix B, and the details of how the local I-stiffened panel model was created and discussion of its results as compared to experimental observations is treated next.

7.2 Local finite element modelling of I-stiffened panel

7.2.1 Finite element model

The global-local modelling approach was used to analyze the I-stiffened panel in Chapter 4 in more detail, particularly relating to the fact that the conventional shell element model presented there contained no failure capability. To overcome this, a local model containing solid elements coupled with interface elements at the skin-stiffener interface was created, allowing the phenomenon of skin-stiffener debonding in the I-stiffened panel to be investigated. Details of this local model are presented here, followed by how it was linked to the shell element model of Chapter 4 using the shell-to-solid submodelling approach discussed earlier.

The local model was a detailed model of a representative section of the panel, so as to investigate the debonding that may occur at the skin-stiffener interface and act as a precursor to final collapse of the panel as has been widely evidenced experimentally and discussed in Chapter 5. The local model had a length of 197.5 mm and a width of 108.5 mm. The length was chosen such that it encompassed two node lines and an anti-node line in the five half-wave buckle configuration that developed in the I-stiffened panel in Chapter 4. The width was chosen to guarantee that the displacements due to the buckle crests and troughs in the global model could be mapped onto the local model using the global-local submodelling approach. It was seen how the panel jumped to a six half-wave configuration later in its postbuckling regime, and hence the relocation of node and anti-node lines would still be guaranteed to occur in the local model as the half-waves got shorter due to the increase in number of buckle crests across the panel skin-bay length. The width was chosen to be wide enough so that effective deformation in the skin due to the panel buckling and postbuckling behaviour would be transferred onto the local model. Figure 7.2 schematically shows which area of the global I-stiffened panel model is replicated in the local model. The region, highlighted by the red cube, consists of the skin and stiffener at a location half-way down the panel length and at the second stiffener from the left when viewing the panel from the stiffener side. Also shown is the final mesh of the solid local model, for which the stiffener and skin were given appropriate dimensions according to Figure 4.15.

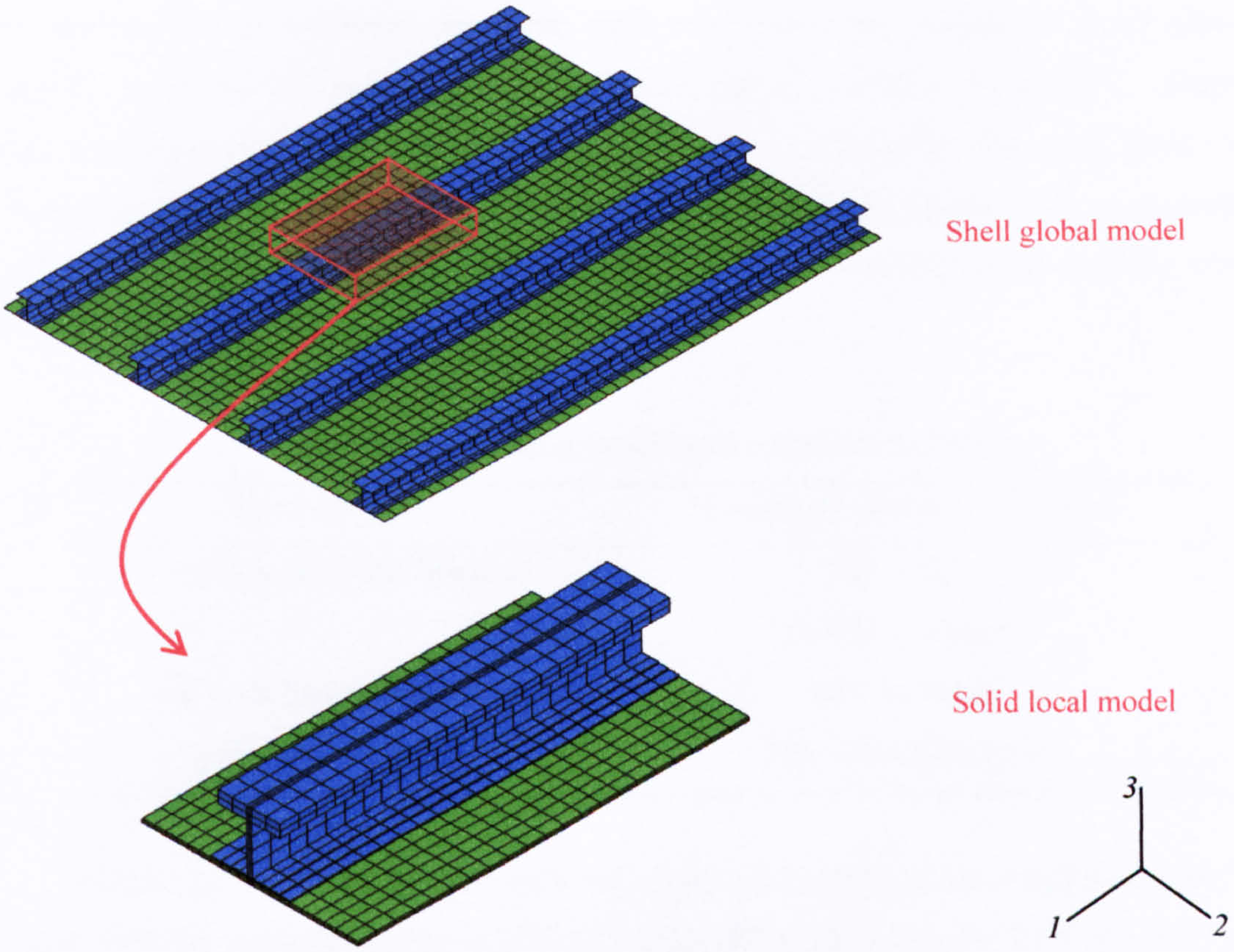

Figure 7.2: Shell global model mesh with region of interest where the solid local model is created.

The approach chosen for the local model was that of using standard linear brick elements. It was discussed earlier how this is computationally very expensive, and in fact prohibitive if an entire model of the I-stiffened panel was to be created using such elements. This is not the case, as will be seen later, when using the global-local submodelling approach. Table 7.1 gives details of the number of elements used in the local model. This was made of three separate parts – the skin, stiffener, and interface layer – subsequently tied together using tie constraints. The bottom surface of the stiffener was tied to the top nodes of the interface elements, whilst the top surface of the skin was tied to their bottom surface. The skin was composed entirely of eight-node linear brick elements, whilst it can be noted in Table 7.1 how the stiffener also contained six-noded triangular elements. These were placed at the ply drop-off locations of the stiffener flanges. It is the possibility of modelling such details as the ply drop-offs which further emphasizes the advantage of adopting a shell-to-solid global-local modelling strategy. In the flanges one element in the thickness direction was used per two plies of the lay-up. For one such element, then two planes of Gauss integration points were created, each one representing a ply. For the stiffener web and cap, two elements were placed in the thickness direction, and in each case appropriate planes of integration points were created always representing one ply per plane. This was also true in the skin part, which had two elements in its thickness direction, each one with eight integration point planes to correctly model the full lay-up of the I-stiffened panel according to Figure 4.15. Extensive mesh sensitivity tests were conducted to ensure that a sufficiently fine mesh guaranteeing convergent results was used. Such test were done by comparing the stiffness degradation contours (discussed later) of the interface elements for increasing mesh densities until no change could be observed.

Table 7.1: I-stiffened panel local model mesh details.

Element type	Number of elements - location
eight-node linear brick	924 – skin
	1,344 – stiffener
six-node linear triangular	84 – stiffener
eight-node interface	336 – interface layer

Figure 7.3 (a) shows an end on view of the final mesh of the I-stiffened panel local model, with an expanded view on a flange drop-off detail in Figure 7.3 (c) which is only possible with the use of standard brick elements. The green area corresponds to the skin, and the differently shades of blue show how the plies drop off in this region. The interface layer holding the skin and stiffener together is shown in red. Also shown, in Figure 7.3 (b) and coloured in pink, is the global model mesh corresponding to the shell mid-surface plane. Local material coordinate systems were established on the skin part, stiffener web, stiffener cap, and stiffener flanges to guarantee the correct material orientations representing the composite lay-up of the panel. The appropriate material properties of Table 4.3 relating to the T300/914C unidirectional prepreg material were assigned together with the individual ply orientations via the solid composite section sub-option available in ABAQUS. This allows the definition of the Gauss integration points through the thickness of an element, so that each ply may be defined with its appropriate material properties and orientation.

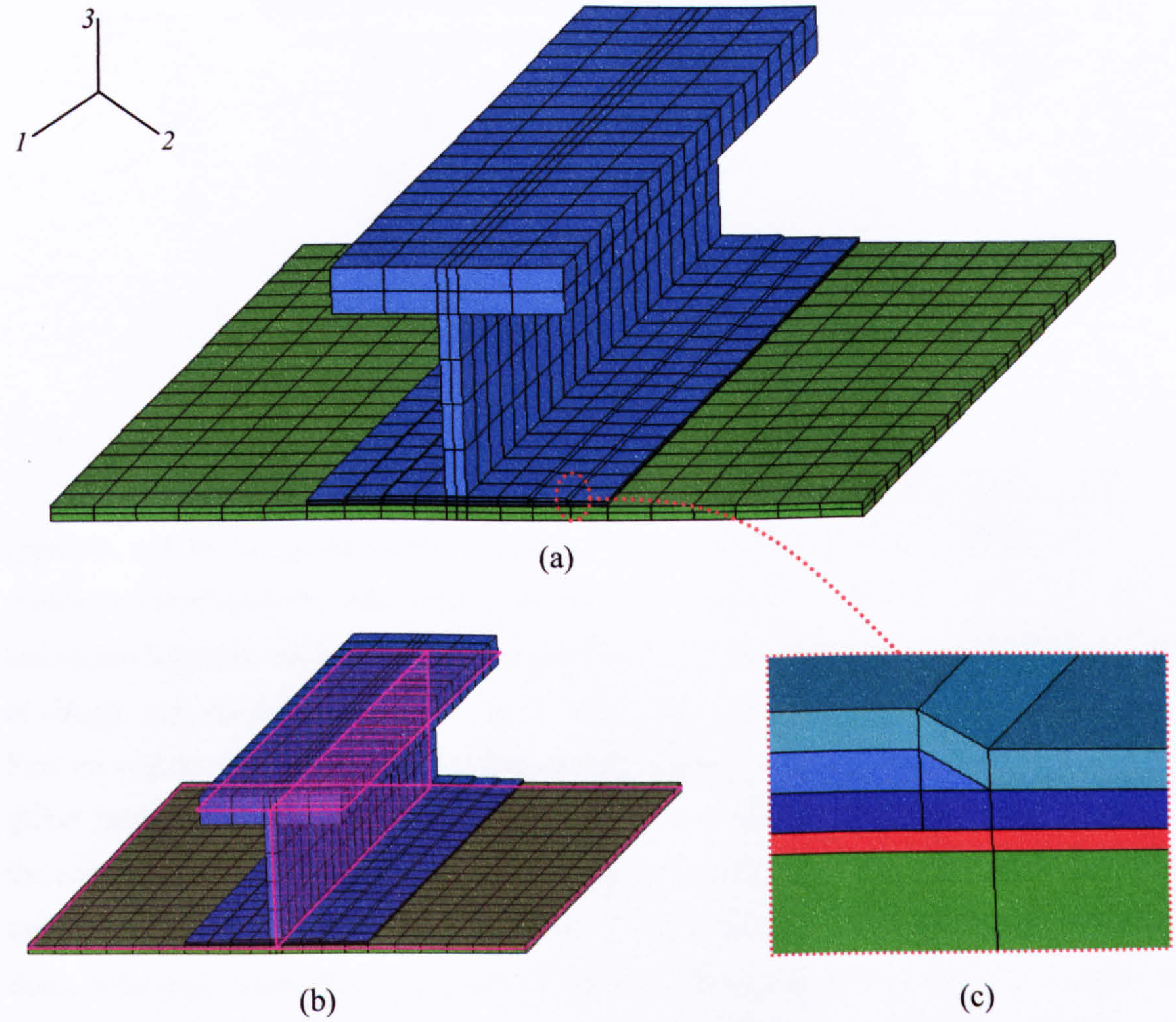

Figure 7.3: Finite element mesh of solid global model (a) with corresponding shell global model boundaries (b) and local flange drop-off detail (c).

The interface elements placed between the skin and stiffener were given a mixed-mode traction separation law with damage initiation being expressed via the quadratic stress-criterion of Equation (5.20) and damage propagation via the BK criterion of Equation (5.24). The I-stiffened panel had the stiffeners secondary bonded onto the skin using FM300 adhesive, and hence the interface properties given to the interface elements were taken from secondary bonded experimental values [80] and are detailed in Table 7.2. The viscous regularization discussed in Appendix A to aid in the convergence of interface elements during analysis was used, and parametric studies were conducted to show that the final adopted viscosity parameter μ of 0.001 was sufficiently small so as to not affect results.

Table 7.2: FM300 skin-stiffener interface properties.

Property	Value
σ_{0I}	61 MPa
$\sigma_{0II}/\sigma_{0III}$	49.8 MPa
G_{IC}	532 J/m^2
G_{IIC}/G_{IIIC}	2,358 J/m^2
Film thickness	0.13 mm
ν_{12}	0.28

The boundary conditions on the local model were entirely dictated by the submodelling approach and by the global model solution. The driving region in the global model was chosen automatically by ABAQUS, but in order for this to happen several modelling techniques had to be applied when creating the local model. The most direct approach is that of simply copying the global model and then creating the local model based on this copy. First the region of interest for the local model was singled out by cutting away the rest of the global model geometry. In the case of the I-stiffened panel, reference points were created at the corners of the area highlighted in red in Figure 7.2 and all material outside this area cut away. This resulted in a shell element model of the local region if interest. Once this was done, solid parts were created in place of the shell element geometry, so that the skin and stiffener were placed correctly relative to the global model shell mid-surface as shown in Figure 7.3 (b) relative to the global co-ordinate system. By adopting this modelling approach, ABAQUS was able to automatically recognise the driving regions in the global model by comparing their nodal global coordinates with those of the corresponding global model. The local model was then specified to have two boundary conditions, one on the skin and one on the stiffener. Figure 7.4 shows the local model mesh, together with the boundaries of the local model which are to be driven. The skin and stiffener are shown separately for display purposes, with driven boundaries highlighted in red.

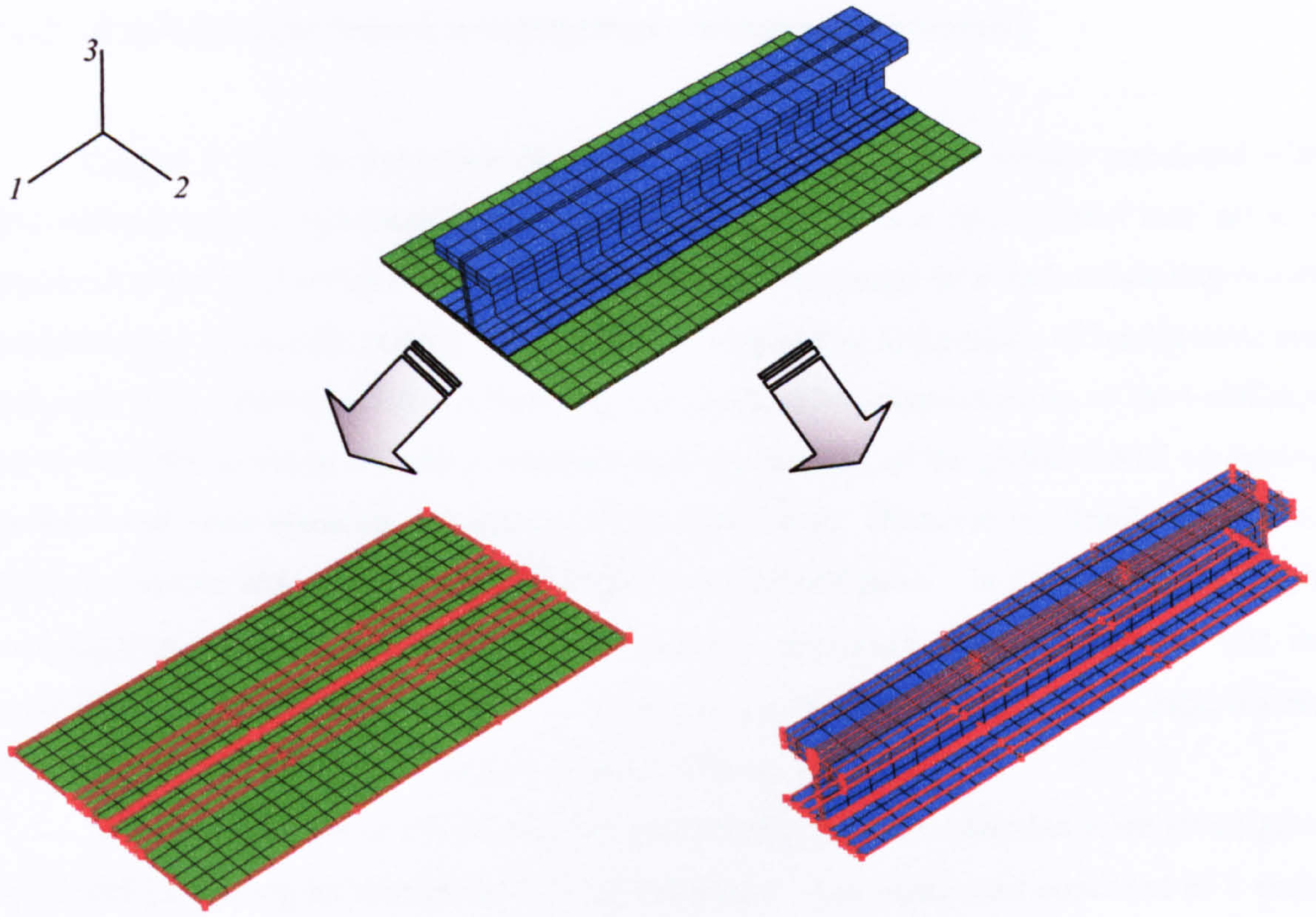

Figure 7.4: Diagram showing local model mesh and respective driven boundaries on the skin and stiffener meshes.

For the driven regions to be driven in Figure 7.4, driven nodes were selected whilst the specific degrees of freedom at the driven nodes driven by the global model solution were established using the centre zone approach described in Appendix B. The centre-zone size was selected to always correspond to 10% of the shell thickness of the global model as suggested in the ABAQUS documentation. No scaling of the pseudo-time variable with which ABAQUS applied the loading on the structure was specified, such that the solution of the global model was imposed directly onto the boundaries of the local model, which was also run as a quasi-static analysis. No solution controls in the form of energy dissipation schemes were required for the local model, as the I-stiffened panel global model displacement solution, including effects due to secondary instabilities, simply acted as a displacement boundary condition on all the driven nodes of the local model. The use of the global-local submodelling approach allowed for the computational cost of an analysis – running of the global model to trace the postbuckling response followed by the local model to investigate the skin-stiffener debonding – to be reduced to 23 minutes on a dual core 1.66 GHz PC.

7.2.2 Experimental failure investigation – ultrasound scanning

Chapter 5 gave an extensive discussion into the failure mechanisms associated with skin-stiffener panels, and emphasized how debonding of the skin and stiffener may act as a precursor to the final collapse of the panel. It was also discussed how such debonding occurs predominantly in specific regions of the panel corresponding to positions of buckle node and anti-node lines. The experimental buckling and postbuckling characteristics of the I-stiffened panel were discussed in chapter 4, together with the success of the global model containing conventional shell elements in capturing such behaviour. However no details were given about the failure characteristics observed on the I-stiffened panel. In this section the failure investigation conducted on the I-stiffened panel is discussed. This is done so that the numerical results obtained via the local model can be then compared to experimental observations, with particular emphasis on skin-stiffener debonding.

The I-stiffened panel failure mechanisms relating to crack initiation were investigated by Cerini [23] using an ultrasound A-scan technique. The equipment consisted of a probe which emitted ultrasound waves and which could be rotated and placed at required locations on the panel. Ultrasound may be used to inspect a component of small thickness for defects such as damage due to delamination or debonding as well as initial defects. This is done by plotting the return signal from the ultrasound against the time-of-flight (TOF), or the time that the signal takes to return to the emitting probe. The TOF is directly proportional to the distance travelled by the ultrasound beam, since its speed is constant.

Cerini discussed how two techniques exist in inspecting the panel. Firstly a signal can be sent through the material and the reflection of the sound wave by the back surface investigated by measuring its amplitude. Maximum amplitude of the return signal means no defects, whilst a reduction in the amplitude would correspond to the ultrasound beam having passed across a defect or delamination. Since the signal would pass the defect twice, one after emission and once on its way back after having being reflected, this can be clearly spotted in an amplitude against TOF plot. The reduction in amplitude of the signal due to the defect causes the ultrasound beam to be scattered or damped, and the amount of reduction in amplitude depends on both the extension of the defect and its ability to shield the ultrasound beam.

The above technique is useful in determining the extent and severity of the damage, but it cannot locate it within the thickness direction of the region being scanned, known as the gate. This can be overcome by positioning the gate to cover most of the region thickness, and recording the point first crossing the gate threshold. Doing this allows the TOF to represent the thickness at which the defect is present, corresponding to the rear panel surface when no damage exists. This allows for the determination of damage location, but not of its severity. In order to observe any skin-stiffener debonding, Cerini positioned the gate across the skin-stiffener interface region. A good bond would produce very little signal, whilst a skin-stiffener debond would result in a large amplitude signal. The I-stiffened panel was loaded and unloaded in three cycles (up to 150 kN, 250 kN, and 350 kN), and each time the ultrasound technique was used to assess the damage at the skin-stiffener interface by comparison with an initial scan of the unloaded panel. Because of the time consuming nature of the ultrasound scan, selected regions of the panel were chosen for scan, corresponding to node and anti-node locations as previous experimental evidence discussed in Chapter 5 pointed towards these regions being more susceptible to skin-stiffener debonding.

Figure 7.5 shows the ultrasound scan results of the panel with no load and at the two loading cycles of 150 kN and 250 kN. Figure 7.6 shows the selected regions of interest at the final loading cycle of 350 kN. The darker the colour of the contours, then the higher the amplitude of the signal. The black areas at the edges of the stiffeners indicate the end of the stiffener flanges rather than a debond, and the darker appearance along the central part of the stiffeners directly under the web even at no load indicated a lower bond quality at this location, possibly due to the triangular filling at the stiffener feet. Figure 7.5 shows how some darkening in contours may be seen for the higher load cycles. This is particularly visible in the areas labelled 3 and 4. In Figure 7.6, where the contours at 350 kN loaded are shown, it is apparent how some debonding has occurred under the stiffener flanges. A high degradation is apparent under stiffener 3 in regions close to anti-node lines, as expected since these regions correspond to the highest buckle deformations and hence maximum bending moment transfer between the stiffener web and stiffener flange/panel skin.

Despite the observations made, Cerini concluded that the ultrasound technique did not provide sufficient guarantee in detecting delaminations and skin-stiffener debonds. A failure mode was however hypothesized by looking at the failure characteristics of the panel. Observing that the third stiffener was greatly damaged and featured a delamination of the skin under the flange in the central area, with the flanges being detached, Cerini suggested that the global failure initiated from a delamination process under the central part of this stiffener causing the skin to buckle outwards. This debonding of the skin and stiffener gradually peeled the rest of the stiffener away from the skin and eventually also the other stiffener as the panel skin continued to bend. The stiffener, no longer supported by the skin, then failed catastrophically. In the next section the results obtained via the analysis of the FE local model will be investigated and compared to the experimental observations just discussed, as well as those relating to the other panels treated in Chapter 5.

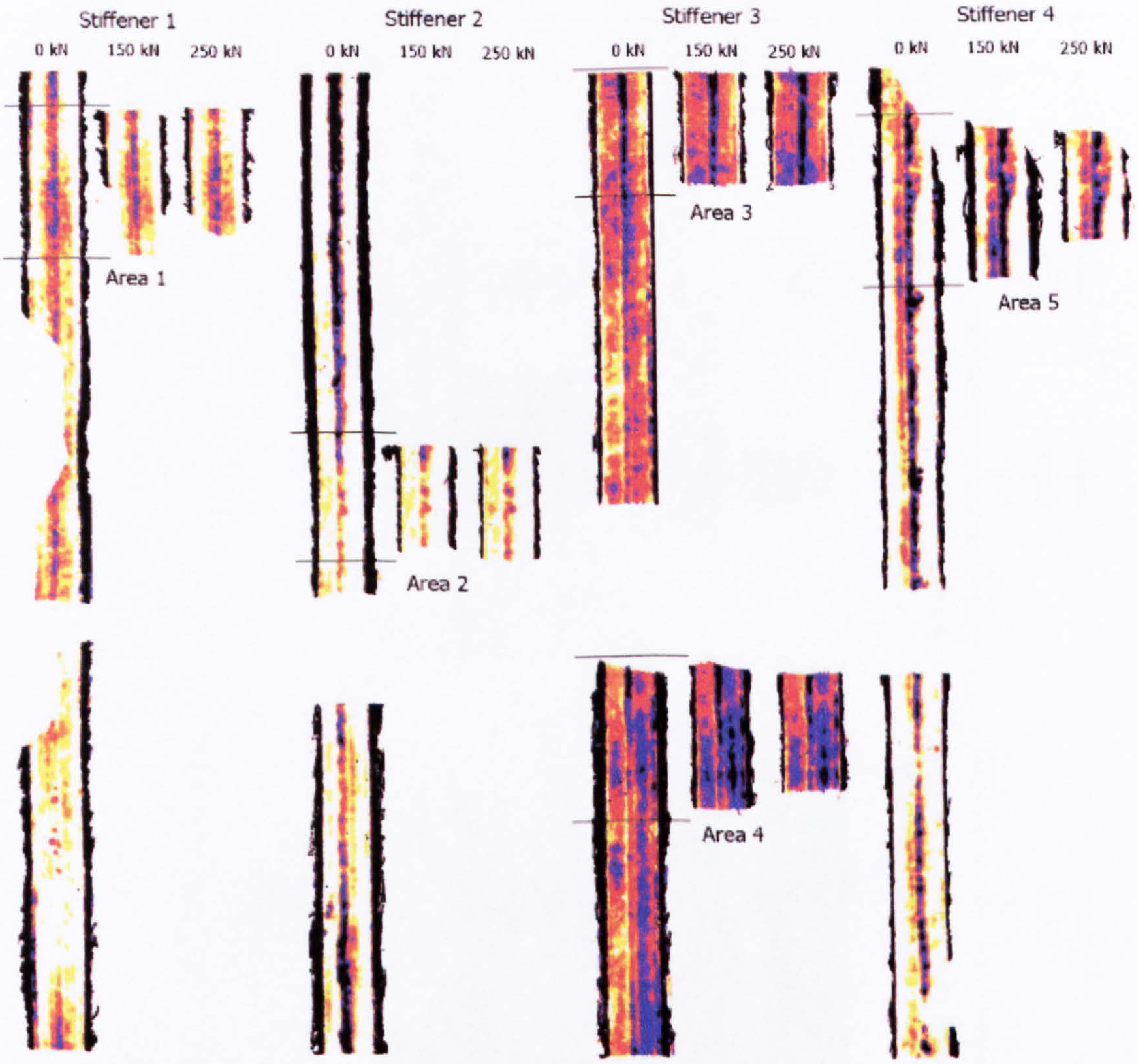

Figure 7.5: Ultrasound scan of I-stiffened panel skin-stiffener interface at no load, 150 kN, and 250 kN. Figure by Cerini [23].

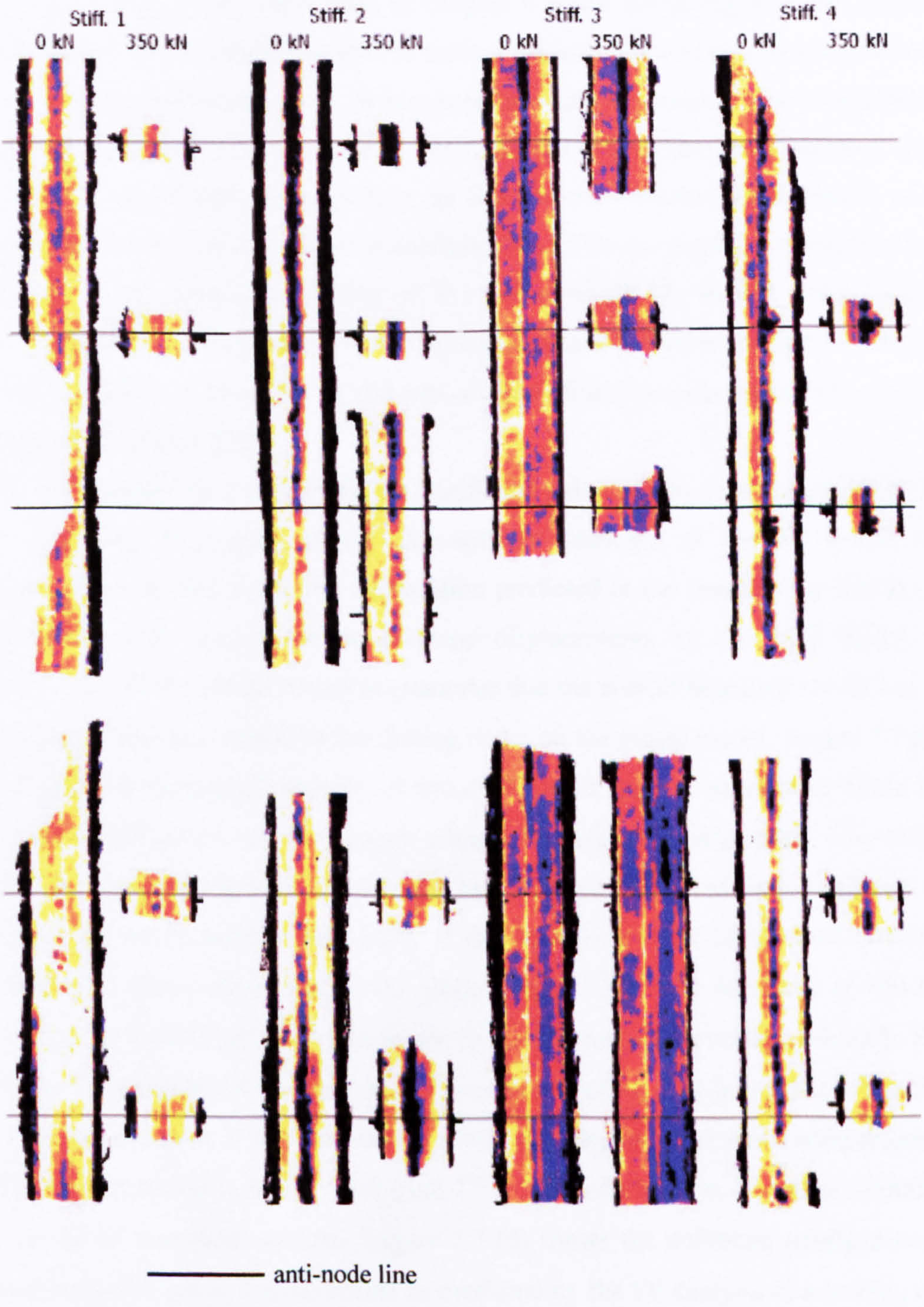

Figure 7.6: Ultrasound scan of I-stiffened panel skin-stiffener interface at selected regions for 350 kN loading. Figure by Cerini [23].

7.2.3 Local model finite element results

The adopted global-local modelling approach meant that a large part of the numerical results validation has already been done in Chapter 4 when discussing how the I-stiffened panel shell element global model was able to capture the buckling and postbuckling behaviour of the experimental I-stiffened panel. It was seen how good agreement was found between the numerically predicted buckling load of 125.2 kN and the experimental buckling load of 120 kN. The FE model was able to predict the five half-wave buckle configuration, and the subsequent mode-jump to a six half-wave configuration. This occurred at a numerical load of 262 kN, close to the experimental load of 241 kN at which the sudden mode-jump was observed. Strain results from the FE model agreed remarkably well with experimental strain gauge results (Figures 4.18-4.20), as did out-of-plane displacements measured by LVDTs (Figure 4.21 and Figure 4.22).

The local model of a section of the I-stiffened panel allowed for the potential skin-stiffener debonding developing at the skin-stiffener interface of the FE model to be investigated. Prior to looking at the degradation predicted at the interface by the interface elements in the local model, the out-of-plane displacements on the local model were compared to those of the global model to guarantee that the correct boundary conditions were in fact applied on the local model by the driving nodes on the global model. Figure 7.7 shows the out-of-plane displacement contours of the shell global model, adjacent to which is the deformed solid local model with its corresponding out-of-plane displacements. Four different load levels are shown in Figure 7.7 (a-d), with the contours updated at every load level so as to encompass the whole displacement field. It can be seen how the local model contours as well as deformed shape match that of the global model. Just after buckling, at 160 kN in Figure 7.7 (a) the I-stiffened panel was in the five half-wave configuration, whilst in Figure 7.7 (b) the mode-jump to six half-waves had occurred resulting in a relocation of the buckle crests. This was apparent in the local model which also displayed the new configuration. As the loading was increased to 500 kN in Figure 7.7 (c) the buckle crests increased in amplitude in both the global and local models. Figure 7.7 (d) shows the deformed configuration and corresponding out-of-plane displacements as predicted by the FE analysis at a loading of 800 kN. This is beyond the loading that was applied to the initial model of the panel, and hence to obtain the results at such a high loading the analysis was rerun with a higher applied compressive end displacement. This was done to asses the interface damage predicted by the analysis at such a high loading, which was much higher than the experimental failure load of the panel. What is interesting to notice from the contours in Figure 7.7 (d) is how another mode-jump occurred in the I-stiffened panel model to a seven half-wave configuration in all the skin bays. This occurred at a numerical load of about 798 kN. Experimentally this took place at the much lower loads of 473 and 486 kN for the left and right skin bays respectively, the central skin bay remaining in a six half-wave configuration (with an elongated upper buckle crest) as shown in Figure 4.17 (c). Reasons for these discrepancies may be attributed to microcracking and other failure mechanisms such as skin-stiffener debonding which act to alter the stiffness of the panel but were not modelled by the shell global model. The local model did however contain interface elements at the skin-stiffener interface and an investigation was conducted to see how the elements degraded as the compressive load on the panel was increased.

Figure 7.8 shows the damage variable D of the interface elements for the same load levels as in Figure 7.7. Since the local model was being driven directly by the global model, the interface element damage was directly influenced by the buckling and postbuckling behaviour of the whole I-stiffened panel. Right after buckling, no damage was observed in the interface elements. Increasing the load meant that the buckle crests increased in magnitude, still remaining in the five half-wave configuration. At a loading of 160 kN, shown in Figure 7.8 (a), some initial stiffness degradation was seen to occur directly under the stiffener web at a location corresponding to a stiffener anti-node line. This correlated well with the experimental observations made by Stevens et al. [8] discussed in Chapter 5. The stiffener flange acted as a step change in bending stiffness to the moment in the skin, and hence the stiffener and flange tended to peel away from one another. Furthermore there was a moment transfer from the stiffener web to the stiffener flanges and the panel skin at the bottom of the stiffener web. Due to this moment transfer the flange on the tension side had a further propensity to debond from the skin. As the loading was increased further, the panel exhibited the mode-jump to the six half-wave configuration. This resulted in the relocation of node and anti-node lines as shown in Figure 7.8 (b) at 265 kN load. Due to this new buckle configuration, the extent of skin-stiffener debonding also changed. The position of the new anti-node lines resulted in the damage "spreading" along the panel stiffener length direction to this new location. In Figure 7.8 (c) at 500 kN load the buckle crests had increased in magnitude, still in the six-half wave configuration, and debonding began to spread across the skin-stiffener interface towards the flange edges. At the very high loading of 800 kN in Figure 7.8 (d) the interface was almost completely debonded.

The interface element damage revealed a lot of important information. Most notably it was seen how the debonding phenomenon is tightly linked to secondary instabilities leading to the panel mode-jumping. When such a mode-jump occurs, the energy released is enough to lead to a sudden increase in the damage across the skin-stiffener interface. This is due to the relocation of anti-node lines where debonding initiates. The vicinity of the I-stiffened panel's failure load to the loading at which the further mode-jump of the side bays to a seven half-wave configuration occurred further strengthened this observation as do many of the other experimental works discussed in Chapter 5. The experimental ultrasound scans conducted by Cerini [23], even if limited in scope, correlated rather well with the results obtained by the local model and its interface elements. Figure 7.6 shows that as the loading was increased darker contours from the ultrasound scan were predominantly located at regions close to locations of buckle anti-node lines. Furthermore the results of the local model strengthened the hypothesis made by Cerini [23] regarding the failure of the I-stiffened panel originating from a delamination process under the central part of the stiffener. As this delamination spread, in particular being promoted by the relocation of anti-node lines due to mode-jumping, the skin peeled away form the stiffeners eventually resulting in panel collapse.

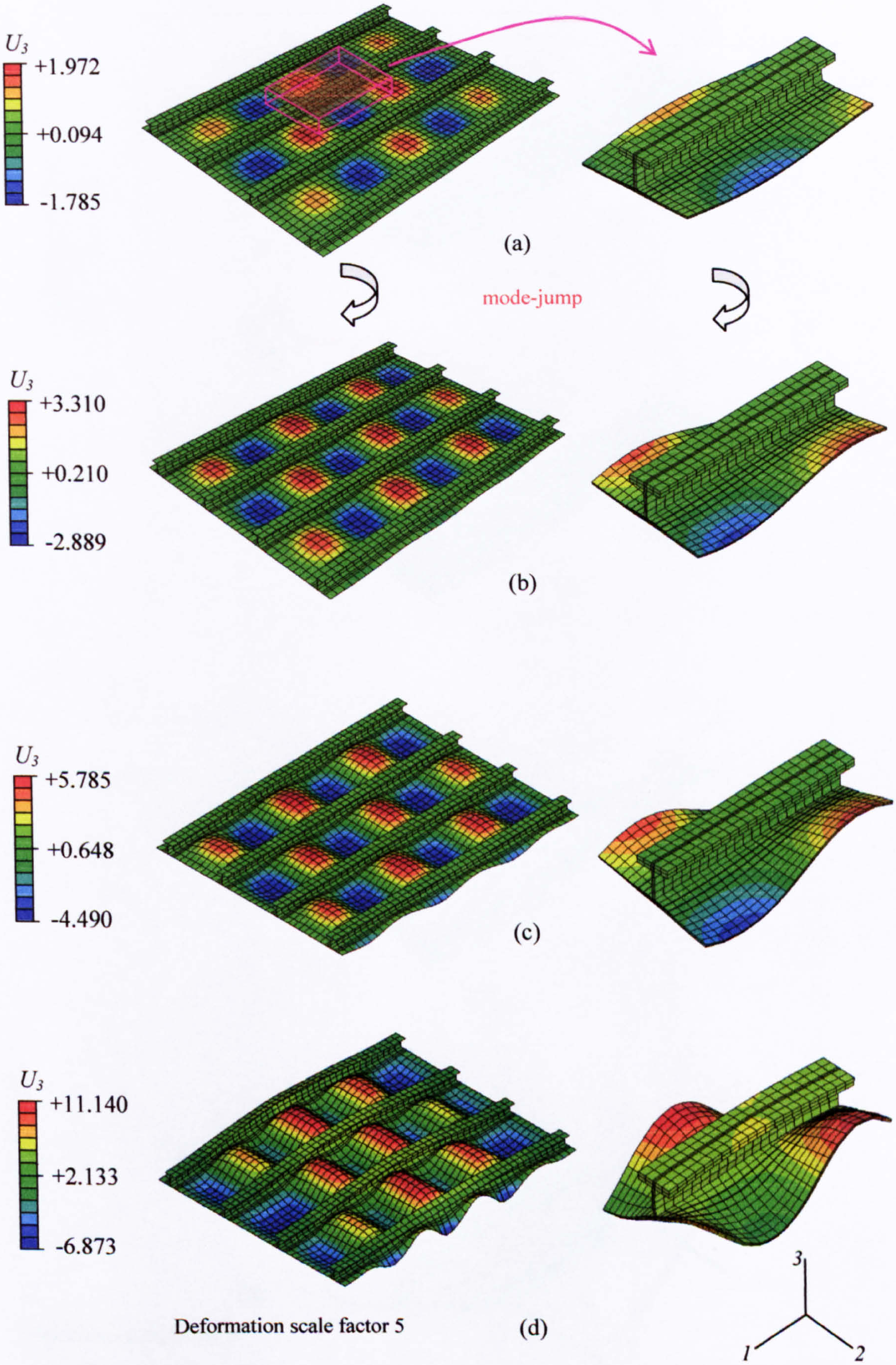

Figure 7.7: Global and local model deformed shapes and out-of-plane displacement contours at loading: (a) 160 kN, (b) 265 kN, (c) 500 kN, (d) 800 kN).

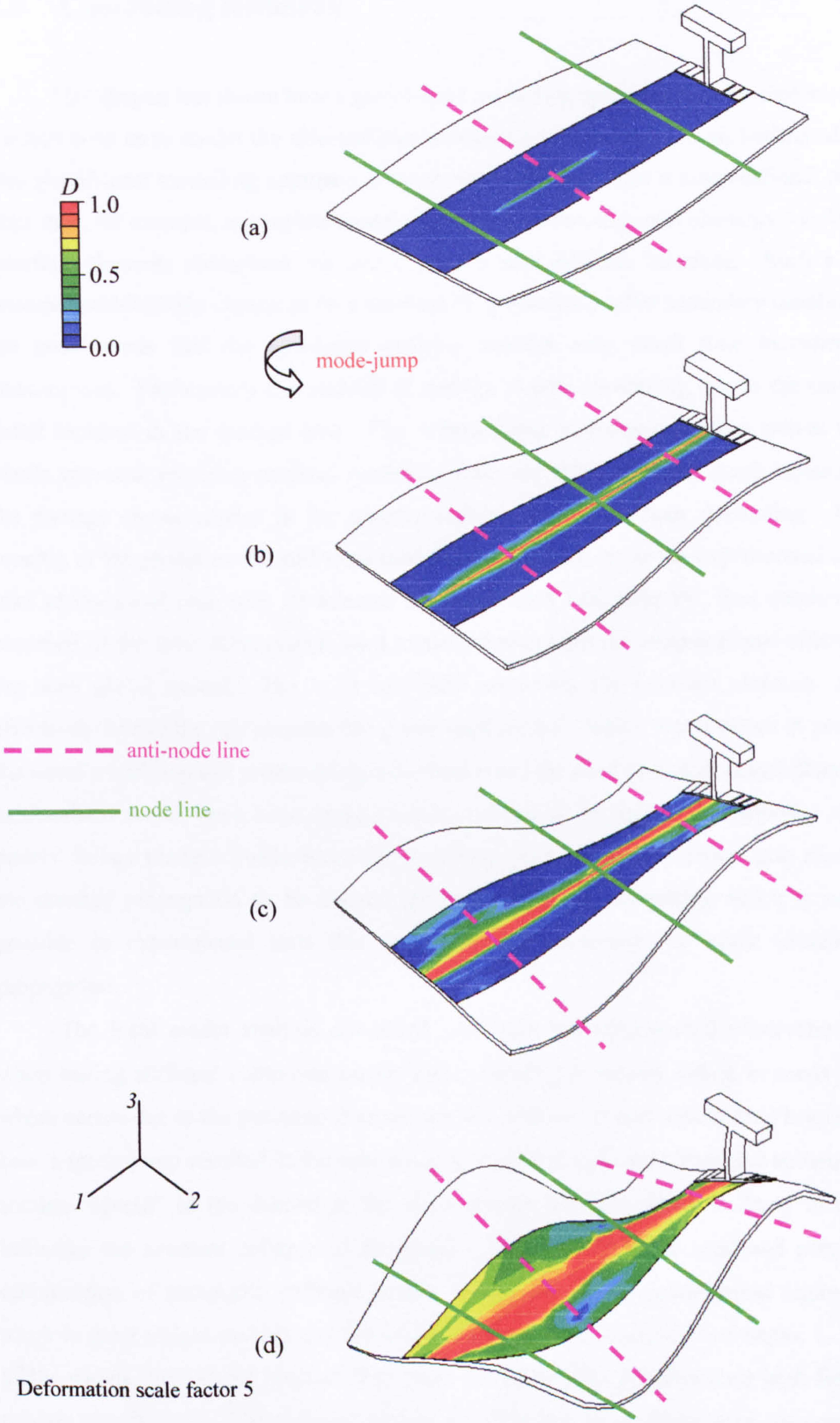

Figure 7.8: Interface element damage at local model skin-stiffener interface at loading: (a) 160 kN, (b) 265 kN, (c) 500 kN, (d) 800 kN).

7.3 Concluding Remarks

This chapter has shown how a global-local modelling approach may be implemented in ABAQUS so as to model the skin-stiffener debonding which occurs in an I-stiffened panel. The global-local modelling approach is much more efficient form a computational point of view than, for example, a complete model of the panel containing solid elements coupled with interface elements throughout the whole panel's skin stiffener interface. Such a model becomes prohibitively expensive on a standard PC particularly when secondary instabilities in the panel mean that the non-linear analysis requires very small time increments for convergence. Furthermore the analysis of damage is time-consuming due to the amount of detail required in the damage area. The submodelling tool discussed thus proves to be a viable approach requiring minimal modelling time and effort allowing quick assessment of the damage characteristics in the panel pertaining to skin-stiffener debonding. In fact, running of the global model and local models in succession up to the experimental collapse load of the panel only took 23 minutes on a dual core 1.66 GHz PC, thus combining the accuracy of the three dimensional local model solution with the computational efficiency of the shell global model. The local submodel containing the interface elements acted to effectively bridge the gap between the global shell model – which was accurate in portraying the panel's buckling and postbuckling behaviour – and the need to look at out-of-plane failure mechanisms which have been experimentally proven to be central to composite stiffened panels' failure modes. Furthermore FE modelling using interface elements also allowed for the damage propagation to be tracked during the loading, something which is not often possible in experimental tests due to the sudden occurrence of crack initiation and propagation.

The local model analysis correlated well with the experimental observations made when testing stiffened composite panels that debonding is closely linked to mode-jumping which occurs due to the presence of secondary instabilities. It was seen in the FE local model how a mode-jump resulted in the relocation of node and anti-node lines and subsequently a sudden "spread" of the debond in the skin-stiffener interface which is likely to radically influence the eventual collapse of the panel. This highlights the need and potential for optimization of composite stiffened panels, whose use in the postbuckling regime would result in great weight savings and reduction of costs as first discussed in Chapter 1. The use of the panels deep in the postbuckling range would only be possible once high fidelity FE models revealing the failure characteristics and their link to mode-jumping are created, and the FE global-local model presented is a step in this direction. In the next chapters, it will be seen how an FE based optimization procedure can be applied so as to attempt to improve a panel's damage resistance in its postbuckling regime. This optimization procedure will also highlight the extreme importance of the low computational cost achievable via the use of the global-local modelling approach discussed.

Chapter 8

Mathematical optimization applied to composite structures

This section introduces mathematical optimization as applied to composite structures, using the concept of a GAs. These mimic the evolutionary process in biology to optimise a population towards a specific objective. A GA was developed and linked to an FE model. The problem of maximizing the buckling load of a plate was used to validate the linking of the actual GA, programmed in MATLAB, to the FE package ABAQUS responsible for the buckling load calculations. This link between the GA and the FE program was then applied to the much more complex problem of optimizing an I-stiffened panel for damage resistance. This brings together all of the aspects presented in the thesis as the I-stiffened panel that was modelled using the global-local shell-to-solid submodelling approach was optimised to minimize skin-stiffener debonding subject to various constraints.

In this chapter previous work relating to the optimization of composite structures is reviewed. First the need for mathematical optimization is discussed and it is shown how a general optimization problem is formulated in terms of its objective function, design variables, and constraints. Following this, a literature review is presented dealing with optimization of simple structures such as plates and then moving on to more complicated structures such as cylindrical shells and complete panels. The concepts of integer programming are then introduced, followed by an introduction to GAs and how they function by mimicking Darwin's theory of evolution. Previous work on optimization studies, conducted using GAs, is also discussed. The approach chosen for the optimization strategy adopted in this work is then presented.

8.1 The need for optimization

8.1.1 Black aluminium structures

As discussed in Chapter 1, composite materials are becoming more and more widespread in structural design. This is particularly true in structures which are required to be lightweight and have specific constraints relating to their stiffness and strength. From a historical perspective, composite materials were initially used as lighter replacements to metal components. This meant that no attention was paid to the tailoring of the material properties of the composites used and the laminate was manufactured so as to behave similarly to an isotropic material, giving rise to "black aluminium structures". An example of this is a $[45,-45,90,0]_S$ laminate which is quasi-isotropic, meaning that its elastic properties are independent of the direction in the plane of the laminate. Such a laminate of T300/5208 graphite/epoxy has a stiffness of about 70 GPa, which is comparable to the stiffness of aluminium, close to 73 GPa [82]. However the composite material has a much lower weight density, yielding an increase in specific stiffness of 1.7 times when compared to aluminium. This effectively means that only slight redesign is required in structural configuration, and hence a weight saving with similar structural behaviour can be achieved by use of the composite component rather than its aluminium counterpart.

8.1.2 Efficient designs through optimization

It soon became apparent how finding a more efficient composite structural design meeting all requirements could be achievable not only by sizing of the geometry of the component, but also tailoring of the properties of the composite material. This refers to the choice of number, orientation, and stacking sequence of the plies making up the laminate. However the behaviour of composite materials, especially relating to the failure modes, is a complex matter. Failure due to delamination and out-of-plane damage mechanisms has been discussed in detail in Chapter 5, where it was also shown how such failure is intimately connected to – in the case of a stiffened panel – the buckling and post-buckling behaviour of the structure. It was seen how in a stiffened composite panel, damage mechanisms which may act as precursors to final failure, are affected by the mode-jumping that may occur in the panel's postbuckling regime, and hence if the weight savings achievable due to operation of the panel in its highly postbuckled state are to be realized, then the design of the structure must take the possible material degradation due to the mentioned damage mechanisms into account.

The increased number of design variables offered by the use of composite materials adds greater complexity to the design process, but also adds a plethora of new possibilities to achieve more efficient designs and hence weights savings. Therefore, the possibility of realizing a design that is safe against failure, coupled with the correct choice of the large number of design variables to have as efficient a design as possible relative to a variety of constraints, makes mathematical optimization of composite structures a powerful tool.

8.2 Classical optimization

8.2.1 Formulation of the optimization problem

Before looking at previous work relating to optimizations conducted on composite structures, a very brief introduction to the main concepts behind mathematical optimization is presented so as to introduce the terminology that will be used in the upcoming chapters. In general every optimization problem has an objective function which is used to measure the "fitness" of any design. This could be any specific parameter of the structure being optimised such as buckling load, fundamental frequency, or weight. Of course there will exist some limits that will dictate the boundaries of the possible optimised design. Such limits are known as constraints. The variables available to the designer during the optimization process are the design variables and include aspects such as choice of material, geometric dimensions, and stacking sequence of a laminate. Design variables may be continuous or discrete. If, for example, a specific dimension could take a value anywhere in a specified continuous range, then this design variable is known as continuous. If on the other hand only several discrete values of the design variable are permitted, then it is know as discrete. An example of this would be a ply orientation taking value of either 0°, 45°, -45° or 90°.

The mathematical notation adopted [82] is usually that of a vector $\mathbf{x}$ with n components to denote the design variables available in the optimization. The domain of these variables is given as X to cater for some – or all – of the variables belonging to a discrete set. The objective function is denoted by $f(\mathbf{x})$, to show that it is a function of the design variables. Constraints are denoted by $g(\mathbf{x})$ and $h(\mathbf{x})$, depending on whether they are inequality or equality constraints. The optimization can hence be formulated as:

$$\text{Minimize } f(\mathbf{x}) \qquad \mathbf{x} \in X \tag{8.1}$$

$$\text{Such that: } h_i(\mathbf{x}) = 0 \text{ , } i = 1,\dots,n_e \tag{8.2}$$

$$\text{Such that: } g_j(\mathbf{x}) \leq 0 \text{ , } j = 1,\dots,n_g \tag{8.3}$$

$$\mathbf{x}^L \leq \mathbf{x} \leq \mathbf{x}^U \tag{8.4}$$

The elements of the vectors $\mathbf{x}^L$ and $\mathbf{x}^U$ are the lower and upper bounds respectively of the values the design variables are allowed to take. In the standard form above, the optimization is specified as a minimization of the objective function. For maximization problems, it is sufficient to change the sign of the objective function or use any other transformation transforming the problem into a minimization. The domain of design points X that satisfy all the constraints is termed the feasible domain, and at a general design point, $\mathbf{x}$, a constraint can either be satisfied or violated. The objective of the optimization is then to find the feasible design that minimizes the objective function.

8.2.2 Available optimization algorithms

Equation (8.1) for the objective function of a general optimization problem together with the constraint Equations (8.2) and (8.3) are known as a nonlinear program which may be solved via nonlinear programming techniques. If the objective function and constraints are linear functions of $\mathbf{x}$, then linear programming techniques may be used to solve the optimization problem. The concept of linear and nonlinear programs is discussed later in this chapter. There are a variety of classical algorithms which may be used to solve both linear and nonlinear optimization problems. The effectiveness of each algorithm and how efficient they are in finding the optimum solution in the design space depends on a variety of factors, namely the nature of the objective function, constraints, and characteristics of the design space. It is beyond the scope of this thesis to go into detail regarding any of these algorithms, details of which may be found in a variety of dedicated textbooks [83,84]. Furthermore, the ultimate aim of this thesis is to develop an FE based optimization routine for a stiffened composite panel which is able to deal with out-of-plane damage mechanisms – a highly nonlinear phenomenon. To this extent, the more recent stochastic search techniques are more suited to the problem. In the next section a literature review of optimization problems involving composite structures is given. These range from simpler optimization of plates to more recent and more complex optimization of complete stiffened panels. Following this, genetic algorithms – a stochastic search technique – are introduced and previous optimization work in this field reviewed.

8.3 Previous optimizations for composite structures

8.3.1 Optimization of composite plates

The optimization of simple plated composite structures has been widely addressed in literature. Adali et al. [85] looked at the design of hybrid symmetric laminated plates consisting of a high-stiffness surface coupled with a low-stiffness core. Two optimization problems were considered. First the best stacking sequence for various geometric parameters and loading conditions to maximize the buckling load was sought. Secondly, material costs were minimized by establishing the minimum number of expensive high-stiffness surface layers required for a minimum buckling load. Buckling load evaluations were conducted using analytical expressions from plate theory. The effects of aspect ratio of the plates and hybridization were investigated for the cases of uniaxial and biaxial loading, and it was shown how cost-effective designs could be achieved with only a small decrease in the buckling load.

Adali et al. [86] also investigated uniaxially loaded laminated plates subject to elastic in-plane restraints along the unloaded edges. The optimization required the optimal lay-up so as to give a maximum combination of buckling load, prebuckling stiffness, and postbuckling stiffness. Because of the combination of the latter parameters in the optimization problem, the design study was effectively a multiobjective optimization which was conducted by maximizing the weighted sum of the buckling load, prebuckling stiffness, and buckling load. This led to compromised solutions and trade-off between the various objectives, but it was found that the majority of designs had high stiffnesses for all three parameters and the trade-off remained minor in most cases.

A further optimization involving composite plates was undertaken by Adali and co-workers [87]. This treated the design of composite plates under buckling load uncertainty. The laminates were subjected to biaxial compressive loads and the buckling load maximized under a worst case in-plane loading condition. The solution to the problem gave the best stacking sequence so as to maximize the buckling load under the worst possible biaxial compressive load case within a specified uncertainty domain, and hence a robust optimal laminate could be found so as to operate within this domain.

The use of exact analytical solutions utilized by Adali et al. [85,86,87] in the work described above is impossible when a problem involves complex geometry, material property, boundary conditions, and loading. Complexities also arise in finding the buckling loads of composite structures when desired conditions are to be specified at panel edges in order to achieve the desired in-plane loading and boundary conditions. Because of this, in their buckling strength optimization of laminated composite plates, Chai et al. [88] used a refined semi-numerical, semi-analytical approach called the finite strip method (FSM). This method was first developed by Khong [89] for stability behaviour analysis of thin-walled structures and then modified by Chai and Khong [90] so as to handle the buckling behaviour of laminated composite plates. It has the primary advantage of being able to deal with a range of simulated load and boundary conditions. FSM was hence used for buckling load evaluations, whilst the optimization itself was conducted using the Complex optimization algorithm [91]. This optimization technique was derived from the Simplex optimization method developed by Spendely et al. [92] and later modified by Nelder and Mead [93]. In general, the choice of optimization method is based on the nature of the objective function and the availability of the partial derivatives of this objective function with respect to the design variables. When the closed form solution for the objective function cannot be expressed analytically and the partial derivatives are not readily available, then the most suitable approach is that of a non-derivatives direct search technique such as the Complex method.

Walker et al. [94] also employed a non-analytical method for the evaluation of plate buckling loads in their optimization of symmetric laminates for maximum buckling load. An FE eigenvalue analysis was employed to evaluate the buckling loads of designs which were then used in an optimization algorithm whose objective was to maximise buckling load including the effects of bending-twisting coupling. Five different boundary condition combinations on the plate edges were considered, together with three biaxial load combinations for plates with aspect ratios in the range of 0.5 to 2.0. The Golden Section Method [84] was used for the optimization process itself. An extension to the above work [95] considered angle-ply laminates subjected to non-uniform loads. This meant that the plate had a non-uniform distribution of loads along its edges, in particular the possibility of point loads, partial uniform loads, and non-uniform loads. Again a variety of boundary conditions and plate aspect ratios were considered, and an FE model to evaluate buckling loads was coupled with the Golden Section Method for the optimization. Walker [96] also considered plates with a circular cutout, again using an FE model for buckling load evaluations and the Golden Section Method for the optimization routine. Results for the optimal lay-up of plates with circular cutouts were compared to those obtained for plates without such cutouts. More recently Walker et al. [97] used the same optimization technique for the optimization of cylindrical shells. The objectives of maximizing the torsional buckling load and the axial buckling load were incorporated by introducing a performance index consisting of the weighted sums of the two single objectives. The solution procedure again used the Golden Section Method and was written in a MATHEMATICA routine. The method was able to maximize a combination of axial and torsional buckling loads with respect to ply angles.

Fukunaga et al. [98] also conducted a similar optimization as those of Walker so as to maximize the fundamental frequencies of simply supported and clamped laminated plates. A mathematical programming method in which four lamination design variables were used as the design variables was adopted. As an optimiser, the modified feasible direction method with the Golden Section Method was used in the Automated Design Sythensis (ADS) program [99]. A slightly different problem was tackled by Yoshi and Biggers [100], who optimised the thickness distribution for isotropic and laminated plates for maximum buckling load. An FE model with a plate element with variable thickness was used to a thickness that can vary smoothly over the plate being optimised. The plate itself had all edges simply supported and edge loading was introduced as a uniform end-shortening across a given edge. It was found that large increases in buckling load could be achieved for both material types and that all optimum designs showed the general characteristic of relatively thin central regions and maximum thickness slightly inboard of the unloaded edges.

Hu and Chen [101] considered the optimization of unsymetrically laminated rectangular plates again for maximum buckling load. Fibre orientations were optimised as the plate was subject to different lateral and in-plane loads. An eigenvalue buckling analysis using the FE package ABAQUS was used in the function evaluations, and the optimization was conducted using a sequential linear programming approach. A variety of plate geometries and boundary conditions were considered, including laminated plates with simply supported edges, laminated plates with clamped edges, as well as laminated plates with circular cutouts again subject to either simply supported or clamped boundary conditions. The same authors had previously used a similar procedure for the buckling load optimization of symmetrically laminated plates [102].

A general formulation for the optimization of general laminated thin-plate structures was presented by Mateus et al. [103]. This formulation allowed for a structure's elastic strain energy, displacements, stresses, natural frequencies, or buckling load to be used as objectives or constraints in an optimization routine. Non-linear mathematical programming techniques were used for the optimization [104]. Several examples were illustrated, relating to a cylindrical panel, a conical panel, and finally a uniformly loaded cantilever.

8.3.2 Recent optimization procedures

As more computational power has become available in recent years, it has been possible to conduct more advanced and complex optimization procedures. Diaconu et al. [105] considered long laminated cylindrical composite shells under combined loads of axial compression and torsion. In the buckling analysis of the shells, 12 lamination parameters were used as design variables with the objective of maximizing the buckling load, and mathematical programming methods employed for the optimization process, which was run for a variety of axial compression and torsion combinations. Kere et al. [106] used an interactive linear descent method [107] for weight minimization of failure strength controlled composite laminates made form orthotropic fibre-reinforced layers. Multiple loading conditions were applied on the laminate to be optimised due to the different in-service conditions that may be encountered by the laminate which was modelled via an FE model.

Narita and Turvey [108] compiled a brief review of research relating to optimum lay-up of plates so as to give maximum buckling loads. They also presented an optimization procedure based on the layerwise optimization procedure originally proposed by Narita [109]. The latter work dealt with optimal lay-ups so as to maximize fundamental free vibration frequencies. The newer optimization procedure maximized buckling loads using a layerwise optimization procedure, which optimised the various ply directions in a sequential rather than simultaneous fashion. The authors commented how the procedure was not always able to find the global optimum to the solution, but even so the results obtained were improvements on the base configurations.

Carrera et al. [110] proposed a two level optimization procedure for the design and analysis of reinforced shell structures made of both metallic and composite materials. The optimization built an interface between a global FE code and a second-level optimization software. NASTRAN was used as the FE code, while the PANDA2 program [111] was used for a panel optimization. Various other structures such as a reinforced circular cylinder and several applications to space structures were also considered. The PANDA2 program mentioned is also discussed in detail by Bushnell and Rankin [112] who combined it with a general nonlinear finite element code named STAGS [29,113] which was specifically designed to cope with stability difficulties such as mode-jumping which may occur in compressively loaded stiffened panels. Optimizations to maximize collapse load were run activating and deactivating a constraint which "allowed" designs to exhibit mode-jumping. It was found that preventing mode-jumping resulted in panels up to 20% heavier than those which exhibited mode-jumping, highlighting the concept that the understanding of the latter phenomenon is crucial for the effective and efficient design of stiffened composite structures.

8.4 Integer programming

8.4.1 Linear integer programming

There is a growing interest in integer programming methods to laminate design. This stems from the fact that most commercially available composite materials come as unidirectional tape with a fixed thickness. When the total thickness of the laminate has to be optimised, the number of layers must be determined hence making the problem an integer programming problem. Furthermore, it is common for optimization to treat the ply orientations as design variables, meaning that the best stacking sequence for a composite part is sought so as to, for example, maximize buckling load or minimize weight. In industry ply orientations commonly take values of 0°, 45°, -45°, 90°. This again transforms the optimization into an integer programming problem as the design variables can only take discrete values.

If the constraints and objective functions are linear functions of the design variables, then an optimization problem is called a linear programming problem. Furthermore, if the design variables are restricted to take only integer variables, then the problem becomes a linear integer programming problem. Several well-known optimization techniques exist for solving linear integer programming problems. Two common techniques are enumeration [82] – suitable for problems with a small number of design variables – and the branch-and-bound algorithm originally proposed by Land and Doig [114]. The latter method relies on calculating upper and lower bounds on the objective functions so that any design resulting in objective functions outside these bounds can be neglected. A discussion of both enumeration and the branch and bound algorithm with appropriate examples for each algorithm can be found in the textbook by Gurdal [82].

8.4.2 Non-linear integer programming

For linear integer programming, the branch and bound algorithm has been implemented into a variety of commercially available computer codes [82]. When the objective function is not a linear function of the design variables then the optimization problem becomes a nonlinear program, and if the design variables can only assume integer values, a nonlinear integer program. Nonlinear programs are much harder to solve, in the sense that compared to linear programs it is more difficult to converge to the global optimum solution. Random search techniques have been formulated which provide a methodical way of searching the design space for the global optimum without the need of computing any derivatives. When a large number of design variables are present, such classical random search techniques fail.

Two algorithms have been developed which are ideally suited to nonlinear optimization problems where a global minimum is sought. The first is simulated annealing [115], and the second GAs [116]. They are able not only to locate solutions very close to the global optimum, but are very powerful when used in problems with discrete design variables. In particular GAs have found consistent use in the problem of stacking sequence optimization. Their main characteristics are discussed next followed by a literature survey of existing work where GAs have been used to optimise composite structures for a variety of objective functions.

8.5 Genetic algorithms

8.5.1 What is a genetic algorithm?

GAs are optimization algorithms based on Darwin's principle of evolution and survival of the fittest. They mimic biology in the sense that when creatures are left to evolve, those traits which are most useful for survival tend to be naturally passed on since the individuals having them have more chance of breeding than individuals without. All the genetic information for each of the individuals is stored in chromosome strings, and then the mechanics of natural genetics evolves these chromosome strings from generation to generation based on operations that result in structured yet randomized exchange of genetic information. GA's were first developed by Holland [117] and mimic the mechanics of natural genetics using simple and easy to program operations which are counterparts of the natural ones observed in nature. All the operations effectively result in simple random exchanges of locations of numbers in strings which represent the design variables. This starts off with the creation of a completely random population where each individual is represented by a genetic string representing its design variables. This initial population is then evaluated in terms of the objective function. Individuals are at this point also penalized if they violate any of the optimization constraints. Having done this, individuals are assigned a fitness value based on their objective function and then selected for breeding. The latter genetic operation occurs through crossover, which is the swapping of genetic traits between individuals. Mutation is then applied, which is the random alteration of a genetic string. This is done with very low probability and is a safeguard against the potential loss of favourable genetic traits. Following mutation, several other proposed genetic operators [82] may be applied prior to reinsertion of the offspring into the population. This marks the end of a generational loop, and the whole process is repeated until an optimum solution is found.

The theoretical properties of GAs are discussed in detail by Goldberg [116]. GAs have proven to be experimentally robust and able to reach global optimum or near-global optimum designs with a high chance. This is because unlike many traditional search algorithms which move from one point of the design space to another, GAs work with a population of strings. This means that keeping a large population and allowing it to evolve drastically increases the chances of obtaining a global optimum or near-global optimum solution. The risk of converging early on in the optimization history to a local optimum is reduced by keeping many solution points which have the potential of being close to the actual global optimum. Furthermore, since GAs involve a completely random search method, repeated genetic optimization may lead to the discovery of different designs which might have comparable performance in terms of the objective function being optimised for. The next section is a literature review of previous work conducted in the field of composite structural optimization where GAs have been used.

8.5.2 Previous genetic optimizations

A lot of research effort has been made in the area of using GAs in the optimization of composite structures, especially plates and stiffened panels. GAs are particularly suited to the optimization of composite structures because of the discrete nature of the problem at hand since, for example, ply angles are typically only available in discrete sets (0°, ±45°, 90°). Le Riche and Haftka [118] tested a GA for maximizing the buckling load of a fixed thickness laminate. The GA was then improved by the same authors [119] so as to define a design for minimum thickness and hence weight. Kogiso [120] applied the same algorithm but coupled the thickness minimization problem with specific failure constraints. Park et al. [121] also used and refined a GA, demonstrating its functionality by optimizing the stacking sequence of both a composite sandwich plate and a composite propeller. More recent work was conducted by Kang and Chun-gon [122] who looked at the minimum weight design of compressively loaded composite plates as well as composite stiffened panels under constrained postbuckling strength. A non-linear FE analysis was used together with a GA for the optimization process. Both the number of plies and ply angles were treated as design variables, and in the case of the stiffened panels, the stiffener size and locations were also included. Kim et al. [123] investigated an optimization method for the strength of composite laminates with ply drop. Although not specific to stiffened panels, this work is nonetheless useful as ply drops are used extensively at stiffener foots in composite stiffened panels. The number of plies and stacking sequence at each ply drop location are appropriately adjusted via the use of a patch-wise optimization method involving non-linear FE analyses and a genetic algorithm.

Much work was also done to refine existing GAs so as to reduce their computational cost. GAs are computationally very expensive, because they require a lot of fitness evaluations every time a population is updated via the "rules" of evolution. Nagendra et al. [124] introduced several small modifications in the genetic operators of an existing GA algorithm for the design of stiffened composite panels. These not only reduced computational cost, but also lead to an even better design of the panels themselves. Gantovnik et al. [125,126] augmented a GA to include memory for continuous variables. This was then applied to stacking sequence design of sandwich composite panels involving both continuous and discrete design variables. A local improvement, or localized search, was also introduced to speed up the GA so that it required less function evaluations to arrive at an optimum solution. A discussion of local improvement was also treated by Lin and Lee [127]. Di Sciuva et al. [128] optimised laminated and sandwiched plates for minimum thickness and maximum buckling load using a variety of different constraints. This was done using two different kinds of evolutionary algorithms, a genetic algorithm similar to those just mentioned, and also a simulated annealing algorithm.

Other researchers have taken slightly different approaches in the optimization of composite structures to the GA approach just discussed. Adams et al. [129] for example, did not follow the panel optimization sub problem route, where only a single panel is considered. In this work a method was presented for constructing a globally blended structure. In its optimization a single genetic optimization was run for the entire structure so as to minimize its weight. Hansel [130] investigated weight minimal laminate structure design by topology optimization. A heuristic approach was adopted where the implemented algorithm removed plies layer by layer gradually where they were not needed. The algorithm also adapted the material distribution in the laminate and applied local directional reinforcement where required based on the specific structural needs. Todoroki and Ishikawa [131] obtained a response surface approximation for the buckling load of laminated composites. The lamination parameters, rather than the individual ply angles, were adopted as variables in the approximation function of the entire design space.

As stated earlier, genetic algorithms are computationally very expensive due to the large number of fitness function evaluations that must be performed for each population set. Of course this must be repeated each time a new population is created via the evolutionary process. When considering composite stiffened panels and their optimization in the postbuckling regime, highly non-linear FE analyses must be used. These, together with the GAs used in the optimization process, can lead to highly prohibitive computational costs, even with the improved GAs discussed earlier. For this reason a new approach has recently emerged, and was discussed by Bisagni and Lanzi [132]. In order to optimise stiffened composite panels for use in the postbuckling regime, a system of neural networks was set up and trained so as to "replace" the non-linear finite element analyses required to characterize the structural response of the panels. Neural networks are a system of small elements called nodes, which are mutually connected by links. Each node takes a specific input, and computes an output to send to the next node. Once trained with specific examples, the neural network was able to successfully characterize the panels' response such as buckling load, collapse load, and prebuckling stiffness. The neural network thus replaced non-linear FE analyses, resulting in great savings in computational power and cost. A GA was then implemented in the actual optimization itself to seek as weight efficient a design as possible. The whole procedure hence allowed for a complete separation between the system modelling and the optimization process. Lanzi and Bisagni [133] illustrated new improvements to the above method. Strength constraints were incorporated directly into the optimization process, and two different scenarios were investigated. In the first a panel was optimised so as to obtain the highest possible ratio between the maximum allowable load and the buckling load, meaning that the postbuckled regime is as "large" as possible. In the second the structure was designed constraining the prebuckling stiffness and the buckling load to set values. In both cases the panel was designed to be as light as possible. Results show that the use of neural networks is indeed advantageous as they offer a huge potential in the reduction of required non-linear FE analyses, and hence great savings in computation time and power.

8.6 Choosing an appropriate optimization method

This chapter has introduced the main concepts behind mathematical optimization and highlighted how the increased number of design variables available when dealing with composite structures makes it an even more appealing and powerful design tool than when optimizing metallic components. More design variables also mean more complexity, so it is crucial for the designer to come up with both an efficient and reliable optimization strategy. It was seen how different optimization strategies exist, but ultimately the choice of which strategy to adopt is largely dependent on the nature of the optimization problem to be solved.

The optimization strategy adopted in this thesis must therefore be suited to the ultimate objective of developing and FE optimization strategy for stiffened composite structures that is able to cope with out-of-plane damage mechanisms such as skin-stiffener debonding. In the case of a stiffened panel, the panel is to be optimised for operation in the postbuckling regime. Chapter 4 showed how the FE package ABAQUS could be used to model an I-stiffened panel's buckling and postbuckling behaviour effectively, including secondary instabilities associated with mode-jumping. Chapter 5 then highlighted how such secondary instabilities strongly influence damage mechanisms including delamination and skin-stiffener debonding. Chapter 6 and Chapter 7 showed how debonding could be modelled within an FE framework for both stiffener runout sections and an I-stiffened panel operating in its postbuckling regime.

The remaining step to achieve the goal of the research project was hence to come up with the optimization routine itself and linking it to the FE models developed. The optimization of a stiffened composite panel including out-of-plane damage mechanisms is a much more complex problem than, for example, a maximization of buckling load for a composite plate. The problem is highly nonlinear and hence not-suited to traditional optimization methods. In this sense the use of a GA seems natural due to the latter's proven ability to come up with global optimum or near-global optimum designs for highly non-linear problems. Furthermore, the design variables in the optimization of the I-stiffened panel are discrete since they would relate to the ply orientations of the individuals plies which are present in the panel, further indicating the use of a GA as appropriate. The only drawback is the computationally expensive nature of using a GA coupled with an FE model due to the large number of function evaluations. To avoid this, the approach of training a neural network system as discussed earlier to replace the nonlinear FE analyses could be used, but this too seemed inappropriate due to the high non-linearity present in the modelling of the damage mechanisms in the composite structure. This highlights the importance of making the FE analyses as computationally cheap as possible, something which has been mentioned repetitively in previous chapters describing the FE models created.

Having chosen a GA as the most suitable optimization method, the GA was coded in MATLAB and its characteristics are discussed in detail in Chapter 9. Instead of dealing straight away with the problem of the panel optimization, a GA was constructed for a well-known plate buckling load maximization problem. Such a problem has been treated in literature and can be solved with more classical optimization methods, and hence acted as a benchmark test for the GA code developed. It also formed the foundation for the testing of how the GA could be effectively linked in an autonomous fashion to the FE package ABAQUS. Having constructed the GA code for this simple buckling load problem, it was modified for the panel optimization as discussed in Chapter 10. Here the results of the optimizations run on the stiffened panel are discussed and it is shown how the GA is able to effectively optimise an I-stiffened panel operating in the postbuckling regime for damage resistance.

Chapter 9

Genetic algorithm to maximize buckling load of a composite plate

Having discussed the need for optimization and the various optimization techniques applicable to composite structures in Chapter 8, this chapter gives details on a GA constructed for the optimization problem of the buckling load maximization of a composite plate under biaxial loads. The problem studied is one which has already been tackled by Haftka and Walsh [134] using the branch-and-bound optimization method. The different approach using a genetic algorithm to solve the same optimization problem is demonstrated here as it forms the basis and validation for the algorithm developed in Chapter 9 for the optimization of an I-stiffened panel for damage resistance. Because of the complex nature of the latter problem, the relatively simple problem of buckling load maximization, widely tackled in the literature, as mentioned in Chapter 8, is chosen as a development platform for the GA algorithm developed.

The GA constructed is discussed in detail, with particular attention not only to the genetic processes that allow the algorithm to find an optimum design, but also to how the GA was linked to the FE package ABAQUS which is responsible for evaluating the buckling loads of the various designs encountered during the optimization process. Different biaxial loads were applied to the plate and the ability of the GA to cope with the search for the optimum lay-up is discussed. Subsequently a contiguous ply constraint was added to the problem and the GA's ability to cope with this additional constraint is also discussed.

9.1 Problem description

The problem considered is that of maximizing the buckling load of a composite plate of given dimensions subject to various biaxial loads. Depending on the load case, the optimum design will correspond to a different stacking sequence of the plies in the plate. The problem formulation follows that of Haftka and Walsh [134] who used integer programming techniques for the formulation of the optimization problem. Such methods are usually rather costly form a computational point of view, but for laminate design problems they often become appropriate due to the discrete nature of the design variables. Haftka and Walsh [134] showed that the stacking sequence design of a laminated plate for buckling can be formulated as a linear problem by using ply-orientation-identity design variables and the invariant properties of the composite material. Discussion of these invariants can be found in the work done by Tsai [135] and Hull [136]. In this thesis the same formulation was implemented, but a genetic algorithm was constructed in MATLAB for the optimization rather than using the branch and bound method. In addition, to show the possibility of linking the GA to the FE package ABAQUS in a fully automated optimization procedure, an FE model was used to find the buckling load of each design considered rather than an analytical expression for the buckling load.

The plate considered had a length a = 508 mm and width b = 254 mm as shown in Figure 9.1. All edges were simply supported, and the plate was loaded in the x and y direction by loads λN_x and λN_y respectively where λ is an amplitude parameter.

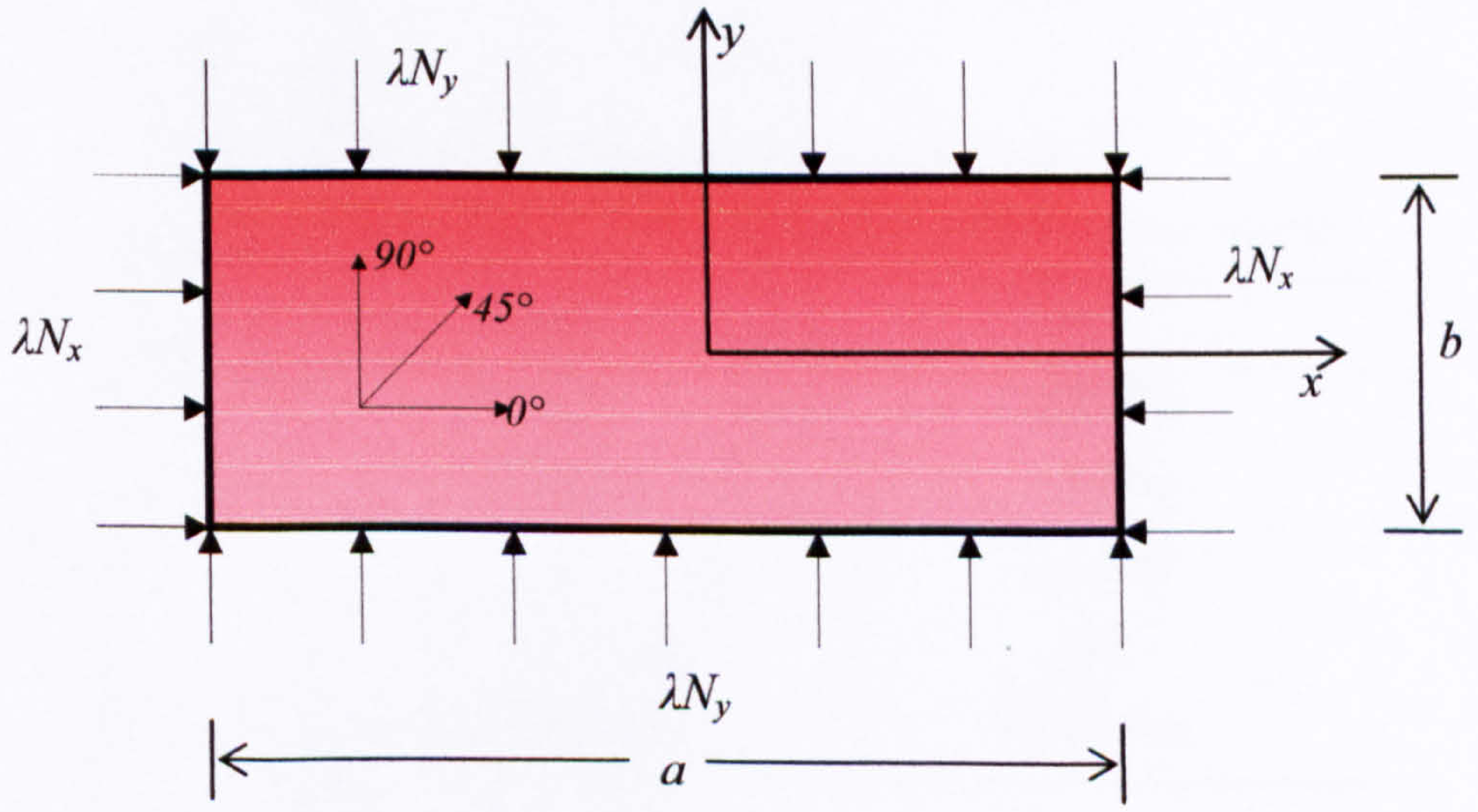

Figure 9.1: Plate geometry and loading.

The plate itself consisted of a composite graphite-epoxy laminate which contained *N* plies and was both symmetric and balanced. Plies could be oriented in any of four directions, 0°, 45°, -45°, and 90°, relative to the coordinate system shown in Figure 9.1. All plies had a thickness *t* and a stacking sequence illustrated in Figure 9.2 where the plate total thickness was denoted by *h*.

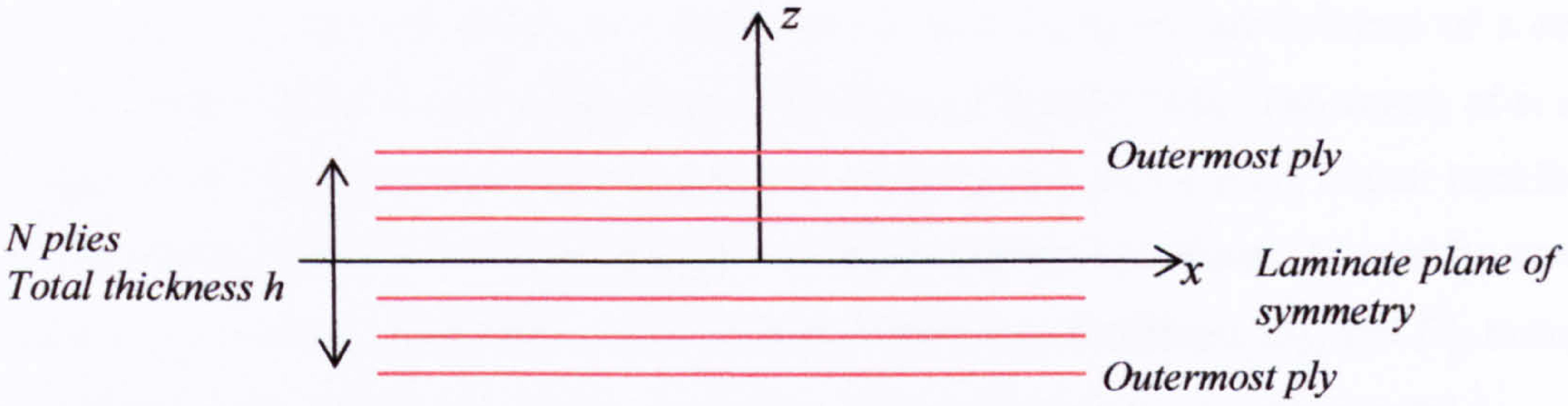

Figure 9.2: Plate stacking sequence.

The material properties of the graphite epoxy laminate are shown in Table 9.1. A variety of biaxial load cases were considered and a different optimization conducted for each one. The load N_x in the *x* direction was set to a value of 175 N/mm and the value of N_y altered so as to achieve N_y/N_x ratios in the range between 0.125 and 2.45. It is known from laminate plate theory that for plate aspect ratio of less than 1.5 the optimum ply orientation is the same as for the uniaxial load case, but for aspect ratios greater than 1.5 then the optimum ply orientation increases rapidly as the ratio of N_y to N_x increases. For large values of N_y/N_x the optimum ply angle is 90°. To investigate the effect of modifying N_y/N_x, the plate dimensions were set to a = 508 mm and b = 254 mm to give an aspect ratio of 2.0. These values correspond to those used by Haftka and Walsh [134].

Table 9.1: Nominal material data for graphite epoxy lamina.

Property	Value
$E_{11tension}$	128 GPa
$E_{22tension}$	13 GPa
G_{12}	6.4 GPa
μ_{12}	0.3
Ply thickness *t*	0.127 mm

An analytical solution exists for the buckling load of the plate of Figures 9.1 and 9.2. When the plate buckles it will do so with m and n half-waves in the x and y directions respectively. This will occur when the load amplitude reaches a critical value λ_{cr} given by:

$$\lambda_{cr}(m,n)=\frac{\pi^2\left[D_{11}(m/a)^4+2(D_{12}+2D_{66})(m/a)^2(n/b)^2+D_{22}(n/b)^4\right]}{(m/a)^2N_x+(n/b)^2N_y} \tag{9.1}$$

The D terms are flexural stiffnesses which can in turn be expressed in terms of a series of integrals and material invariants as done by Haftka and Walsh [134]. The values of m and n – the number of half-waves for the buckling load of the plate – to yield the lowest buckling load will depend on both the lay-up of the plate and the loading condition. It must be noted that Equation (9.1) is not accurate for large values of the flexural stiffness D_{16} and D_{26} terms. The value of these two terms may measured by the non-dimensional parameters γ and δ.

$$\gamma=\frac{D_{16}}{\left(D_{11}^3D_{22}\right)^{1/4}} \tag{9.2}$$

$$\delta=\frac{D_{26}}{\left(D_{22}^3D_{11}\right)^{1/4}} \tag{9.3}$$

When both γ and δ are below 0.2, then the effect of D_{16} and D_{26} is negligible [137]. Haftka and Walsh [134] minimized these by manually modifying the position of 45° and -45° plies in the optimum designs. The objective of the optimization procedure is to find the lay-up that maximizes the buckling load of the plate for various biaxial loading conditions.

9.2 Finite element model

Rather than using Equation (9.1), an FE model was constructed for the plate in ABAQUS for buckling load evaluations. Conventional four-noded linear shell elements, with six degrees of freedom at each node, were used to discretize the plate, using 20 elements along its length and 10 elements in the width for a total of 200 elements. Mesh sensitivity tests were conducted to ascertain that a fine enough mesh was used. A single composite shell section was used to define the lay-up of the panel, which changed according to the specific design being considered during the optimization process to maximize the buckling load. Boundary conditions were applied on the edges of the plate to replicate the simple supports, and a material coordinate system aligned to that of Figure 9.1 created to ensure correct orientation of the plies. Distributed shell edge loads were applied to replicate the N_x and N_y loads. Figure 9.3 (a) shows the plate model and its associated mesh.

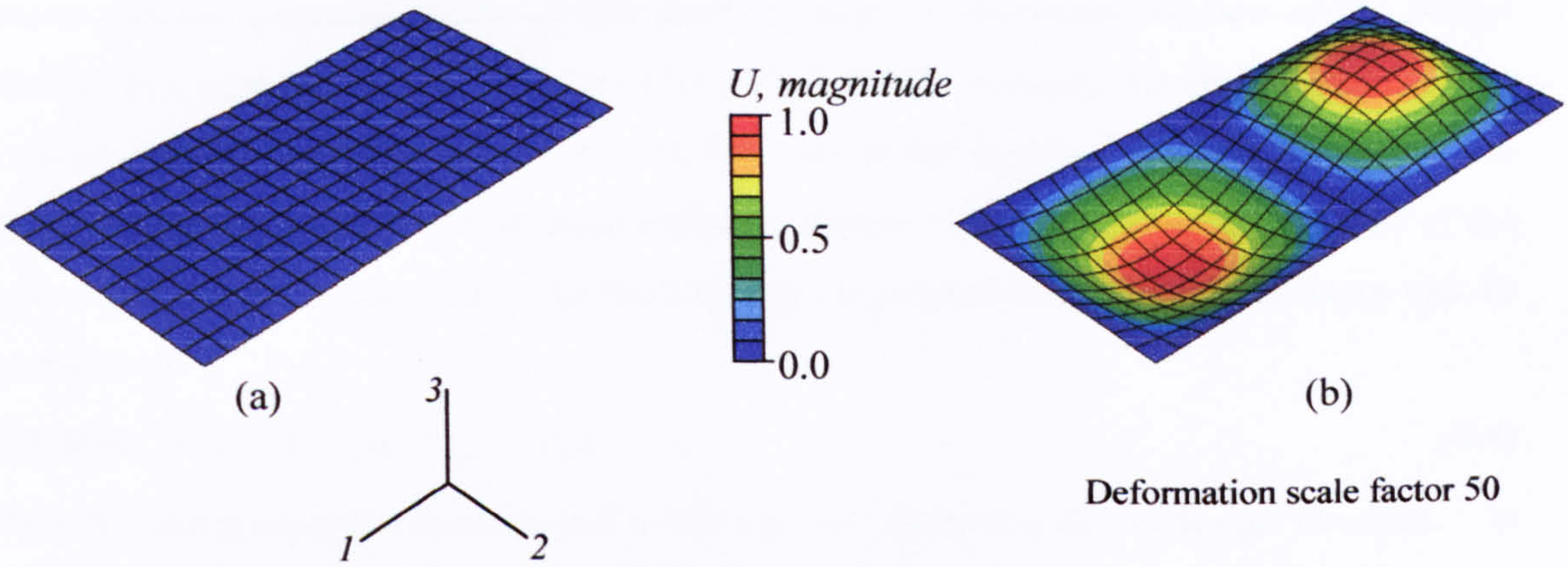

Figure 9.3: FE mesh for plate buckling problem (a) and deformed shape (b) for a $[90]_{16}$ subject to a N_y/N_x ratio of 2.45.

A linear eigenvalue buckling analysis was used to evaluate the numerical buckling load of the plate being considered. Table 9.2 shows the results obtained comparing the buckling load as predicted by the linear eigenvalue buckling analysis and those obtained using Equation (9.1). A variety of representative plate lay-ups as well as N_y/N_x ratios are shown (for N_x = 175 N/mm), and it is clear how accurate the FE linear eigenvalue buckling analysis is in predicting the buckling load with percentage differences not exceeding 1.7%. The linear eigenvalue buckling analysis also showed the predicted buckling mode shape, as shown in Figure 9.3 (b) for a plate with a lay-up of $[90]_{16}$ subject to a N_y/N_x load ratio of 2.45.

Table 9.2: Results of linear eigenvalue analysis on hat-stiffened panel.

N_y/N_x	Lay-up	λ_{cr} (anal.)	λ_{cr} (FE)	% diff.
0.125	$[45,-45_2,45,-45,45_2,-45]_S$	154.06	151.49	1.67
0.5	$[45,90,-45,90_3,-45,45]_S$	94.29	92.85	1.53
2.45	$[90]_{16}$	31.06	31.02	0.001

Having constructed an FE model able to evaluate the buckling load of any plate lay-up being considered subject to a specific biaxial loading condition, the algorithm to conduct the optimization was formulated.

9.3 Formulation of the optimization problem

The first step in any optimization problem is the definition of an objective function which is either maximized or minimized. The variables used in the optimization – those which are allowed to vary – are termed the design variables. In a GA the application of the various genetic operators to the search problem requires the representation of the design variables in a suitable fashion in terms of bit strings which represent the chromosome strings in nature and the evolutionary process. In the case of the buckling load maximization, the objective function is the buckling load, whilst the design variables are the orientations of the various plies in the composite. Mathematically, a general maximization problem can be expressed as:

Maximize $f(\mathbf{x})$, $\mathbf{x} = \{x_1, x_2, x_3, x_4\}$ (9.4)

where f(**x**) is the objective function and **x** is the vector containing all the design variables. In the current problem, the optimization required the maximization of the critical buckling load $\lambda_{cr}(m,n)$ of Equation 9.1 for a laminate with a specified thickness, where the FE model created was used for the evaluation of $\lambda_{cr}(m,n)$ to show how an autonomous link between the optimization GA algorithm and the FE model can be established.

A formulation using ply-orientation-identity variables is useful when considering problems for stacking sequence optimization where the plies can only take a specific number of orientations. This is typical in composite lay-ups such as plates or stiffened panels, where available orientations are usually 0°, 45°, -45°, and 90°. As mentioned in the problem description, the plate had a symmetric lay-up, meaning that only half of the lay-up needed to be specified, and also had to be balanced. The stacking sequence can then be defined in terms of four variables, knows as ply-orientation-identity variables. Each of these variables represents one of the four possible orientations, and assumes a value of 1 if a specific ply is oriented in that direction and a value of 0 otherwise. The variable o_i represents 0°, n_i 90°, f^p_i 45°, and f^m_i -45°. The plies are numbered using the index i, which takes values $i = 1,\ldots N/2$ where N is the total number of plies in the laminate, in this case eight, representing half the lay-up of the 16-ply symmetric laminate. Adopting this formulation, the optimization problem could be stated as follows:

Find o_i, n_i, f_i^p, f_i^m for $i=1,\ldots,N/2$ (9.5)

To **maximize** $\lambda_{cr}(m,n)$ $m = 1,\ldots,m_{max}$ $n=1,\ldots,n_{max}$ *(buckling constraint)* (9.6)

Such that: $o_i + n_i + f_i^p + f_i^m = 1$ for $i = 1,\ldots,N/2$ *(ply identity constraint)* (9.7)

and $\sum_{i=1}^{N/2}\left(f_i^p - f_i^m\right) = 0$ *(balanced laminate constraint)* (9.8)

It is often easier, for reasons discussed later, to work in terms of a minimization rather than a maximization problem. This is easily done by seeking to minimize a constant value minus the buckling load $\lambda_{cr}(m,n)$. A constant value of 2,000 was chosen in this problem so as to have a positive value for the optimization variable at all times. The new formulation was hence:

Find o_i, n_i, f_i^p, f_i^m for $i=1,\ldots,N/2$ (9.9)

To **minimize** $\lambda_{cr}(m,n)$ $m = 1,\ldots,m_{max}$ $n=1,\ldots,n_{max}$ *(buckling constraint)* (9.10)

Such that: $o_i + n_i + f_i^p + f_i^m = 1$ for $i = 1,\ldots,N/2$ *(ply identity constraint)* (9.11)

and $\sum_{i=1}^{N/2}\left(f_i^p - f_i^m\right) = 0$ *(balanced laminate constraint)* (9.12)

Having formulated the optimization problem, the GA was constructed in MATLAB using the Genetic Algorithm Toolbox by Chipperfield et al. [138]. This toolbox adds MATLAB functions which are able to perform many of the genetic operations. The toolbox works for a general minimization problem, and it is for this reason that the problem was transformed into a minimization as mentioned above. The full GA code for the optimization is available in Appendix C. It consists of three separate MATLAB scripts. The first, named *Critical_buckling_load_memory* is the actual GA, *Plate_buckle_abaqus_memory* is the function used to call up ABAQUS and conduct the function evaluations, and *constraints* is a function dealing with the various constraints. The next section explains the GA in detail whilst Figure 9.4 shows a flowchart of the algorithm developed. A number for each step of the GA is given in the explanations of the next section and may then be cross-referenced with specific sections of the code in Appendix C.

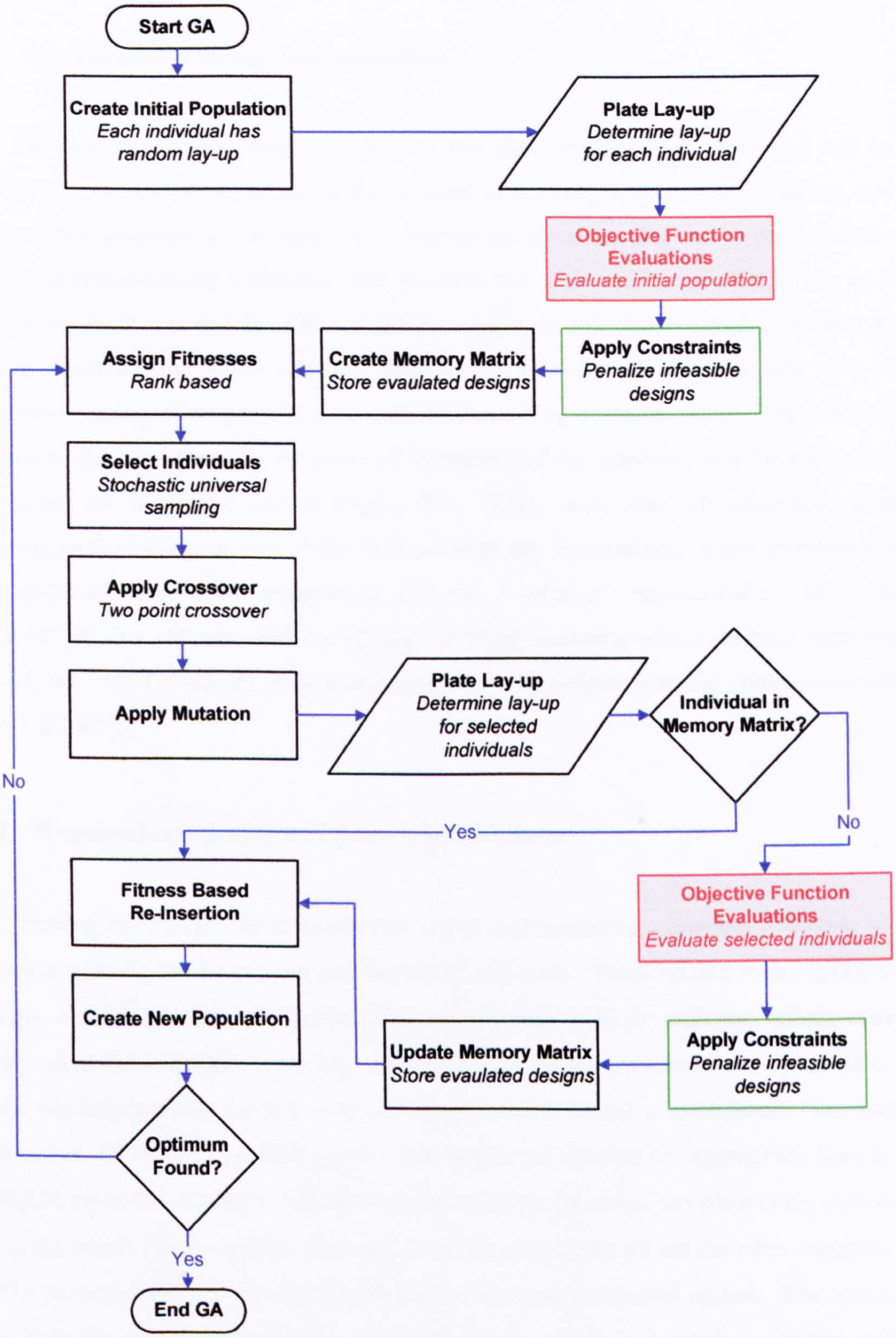

Figure 9.4: Flowchart of developed GA for buckling load maximization of a composite plate.

9.4 The genetic algorithm

9.4.1 Chromosome string representation

The first step in the creation of the GA was deciding how each individual was to be represented. As described earlier, in the problem of stacking sequence optimization, and in the case when orientations are limited to a discrete set of values, this can be done via the use of ply-orientation-identity variables. The laminate had a set number of plies, given by $N = 16$. The laminate was also symmetric, and therefore only $N/2$ design variables needed to be used to describe the whole stacking sequence. The method adopted was that of a chromosome string of length $N/2$, with each bit describing one orientation. The leftmost bit represented the ply closest to the plane of symmetry of the laminate, and the rightmost bit represented the outermost ply in Figure 9.2. There were four ply-orientation-identity variables, each relating to one of the four possible ply orientations. Each orientation was hence given an integer value in the set (1, 2, 3, 4). A value of 1 represented a 0° ply, a value of 2 a 45° ply, 3 a -45° ply, and 4 a 90° ply. A 16 ply laminate with a stacking sequence of $[45, -45, 90, -45, 45, -45, 90, 45]_S$ would therefore be described with the chromosome string [2 3 4 3 2 3 4 2].

9.4.2 Required composite and genetic parameters

Having established the chromosome string representation, parameters relating to the composite plate had to be entered into the MATLAB code. These related to the thickness of each ply, number of integration points to be used by ABAQUS for each ply, and the material name used in the ABAQUS input file. The reason for these parameters to be specified is due to how the link between the GA code and the ABAQUS model is established. The plate is described in ABAQUS as a shell section and MATLAB changes the appropriate lines in the ABAQUS input file relating to this shell section to correctly model any plate being considered during the search for the optimum lay-up. The parameters also set are the other variables that ABAQUS requires for the correct specification of the composite shell section. The number of plies N in the composite was also set at this stage, which is labeled (1) in the code of Appendix C.

Genetic parameters relating to the genetic search were also set. These will be discussed individually later, but relate to the initial population size, maximum number of generations allowed, generation gap, and probability of crossover for the individuals. The section of code where these parameters are set is shown as (2) in Appendix C.

9.4.3 Initial population

Once the chromosome representation for each individual determined, the initial population was created. Most genetic algorithms, including the one implemented here, work with a fixed size population which stays constant in size from generation to generation. The initial population was hence represented by a matrix of size *NIND* x *N/2*, where *NIND* was the number of individuals in the population and *N/2* corresponded to half the lay-up, hence automatically satisfying the symmetric requirement of the laminate. Each row in the matrix represented an individual's lay-up using the ply-identity variables as previously described. The value of *NIND* was to 40, as this was found to guarantee a big enough population so as to find the optimum lay-up after the genetic algorithm completed. Initial population creation is labeled (3) in Appendix C.

9.4.4 Buckling load evaluation

Having created the initial population of random individuals, the next step in the GA was to evaluate each of the individuals relative to their objective function which corresponded to the buckling load. To show how a GA can be linked in an automatic fashion to the FE package ABAQUS the buckling load was found using the FE model for the plate described earlier. Calling up of the linear eigenvalue analysis performed by ABAQUS was done via a separately coded MATLAB function *Critical_buckling_load_memory* which is also shown in Appendix C and is denoted by a grey rectangle in Figure 9.4. As with any MATLAB function, several inputs were required from the main code where the function is called upon. *Critical_buckling_load_memory* reads in the population matrix *Chrom* together with the composite and genetic parameters. Having done this each individual was transformed into its actual ply orientations rather than the 1-4 integer values. Then, in sequential fashion for each individual, a lay-up file was created corresponding to the lines in the ABAQUS input file used to describe the shell section of the plate. These contained the material name, number of integration points, ply thickness, and orientation of each ply which varied from individual to individual as dictated by the genetic algorithm. Having all the required information for the plate, this was inserted into the ABAQUS input file and the linear eigenvalue analysis run. The buckling load was then extracted for each individual and an array created with the buckling loads for all of the individuals in the population. Hence, the function *Critical_buckling_load_memory* may be thought of as a black box which provides the important link between the GA and ABAQUS. It takes the genetic and composite parameters together with the chromosome strings of the individuals to be evaluated and returns the buckling loads for each individual. The number (4) shows the point in the GA code of Appendix C where the function is called upon, whilst the full code of the function itself is also available in the same Appendix.

9.4.5 Application of constraints

Having evaluated the buckling load for each individual in the population, constraints were applied. As mentioned earlier using eight design variables to represent just half the laminate guarantees the symmetric constraint, but the necessity for the laminate to be balanced had to be taken into account. In Appendix C, the point labelled (5) shows how this was done with the use of another MATLAB function created, called *Constraints*. In the flowchart of the algorithm in Figure 9.4 calling of this function is denoted by a green bound square. This function took in the vector of buckling loads and the matrix of all the individuals and outputs another vector containing the "penalized" buckling loads. What the function effectively did – the code is available in Appendix C – was artificially reduce the buckling load for those individuals which are not balanced by taking their previously FE calculated buckling load and reducing it by a large factor hence increasing its objective function when the problem is turned into a minimization. This effectively "fooled" the GA in seeing those penalized individuals as performing much worse than those which satisfy the balanced laminate constraint.

9.4.6 Fitness assignment and selection

Once the buckling loads for all the individuals in the population had been found, a fitness value was assigned to each individual corresponding to section (8) of the code in Appendix C. The scheme used was that of generalized rank-based fitness with a selective pressure of 2. What this meant is that all the individuals in the population were ranked according to their objective function. The individual with the best objective function, in this case the highest buckling load, was given a fitness of 2, the worst individual a value of 0, and all other individuals fitness values between 0 and 2, with values assigned in a linear fashion.

Fitness values having been assigned, individuals were selected for breeding in part (9) of the MATLAB code. This process is known as selection, and in this particular GA was performed using the method of stochastic universal sampling, although other methods, such as roulette wheel selection, exist [82]. Stochastic universal sampling provides zero bias and minimum spread. Bias measures the difference between an individual's normalized fitness and the expected probability that it will be involved in reproduction, while spread measures the range of possible number of offspring that any particular individual may have. Stochastic universal sampling works as shown in Figure 9.5 below:

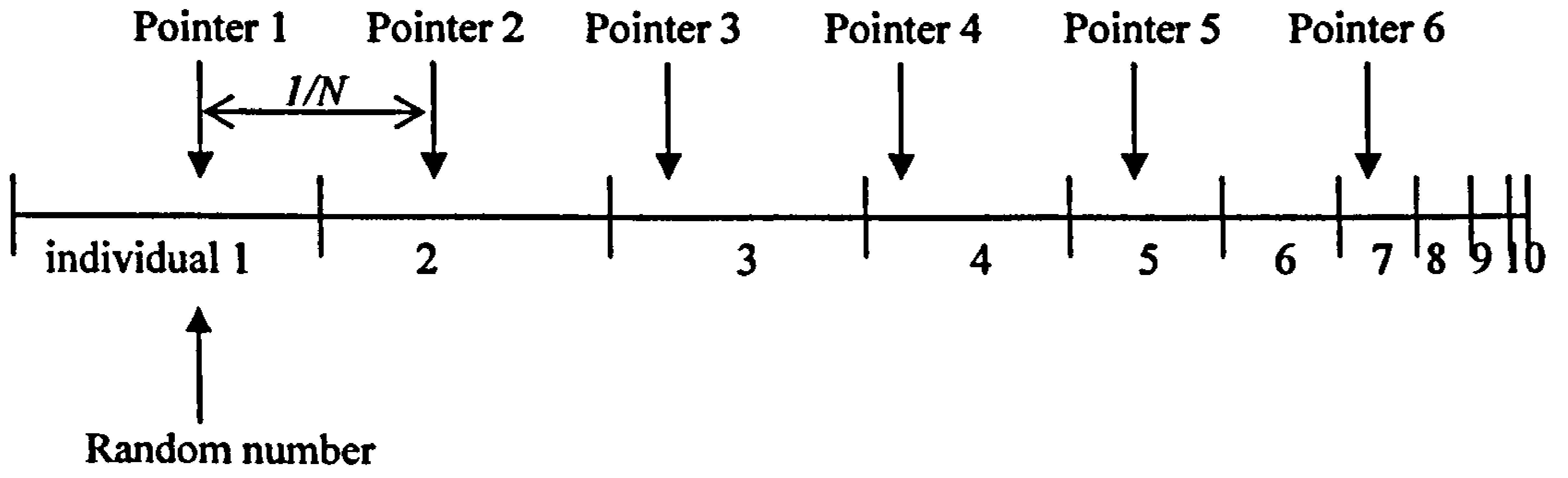

Figure 9.5: Stochastic universal sampling.

Figure 9.5 shows 10 individuals, with individual 1 having the greatest fitness, and individual 10 being the least fit. Each individual is mapped to a segment of the line, with the length of each segment being proportional to that individual's fitness. A pointer is then created for each individual to be selected. In this case, out of 10 individuals, 6 are to be selected for reproduction, and therefore 6 pointers are generated. For *N* individuals to reproduce, *N* pointers are generated. These pointers are equidistant from one another, their separation being given by *1/N*. The position of the first pointer is determined by a randomly generated number lying between 0 and *1/N*. The position of the pointers then dictates the individuals to be selected for reproduction. The number of individuals to be selected for reproduction out of the whole population is known as the generation gap, and for this particular genetic algorithm, was set to 95%.

9.4.7 Crossover

Crossover is the actual reproduction of the individuals, where genetic information is shared amongst them to produce offspring individuals. Two-point crossover is used in this genetic algorithm. Booker [139] showed that two-point crossover is more efficient than single-point crossover. Crossover with more points is also possible, but this means that the process becomes more random and the performance of the algorithm might be penalized, as discussed by De Jong [140]. Two-point crossover works by creating two randomly placed cut-off points in each individuals string and then swapping information between two individuals to create the offspring. An example is shown in Figure 9.6.

Parent 1: 4 3 / 3 4 2 1 4 / 3
Parent 2: 1 3 / 4 2 1 1 2 / 1
Offspring 1: 4 3 / 4 2 1 1 2 / 3
Offspring 2: 1 3 / 3 4 2 1 4 / 1

Figure 9.6: Two-point crossover.

As can be seen, the genetic information is exchanged between the two parents to produce the two offspring. The random cut-off points determine which chromosomes are to be swapped. Crossover in the plate buckling load maximization GA was applied with a probability of 0.7 and is labelled (10) in the MATLAB code of Appendix C.

9.4.8 Mutation

Mutation – (11) in the GA code of Appendix C – was applied to the generated offspring after crossover so as to prevent the loss of potentially favourable genetic traits. This is especially true in cases when integer coding is used as in this case, as there is always the possibility that no individual in the generated initial population has a particular gene, and without mutation this gene will never appear in future generations. Also, inferior designs with lower fitnesses which might not be chosen for reproduction might have some desirable genes which without mutation would be lost as the genetic algorithm evolves from generation to generation. Mutation also makes sure that the crossover operator remains effective, as in the later stages of the optimization the population might become more uniform and crossover becomes less effective.

Mutation works by changing a bit at random in a string. This is done with a very low probability, in this case set to $1/L$ where L is the number of bits in each individual's chromosome string. In this genetic algorithm this is half the number of plies in the laminate. In this way mutation acts a sort of safety net to recover good genetic material which may have been lost during selection and crossover.

9.4.9 Reinsertion

Mutation is the last of the genetic parameters which was applied to the population of the GA. Following this all the new offspring were evaluated as before by calling up the *Critical_buckling_load_memory* function and constraints were then applied in the same way as discussed earlier in sections (12) and (13) of the MATLAB GA algorithm shown in

Appendix C. After this was completed the evaluated offspring were reinserted into the population in section (14) of the code. A variety of methods exist for this, but fitness-based re-insertion was implemented. This means that all of the created offspring replaced the least fit members of the population. The population size was set to stay constant form generation to generation. This method tends to preserve the most fit individuals, which have a propensity to have the most desirable genetic traits, and hence aided in reaching the optimal solution earlier.

9.4.10 Termination

The genetic algorithm was set to repeat the process just described until the optimal stacking sequence was found. This was done via a variable which tracked the generation number that is incremented – in Section (16) of the code – after reinsertion of each new generation was made. A termination scheme is however required to end the evolutionary process once an optimum design has been found. Common termination schemes involve just setting a maximum number of iterations and letting the algorithm run. This is however not very efficient. If too high a number is set, then function evaluations are conducted for no reason and it just takes longer to get the required results. If too low a number is set, then the GA will abort before the optimum design has been found. To avoid this, careful investigations need to be conducted so as to select a suitable number of maximum number of generations. The approach used here was to specify a termination condition in section (15) of the MATLAB GA code. This was chosen to be that five successive individuals in the population after any iteration are the same. If this is so then it was deemed that the optimal design had been found and the algorithm stopped. In the possibility that the algorithm doesn't find an optimum, a limiter to the number of generations was also set. This is specified as 60, and was just introduced as a "safety margin" to terminate the algorithm in case it was unable to find the optimum stacking sequence and corresponding buckling load factor.

9.4.11 Memory capability

In order to reduce computational costs, the GA was modified to avoid identical function evaluations. In order to do this, all the information relating to each function evaluation was stored in a file. As the GA progressed and was about to evaluate an individual, the file was scanned. If the particular individual had already been evaluated then the same objective function was used, avoiding a new function evaluation. This helped to significantly reduce computational time, especially in the latter stages where the GA was converging to the optimum and most of the individuals in the population had already appeared in previous generations.

The way in which this memory capability was implemented was by creating a three-dimensional array of all the evaluated individuals and their corresponding objective function values. Each "layer" of the three dimensional array corresponded to a generation in the evolutionary process, and contained the chromosome string of each individual in that population and its objective function values. This is illustrated in Figure 9.7 where each colour relates to a different generation. Prior to each function evaluation, the memory array is scanned to see whether the current individual has already been evaluated. If this is the case then the objective function value is taken from the memory value rather than re-evaluating the same individual again. The first layer in the memory array is the base population with its objective function values and is created in section (7) of the MATLAB code in Appendix C. A new "layer" to the memory was then added in section (17) after each new generation has been evaluated.

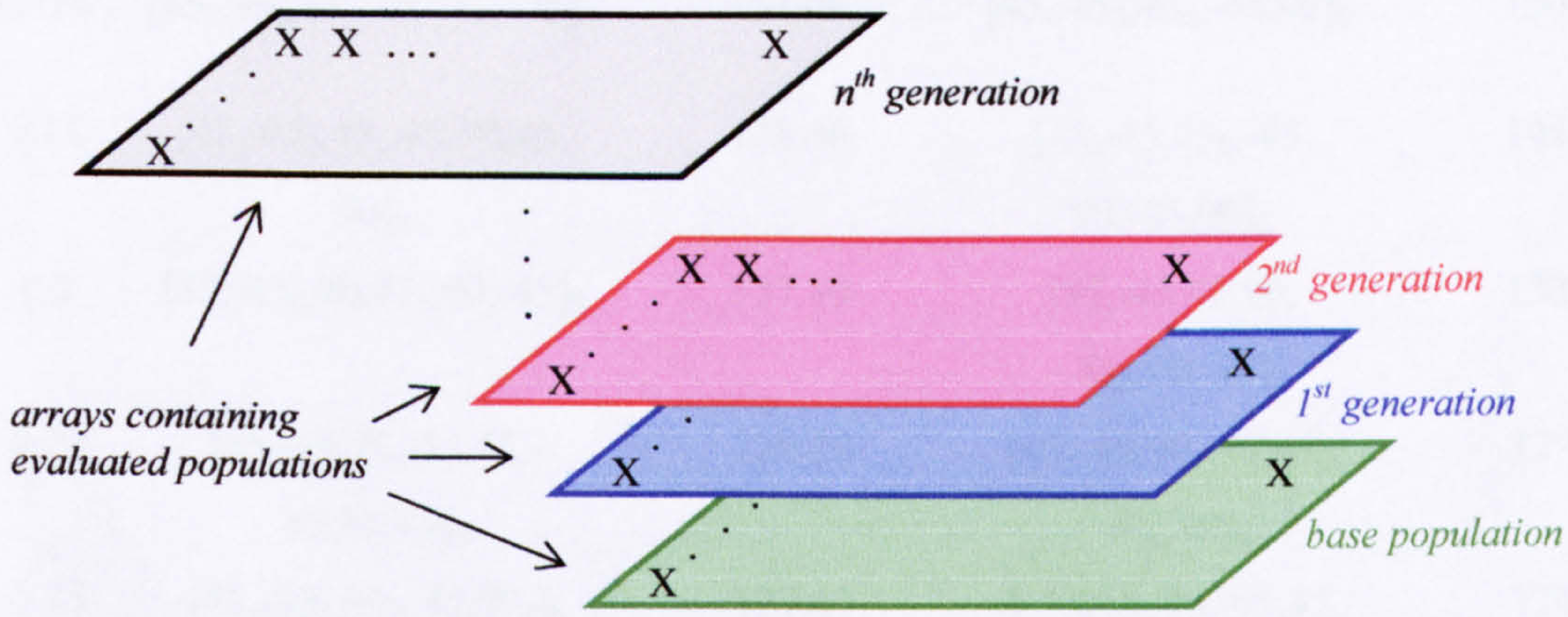

Figure 9.7: Three-dimensional layered array for the storage of evaluated designs for memory capability of GA.

9.5 Optimization results

9.5.1 No contiguous ply constraint

The GA described was run for a large variety of load cases and the results obtained relating to the optimum design's lay-up and its corresponding buckling load compared to those documented by Haftka and Walsh [134] as illustrated in Table 9.3. Having done this several load cases were rerun adding a contiguous ply constraint, which is discussed in the next section.

Table 9.3: Optimal stacking sequences and buckling loads as given by the GA linked with ABAQUS and by the branch and bound method (BB) by Haftka and Walsh [134] for N=16, N_x=175 N/m, and varying N_y/N_x.

N_y/N_x	Optima Lay-up (BB)	λ_{cr} (BB)	Optimal Lay-up (GA)	λ_{cr} (GA)
0.125	$[45,-45_2,45,-45,45_2,-45]_S$	154.06	$[45,-45_3,45_2,-45,45]_S$	150.73
0.15	$[45,-45_2,45,-45,90,45,90]_S$	148.46	$[45,-45,45_2,-45,90,-45,90]_S$	141.29
0.2	$[45,-45_2,90,45_2,90,-45]_S$	137.10	$[45,-45,45,90,-45_2,90,45]_S$	133.86
0.24	$[45,-45,90,-45,45,-45,90,45]_S$	129.28	$[45,-45,90,-45,45_2,-45,90]_S$	127.57
0.25	$[45,-45_2,90_2,45,90_2]_S$	127.49	$[-45,45,90,-45,45,90,-45,45]_S$	124.51
0.5	$[45,90,-45,90_3,-45,45]_S$	94.29	$[90,45,-45,90,-45,90,45,90]_S$	93.15
1.0	$[90,45,90_4,-45,90]_S$	61.99	$[90_2,45,90,-45,90,-45,45]_S$	61.77
1.5	$[90_3,45,90_2,-45,90]_S$	46.18	$[90_3,-45,45,90_3]_S$	45.32
2.0	$[90_5,45,-45,90]_S$	36.84	$[90_5,45,90,-45]_S$	36.48
2.1	$[90_5,45,90,-45]_S$	35.40	$[90_5,-45,45,90]_S$	35.34
2.4	$[90_6,-45,45]_S$	31.64	$[90_6,45,-45]_S$	31.69
2.45	$[90_{16}]$	31.06	$[90_{16}]$	31.02

Table 9.3 shows how for a N_y/N_x value of 0.125 the optimal design was found to be a laminate with all 45° and -45° plies. As the value of N_y was increased, then there was a stage between $N_y/N_x = 0.125$ and $N_y/N_x = 0.15$ where 90° plies started to emerge. As the biaxial loading ratio increased further, the number and position of the 90° plies in the stacking sequence changed, and the critical buckling load was progressively reduced. For $N_y/N_x = 0.5$ for example, there were four 90° plies in the laminate half lay-up. This number continued to increase, as is evident in the results for $1.0 \leq N_y/N_x \leq 2.4$ where more and more 90° plies were generated on the outside of the laminate. Eventually a loading condition was reached, corresponding to $N_y/N_x = 2.4$ where a subsequent increase in N_y led to the optimal laminate being all 90° as the loading in the y direction significantly "prevails" over the loading in the x direction. The same general observations could be made for the results obtained by Haftka and Walsh [134] using the branch-and-bound method. For a given loading case, the optimal design using the FE analyses and the branch-and-bound method contained the same number of 90° plies. The position of these and of the 45° and -45° plies however somewhat varied. This is because movement of the ±45° plies in the stacking sequence has a small effect on the buckling load of the plate. Values for the buckling loads are quite similar when comparing the two optimization methods, indicating that the FE analysis driven genetic algorithm is a viable optimization method for the problem considered. In general, even in instances when slightly different design were obtained by the two optimization processes, the performance of such designs was very similar. The general trend of the GA of converging to designs with a lower buckling load than those obtained by the branch and bound method could be attributed to the GA possibly converging to designs very close to the global optimum, as is evidenced by the designs generally having the same number of 45° and -45° plies but in possibly different locations.

9.5.2 Contiguous ply constraint

Having run the GA for a variety of load cases and assessed its capability in finding appropriate lay-ups to maximize the buckling load of the composite plate, an additional constraint was added into the problem specified by Equations 9.9-9.12. In composite laminates, if the number of contiguous plies in the same direction is large, then problems of matrix cracking may arise. In the optimization problem discussed above, nothing was done to limit the number of such contiguous plies. Considering the case of $N_y/N_x = 2.0$, the optimal stacking sequence for this load case was $[90_5,45,90,-45]_S$. The five 90° plies at the outer part of the laminate may be subject to matrix cracking. To prevent this, a further constraint was introduced into the problem formulation. The constraint penalized, again via a penalty parameter, those designs which contain four or more contiguous plies in the same direction. It must be noted that since half the laminate is considered, due to its symmetric lay-up, the constraint is also violated if the two plies closest to the plane of symmetry are in the same direction. As in the case of the other constraints, the penalty artificially reduced the particular laminates' buckling load in the *Constraints* function of Appendix C, hence resulting in them having a smaller fitness value and decreasing their chances of survival from generation to generation. The genetic algorithm was run with all parameters unchanged, for the case $N_y/N_x = 2.0$ with the addition of this constraint. Table 9.4 shows the results obtained.

Table 9.4: Optimal lay-up and critical buckling load for $N_y/N_x = 2.0$ with and without the constraint on the number of contiguous plies in the same direction.

$N_y/N_x = 2.0$	Optima Lay-up (BB)	λ_{cr} (BB)	Optimal Lay-up (GA)	λ_{cr} (GA)
No contiguous ply constraint	$[90_5,45,-45,90]_S$	36.84	$[90_5,45,90,-45]_S$	36.48
Contiguous ply constraint	$[90_4,45,90_2,-45]_S$	36.59	$[90_3,-45,45,90,45,-45)_S$	35.07

As it can be noted, adding the constraint split the group of six 90° plies. Three of the plies remained at the outer part of the laminate, and a -45° and 45° ply separated them from the other 90° ply, before a 45°/-45° ply pair adjacent to the plane of symmetry of the lay-up. The buckling load as a consequence of the constraint was only reduced by a small amount.

9.6 Conclusions

Genetic algorithms, mimicking biology in its process of evolution, offer an advantage over traditional optimization methods in that they have more of a chance of converging to a global optimal solution rather than potentially being trapped in local optima. This is because of the random aspect of genetic algorithms, where many solution points that have the potential of being close to the optima are considered, rather than converging straight to a potentially local optimum solution early on in the optimization process. Genetic algorithms require more objective function evaluations than traditional methods, but they do not require any derivative knowledge or other secondary information apart from the objective function itself. Furthermore their structure makes it possible to run them using parallel computation. This possibility was however unavailable from a computational point of view in the current research project.

The present work has shown how an evolutionary algorithm could be implemented in MATLAB to perform optimization of a laminate stacking sequence for maximum buckling load. The optimization problem was formulated in terms of an objective function and several constraints imposed. Integer design variables were used to represent the discrete values that the ply orientations may take. Function evaluations were conducted via FE analyses in ABAQUS, and the whole optimization routine was fully automated. The algorithm was able to find the optimal stacking sequence for a variety of biaxial load cases. It was also easily modifiable to accommodate other constraints such as a limit on the number of contiguous plies in the same direction in order to avoid potential matrix cracking problems. This optimization routine shows how ABAQUS can be linked to an optimization routine and forms the basis for the next chapter which utilizes this same GA to fulfil the main goal of this research work, that of developing and FE based optimization strategy for the optimization of a stiffened composite panel operating in its postbuckling regime. In this view, the current GA for the buckling load maximization can be viewed as a validation tool for the algorithm of Chapter 10.

Chapter 10

Optimization of an I-stiffened panel for damage resistance

A limitation of the optimization procedures discussed in Chapter 8 is that they do not account for failure mechanisms which may occur prior to overall buckling collapse or in-plane structural failure. Such mechanisms are primarily associated with delamination, particularly at the skin-stiffener interface which may lead to rapid degradation in structural integrity, as has been observed experimentally. This chapter describes how an optimization procedure accounting for such mechanisms was developed using all of the analysis tools that have been discussed in previous chapters.

The optimization procedure is applied to find a revised stacking sequence for the I-stiffened panel discussed in Chapter 4 and Chapter 7. The global FE model in Chapter 4 was able to model the panel's buckling and postbuckling behaviour including the effects of secondary instabilities resulting in sudden mode-jumps in the panel's postbuckling configuration. Chapter 7 showed how a local model of the same panel could be created and linked directly to the global model solution. This local model contained interface elements at the skin-stiffener interface able to capture the skin-stiffener debonding which resulted as the panel was loaded deeper into its postbuckling regime. In Chapter 9 a GA was used to optimise the stacking sequence of a plate for maximum buckling load. This chapter uses the same GA, coupled with the global and local FE models of the I-stiffened panel to optimise parts of its stacking sequence so as to increase its damage resistance in postbuckling. The optimization problem is formulated in a similar fashion to the plate buckling load optimization of Chapter 9, and then the results of two different optimizations are discussed, comparing the optimised and non-optimised panel designs. The term "non-optimised " will be used to refer to the original I-stiffened panel as first seen in Chapter 4, and refers to its non-optimised configuration purely in terms of the damage resistance optimization presented.

10.1 Problem Description

The optimization problem considered was that of optimizing the I-stiffened composite panel discussed in Chapter 4 and Chapter 7 for damage resistance in its postbuckling regime. The panel had a length of 850 mm and was 604 mm wide as shown in Figure 4.14. The stiffeners were secondary bonded onto the skin via the use of FM-300 adhesive, whilst the ends of the panel were machined flat and parallel after being potted in epoxy resin and fibreglass, reducing the effective span of the panel to 790 mm. Figure 4.15 shows the dimensions and lay-up of the I-stiffeners together with the ply drop-off scheme adopted in the stiffener flanges.

The objective was to develop an optimization procedure which would allow the panel to have an increased damage resistance in its postbuckling regime. The first step was to come up with a suitable model of the panel able to track its behaviour in the postbuckling regime. The conventional shell element FE model of Chapter 4 proved successful in doing this, and it was seen how both out-of-plane displacements and strains, as predicted by the numerical model, agreed well with those obtained experimentally by LVDTs and strain gauges respectively. In both its experimental testing and in the FE nonlinear analyses, the panel was seen to buckle into a five half-wave configuration. As the loading was increased, then the panel was seen to exhibit a sudden mode-jump to six half-waves in all of its skin bays. When this global model was linked to the local model containing interface elements, as described in detail in Chapter 7, the skin-stiffener interface rapidly degraded when the sudden mode-jump occurred. Before the mode-jump, degradation was only seen in elements directly below a buckle anti-node line. As the loading was increased, damage remained relatively localized in this region spreading outwards towards the flange edges. As the buckle crests relocated, so did the damage, spreading in the lengthwise direction in an abrupt fashion to "follow" the relocation of the anti-node lines.

The objective of the optimization was to minimize this growth of the damage at the skin-stiffener interface by tailoring the lay-up of various parts of the panel. The approach adopted was that of extending the GA described in Chapter 9 and linking it to the global-local ABAQUS models which were responsible for objective function evaluations in a similar way as the GA was linked to the simple plate FE model for eigenvalue buckling load evaluations in the previous chapter.

10.2 Finite element models and optimization routine

10.2.1 Global and local finite element models

During the optimization process each different design for the I-stiffened panel had to be evaluated, and the FE global-local models presented in Chapter 4 and Chapter 7 were used to do this. Both of these models have been discussed in detail as well as having been validated against experimental results and observations in previous chapters, and hence only a brief overview of the models and how they were linked together and with the optimization process is given here.

The global model of the I-stiffened panel contained 2,800 four-noded shell elements as shown in Figure 4.23 with local coordinate systems created on the panel so as to guarantee the correct stacking of the laminate plies as in the actual experimental panel. The material properties of Table 4.3 were assigned to the whole model, and flange drop-offs modelled via the use of shell offsets. Clamped boundary conditions on both ends of the panel were originally set, before one end was given a displacement compressive boundary condition to replicate the compressive experimental test. Side edges were kept free from any restraint. A linear eignevalue analysis of the model revealed the eigenvalues and mode shapes, which were then used as initial geometric imperfections in a nonlinear quasi-static analysis able to trace the whole buckling and postbuckling behaviour of the panel. A linear superposition of the first three buckle mode shapes with a maximum amplitude of 3% of the skin thickness was used.

The local model was a representative section of the I-stiffened panel allowing the investigation of the debonding at the skin-stiffener interface via the use of interface elements. It had a length of 197.5 mm and a width of 108.5 mm, so that relocation of node and anti-node lines during a mode-jump would occur within the local model boundaries. Standard brick elements were used in the local model, with planes of Gauss points representing individual plies set up within the brick elements. Three separate parts constituted the model, one for the stiffer, one for the skin, and one for the interface layer bonding the two together. The use of 3D elements made it possible to model details such as ply drop-offs, and similar to the global model, local coordinate systems allowed for the correct modelling of the ply orientations throughout the skin and stiffener. The skin and stiffener parts were tied to the bottom and top nodes respectively of the interface elements composing the skin-stiffener interface part using tie constraints. A bi-linear traction separation law was used for the interface elements coupled with a mixed mode damage initiation and propagation criterion as discussed in detail in Chapter 7. The global model solution drove the local model in the sense that the displacements at the nodes of the global model acted as boundary conditions for the local model using the shell-to-solid submodelling technique available in ABAQUS and discussed in Appendix B.

10.2.2 Linking the finite element models with the optimization procedure

The optimization problem was that of finding a revised stacking sequence for certain regions of the panel to minimize the damage at the skin-stiffener interface in the panel's postbuckling regime. A change in stacking sequence of the panel resulted in changes in both the global and local models. The stacking sequence of the panel was dictated by the optimization, and once a specific design was to be evaluated, a means of linking the global model, local model, and optimization procedure had to be found. The approach taken is shown graphically in Figure 10.1.

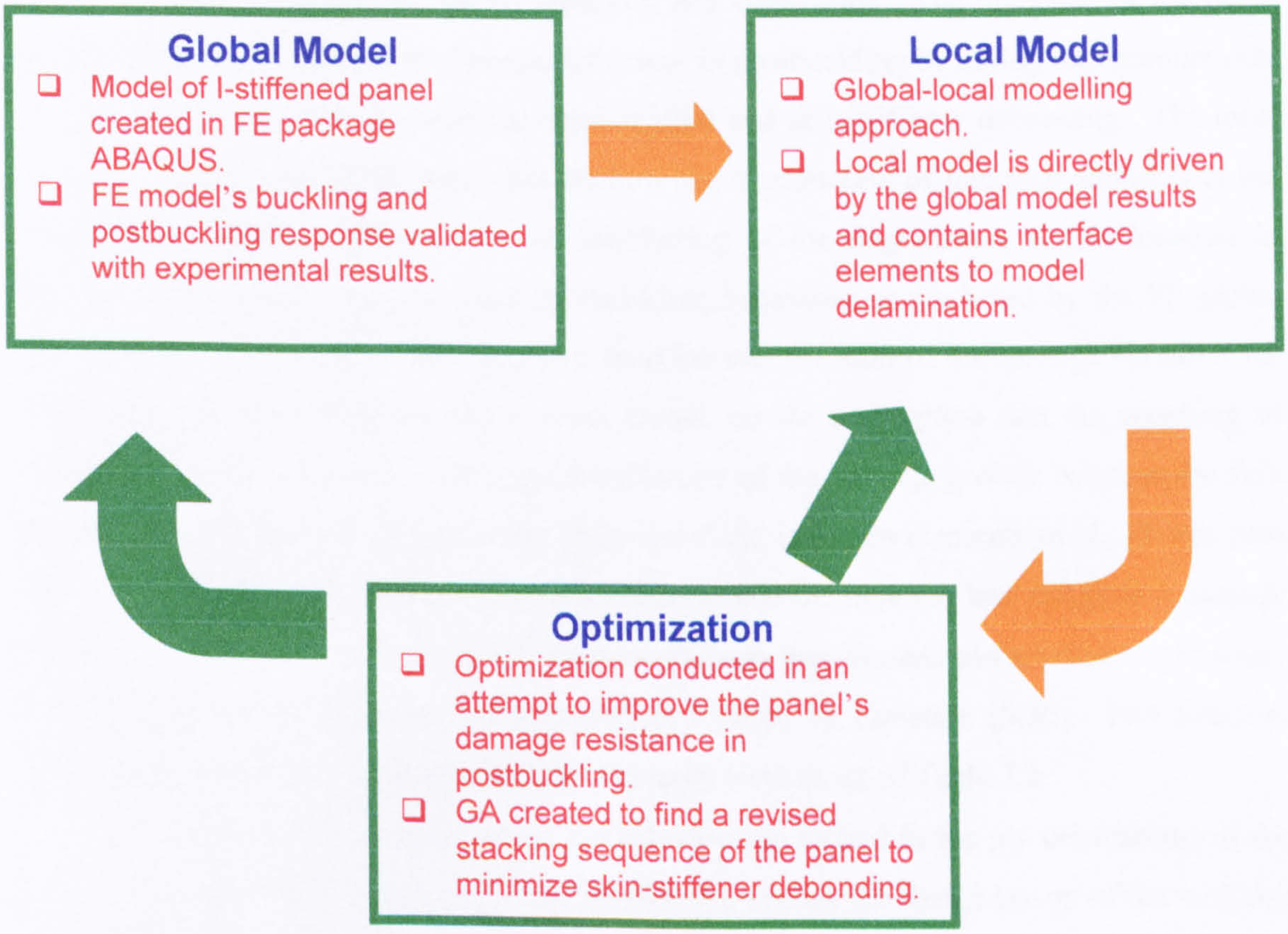

Figure 10.1: Diagram showing linking of global and local FE models with optimization algorithm.

Considering a given panel lay-up, changed as required by the optimization procedure, then this lay-up was automatically input into the FE global model. This allowed for evaluation of the panel's buckling and postbuckling response. This solution, together with the lay-up of the panel itself, was then an input to the local model which was able to track the damage at the skin-stiffener interface via the interface elements. An objective function based on a damage parameter was used in the optimization, and was automatically "read" by the optimization procedure from the ABAQUS output files, before moving on to a new design. The formulation of the optimization problem is discussed next.

10.3 Formulation of the optimization problem

10.3.1 Objective function, design variables, and constraints

In Chapter 8 the features of a general mathematical optimization were discussed, relating to objective function, design variables, and constraints. The objective of the panel optimization was to increase its damage resistance in postbuckling by taking into account out-of-plane damage mechanisms such as delamination and skin-stiffener debonding. The local FE model for the I-stiffened panel showed how the introduction of interface elements at the skin-stiffener interface allowed for the monitoring of the degradation at this location in response to the panel's buckling and postbuckling behaviour as predicted by the FE global model. A natural choice for the objective function was the sum of the damage variables for each of the interface elements in the local model, on the assumption that the summing of damage across the interface gives a good indication of the damage growth between the skin and stiffener. Chapter 5 discussed the features of the interface elements used. It was also seen how a bilinear mixed mode damage initiation and degradation law assigned a damage variable D which took a value of "0" when no damage was present and a value of "1" when complete stiffness degradation had occurred as dictated by Equation (5.30). The interface parameters used in the I-stiffened panel local model were those of Table 7.2.

The design variables available in the optimization related to the ply orientations of the panel. Two separate optimizations were considered, one on the flange lay-up of the stiffener and another on the lay-up of the panel skin. Ply orientations were allowed to take values of 0°, 45°, -45°, and 90°, commonly used in industry, transforming the optimization problem into a nonlinear integer programming problem. Modifying of the panel lay-up changes both its buckling and postbuckling behaviour. When this happened, then it was not just sufficient to minimize the extent of element degradation at the interface in order to increase the panel's damage resistance. The optimization could in fact come up with a design which did indeed show less damage at the skin-stiffener interface, but corresponded to a completely unrealistic design for a panel in the sense that it had a low buckling load or stiffness. Because of this two different constraints were imposed on the optimization. As was seen in Chapter 4, the I-stiffened panel FE model predicted the panel to have a buckling load of 125.2 kN and prebuckling stiffness of 140.9 kN. In the optimization, constraints were set penalizing those designs which had a buckling load or stiffness more than 10% lower than that of the original, non-optimised I-stiffened panel.

10.3.2 Panel flange and skin lay-up optimizations

Having defined the objective function, design variables, and constraints to be used, an optimization strategy to find the best stacking sequence in the I-stiffened panel flanges was formulated to increase the panel's damage resistance in postbuckling. The problem was defined as the minimization of the sum of the total damage in all of the interface elements at the skin-stiffener interface in the local FE model. The experimentally observed collapse load of 525 kN was used as the point at which the panel's damage resistance was to be improved as this seemed a good interpretation for the load level at which the panel was to be optimised for damage resistance. Figure 10.2 below shows the lay-up of the panel stiffener and skin. The way in which the panel was manufactured, meant that most of the plies in the flanges continued into the stiffener web and cap. This is visible in the C-scan images of the stiffener flange at the web end and of the stiffener web in Figure 4.16 (a) and (b) respectively. Therefore changes in the flange plies, whose orientation is being optimised also lead to changes in the lay-up of other portions of the stiffener. Such plies are highlighted in red in Figure 10.2.

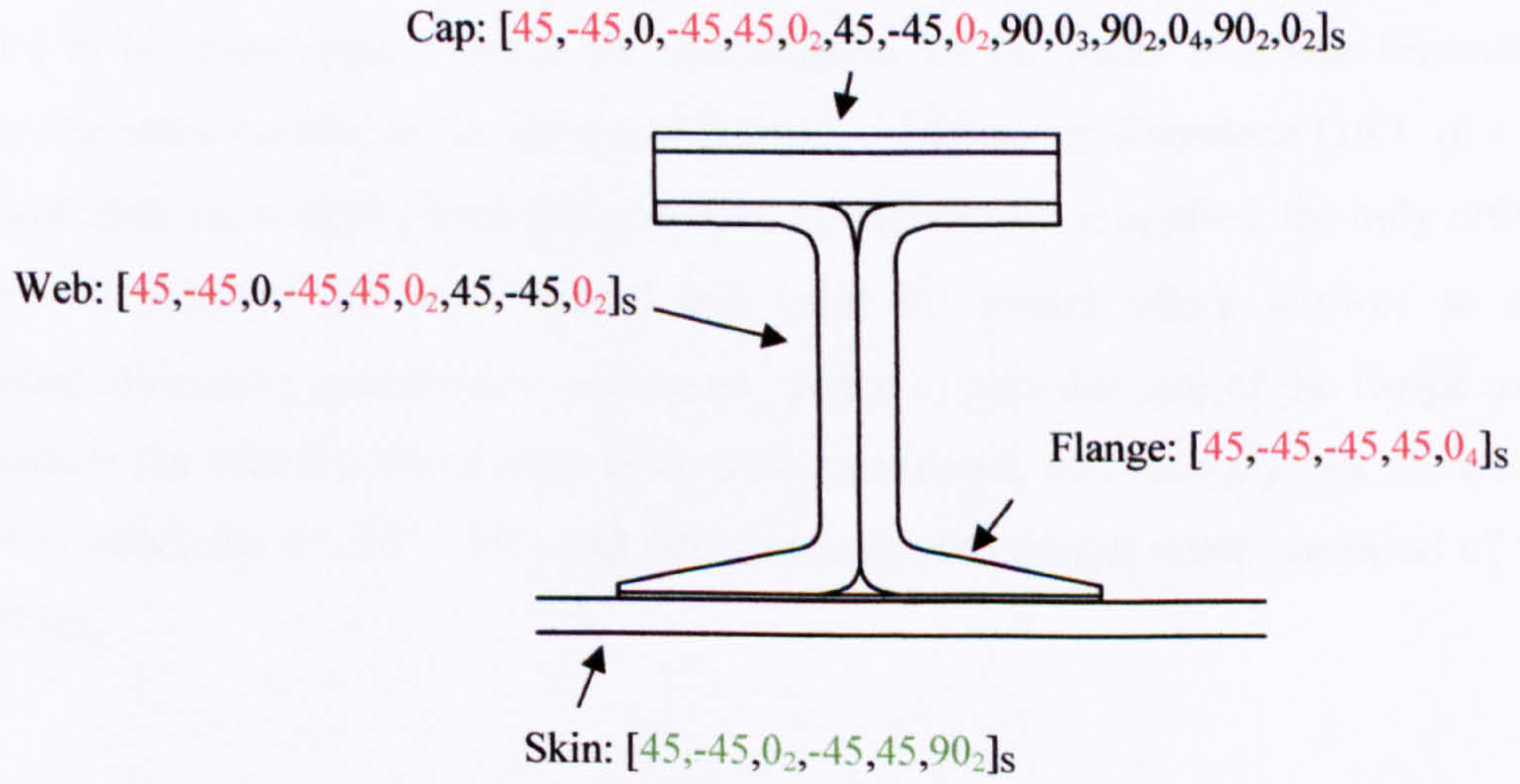

Figure 10.2: I-stiffened panel lay-up showing plies in flange lay-up (red) and skin lay-up (green) optimizations.

The formulation problem was formulated in exactly the same fashion as in the optimization of the plate stacking sequence for buckling load maximization of Chapter 9. Using ply-identity variables, which assume a value of 1 when a specific ply is oriented in that direction and a value of 0 otherwise, the optimization problem was formulated mathematically as:

Find o_i, n_i, f_i^p, f_i^m for $i=1,\ldots,8$ (10.1)

To **minimize** $\sum_{j=1}^{elements} D$ (10.2)

Such that: $o_i + n_i + f_i^p + f_i^m = 1$ for $i = 1,\ldots,8$ *(ply ident. constraint)* (10.3)

and $\lambda_{cr} \geq 112.7\,\text{kN}$ *(buckling load constraint)* (10.4)

and $\lambda_{cr}/\delta_{cr} \geq 171.3\,\text{kN}$ *(prebuckling stiffness constraint)* (10.5)

Elements is the total number of interface in the local FE model whose damage variable D needs to be summed in order to obtain the objective function. λ_{cr} is the buckling load of the design being evaluated, whilst δ_{cr} is the applied end displacement on the panel at which this buckling occurs. The values 112.7 kN and 171.3 kN correspond to the constraints on the buckling load and prebuckling stiffness, which must not be more than 10% lower than the buckling load and prebuckling stiffness values of 125.2 kN and 140.9 kN of the non-optimised panel.

A second separate optimization was run on the lay-up of the panel skin. In Figure 10.2 the plies whose orientations could be altered during the optimization process are highlighted in green. It is noticed that the symmetric panel skin contained a total of sixteen plies, meaning that the orientation of eight plies may be optimised for in order for the symmetry constraint to be maintained. Hence the optimization for the panel skin was formulated in precisely the same manner as for the panel flanges, as shown by Equations (10.1-10.4). The same constraints on buckling load and prebuckling stiffness were applied, the only difference being which plies of the panel global and local FE model where allowed to change orientations during the optimization procedure. Since in both the case of the flange and skin optimizations the orientations of eight plies were considered, and each ply was allowed to be oriented in either the 0°, 45°, -45°, and 90° directions, the design space consisted of 65,536 possibilities.

10.3.3 Optimization algorithm

The optimization problem of Equations (10.2-10.5) was solved by constructing a GA in MATLAB as was done in Chapter 9 for the buckling load optimization of a composite plate. The mechanics of the genetic algorithm including its genetic operations were very similar to those of Chapter 9, but modifications to the code had to be made in order to correctly link the GA to both the global and local FE models of the panel and modify such models to reflect changes in the lay-up of the panel as dictated by the genetic optimiser. Figure 10.3 shows a flowchart of the GA developed for both the skin and flange lay-up optimizations of the I-stiffened panel. This is a similar algorithm to that used in Chapter 9 and shown in Figure 9.4, the main difference being in the grey boxes relating to the function evaluations, which now required the degradation in the interface elements at the skin-stiffener interface of the local model rather than simply the buckling load of a plate. The complete GA code is shown in Appendix D. The MATLAB code named *GA* is the actual optimization code, which then linked to a function named *Abaqus_analyses* responsible for the link of the GA with ABAQUS and the objective function evaluations. Another function – *Convert* – was used to convert the chromosome strings from the integer ply-identity variables to the actual ply orientations, whiles the constraints on buckling load and prebuckling stiffness were handled directly within the *Abaqus_analyses* function. In the next section the GA code will be explained, concentrating on the new aspects relative to the code used in the buckling load optimization. In Appendix D a number coding system is used to cross-reference sections in the code of the MATLAB script *GA* and a letter coding system for sections of the *Abaqus_analyses* function with the explanations of the next section.

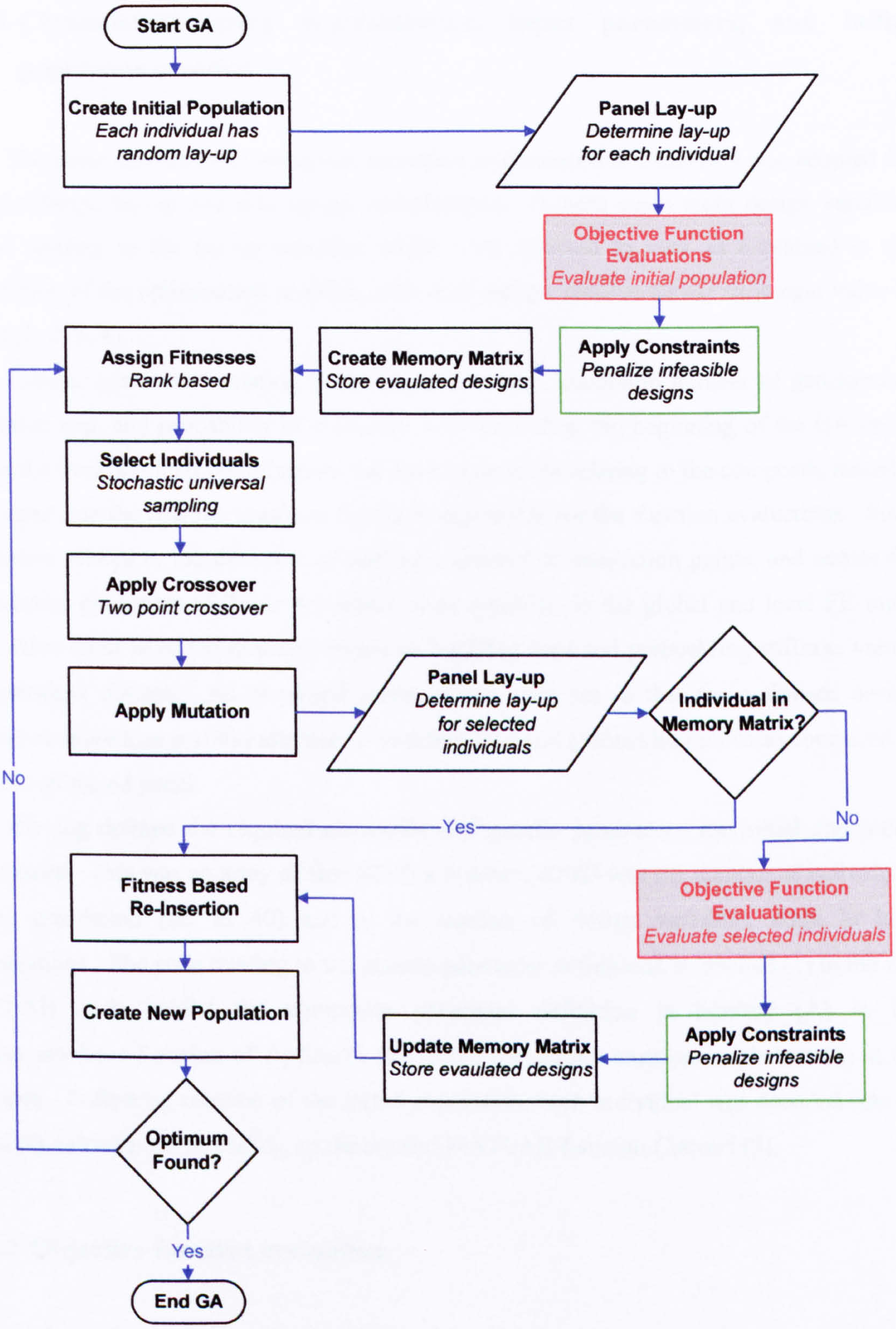

Figure 10.3: Flowchart of developed GA for optimization of I-stiffened composite panel for damage resistance.

10.4 The genetic algorithm

10.4.1 Chromosome string representation, input parameters, and initial population creation

The same chromosome string representation as discussed in Chapter 9 was adopted for both the flange lay-up and skin lay-up optimizations. In both cases eight design variables existed relating to the lay-up variables which were allowed to vary as explained in the formulation of the optimization problem, with each design variable taking an integer value in the set (1, 2, 3, 4).

Genetic parameters relating to the population size, maximum number of generations, generation gap, and probability of crossover were entered at the beginning of the GA code. Unlike the buckling load optimization, the input parameters relating to the composite material were input into the *Abaqus_analyses* function responsible for the function evaluations. Such parameters related to the thickness of each ply, number of integration points, and names for the material properties of Table 4.3 which were specified in the global and local FE input files. Also input were the required minimum buckling load and prebuckling stiffness values for optimised designs. As discussed earlier, these were set so that the optimised design showed no more than a 10% reduction in buckling load and prebuckling stiffness compared to the non-optimised panel.

Having defined the required composite and genetic parameters, the initial population was created. This was an array of size *NIND* x *N* where *NIND* was the number of individuals in the population (set as 40) and *N* the number of design variables, eight in both optimizations. The code relating to the genetic parameter definitions is labelled (1) in the GA MATLAB code, whilst the composite parameter definition is labelled (A) in the *Abaqus_analyses* function of Appendix D. Initial population creation is labelled (2) in the GA code. Following creation of the initial population, each individual was decoded into its actual ply orientations by calling up the created MATLAB function *Convert* (3).

10.4.2 Objective function evaluation

Following the creation of the initial population and the conversion of each individual into actual ply orientations, this population was evaluated in terms of its objective function. This was the main challenge in the creation of the optimization procedure since the objective function was now the skin-stiffener debonding at the skin-stiffener interface of the local model as measured by the sum of the damage variable in the interface elements. In Figure

10.2 relating to the GA flowchart, function evaluations are denoted by the grey box with the red border. Figure 10.4 is another flowchart showing exactly how the function evaluations are conducted in the *Abaqus_analyses* function found in Appendix D (4). The process shown graphically by the flowchart is described below.

Following the definition of the various composite parameters required (A), the panel lay-up was defined. Parts of the panel's lay-up did not change during the optimization process, whilst others were dictated by the design variables which were being optimised for. The code in Appendix D relates to the skin lay-up optimization rather than the flange lay-up optimization. Hence variables describing the lay-up of the panel stiffeners which do not change during the optimization were created, relating to the stiffener flanges, cap, and web (B). Following this, the design variables of the individual being evaluated were decoded so that they defined the lay-up of the skin part of the I-stiffened panel (C). Having done this, text files were created for each component of the lay-up that was required by the ABAQUS input files of both the local and local FE models (D). Whenever an ABAQUS analysis was run, these text files replaced the lines in the input files relating to the lay-up of the panel so that different panel lay-ups could be evaluated. For the case of the flange optimization, the design variables were simply used in the creation of the flange text files rather than the skin. In this case the web and cap lay-up text files also needed to be modified since as mentioned earlier plies in the flanges are continued into the web and cap due to the way the I-stiffened panel was manufactured. Most of the code script in *Abaqus_analyses* is devoted to this text file creation.

Having created the files required for the correct modelling of the panel lay-up, the global model was run for the specific individual (E). A linear eigenvalue analysis was used to determine the buckling load of the panel and its buckle mode shapes as well as the prebuckling stiffness since both the buckling load and displacement were found via the FE analysis. The mode shapes were then used as geometric imperfections for the non-linear analysis to trace the panel design's buckling and postbuckling behaviour (F). For visualization purposes, the load displacement curve for each design was plotted in MATLAB after each evaluation (G). This showed just how the change in lay-up in each design changed the response of the panel. The points used to plot the load-displacement curve were also saved in a text file in case they were required for future reference (H).

The whole postbuckling response of the panel having been obtained, the local model was run using the global model solution in order to obtain the degradation in the interface elements at the skin-stiffener interface as already discussed in Chapter 7 (I). The damage variable D in each element was summed so as to obtain the objective function of each individual to be used as the objective function in the optimization procedure (J). The only remaining step was to apply the constraints on the buckling load and prebuckling stiffness, and designs violating these constraints were penalized by adding a value of 100 to the objective function (K). This "fooled" the GA into thinking that infeasible individuals had a higher damage than feasible designs and hence made them less likely to be bred into future generations. Interface damage values for the population being evaluated were then fed back to the GA which used the objective function for the subsequent genetic operations just as was done in Chapter 9.

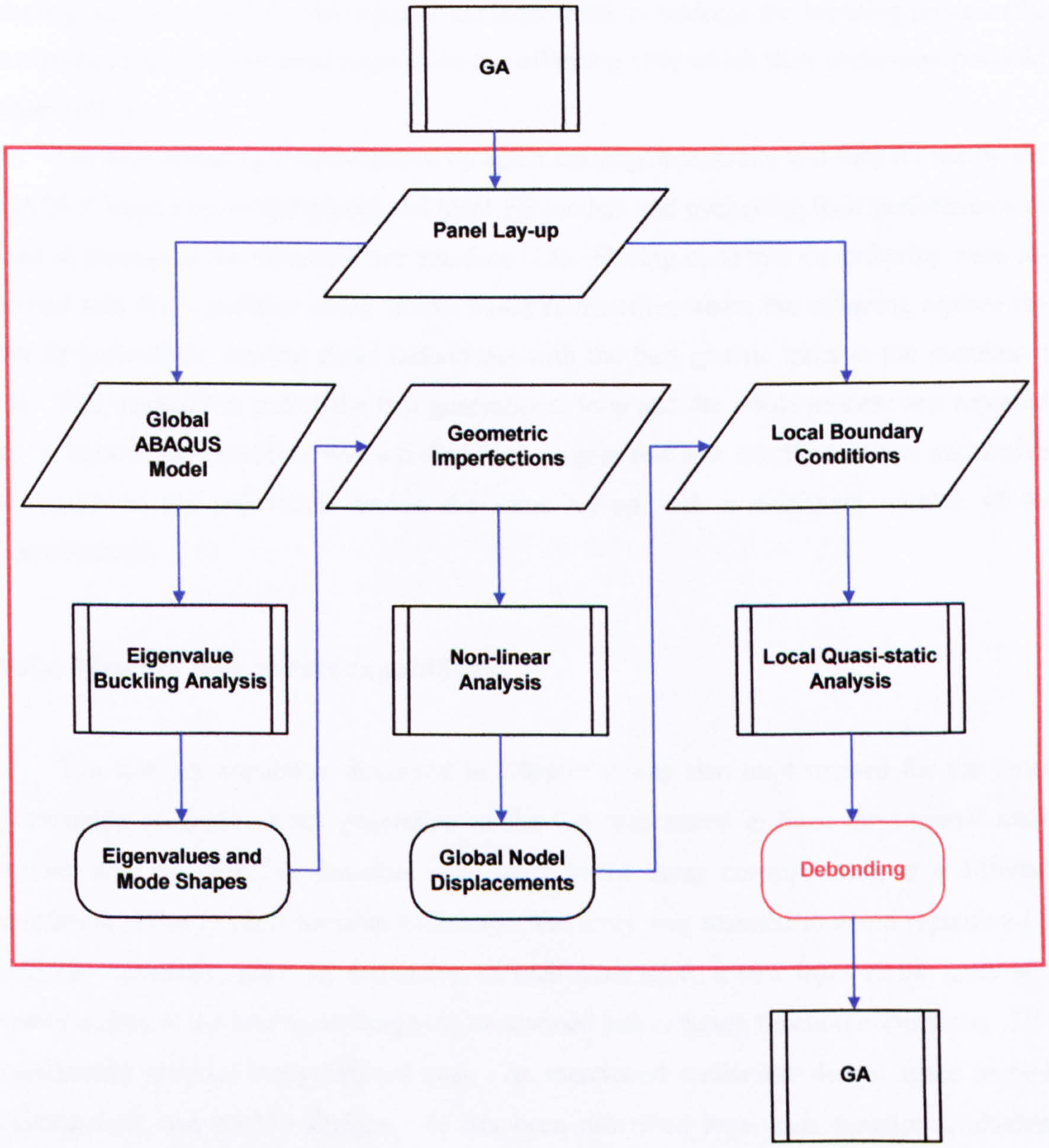

Figure 10.4: Flowchart showing interaction of the GA with the global model eigenvalue and non-linear analyses and local model skin-stiffener debonding analysis.

10.4.3 Genetic operators

Following evaluation of the initial population relative to the damage resistance of the various panel lay-ups, the classic genetic operators were applied as shown in the GA flowchart of Figure 10.2 and labelled in the *GA* code of Appendix D. This was done after initiation of the generational loop (5). A generalised rank-based fitness scheme was used to assign fitness values (8) to all the individuals in the population. This meant ranking all individuals in terms of their skin-stiffener interface damage, and assigning a fitness value of 2 to the individual with the least damage, and a value of 0 to the one with the most damage. All other individuals were linearly assigned fitness value in the 0-2 range. Stochastic universal sampling was then used for selection of the individuals to undergo the breeding process (9). Two-point crossover was used to produce the offspring (10) which then underwent possible mutation (11).

The new offspring were evaluated by again creating appropriate text files for use by the ABAQUS input files of the global and local FE models and evaluating their performance in terms of damage at the skin-stiffener interface (12). Having done this the offspring were re-inserted into the population using fitness based re-insertion where the offspring replace the least fit individuals, leaving those individuals with the best genetic traits in the population (13). This marked the end of the first generational loop and the whole process was repeated until a termination condition was satisfied (14). Again this was specified as five successive individuals in the population having the same lay-up with a maximum number of 40 generations set.

10.4.4 Memory and restart capabilities

The memory capability discussed in Chapter 9 was also implemented for the panel optimization code (6). Each generation of the GA was stored in three dimensional array together with its objective function, each layer in the array corresponding to a different generation. Prior to each function evaluation, the array was scanned to avoid repetitive FE analyses. Similarly, after the evaluation of each generation, a new layer in the array was created adding to the evaluated designs to be scanned before future function evaluations. This considerably reduced computational cost. As mentioned earlier the design space in both optimizations was 65,536 designs. It has been described how each function evaluation required a linear eigenvalue analysis of the global FE model, a non-linear analysis of the global FE model, and a quasi-static analysis of the local model containing the interface elements. In the description of these models in previous chapters great emphasis was placed on making the FE analyses as computationally cheap as possible, achievable by the use of the global-local modelling approach. Nonetheless the need for repetitive function evaluations meant that the optimization took about 80 hours when run on a standard 2.4 GHz PC. It will be seen later how, for example, the flange lay-up optimization took 16 generations to converge. With the population size of 40 used, this would mean 640 different function evaluations, but the addition of the memory capability reduced the computational cost of the optimization by 59.1% to just 262 function evaluations. The absence of the memory capability would have meant the same optimization routine taking about 195 hours to converge. Even with the addition of the memory capability, the computational cost of the optimizations would greatly decrease with the use of parallel computing or a more powerful processor able to handle the FE analyses more efficiently.

To avoid loss of data due to an unexpected termination of the code, a restart capability was added so that the code could restart after a specific generation (7). This also made it possible to run the code for a couple of generations, interrupt it, and then continue it at a later time. This restart capability was achieved by saving genetic strings, objective functions, and generation numbers into text files and giving the user the choice of starting the optimization from a new random base population or restarting from these saved text files.

10.5 Flange lay-up optimization results

10.5.1 Genetic algorithm convergence and optimum flange lay-up

The GA for the optimization of the I-stiffened panel's flange lay-up showed convergent results subject to the termination criterion previously discussed after 16 generations. The optimal flange lay-up was found to be $[90,45,0_2,-45,0,90,-45]$. Because of the fashion in which the panel was manufactured, relating as to how plies originating in the stiffener flanges continued into the stiffener web and cap (as shown by the red plies in Figure 10.2), the optimal lay-up of the rest of the panel is detailed in Table 10.

Table 10.1: Lay-up of optimised flange lay-up design.

	Lay-up
Flange	$[90,45,0_2,-45,0,90,-45]$
Web	$[90,45,0_3,-45,0,45,-45,90,-45]_S$
Cap	$[90,-45,0_3,-45,0,45,-45,90,-45,90,0_3,90_2,0_4,90_2,0_2]_S$
Skin	$[45,-45,0_2,-45,45,90_2]_S$

The convergence of the GA was investigated and the results shown in Figure 10.5, which shows a plot of the average objective function in each generation of the GA plotted against the generation number. The average objective function is normalized against that of the optimal individual. In the first generation, or base population, all individuals are completely random, and as expected the normalized average objective function of the individuals in the population is high as many of them violate the constraints. As the GA is left to evolve, the most desirable genetic traits begin to "spread" in the population via the genetic operators, lowering the normalized average objective function. It can be noted that there are instances where the normalized average objective function actually increases with increasing generation number. This is due to the GA considering new designs, hence exploring new areas of the design space. Such new designs may violate the constraints, hence increasing the average objective function of the whole population. After convergence some individuals violating the constraints and far form the optimum still existed in the population and hence the average normalized objective function is not quite as low as one.

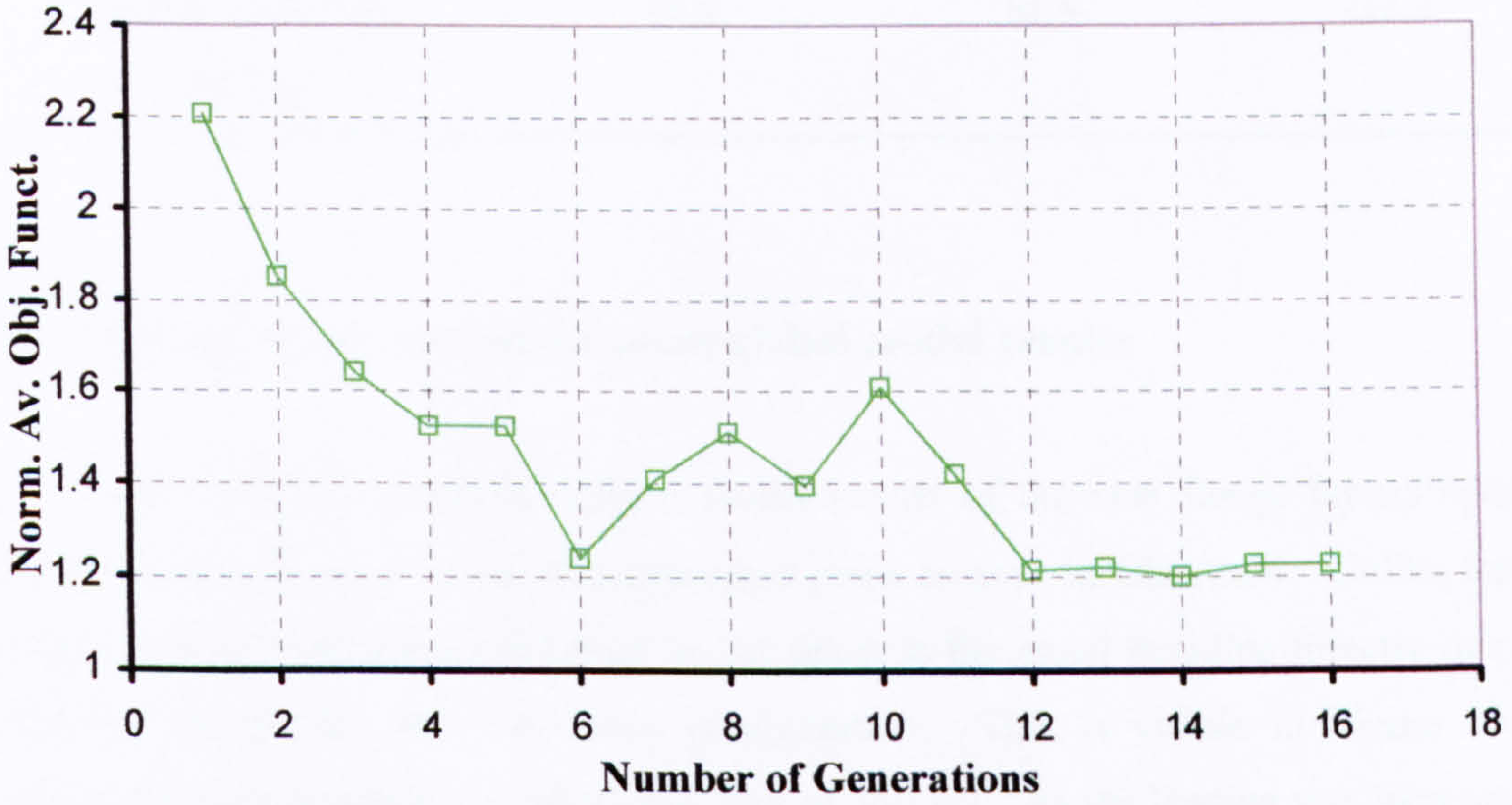

Figure 10.5: Reduction of average normalized objective function with increasing GA generations for flange lay-up optimization.

The ABAQUS buckling analysis gave a buckling load for the optimised flange lay-up design of 124.9 kN, almost identical to 125.2 kN of the non-optimised panel. The prebuckling stiffness and postbuckling stiffness of the new panel configuration were 181.0 kN and 142.8 kN respectively. These corresponded to a 4.9% and 9.1% reduction in the respective stiffness values, showing how the GA was able to find an optimised flange lay-up within the specified constraints. At the experimental collapse load of 525 kN of the experimental, non-optimised panel for which the optimization was conducted, the decrease in the total skin-stiffener interface element damage as predicted by the FE local model was reduced by 12.7% when comparing the new flange lay-up optimised configuration with the non-optimised I-stiffened panel. The results just discussed are compared in Table 10.2, whilst a comparison of the buckling and postbuckling behaviour as found by the FE global model and of the damage growth in the skin-stiffener interface as modelled by the FE local model is done in the next sections.

Table 10.2: Comparison of optimised and non-optimised flange lay-up panel designs.

	Non-optimised	Optimised	% Diff.
Flange Lay-up	$[45,-45,-45,45,0_4]_S$	$[90,45,0_2,-45,0,90,-45]_S$	
Buckling Load (kN)	125.2	124.9	-0.2
Prebuckling Stiffness (kN/mm)	190.3	181.0	-4.9
Postbuckling Stiffness (kN/mm)	157.1	142.8	-9.1
Interface Element Damage	93.8	81.9	-12.7

10.5.2 Flange lay-up optimised panel global model results

Figure 10.6 compares the global model results of the new flange lay-up optimised configuration with those of the non-optimised panel as seen in Chapter 4. Unlike the non-optimised panel, the optimised flange lay-up leads to the panel buckling directly into a six half-wave rather than five half-wave configuration. This is visible in Figure 10.6 (a) corresponding to an applied compressive load of 160 kN. As the loading was increased, the buckle crests deepened but the panel remained in the six half-wave configuration. The non-optimised panel exhibited the mode-jump to the six-half-wave configuration at a loading of 262 kN, meaning that at 265 kN and 500 kN loading the two panels showed very similar behaviour as evidenced by Figure 10.6 (b) and Figure 10.6 (c). The optimised flange lay-up panel exhibited a further mode-jump in all skin-bays to a seven half-wave configuration at a loading of 680 kN and remained in such a postbuckled state until the high loading of 800 kN of Figure 10.6 (d). At this loading the non-optimised panel also displayed a seven half-wave configuration albeit with a slightly different appearance with some of its buckle crests being elongated.

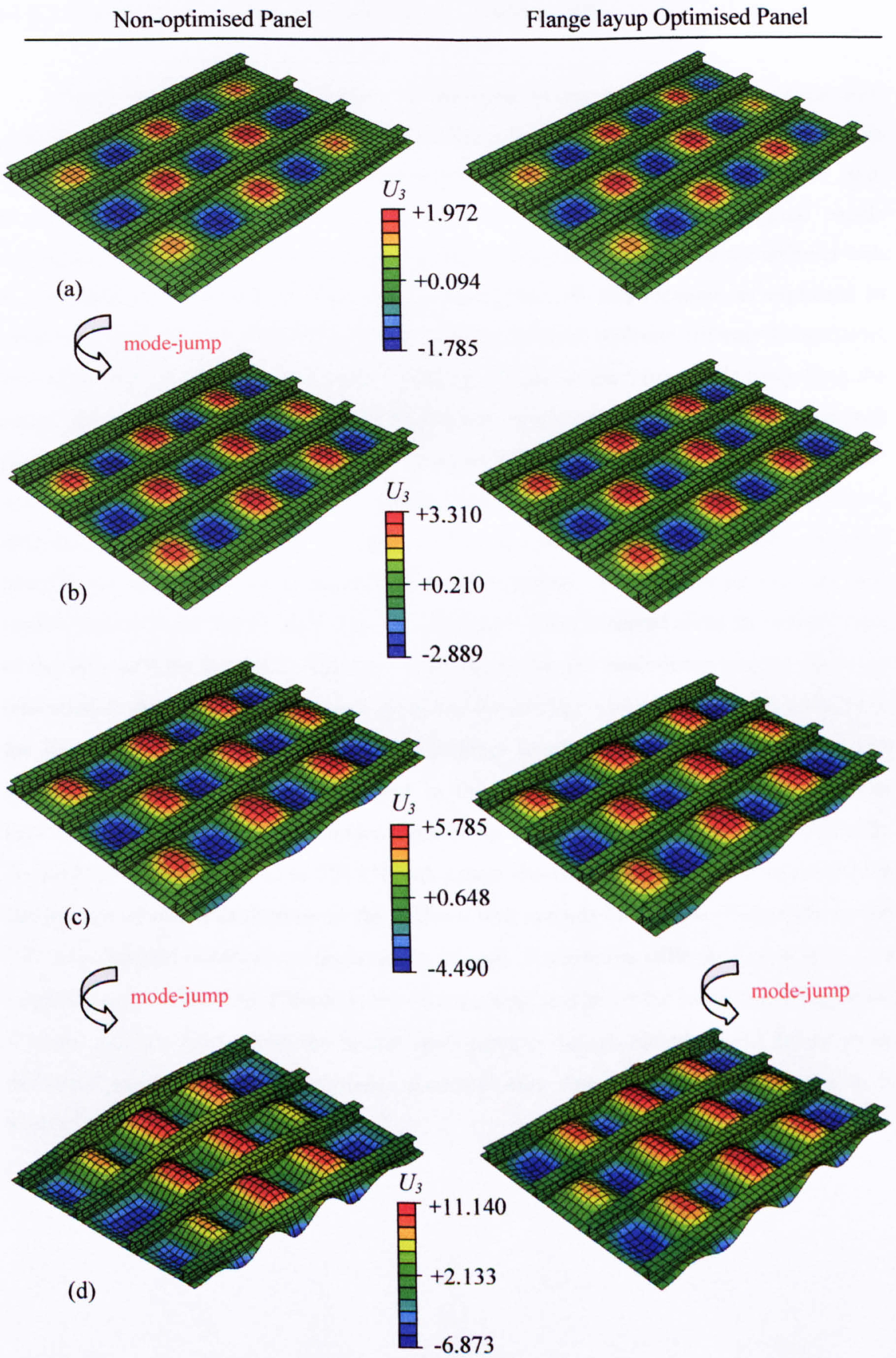

Figure 10.6: Numerical analysis deformed shape (scale factor five) and out-of-plane displacement contour plots for non-optimised I-stiffened panel and flange lay-up optimised I-stiffened panel global models at loading: (a) 160 kN, (b) 265 kN, (c) 500 kN, (d) 800 kN.

10.5.3 Flange lay-up optimised panel local model results

Figure 10.7 shows a comparison of the local model results for the original non-optimised panel of Chapter 7 and the optimum flange lay-up panel as found by the GA. Both local models were directly driven by their respective global model solutions of Figure 10.6. in Figure 10.7 (a) for 160 kN load, in both the optimised and non-optimised panels degradation of the interface elements was limited to a location directly under the stiffener web at a position corresponding to a buckle anti-node line. At this location, as explained in Chapter 5, there was a moment transfer between the stiffener web and stiffener flange/panel skin at the foot of the web. This acted to pull the flange on the tension side away from the panel skin hence promoting debonding in the non-optimised and flange lay-up optimised panels. The different buckling configurations (six half-wave against five half-wave for the optimised and non-optimised panels) meant that stiffness degradation was occurring at different locations in the panels. In Figure 10.7 (b) at a loading of 260 kN the non-optimised panel had mode-jumped to the six half-wave configuration. The deformation of both local models is similar, but the damage in the non-optimised panel is spread along the whole length of the skin-stiffener interface. The reason for this is that the mode-jump brought about the relocation of the anti-node lines hence spreading the damage – which had already initiated in the five half-wave configuration – in the stiffener length direction. The panel with the optimised flange lay-up however stayed in the same six half-wave configuration after buckling, and hence avoided the sudden mode-jump which caused the abrupt debond growth. As the loading was increased to 500 kN both panels showed deepening buckle crests and the damage spread outwards form under the stiffener web towards the flanges. This again agreed with experimental observations discussed in Chapter 5 where the stiffener flange acted as a step change in the bending stiffness to the skin moment, and hence the latter tended to pull the skin and stiffener apart. After the further mode-jump in the non-optimised and flange lay-up optimised panels the two skin-stiffener interface were almost completely debonded as is visible in Figure 10.7 (d).

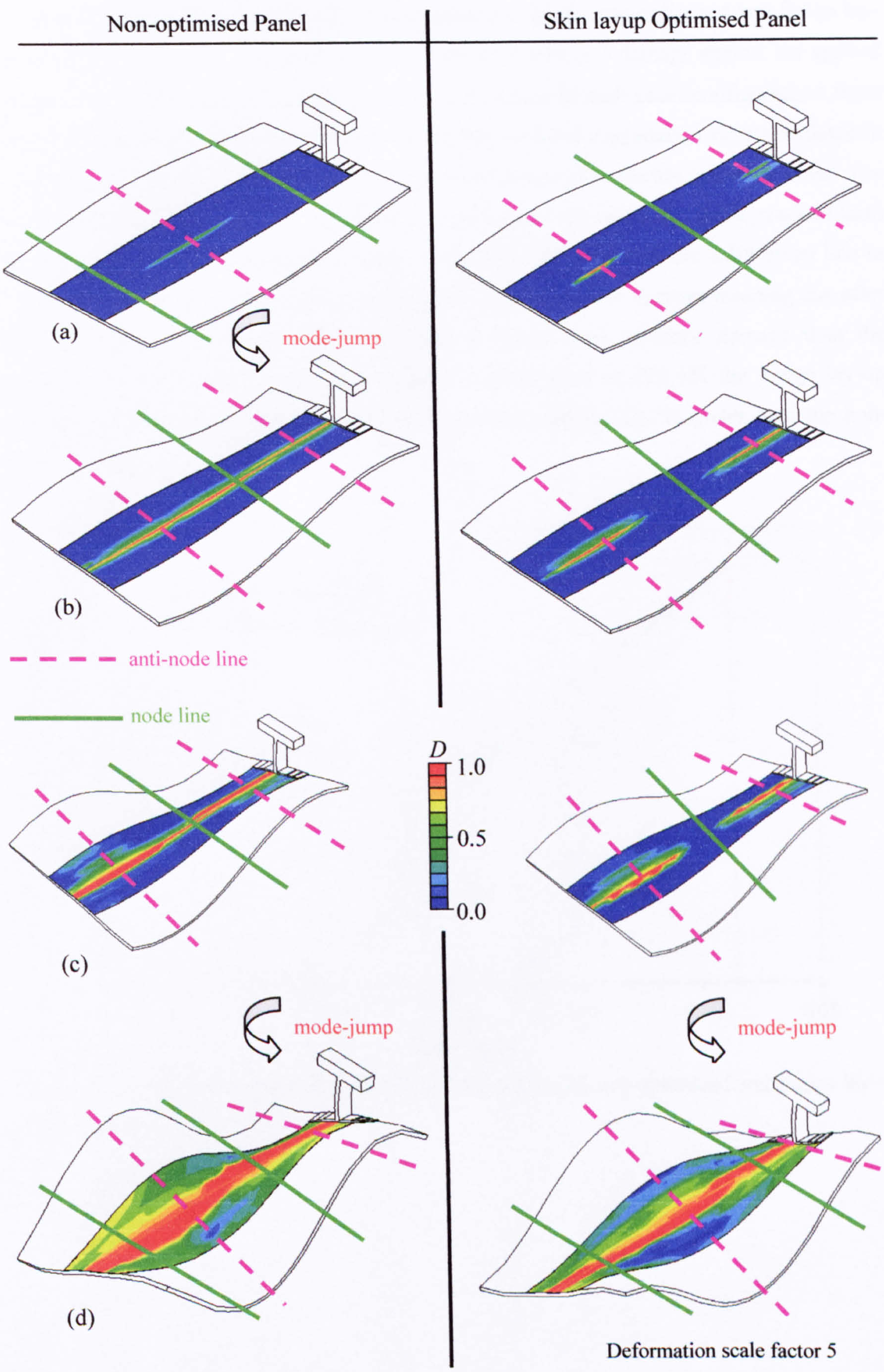

Figure 10.7: Interface element damage at local model skin-stiffener interface comparison for non-optimised and flange lay-up optimised panels at loading: (a) 160 kN, (b) 265 kN, (c) 500 kN, (d) 800 kN.

The growth of the debond at the skin stiffener interface for the non-optimised and flange lay-up optimised panel was compared by plotting the total interface damage against the applied compressive load as shown in Figure 10.8. It is clear how in both panel configurations there was no damage until about 150 kN. At this loading stiffness degradation slowly initiated in those elements directly under the stiffener web at positions of the buckle anti-node lines. The total interface damage was very similar in non-optimised and optimised configurations until the mode jump in the non-optimised panel at 262 kN. As shown by the solid green line in Figure 10.8, the mode-jump suddenly increased the total interface damage meaning that after the mode-jump the non-optimised panel had a higher total interface damage than the optimised configuration. At the experimental collapse load of 525 kN the flange lay-up optimised configuration showed a total skin interface damage 12.7% lower than the non-optimised panel.

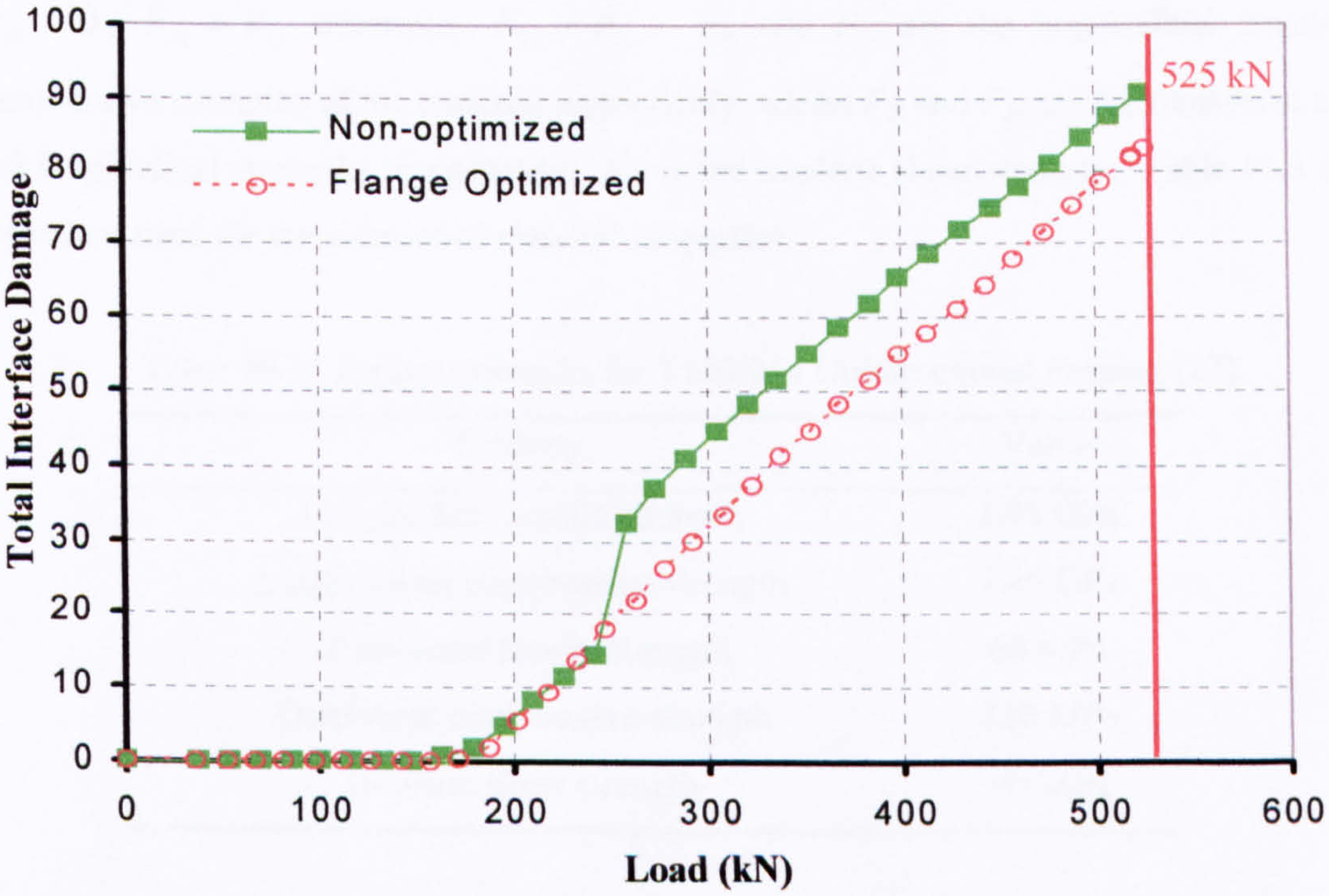

Figure 10.8: Comparison of skin-stiffener debond growth in non-optimised and flange lay-up optimised panels.

10.5.4 Local ply failures

The Tsai-Hill criterion was adopted to check whether the optimised flange layup panel had any local ply failures at the 525 kN load at which the optimization was conducted. This was done by activating the Tsai-Hill failure index capability for the flange layup optimised panel global model in ABAQUS [39]. The Tsai-Hill failure index predicts that local failure happen in the material if the failure index I_F exceeds a value of 1.0 where I_F is given by Equation (10.6):

$$\text{Find } I_F = \frac{\sigma_{11}^2}{F_{11}^2} + \frac{\sigma_{22}^2}{F_{11}^2} - \frac{\sigma_{11}\sigma_{22}}{F_{11}^2} + \frac{\sigma_{12}^2}{F_{12}^2} \qquad (10.6)$$

In Equation (10.6) σ_{11} and σ_{22} are the stress components along the principal material directions and σ_{12} is the shear stress. If $\sigma_{11} > 0$, $F_{11} = F_{1t}$ otherwise $F_{11} = F_{1c}$. If $\sigma_{22} > 0$, $F_{22} = F_{2t}$ otherwise $F_{22} = F_{2c}$. F_{1t} and F_{1c} are the longitudinal tensile and compressive strengths of the material respectively, whilst F_{2t} and F_{2c} are the transverse tensile and longitudinal strengths respectively. F_{12} is the in-plane shear strength. Table 10.3 shows the values used for the mentioned material properties.

Table 10.3: Failure strengths for T300/914 Unidirectional Prepreg [23].

Property	Value
Longitudinal tensile strength	1.95 GPa
Longitudinal compressive strength	1.45 GPa
Transverse tensile strength	60 MPa
Transverse compressive strength	210 MPa
In-plane shear strength	90 MPa

Figure 10.9 shows a contour plot of the Tsai-Hill failure index I_F. A value of 1, corresponding to a contour of red means that the failure index has exceeded a value of 1 and ply failure has occurred. As is visible from Figure 10.9, this did not occur at the loading of 525 kN for which the panel was optimised, meaning that the panel was able to operate in its postbuckling regime up to this loading without any local failure. The investigation also showed how damage at the skin-stiffener interface as modelled by the interface elements occurred before any local ply failures.

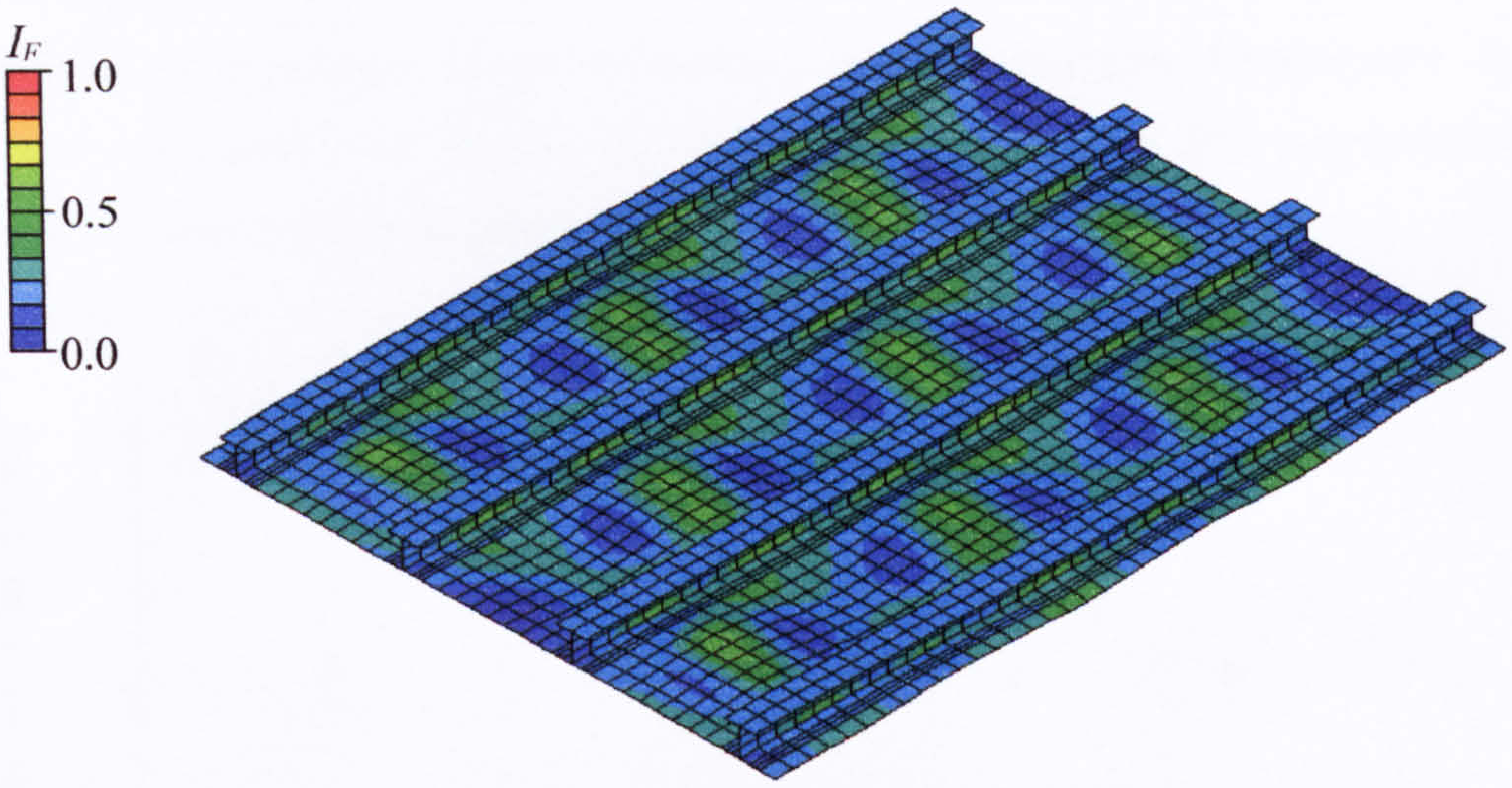

Figure 10.9: Tsai-Hill failure criterion for I-stiffened flange layup optimised configuration at 525 KN load.

10.6 Skin lay-up optimization results

10.6.1 Genetic algorithm convergence and optimum skin lay-up

Running of the GA to find an optimum skin lay-up led to conversion after 19 generations. The optimal skin lay-up was found to be $[-45,45,0,45,-45,90,-45,45]_S$. Table 10.4 shows the optimised panel lay-up. Since only the skin was optimised the stiffener has the same lay-up as the non-optimised I-stiffened panel.

Table 10.4: Lay-up of optimised skin lay-up design.

	Lay-up
Flange	$[45,-45,-45,45, 0_4]$
Web	$[45,-45,0,-45,45,0_2,45,-45,0_2]_S$
Cap	$[45,-45,0,-45,45,0_2,45,$ $-45,0_2,90,0_3,90_2,0_4,90_2,0_2]_S$
Skin	$[-45,45,0,45,-45,90,-45,45]_S$

Figure 10.10 shows a graph of the normalized average objective function against the number of generations. It is evident that the normalized average objective function again decreased as the population of the GA evolved from generation to generation. The initial population contained many individuals far from the optimum and hence the objective function corresponding to the skin-stiffener interface damage was high. Once convergence occurred,

the average normalised objective function was not as low as 1.0 since some individuals still existed in the population which had damage values higher than the optimum and possibly violated constraints even though the termination condition of five successive individuals having the same lay-up was achieved.

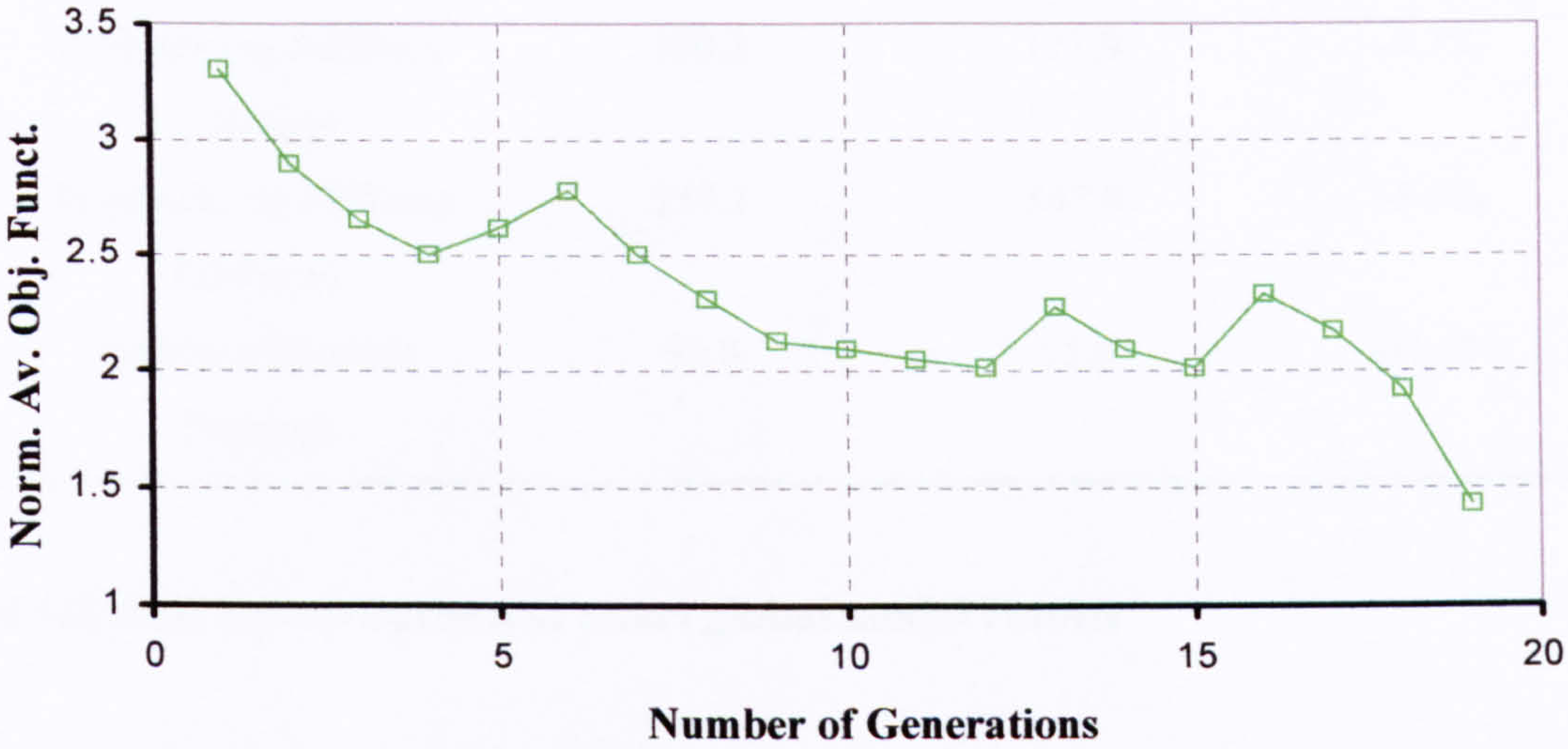

Figure 10.10: Reduction of average normalized objective function with increasing GA generations for skin lay-up optimization.

Table 10.5 compares the performance of the optimised panel to the original non-optimised configuration. The linear bucking analysis predicted a buckling load of 140.9 kN compared to 125.2 kN for the non-optimised configuration. This meant that the optimised panel actually had a buckling load of 12.5% higher than that of the original panel. The prebuckling stiffness was reduced by 9.7% from 190.3 kN/mm to 171.9 kN/mm whilst the postbuckling stiffness by 5.9% from 157.1 kN to 147.8 kN. These values demonstrate how the constraints applied in the GA were effective in preserving both the buckling load and stiffness of the I-stiffened panel. The total damage at the skin-stiffener interface corresponding to the objective function in the optimization was reduced by 41.4%, showing the effectiveness of the GA in finding a new skin configuration to increase the damage resistance of the panel in its postbuckling regime. The behaviour of the optimised panel is discussed next by comparing its global and local model FE results to those of the original non-optimised panel.

Table 10.5: Comparison of optimised and non-optimised skin lay-up panel designs.

	Non-optimised	Optimised	% Diff.
Skin Lay-up	$[45,-45,0_2,$ $-45,45,90_2]_S$	$[-45,45,0,45,$ $-45,90,-45,45]_S$	
Buckling Load (kN)	125.2	140.9	+12.5%
Prebuckling Stiffness (kN/mm)	190.3	171.9	-9.7%
Postbuckling Stiffness (kN/mm)	157.1	147.8	-5.9%
Interface Element Damage	93.8	55.0	-41.4%

10.6.2 Skin lay-up optimised panel global model results

Figure 10.11 shows the global model results of the skin lay-up optimised panel comparing them to the non-optimised panel as first seen in Chapter 4. The global model results showed that the optimised configuration of the panel still buckled in the five half-wave configuration as seen in Figure 10.11 (a). The direction of buckling is the opposite in the two panels as seen by the out-of-plane displacement contours. As the loading was increased and the non-optimised panel mode-jumped to the six half-wave configuration at 262 kN, the optimised skin lay-up meant that the optimised panel remained in the five half-wave configuration with the buckle crests deepening as seen in Figure 10.11 (b) and (c). A mode-jump did eventually happen at a loading of 580 kN. First the middle skin-bay jumped to a six half-wave configuration followed by the side bays jumping to seven half-waves at 631 kN. The optimised panel remained in this configuration until very high loads as seen in Figure 10.11 (d).

10.6.3 Skin lay-up optimised panel local model results

The local model results for the optimised skin lay-up panel were also compared to those of Chapter 7 relating to the non-optimised I-stiffened panel. Figure 10.12 shows the skin-stiffener debonding at various different load levels. The non-optimised and optimised designs at the loads of Figure 10.12 (a) and (b) show very similar damage levels, but it is apparent how the panel buckled in the opposite direction. Damage was localized at the location of buckle anti-node lines where bending moments are at a maximum and directly under the stiffener web. When the non-optimised panel mode-jumped in Figure 10.12 (b), the damage spread in the stiffener lengthwise direction due to the relocation of the node and anti-node lines. This did not happen in the optimised skin lay-up panel as the buckle crest grew deeper but remained in the same location as visible in Figure 10.12 (c). Damage spread outwards from the web towards the stiffener flanges but remained localized. Hence it was the different postbuckling behaviour of the skin lay-up optimised panel, exhibiting a delayed mode-jump, that was responsible for increasing the damage resistance. This continued until the optimised panel mode-jumped as well, and Figure 10.12 (d) shows how both designs showed an almost completely debonded interface for very high loads.

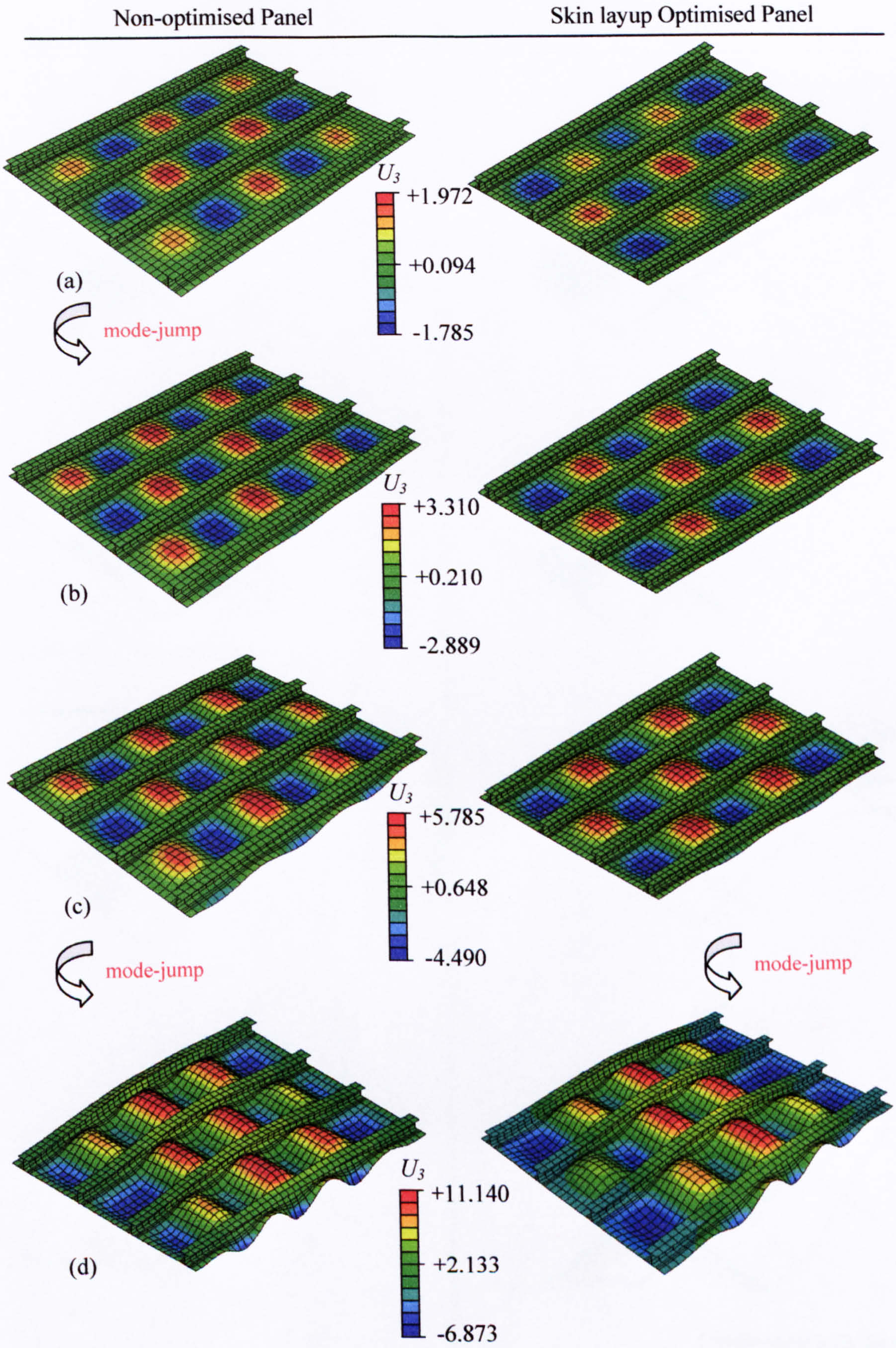

Figure 10.11: Numerical analysis deformed shape (scale factor five) and out-of-plane displacement contour plots for non-optimised I-stiffened panel and skin lay-up optimised I-stiffened panel global models at loading: (a) 160 kN, (b) 265 kN, (c) 487 kN, (d) 800 kN.

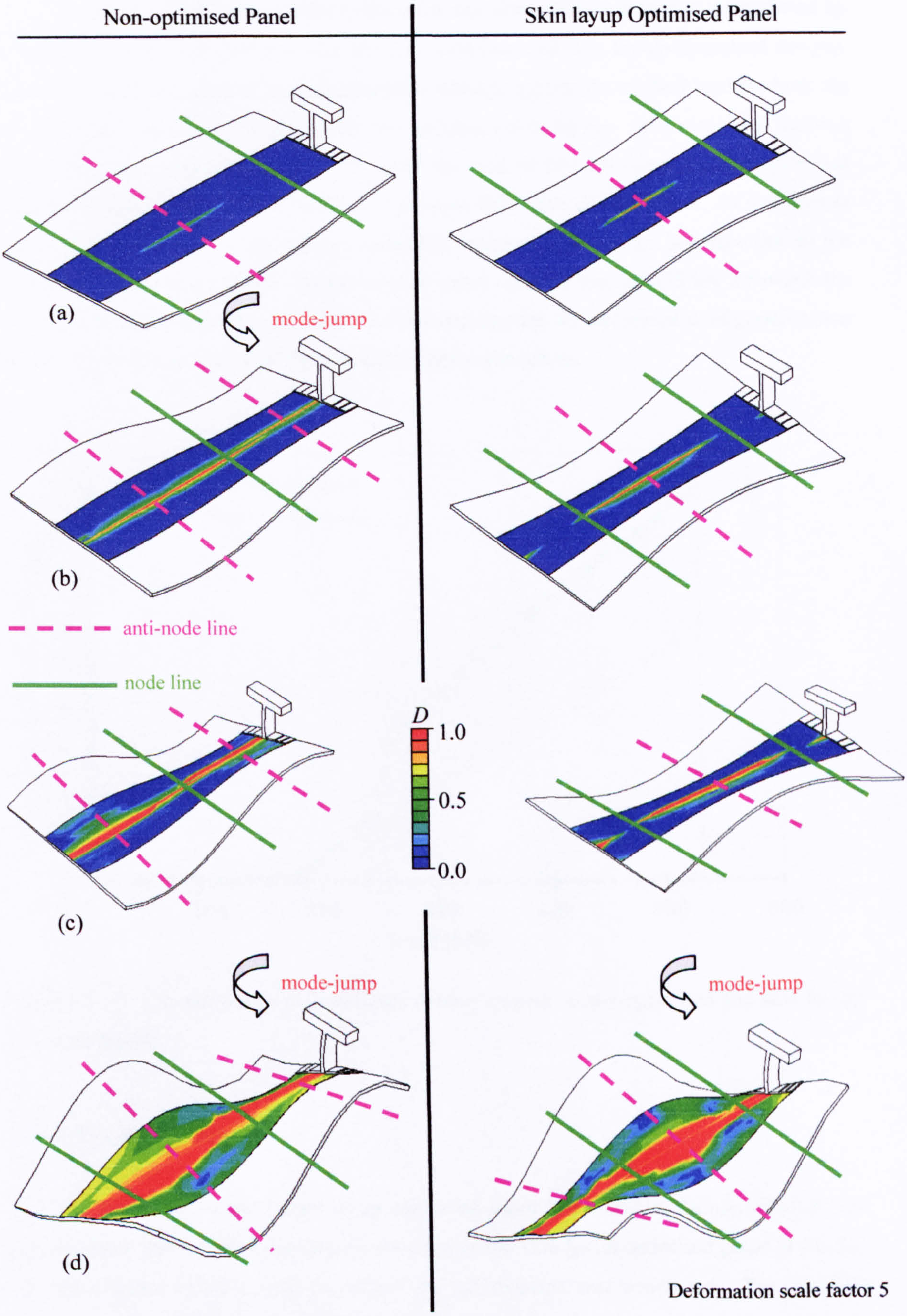

Deformation scale factor 5

Figure 10.12: Interface element damage at local model skin-stiffener interface comparison for non-optimised and skin lay-up optimised panels at loading: (a) 160 kN, (b) 265 kN, (c) 500 kN, (d) 800 kN.

The growth of the skin-stiffener debond at the skin stiffener interface as predicted by the local FE model was compared for the non-optimised and skin lay-up optimised designs. Figure 10.13 shows a plot of the total interface damage against the applied load for both the non-optimised panel and the panel with the optimised skin lay-up. It is clear how the two panels show very similar damage levels until the load of 262 kN when the non-optimised panel mode-jumps form the five half-wave to the six half-wave configuration. As was seen in Figure 10.11, this lead to the damage spreading lengthwise across the interface due to the relocation of the buckle crests. At the original panel collapse load of 525 kN for which the optimization was conducted, the total interface damage for the optimised configuration was reduced by 41.4% as a result of the skin optimization procedure.

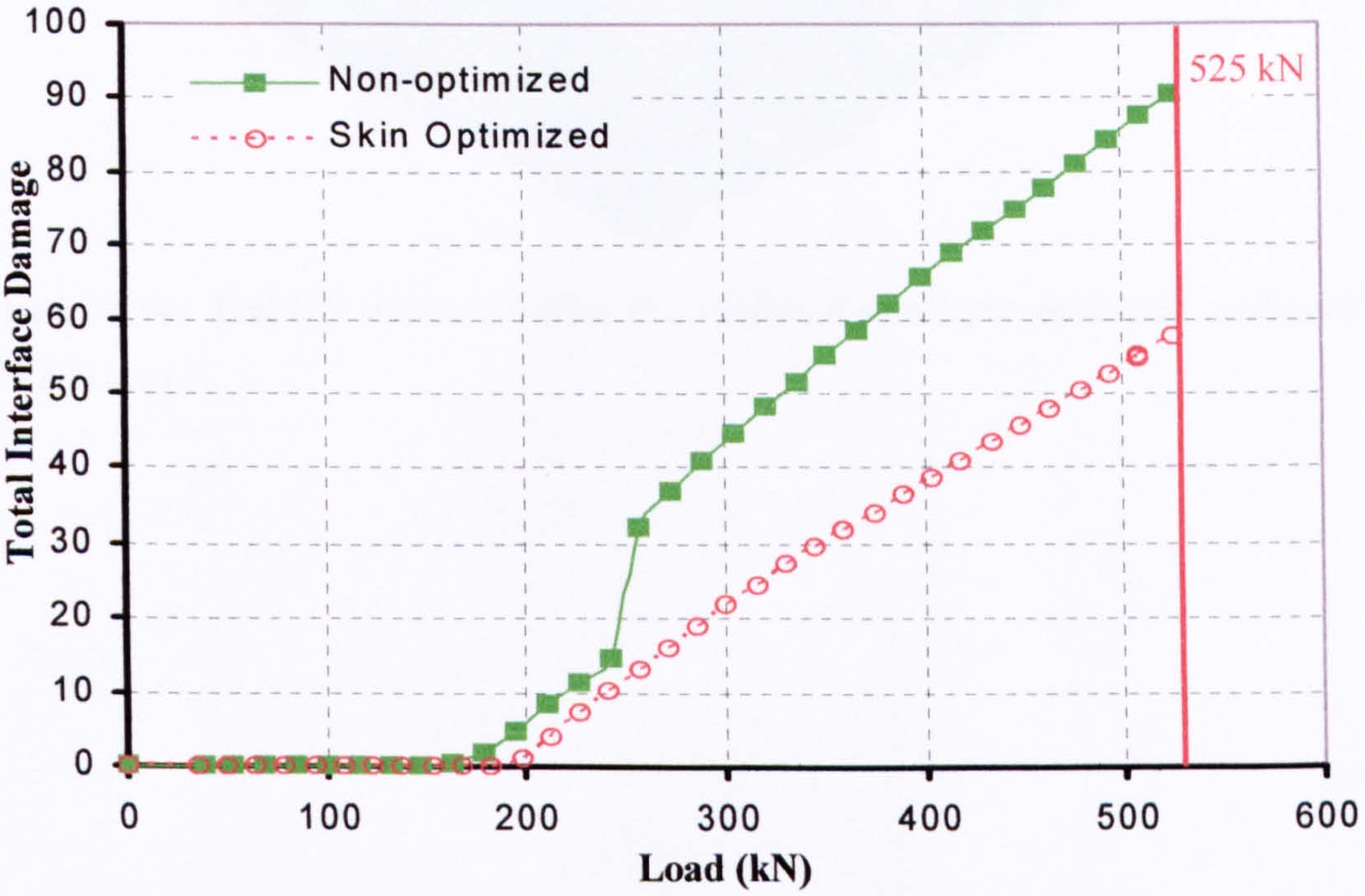

Figure 10.13: Comparison of skin-stiffener debond growth in non-optimised and skin lay-up optimised panels.

10.6.4 Local ply failures

As was done for the flange layup optimised panel, the Tsai-Hill failure criterion was used to check that no local ply failures occurred in the skin layup optimised panel at the 525 kN experimental collapse load for which the optimization was conducted. The Tsai-Hill criterion is given by Equation (10.6) and the material failure strengths used are those of Table 10.3. Figure 10.14 shows the Tsai-Hill failure index I_F contours on the skin layup optimised panel. Equation (10.6). It can be seen how the skin-layup optimised panel global model did not predict any local ply failure occurring before the loading for which the optimization was conducted, meaning that damage occurred at the skin-stiffener interface as shown by the interface element degradation prior to any local ply failures in the panel.

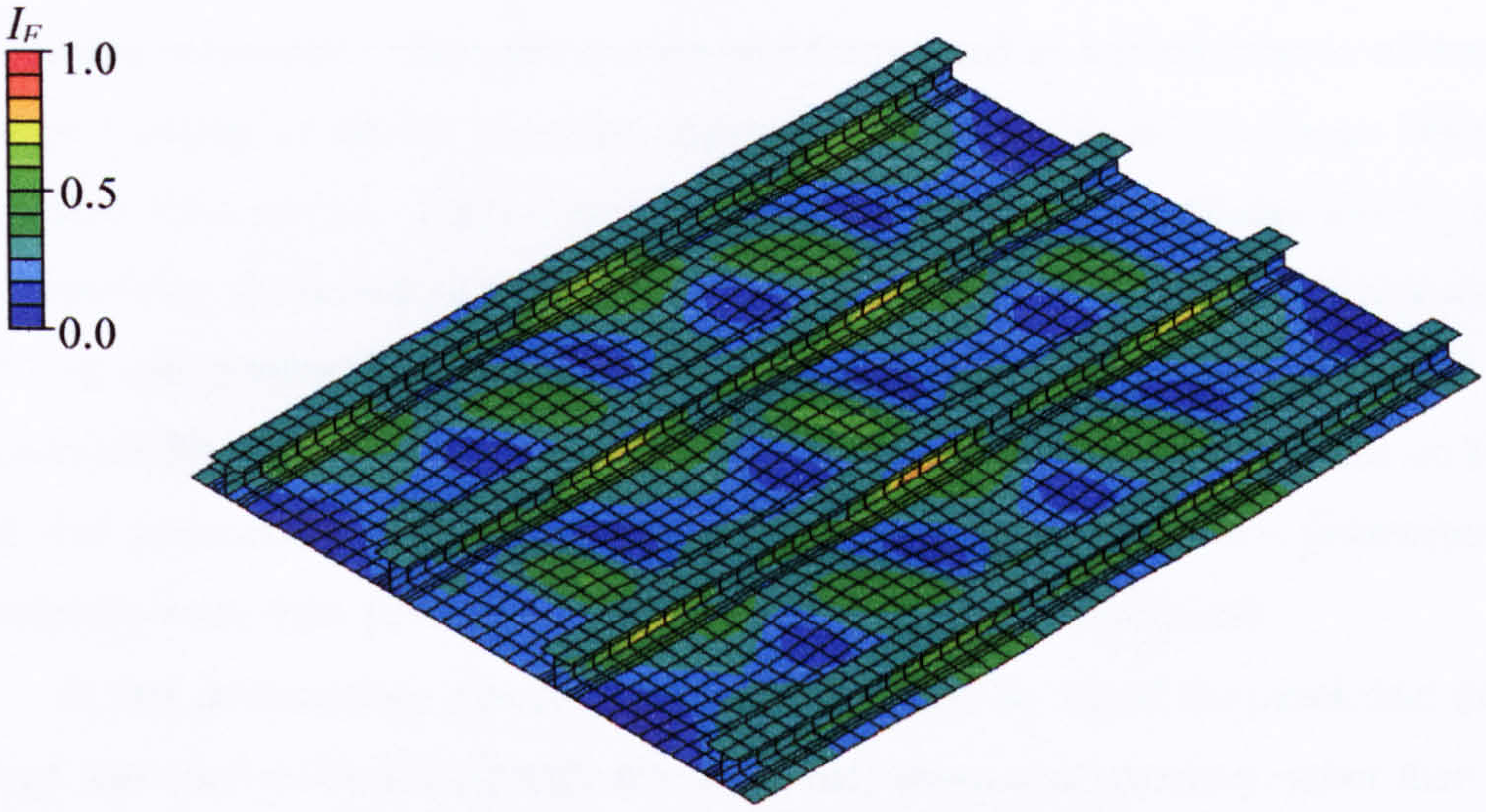

Figure 10.14: Tsai-Hill failure criterion for I-stiffened skin layup optimised configuration at 525 KN load.

10.7 Concluding remarks

In this chapter it was shown how a similar GA to that used in the buckling load maximization for a composite plate was coupled with the global and local FE models of the I-stiffened panel seen in Chapter 4 and Chapter 7 in order to optimise various parts of its lay-up for damage resistance. The optimization was formulated as a minimization of the sum of the damage variable of all the interface elements placed at the skin-stiffener interface of the ABAQUS local model. Each function evaluation meant the automatic linking between the GA specifying the lay-up of the panel and the running of the ABAQUS global model for the buckling and postbuckling behaviour of the panel followed by the local model which was responsible for the objective function calculation. Constraints were imposed on the buckling load and prebuckling stiffness of the designs so that the latter two parameters were not reduced by more than 10% relative to the original non-optimised panel.

A first optimization was conducted on the flange lay-up of the panel, and the optimised design was seen to buckle directly into a six half-wave configuration rather than a five half-wave configuration followed by a sudden mode jump to the six half-wave configuration. In terms of the skin-stiffener interface debond growth, this meant that the optimised configuration showed a reduction in the total damage by 12.7% at the experimental collapse load of 525 kN when compared to the non-optimised configuration. A greater damage resistance was achieved by optimizing the panel skin. The design with the optimised skin lay-up showed a reduction in the total damage of the interface elements of 41.4% at the 525 kN load. The panel still buckled in a five half-wave configuration, but was characterized by the mode-jump to the six half-wave configuration being delayed from the 262 kN load as was observed numerically in the non-optimised panel to 580 kN. Both optimization procedures showed how the adopted method of a GA coupled and automatically linked with ABAQUS models responsible for the objective function evaluations proved to be an effective way of developing and optimization process able to take into account damage mechanism which may occur prior to in plane failure and global collapse.

Chapter 11

Conclusions and future work

This chapter draws conclusions on all the work presented. This relates to the FE modelling of the buckling and postbuckling behaviour of stiffened composite structures, FE modelling of out-of-plane damage mechanisms, and the development of an FE based optimization procedure used in the optimization for damage resistance of an I-stiffened panel operating in its postbuckling regime.

Future work is then discussed relating to how the work presented may be extended to look at the lay-up optimization of different composite structures, optimizations relating to geometric features such as the number of stiffeners in a stiffened panel or local details such as capping strips and overlay plies in stiffener flanges. Ways of improving the efficiency of the GA code are also discussed together with the possibility of extending the optimization routine so as to link it to more detailed FE models which also take into account in-plane damage of composites.

11.1 Conclusions

11.1.1 Modelling postbuckling stiffened composite aerostructures

As the next generation of aircraft is set to contain more and more composites as a weight percentage, the use of composite materials in skin-stiffener type structures such as fuselage panels and wing skins has become of ever increasing interest. A particular need has arisen in understanding the behaviour of such structures under very high loading. The reason for this is that great weight saving may be achieved in operating the structures past their buckling load and deep into their postbuckling regime. In order for this to happen, the postbuckling behaviour of the structure in question must be fully understood as must its failure characteristics. Currently the design of primary composite aerostructures is conservative due to the relative weakness of the skin stiffener interface due to through-thickness stresses arising from deformations due to buckling. Secondary instabilities exacerbate this problem by causing abrupt dynamic configuration changes which have been experimentally proven to closely effect the damage mechanisms seen in stiffened composite structures.

Experimental investigations to asses the buckling and postbuckling behaviour of stiffened composite structures are widespread in literature as seen in Chapter 2. In order to reduce the number of such experimental tests, FE models able to capture their buckling and postbuckling behaviour including the effects of mode-jumping are required. In Chapter 3 it was shown how this is achievable in the FE package ABAQUS by combining linear eigenvalue buckling analyses able to find the buckling load and buckle mode shapes of a structure with non-linear solution algorithms able to trace the whole postbuckling response. It is required to add initial geometric imperfections into the model to reduce bifurcation points into limit points, and this is easily achievable by first conducting a linear eigenvalue buckling analysis on the structure and using the resulting eigenmodes as scaled geometric imperfections with magnitude typically a few percent of a representative thickness in the model such as the skin in a stiffened panel. Even with the addition of imperfections, convergence difficulties arise when secondary instabilities in the load-displacement history occur, and to circumvent these various numerical tools have been presented. These include the use of the arc-length method or coupling the incremental Newton-Raphson technique with energy dissipation schemes.

In Chapter 4 the numerical techniques were applied to model the buckling and postbuckling behaviour of two different stiffened panels. The first was a hat-stiffened panel with integrated hat-stiffeners, whilst the second was an I-stiffened panel with its stiffeners secondary bonded onto the skin using an adhesive. In both cases the FE model containing conventional shell elements was discussed, and numerical results relating to strains and out-of-plane displacements were compared to their experimental counterparts obtained from strain gauges and LVDTs.

Both experimentally and numerically, the hat-stiffened panel buckled into a three half-wave configuration which saw the gradual formation of a "waist" in the middle buckle crest as the compressive loading was increased. In the experimental panel a dynamic mode-jump to a five half-wave configuration was observed at a loading of 66 kN, and the first evidence of visible damage occurred at 79 kN prior to panel collapse at 103 kN due to the local buckling of the hat-stiffeners. The numerical model was able to capture the three half-wave buckle configuration and the formation of the waist in the central half-wave, but the mode-jump to a five half-wave configuration did not occur. This could be possible attributed to the presence of microcracking and delamination in the panel which are not accounted for in the FE model, and in reality change the stiffness of the structure and could therefore be responsible for the sudden mode-jump. Numerical strains and out-of-plane displacements compared well with experimental values in the initial postbuckling regime, but only a fair correlation was found in the deeper postbuckling regime due to the mentioned mode-jump.

The I-stiffened panel was seen to experimentally buckle into a five half-wave configuration at a loading of about 120 kN. The same buckle configuration was predicted by the FE model at a loading of 125.2 kN. At a loading of 241 kN the experimental panel suddenly mode-jumped to a six half-wave configuration in all of the skin bays, and this was accurately modelled by the FE panel at a loading of 262 kN. Strains and out-of-plane displacements compared extremely well even deep into the panel's postbuckling regime. Further mode-jumps to a seven half-wave configuration were observed experimentally at loadings of 473 kN and 486 kN in the left and right skin bays respectively, but these were not seen to occur in the FE model until very high loadings past the actual collapse load of 525 kN for the experimental panel. Like for the hat-stiffened panel, a possible explanation for this could be the inability of the FE model to model matrix microcracking and delamination which may have occurred experimentally at these high loadings.

11.1.2 The modelling of failure mechanisms

Chapter 5 highlighted the need of FE models being able to capture damage mechanisms such as delamination and skin-stiffener debonding, giving particular reference to the FE models of the stiffened composite panels of Chapter 4. A literature review was conducted on previous work dealing with failure mechanisms in various composite structures, before discussing the two major approaches of modelling out-of-plane damage in composites – VCCT and interface elements. VCCT was introduced briefly before introducing the formulation behind the interface elements available in the FE package ABAQUS. Single and mixed mode formulations for these elements were presented followed by validation under pure Mode I loading through a DCB example problem.

The interface elements were used to model two different runout specimens in Chapter 6. These models contained continuum shell elements to efficiently replicate the stiffener and skin, and interface elements at the skin-stiffener interface to model debonding. Strain results were found to match experimental strain gauge readings well, and the FE models were able to show how initial failure of the specimens was dominated by Mode II crack propagation through the skin-stiffener interface. The first, thinner specimen showed sudden crack propagation leading to collapse, whilst the second, thicker specimen displayed initially unstable but then stable crack growth.

Further use of interface element was made in Chapter 7 where a global-local modelling approach was introduced to model the skin-stiffener debonding in the I-stiffened panel first seen in Chapter 4. The model in the latter chapter contained no failure capability, and hence a local detailed model of a representative section of the skin and stiffener was developed. This model was constructed using standard brick elements so that detailed geometric features such as the flange drop offs could be captured. The local model was driven directly by the global model solution in the sense that the displacements computed by ABAQUS for the global model were applied as boundary conditions on the local model. The growth of skin-stiffener debonding was seen to initiate directly under a stiffener web at a position corresponding to a stiffener anti-node line. This agreed with experimental results which indicated that and anti-node line the moment transfer between the stiffener web and flange/panel skin acted to pull the flange away from the panel. As the loading was increased, so did the stiffness degradation in the interface elements, but the damage remained localized. This was not the case when the panel mode-jumped to the six half-wave configuration, which saw the relocation of the buckle anti-node lines leading to a growth of the debond under the stiffener web in the stiffener lengthwise direction. As the loading was increased further almost all of the interface elements at the skin-stiffener interface became completely degraded.

11.1.3 Developed optimization routine

Traditionally engineering design has been largely based on experience, but mathematical optimization has provided the designer with additional tools to be applied in the design process. The design procedure can be set out as a well defined process with a specific objective such as minimizing weight or maximizing buckling load, and design variables which may be altered in order to achieve this objective. Composite materials have added a whole new dimension to mathematical optimization as they allow the tailoring of the material properties by, for example, optimizing the ply orientations of a laminate. In Chapter 8 optimization was introduced, giving a literature review of existing work relating to composite structure optimization ranging from buckling load maximizing of a simple plate to weight minimization of complete panels. The concepts of linear and non-linear integer programming were introduced, followed by the concepts behind GAs and how they mimic Darwin's theory of evolution by driving an initial population towards an optimum via the application of genetic operators such as selection, crossover, and mutation. In Chapter 9 a GA was constructed to maximize the buckling load of a composite plate. The GA was constructed and effectively linked with an FE model responsible for the buckling load evaluations of each design. The GA was able to find the optimal stacking sequence of the plate subject to different biaxial load scenarios, and results were compared to those obtained in literature via the branch-and-bound optimization method. The GA acted as a validation for the FE based optimization procedure in Chapter 10 by showing how the GA and an FE model may be linked in an autonomous fashion.

The GA was modified in Chapter 10 so as to optimise the lay-up of certain regions of the panel in order to increase its damage resistance. The optimization problem was formulated as a minimization of the sum of the damage variable in the interface elements at the skin-stiffener interface of the FE local model. At each function evaluation of the GA, this was linked to the global FE model discussed in Chapter 4 for the I-stiffened panel in order to conduct eigenvalue buckling analyses and subsequently a nonlinear analysis able to trace the buckling and postbuckling behaviour of the panel. The lay-up of the panel was updated by the MATLAB code creating a series of text files which were then atomically read by the ABAQUS input files. The global model solution then drove the local FE model which was responsible for finding the damage at the skin-stiffener interface and hence objective function. Two separate optimizations were conducted, one on the flange lay-up of the panel stiffeners and one on the lay-up of the panel skin. Constraints were added so that the optimised designs would have buckling load and prebuckling stiffness reductions of no greater than 10% when compared to the original non-optimised design.

The GA was able to find a revised skin lay-up which reduced the damage at the skin-stiffener interface by 41.4% at the experimental collapse load of 525 kN, with an increase in buckling load of 12.5% and reduction in prebuckling and postbuckling stiffnesses of 9.7% and 5.9% respectively relative to the non-optimised design. The reduction in the debonding at the skin-stiffener interface was a result of the change in the postbuckling behaviour of the panel due to the change in skin lay-up. This delayed the mode jump from the five to the six half-wave configuration and hence postponed the growth of the skin-stiffener debonding in the lengthwise direction under the stiffener web.

The GA optimization procedure coupled with all the analysis and modelling techniques proposed showed how it was possible to accomplish the objective of this research project of developing an FE based optimization procedure for composite stiffened structures which takes into account out-of-plane damage mechanisms. The work developed also made it possible to appreciate various routes which could be explored so as to extend the capability of the optimization procedure in future work, which is discussed in the next section.

11.1.4 Applicability of the developed optimization strategy

The work presented has shown how it was possible develop an optimization methodology to be applied to stiffened composite structures. This methodology is able to combine the FE modelling of the structure being optimised and the optimization procedure in a wholly autonomous fashion, while still keeping the modelling and optimization stages separate. This aspect of the methodology renders it applicable to different optimization problems such as the lay-up optimization of different composite structures, as well as allowing it to be extendable to geometric optimization as suited to a user's specific needs. The same GA as presented can be used for the optimization stage, whilst a new FE model can be introduced so as to optimise a different structure. Furthermore, the same design string representation could be used not only to represent lay-up of a composite structure, but also specific geometric features such as stiffener runout taper angles or geometric thicknesses.

As presented, the optimization methodology only accounts for out-of-plane failure mechanisms associated with skin-stiffener debonding by making use of interface elements. In future this could be extended to include in-plane failure capabilities where user subroutines with specific failure laws could be included in the FE models of the structure being modelled and then incorporated into the definition of the optimization problem. Once this is done, and validated models able to capture and include all the failure modes associated with the composite structure to be optimised are used in the optimization problem, then the methodology presented could be an important tool in composite structural design. Such aspects of future enhancements to the optimization methodology are presented and discussed next.

11.2 Future work

11.2.1 Lay-up optimization of composite structures

The optimization procedure developed showed how it was possible to optimise an I-stiffened panel in order to improve its damage resistance in its postbuckling regime. This optimization procedure as applied to an I-stiffened panel is just one example of how the proposed methodology of coupling a GA for the optimization process to FE models with failure capability responsible for the function evaluations may be used to optimise a composite structure.

The lay-up optimization of a composite structure other than the I-stiffened panel considered could be carried out by simply replacing the FE models of the I-stiffened panel with whatever structure is to be investigated. The same GA could be used, with specific sections of the ABAQUS input files relating to the lay-up of the components to be optimised being altered by the GA code prior to running of the FE models for the function evaluations. The only requirement would be that of the FE models having being validated against experimental work so as to ensure their accuracy. A natural choice for a structure that could be considered for lay-up optimization would be a different stiffened composite panel, such as the ones discussed in the literature review of Chapter 2.

11.2.2 Thickness and geometry optimization

A further extension to the work conducted would be to consider geometric changes in structures for the optimization problem. The simplest form of geometric change would be the optimization of the thickness of certain parts of a composite structure. In Chapter 9 and Chapter 10 it was seen how integer variables were used to represent the ply orientations of 0°, 45°, -45°, and 90°. A fifth possibility for these variables could be added to represent an "empty" ply. Hence the same GA cold be used but it would be allowed to introduce empty plies into the laminate hence also controlling its thickness. If this is done, care has to be taken to make sure that empty plies only occur on the outside of the laminate and that the geometry of the structure considered in the FE model is modified accordingly to represent the change in thickness.

Another example of geometric optimization would be the number of stiffeners in a stiffened panel or the dimensions of the stiffeners themselves. These could be included as design variables into the optimization problem, and coupled with the lay-up of the panel into a complete optimization which could still be solved using the GA developed. The biggest challenge is again the linking of the GA optimization code with the FE models. Not only will the lay-up of the composite structure being considered change, but also geometric changes will have to be carried out on the FE input files as each different design is being evaluated. In the FE package ABAQUS, such changes could be incorporated by writing a MATLAB code which modifies the nodal coordinates in the model as specified in the ABAQUS input file directly. Each time a new design is encountered, the lay-up as well as these new nodal coordinates would be updated prior to objective function evaluations.

Another interesting possibility would be the optimization of stiffened composite cylindrical shells such as the ones that have been tested experimentally by Bisagni [141,142]. Again a possible optimization could be conducted so as to not only optimise the lay-up of the cylindrical shells, but also the number of stiffeners and other geometric dimensions to allow the shells to operate deeper in their postbuckling regime. The collapse load of the shells as predicted by an FE analyses could be used as objective function, or if using interface elements to model out-of-plane damage mechanisms then the same approach as for the I-stiffened panel optimization of using the sum of the damage variable across, for example, the skin stiffness interface as the objective function could be adopted.

The stiffener runout models considered in Chapter 6 would also be suitable for an optimization as discussed above combining design variables describing the lay-up of the specimens with design variables relating to geometric aspects. As was discussed in the literature review of Chapter 5, a lot of experimental work has been conducted looking at how tapering of a stiffener web near the runout end, tapering of the stiffener foot, and the introduction of a web cut-off could increase the collapse load of stiffener runouts. Having created the FE models seen in Chapter 6 for two different runout configurations and seeing how the introduction of interface elements at the skin-stiffener interface was able to not only accurately predict the failure loads of the two panels, but also relate to the different failure modes of the two specimens, these models could be used as a basis for an optimization procedure. The ply orientations in the specimens could be used as design variables, but also geometric changes relating to web tapering, foot tapering, and web cut-offs could be considered. For example, the taper angle of the web towards the runout end could be allowed to vary in the optimization process allowing the GA to find an optimal taper angle which maximizes the collapse load of the stiffener runout. Once again the major challenge would be the automatic modification of the ABAQUS input file to represent the geometric changes in the runout.

11.2.3 Effect of local geometric features

Another aspect which could be considered in the optimization would be the effect of specific local geometric features. In chapter 5 it was discussed how Vijayaraju et al. [56] tested carbon/epoxy T-pull specimens under peel load conditions to study their failure behaviour at the skin-stiffener interface. The effect of capping strips – additional plies placed between the skin and stiffener to increase the longitudinal bending stiffness of the structure – and overlay plies – additional plies covering the ply drops in the stiffener flanges – was investigated to see whether such local features can delay the onset of skin-stiffener debonding. To reduce the experimental testing in such investigations, an optimization procedure linking a GA with an FE model able to incorporate the above features could be developed. Here the global-local modelling approach as used in the optimization of the I-stiffened panel would again be required since it would be computationally very expensive to incorporate such specific local geometric features in a global model. Instead they could be modelled in a detailed local model which only takes into account the specific geometric region of interest. Such an optimization methodology would be useful in giving great insight into how specific local features could be used in alleviating local stresses which promote skin-stiffener debonding.

11.2.4 Improvements to the genetic algorithm

The possible future work relating to geometric optimization and in particular the investigation of specific local geometric features will bring considerable additional complexities into the FE models required to model the structures being optimised. It was seen how the local modelling of the I-stiffened panel using standard brick elements made it possible to model in detail the ply drop offs in the stiffener flanges. Modelling of refined geometric features will require such 3D models with very fine meshes, greatly increasing the computational effort required to run the FE analyses for the function evaluations. The non-linearity introduced by the damage models also makes it unsuitable for the use of alternative techniques such as neural networks as discussed in Chapter 8. Therefore it becomes apparent how modifications and improvements to the structure of the optimization GA code itself would be highly beneficial so as to attempt to speed up the convergence of the algorithm. Consider a reduction of 10% in the number of individuals in each population, coupled with a 10% reduction in the number of generations this population has to go through before convergence. This would lead to a 19% decrease in number of function evaluations. Because of this, work conducted to refine the GA and its genetic operators so as to improve its efficiency would prove very practical. As was discussed in the literature survey of previous work conducted with GAs in Chapter 8, many refinements such as local improvement, modified selection methods, modified crossover and mutation operators, as well as ways to reduce population size exist but were not explored in the optimization routine presented. A study into the use of these improvements and modifications and how they effect the convergence rate of the GA would be extremely beneficial to any optimization GA code.

11.2.5 Combining different failure mechanisms

The optimization routine optimised an I-stiffened panel for damage resistance in its postbuckling regime taking into account damage mechanisms relating to out-of-plane failure such as skin-stiffener debonding and delamination. Naturally, other failure mechanisms, especially in-plane damage, exist in composite materials and the modelling of these failure mechanisms is an ever-growing research field. ABAQUS makes it possible to create user subroutines which allow the user to code up their own damage laws to be used in the elements placed in FE models. A natural extension to the work presented would be to use the same optimization methodology presented coupling a GA to FE models which not only have the out-of-plane damage capability provided by the interface elements, but are also able to capture in plane damage mechanisms. This would be a major step in the field of composite modelling and optimization as a considerable reduction of costs relating to experimental testing could be achieved as reliable FE models of composite structures able to capture a variety of failure modes are used to find optimal configurations for specific composite components.

References

[1] I. M. Daniel, and O. Ishai. *Engineering mechanics of composite materials.* Oxford University Press, 2nd Edition, New York, 2006.

[2] S. R. Swanson. *Introduction to design and analysis with advanced composite materials.* Prentice Hall, 1st Edition, Upper Saddle River, NJ, 1997.

[3] G. Chambost. *La Grande Aventure de l'Airbus A380.* Editions Sud Ouest, Lucon, France, 2005.

[4] DLR. Improved material exploitation at safe design of composite airframe structures by accurate simulation of collapse. *International Conference on Buckling and Postbuckling Behaviour of Composite Laminated Shell Structures*, Eliat, Israel, 1-2 March 2004.

[5] W. J. Supple. Coupled branching configurations in the elastic buckling of symmetric structural systems. *International Journal of MEchanical Sciences*, 9 (2): 97-112, 1967.

[6] W. J. Supple. On the change in buckle pattern in elastic structures. *International Journal of Mechanical Sciences*, 10 (9): 737-745, 1968.

[7] W. J. Supple. Changes in wave-form of plates in the post-buckling range. *International Journal of Solids and Structures*, 6: 1243-1258, 1970.

[8] K. A. Stevens, R. Ricci, and G. A. O. Davies. Buckling and postbuckling of composite structures. *Composite Structures*, 26 (3): 189-199, 1995.

[9] R. Krueger. Virtual Crack Closure Technique: History, Approach and Applications. *Applied Mechanics Review*, 57 (2): 109-143, 2004.

[10] E. F. Rybicki, and M. F. Kanninen. A finite element calculation of stress intensity factors by a modified crack closure integral. *Engineering Fracture Mechanics*, 9 ((4)): 931-938, 1977.

[11] P. P. Camanho, and C. G. Davila. Mixed-mode decohesion finite elements for the simulation of delamination in composite materials. *NASA-Technical Paper 211737*, National Aeronautics and Space Agency, USA, 2002.

[12] M. Stein. Loads and deformations of buckled rectangular plates. *Technical Report R-40, NASA*, 1959.

[13] G. Z. Harris. Buckling and post-buckling of orthotropic laminated plates. *AIAA Paper 75-813*, 1975.

[14] W. M. Banks. The post buckling behaviour of composite panels. *Proceedings of the 1975 International Conference on Composite Materials, ICCM, Vol. 2*, Geneva, Switzerland, 1976.

[15] J. H. J. Starnes, and M. Rouse. Postbuckling and failure characteristics of selected flat rectangular graphite-epoxy plates loaded in compression. *AIAA Paper 81-0543*, 1981.

[16] M. P. Nemeth. Buckling and postbuckling behaviour of laminated composite plates with a cutout. *NASA Technical Paper 3587, National Aeronautics and Space Administration*, Hampton, Virginia, 1996.

[17] J. H. J. Starnes, N. F. Knight Jr., and M. Rouse. Postbuckling behaviour of selected flat stiffened graphite-epoxy panels loaded in compression. *AIAA Journal*, 23 (8): 1236-1246, 1985.

[18] G. Romeo. Experimental investigation on advanced composite-stiffened structures under uniaxial compression and bending. *AIAA Journal*, 24 (11): 1823-1830, 1986.

[19] B. G. Falzon, K. A. Stevens, and G. A. O. Davies. Postbuckling behaviour of a blade-stiffened composite panel loaded in uniaxial compression. *Composites Part A: Applied Science and Manufacturing*, 31 (5): 459-468, 2000.

[20] K. A. Stevens, S. Specht, and G. A. O. Davies. Postbuckling failure of carbon-epoxy compression panels. *Proceedings of ICCM-11*, Gold Coast, Australia, 14-18 July 1997.

[21] B. G. Falzon, and G. P. Steven. Buckling mode transition in hat-stiffened composite panels loaded in uniaxial compression. *Composite Structures*, 37 (2): 253-267, 1997.

[22] B. G. Falzon. The behaviour of damage tolerant hat-stiffened composite panels loaded in uniaxial compression. *Composites: Part A*, 32 (9): 1255-1262, 2001.

[23] M. Cerini. Investigation of secondary instabilities in postbuckling stiffened composite structures. *Department of Aeronautics, Imperial College London, PhD Thesis*, 2005.

[24] C. Kong, I. C. Lee, C. G. Kim, and C. S. Hong. Postbuckling and failure of stiffened composite panels under axial compression. *Composite Structures*, 42 (1): 13-21, 1998.

[25] S. P. Timoshenko, and J. M. Gere. *Theory of Elastic Stability.* McGraw-Hill Book Company Inc., 2nd, 1961.

[26] S. P. Timoshenko, and S. Woinowsky-Krieger. *Theory of Plates and Shells.* McGraw-Hill Book Company Inc., 2nd, 1959.

[27] Z. P. Bazant, and L. Cedolin. *Stability of Structures.* Dover Publications Inc., New York, 2003.

[28] M. S. Anderson, and W. J. Stroud. A general panel sizing computer code and its application to composite structural panels. *AIAA Journal*, 17: 892-897, 1979.

[29] B. O. Almroth, and F. A. Brogan. The STAGS computer code. *NASA CR-2950, NASA Langley Research Center*, Hampton, VA, 1978.

[30] D. Hitchings. FE77 User Manual. *Imperial College of Science, Technology, and Medicine*, London, 1994.

[31] E. Riks. The application of newton's method to the problem of elastic stability. *Journal of Applied Mechanics*, 39: 1060-1066, 1972.

[32] G. A. Wempner. Discrete approximations related to non-linear theories of solids. *International Journal of Solids and Structures*, 7 (11): 1581-1599, 1971.

[33] M. A. Crisfield. *Non-Linear Finite Element Analysis of Solids and Structures.* John Wiley & Sons, 1st Edition, Chichester, UK, 1991.

[34] M. Cerini, and B. G. Falzon. The reliability of the arc-length method in the analysis of mode-jumping problems. *44th AIAA/ASME/ASCE/AHS Structures, Structural Dynamics, and Materials Conference*, Norfolk, Virginia, 7-10 April, 2003.

[35] E. A. De Souza Neto, and Y. T. Feng. On the determination of the path direction for arc-length methods in the presence of bifurcations and 'snap-backs'. *Computer Methods in Applied Mechanics and Engineering*, 179 (1): 81-89, 1999.

[36] E. Riks, C. Rankin, and F. A. Brogan. On the solution of mode jumping phenomena in thin-walled shell structures. *Computer Methods in Applied Mechanics and Engineering*, 136 (1-2): 59-92, 1996.

[37] B. G. Falzon, and M. Cerini. An automated hybrid procedure for capturing mode-jumping in postbuckling composite stiffened structures. *Composite Structures*, 73 (2): 186-195, 2006.

[38] E. Hinton. *NAFEMS introduction to nonlinear finite element analysis*. Glasgow, 1992.

[39] ABAQUS. *ABAQUS 6.6 Documentation*. 1st Edition, Providence, RI, 2004.

[40] S. Ramaswami. Towards optimal solution techniques for large eigenproblems in structural mechanics. *MIT, PhD Thesis Thesis*, 1979.

[41] J. H. Wilkinson. *The Algebraic Eigenvalue Problem*. Oxford University Press, Oxford, 1965.

[42] K. J. Bathe, and E. L. Wilson. Towards optimal solution techniques for large eigenproblems in structural mechanics. *Proceedings of the ASCE, EM6*, 98: 1471–1485, 1972.

[43] T. Ericsson, and A. Ruhe. The spectral transformation Lanczos method for the numerical solution of large spare generalized symmetric eigenvalue problems. *Mathematics of Computation*, 35: 1251-1268, 1980.

[44] B. N. Parlett. *The Symmetric Eigenvalue Problem*. Prentice-Hall, Englewood Cliffs, New Jersey, 1980.

[45] H. D. Simon. The Lanczos algorithm with partial reorthogonalization. *Mathematics of Computation*, 42: 115-142, 1984.

[46] B. N. Parlett, and B. Nour-Omid. Toward a black box Laczos program. *Computer Physics Communications*, 53 (169-179): 1989.

[47] R. G. Grimes, J. G. Lewis, and H. D. Simon. A shifted block Lanczos algorithm for solving sparse symmetric generalized eigenproblems. *SIAM Journal on Matrix Analysis and Applications*, 15 (1): 228-272, 1994.

[48] E. Ramm. *Strategies for Tracing the Nonlinear Response Near Limit Points, Edited by W. Wunderlich, E. Stein, and K. J. Bathe.* Springer-Verlag, Berlin, 1981.

[49] J. L. Batoz, and G. Dhatt. Incremental displacement algorithms for non-linear problems. *International Journal for Numerical Methods in Engineering*, 14 (8): 1262-1266, 1979.

[50] R. D. Cook, D. S. Malkus, M. E. Plesha, and R. J. Witt. *Concepts and Applications of Finite Element Analysis*. John Wiley & Sons, 4th Edition, New York, 2002.

[51] K. J. Bathe. *Finite Element Procedures*. Prentice Hall, New Jersey, 1996.

[52] G. M. Stanley, and C. A. Felippa. Computational procedures for postbuckling of composite shells. *N89-24642, NASA Technical Paper*, 1989.

[53] S. Nagendra, Z. Gurdal, and R. T. Hafta. Buckling and failure characteristics of compression-loaded stiffened composite panels with a hole. *Composite Structures*, 28 (1): 1-17, 1994.

[54] B. G. Falzon, and D. Hitchings. The behaviour of compressively loaded stiffener runout specimens - Part II: Finite Element Analysis. *Journal of Composite Materials*, 37 (6): 481-501, 2003.

[55] N. F. Knight Jr., and J. H. Starnes Jr. Postbuckling behaviour of selected curved stiffened graphite-epoxy panels loaded in axial compression. *AIAA Journal*, 26 (3): 344-352, 1988.

[56] K. Vijayaraju, P. D. Mangalgiri, and B. Dattaguru. Experimental study of failure and failure progression in T-stiffened skins. *Composite Structures*, 64 (2): 227-234, 2004.

[57] B. G. Falzon, G. A. O. Davies, and E. Greenhalgh. Failure of thick-skinned stiffener runout sections loaded in uniaxial compression. *Composite Structures*, 53 (2): 223-233, 2001.

[58] B. G. Falzon, and G. A. O. Davies. The behaviour of compressively loaded stiffener runout specimens - Part I: Experiments. *Journal of Composite Materials*, 37 (5): 381-400, 2003.

[59] E. Greenhalgh, and H. G. Garcia. Fracture mechanisms and failure processes at stiffener run-outs in polymer matrix composite stiffened panels. *Composites: Part A*, 35 (12): 1447-1458, 2004.

[60] C. Meeks, E. Greenhalgh, and B. G. Falzon. Stiffener debonding mechanisms in post-buckled CFRP aerospace panels. *Composites: Part A*, 36 (7): 934-946, 2004.

[61] E. Greenhalgh, S. M. Bishop, and D. Bray. Characterization of impact damage in skin-stringer composite structures. *Composite Structures*, 36 (3-4): 187-207, 1996.

[62] J. F. M. Wiggenraad, P. Arendsen, and J. M. da Silva Pereira. Design optimization of stiffened composite panels with buckling and damage tolerance constraints. *AIAA Paper 98-1750*: 420-430, 1998.

[63] J. F. M. Wiggenraad, R. W. A. Vercammen, P. Arendsen, and L. C. Ubels. Design optimization of stiffened composite panels for damage resistance. *41st AIAA/ASMIE/ASCE/AHS/ASC Structures, Structural Dynamics, and Materials Conference and Exhibit*, Atlanta, GA, 3-6 April 2000.

[64] J. W. H. Yap, M. L. Scott, R. S. Thomson, and D. Hachenberg. The analysis of skin-to-stiffener debonding in composite aerospace structures. *Composite Structures*, 57 (1-4): 2002.

[65] N. D. Fleshner, and C. T. Herakovich. Predicting delamination in composite structures: Advances in the statics and dynamics of delamination. *DLR*, Germany, 2003.

[66] A. A. Griffith. The phenomena of flow and rupture in solids. *Philosophical Transactions of the Royal Society, A221*, 163-198, 1920.

[67] G. R. Irwin. *Fracture*. Handbuch der Physik, Vol. V, Springer, New York, 1958.

[68] D. S. Dudgale. Yielding of steel sheets containing slits. *Journal of the Mechanics and Physics of Solids*, 8: 100-104, 1960.

[69] G. I. Barenblatt. Mathematical theory of equilibrium cracks in brittle failure. *Advances in Applied Mechanics*, 77: 55-129, 1962.

[70] S. T. Pinho, L. Iannucci, and P. Robinson. Formulation and implementaion of decohesion elements in an explicit finite element code. *Composites: Part A*, 37: 778-789, 2006.

[71] W. Cui, M. R. Wisnom, and M. Jones. A comparison of failure criteria to predict delamination of unidirectional glass/epoxy specimens waisted through the thickness. *Composites*, 23 (3): 158-166, 1992.

[72] M. L. Benzeggagh, and M. Kenane. Measurement of mixed-mode delamination fracture toughness of unidirectional glass/epoxy composites with mixed-mode bending apparatus. *Composites Science and Technology*, 56 (4): 439-449, 1996.

[73] J. P. M. Goncalves, M. F. De Moura, P. T. De Castro, and A. T. Marques. Interface element including point-to-surface constraints for three-dimensional problems with damage propagation. *Engineering Computations*, 17 (1): 28-47, 2000.

[74] G. Alfano, and M. A. Crisfield. Finite element interface models for the delamination analysis of laminated composites: mechanical and computational issues. *International Journal for Numerical Methods in Engineering*, 50: 1701–1736,

[75] M. J. Shuart, D. R. Ambur, D. D. J. Davis, R. C. Davis, F. L. Farley, C. G. Lotts, and J. T. Wang. Technology integration box beam failure study. *NASA Technical Report N95-28847*, 1992.

[76] D. D. J. Davis, F. L. Farley, D. R. Ambur, R. C. Davis, M. J. Shuart, J. T. Wang, and C. G. Lotts. An analytically designed subcomponent test to reproduce the failure of a composite wing box beam. *AIAA Conference Paper 93-1344*, 1993.

[77] W. G. Brooks. Load test report on compression stiffener runout panel. *BAE Report*, 1995.

[78] B. G. Falzon, D. Hitchings, and G. A. O. Davies. Failure prediction of thick structural composites. *Final Report, SMC/4/969, Imperial College of Science, Technology & Medicine, London , UK*, 2000.

[79] B. G. Falzon, D. Hitchings, and T. Besant. Fracture mechanics using a 3D composite element. *Composite Structures*, 45 (1): 29-39, 1999.

[80] BAE. Skin/Stringer interface bond: Mode I and Mode II fracture toughness tests. *National Physics Laboratory, Teddington, UK*, 1999.

[81] W. Cui, M. R. Wisnom, and M. I. Jones. Effect of through thickness tensile and compressive stresses on delamination propagation fracture energy. *Journal of Composite Technology and Research*, 16 (4): 329-335, 1994.

[82] Z. Gurdal, R. T. Hafta, and P. Hajela. *Design and Optimization of Laminated Composite Materials*. John Wiley & Sons, Inc., 1st Edition, New York, NY, 1999.

[83] J. S. Arora. *Introduction to optimum design*. McGraw-Hill, New York, 1989.

[84] R. T. Haftka, and Z. Gurdal. *Elements of structural optimization*. Kluwer Academic, 3rd Edition, Dordrecht, 1992.

[85] S. Adali, A. Richter, V. E. Verijenko, and E. B. Summers. Optimal design of hybrid laminates with discrete ply angles for maximum buckling load and minimum cost. *Composite Structures*, 32 (1-4): 409-415, 1995.

[86] S. Adali, M. Walker, and V. E. Verijenko. Multi-objective optimization of laminated plates for maximum prebuckling, buckling and postbuckling strength using continuous and discrete ply angles. *Composite Structures*, 35 (1): 117-130, 1996.

[87] S. Adali, F. Lene, G. Duvaut, and V. Chiaruttini. Optimization of laminated composites subject to uncertain buckling loads. *Composite Structures*, 62 (3-4): 261-269, 2003.

[88] G. B. Chai, K. T. Ooi, and P. W. Khong. Buckling strength optimization of laminated composite plates. *Composites & Structures*, 46 (1): 77-82, 1993.

[89] P. W. Khong. Development of a microcomputer finite strip analysis for thin walled structures. *University of Strathaclyde, PhD Thesis*, 1988.

[90] G. B. Chai, and P. W. Khong. Stability study of coupling responses in laminates. *Journal of Composites Technology and Research*, 13 (3): 187-190, 1991.

[91] M. J. Box. A new method of constraints optimization and comparison with other methods. *The Computer Journal*, 8 (1): 42-52, 1965.

[92] W. Spendley, G. R. Hext, and F. R. Himsworth. Sequential application of simplex designs in optimization and evolutionary operation. *Technometrics*, 4 (4): 441-461, 1962.

[93] J. A. Nelder, and R. Mead. A Simplex method for function minimisation. *The Computer Journal*, 7 (1): 308-313, 1964.

[94] M. Walker, S. Adali, and V. E. Verijenko. Optimization of symmetric laminates for maximum buckling load including the effects of bending-twisting coupling. *Computers & Structures*, 58 (2): 313-319, 1996.

[95] M. Walker, S. Adali, and V. E. Verijenko. Optimal design of symmetric angle-ply laminates subject to nonuniform buckling loads and in-plane restraints. *Thin Walled Structures*, 26 (1): 45-60, 1996.

[96] M. Walker. Optimal design of symmetric laminates with cutouts for maximum buckling load. *Computers & Structures*, 70 (3): 337-343, 1999.

[97] M. Walker, and T. Reiss. Application of MATHEMATICA to the optimal design of composite shells for improved buckling strength. *Engineering Computations*, 15 (2): 260-267, 1998.

[98] H. Fukunaga, H. Sekine, M. Sato, and A. Iino. Buckling design of symmetrically laminated plates using lamination parameters. *Computers & Structures*, 57 (4): 643-649, 1995.

[99] G. N. Vanderplaats, and H. Sugimoto. A general purpose optimization program for engineering design. *Computer and Structures*, 24 (1): 13-21, 1986.

[100] M. G. Joshi, and S. B. Biggers Jr. Thickness optimization for maximum buckling loads in composite laminated plates. *Composites Part B: Engineering*, 27 (2): 105-114, 1996.

[101] H. Hu, and Z. Chen. Buckling optimization of unsymmetrically laminated plates under transverse loads. *Structural Engineering and Mechanics*, 7 (1): 19-33, 1999.

[102]H. Hu, and B. Lin. Buckling optimization of symmetrically laminated plates with various geometries and end conditions. *Composites Science and Technology*, 55 (3): 277-285, 1995.

[103]H. C. Mateus, C. M. Mota Soares, and C. A. Mota Soares. A model for the optimum design of thin laminated plate-shell structures for static, dynamic, and buckling behaviour. *Composite Structures*, 32 (1): 60-79, 1995.

[104]G. N. Vanderplaats. *Numerical optimization techniques for engineering design with applications*. McGraw-Hill, Chapter 6, New York, 1984.

[105]C. G. Diaconu, M. Sato, and H. Sekine. Buckling characteristics and layup optimization of long laminated composite cylindrical shells subjected to combined loads using lamination parameters. *Composite Structures*, 58 (4): 423-433, 2002.

[106]P. Kere, M. Lyly, and J. Koski. Using multicriterion optimization for strength design of composite laminates. *Composite Structures*, 62 (3-4): 329-333, 2003.

[107]P. Kere, and J. Koski. Multicriterion optimization of composite laminates for maximum failure margins with an interactive descent algorithm. *Structural and Multidisciplinary Optimization*, 23 (6): 436-447, 2002.

[108]Y. Narita, and G. J. Turvey. Maximizing the buckling loads of symmetrically laminated composite rectangluar plates using a layerwise optimization approach. *Proceedings of*

the Institution of Mechanical Engineers, Part C: Journal of Mechanical Engineering Science, 218 (7): 681-691, 2004.

[109]Y. Narita. Layerwise optimization for the maximum fundamental frequency of laminated composite plates. *Journal of Sound and Vibration*, 263 (5): 1005-1016, 2003.

[110]E. Carrera, L. Mannella, G. Augello, and N. Gualtieri. A two-level optimization feature for the design of aerospace structures. *Proceedings of the Institution of Mechanical Engineers*, 217 Part G: 189-206, 2003.

[111]D. Bushnell. PANDA2-program for minimum weight design of stiffned, composite, locally buckled panels. *Computer and Structures*, 25 (4): 469-605, 1987.

[112]D. Bushnell, and C. C. Rankin. Optimization of stiffened panels in which mode jumping is accounted for. *AIAA Paper 97-1141*: 105-145, 1998.

[113]C. C. Rankin, S. P., and F. A. Brogan. Enhancements to the STAGS computer code. *NASA CR 4000, NASA Langley Research Center*, Hampton, VA, 1986.

[114]A. H. Land, and A. G. Doig. An automatic method for solving discrete programming problems. *Econometrica*, 28 (3): 497-520, 1960.

[115]P. J. M. van Laarhoven, and E. Aarts. *Simulated annealing: theory and applications.* D. Reidel Publishing, Dordrecht, The Netherlands, 1987.

[116]D. E. Goldberg. *Genetic Algorithms in Search, Optimization, and Machine Learning.* Addison-Wesley Publishing Co. Inc., 1st Edition, Reading, MA., 1989.

[117]J. H. Holland. *Adaptation in natural and artificial systems.* University of Michigan Press, Ann Arbor, MI, 1975.

[118]R. Le Riche, and R. T. Haftka. Optimization of laminate stacking sequence for buckling load maximization by genetic algorithm. *AIAA Journal*, 31 (5): 951-970, 1993.

[119]R. Le Riche, and R. T. Haftka. Improved genetic algorithm for minimum thickness composite laminate design. *Composites Engineering*, 5 (2): 143-161, 1994.

[120] N. Kogiso, L. T. Watson, Z. Gurdal, R. T. Hafta, and S. Nagendra. Minimum thickness design of composite laminates subject to buckling strength constraints by genetic algorithm. *Mechanics of Composite Materials and Structures* 1(1): 95-117, 1994.

[121]J. H. Park, J. H. Hwang, C. S. Lee, and W. Hwang. Stacking sequence design of composite laminates for maximum strength using genetic algorithms. *Composite Structures*, 52 (2): 217-231, 2001.

[122]J. Kang, and K. Chun-gon. Minimum-weight design of compressively loaded composite plates and stiffened panels for postbuckling strength by genetic algorithm. *Composite Structures*, 69 (2): 239-246, 2003.

[123]J. S. Kim, C. G. Kim, and C. S. Hong. Optimum design of composite structures with ply drop using genetic algorithm and expert system shell. *Composite Structures*, 46 (2): 171-187, 1999.

[124]S. Nagendra, D. Jestin, Z. Gurdal, R. T. Hafta, and L. T. Watson. Improved genetic algorithm for the design of stiffened composite panels. *Computers & Structures*, 58 (3): 543-555, 1996.

[125]V. B. Gantovnik, Z. Gurdal, and L. T. Watson. A genetic algorithm with memory for optimal design of laminated sandwich composite panels. *Composite Structures*, 58 (4): 513-520, 2002.

[126]V. B. Gantovnik, C. M. Anderson-Cook, Z. Gurdal, and L. T. Watson. A genetic algorithm with memory for mixed discrete-continuous design optimization. *Computers & Structures*, 81 (20): 2003-2009, 2003.

[127]C.-C. Lin, and Y.-J. Lee. Stacking sequence optimization of laminated composite structures using genetic algorithm with local improvement. *Composite Structures*, 63 (3-4): 339-345, 2004.

[128]M. Di Sciuva, M. Gherlone, and D. Lomario. Multiconstrained optimization of laminated and sandwich plates using evolutionary algorithms and higher-order plate theories. *Composite Structures*, 59 (1): 149-154, 2003.

[129]D. B. Adams, L. T. Watson, Z. Gurdal, and C. M. Anderson-Cook. Genetic algorithm optimization and blending of composite laminates by locally reducing laminate thickness. *Advances in Engineering Software*, 35 (1): 35-43, 2004.

[130]W. Hansel. A heuristic and a genetic topology optimization algorithm for weight-minimal laminate structures. *Composite Structures*, 58 (2): 287-294, 2002.

[131]A. Todoroki, and T. Ishikawa. Design of experiments for stacking sequence optimization with genetic algorithm using response surface approximation. *Composite Structures*, 64 (3-4): 349-357, 2004.

[132]C. Bisagni, and L. Lanzi. Post-buckling optimization of composite stiffened panels using neural networks. *Composite Structures*, 58 (2): 237-247, 2002.

[133]L. Lanzi, and C. Bisagni. Minimum weight optimization of composite stiffened panels using neural networks. *44th AIAA/ASME/ASCE.AHS Structures, Structural Dynamics, and Materials Conference*, Norfolk, VA, April 7-10, 2003.

[134]R. T. Hafta, and J. L. Walsh. Stacking-sequence optimization for buckling of laminated plates by integer programming. *AIAA Journal*, 30 (3): 814-819, 1992.

[135]S. W. Tsai. *Composite Materials Workshop.* Technomic Publishing Co., 1st Edition, Stamford, CT, 1968.

[136]D. Hull. *An Introduction to Composite Materials.* Cambridge University Press, Cambridge, UK, 1981.

[137]M. P. Nemeth. Importance of anisotropy on buckling of compression-loaded symmetric composite plates. *AIAA Journal*, 24 (11): 1831-1835, 1986.

[138]A. Chipperfield, P. Fleming, H. Pohlheim, and C. Fonseca. Genetic algorithm toolbox user's guide. *University of Sheffield*, Sheffield, UK, 1994.

[139]L. Booker. *Improving Search in Genetic Algorithms, in Genetic Algorithms and Simulated Annealing, Edited by L. Davis.* Morgan Kaufmann Publishers, Inc., Los Altos, CA, 1987.

[140]K. A. De Jong. Analysis of the behaviour of a class of genetic adaptive systems. *University of Michigan, Doctoral Dissertation Thesis*, 1975.

[141]C. Bisagni, and P. Cordisco. Testing of stiffened composite cylindrical shells in the postbuckling range until failure. *AIAA Journal*, 42 (9): 1806-1817, 2004.

[142]C. Bisagni, and P. Cordisco. Post-buckling and collapse experiments of stiffened composite cylindrical shells subjected to axial loading and torque. *Composite Structures*, 73 (2): 138-149, 2006.

[143]Y. Mi, and M. A. Crisfield. Analytical derivation of load/displacement relationships for mixed-mode delamination and comparison with finite element results. *Department of Aeronautics, Imperial College London*, London, 1996.

[144]Y. Mi, M. A. Crisfield, G. A. O. Davies, and H. B. Hellweg. Progressive delamination using interface elements *Journal of Composite Materials*, 32 (14): 1246-1272, 1998.

Appendix A

Double cantilever beam problem for interface element validation

The interface element formulation presented in Chapter 5 needs to be validated with problems where an analytical solution is known prior to the modelling of complicated structural components. Traditionally, interface element validation is done by modelling three different standard tests – a double cantilever (DCB) test, an end notched flexure (ENF) test, and a Mixed Mode Bending (MMB) test. DCB tests aim to replicate pure Mode I loading, ENF tests pure Mode II, and MMB tests mixed mode loading. Since such element validation has been done by a variety of authors, and only a DCB problem is considered here by creating an ABAQUS model and comparing the numerical solution with closed form solutions proposed by Mi and Crisfield [143] and Mi et al. [144].

Figure A.1 shows the DCB problem considered. It consists of a beam of length *L*, unit width *B*, second moment of area *I*, which is made of an isotropic material with a Young's modulus *E*. The height of the beam is *2h*, with the interface where crack propagation can occur located on the central longitudinal axis of symmetry of the beam. The initial crack has a length *a*, and in order to propagate this crack further into the beam, a displacement controlled opening load is applied at the left hand end as illustrated. The right hand side of the beam is considered clamped. The beam considered was modelled in 2D, and hence a unit width *B* was taken.

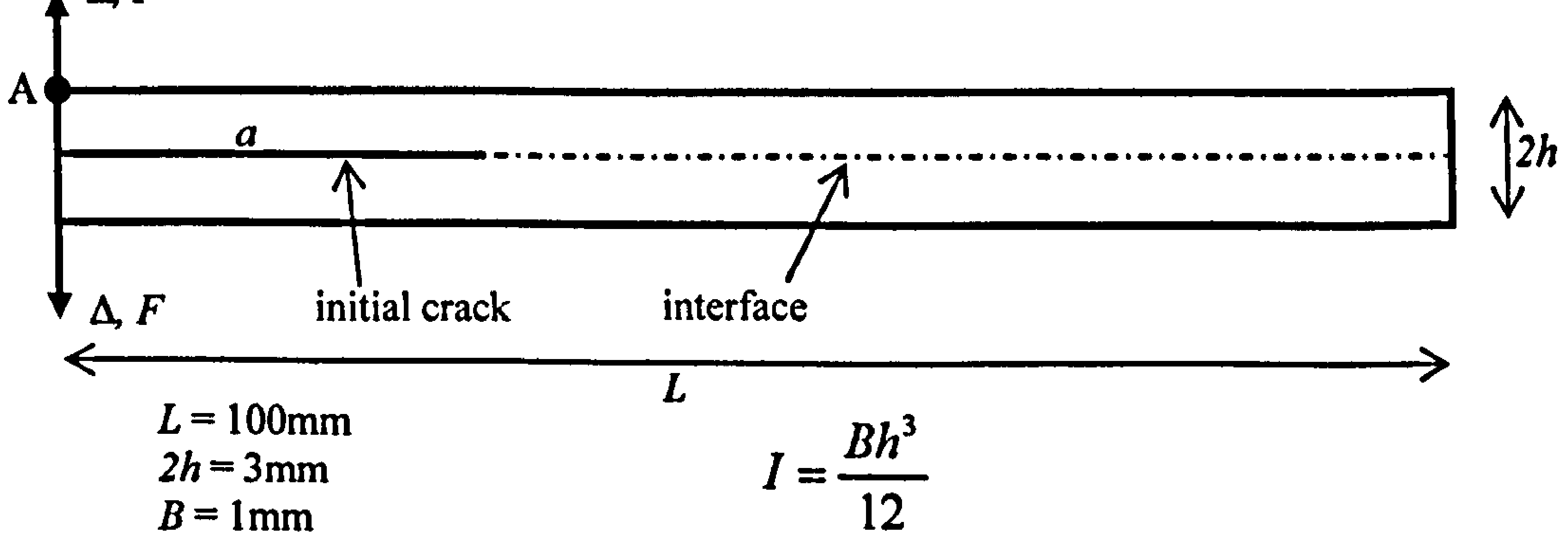

Figure A.1: DCB test problem for interface element validation.

The configuration shown in Figure A.1 was modelled in ABAQUS. Four-noded bilinear elements were used to model the beam, with two elements above the interface and two elements below. The number of elements in the lengthwise direction of the beam was altered to asses the mesh sensitivity of the problem. A range of 100 to 400 elements along the beam length were used. The same mesh density was used in the interface, were zero-thickness interface elements were inserted to model the propagation of the crack. The beam material was given a Young's modulus E = 135,000 N/mm^2 and Poisson's ratio ν = 0.25, whilst the interface elements were given a bilinear traction separation law. The constitutive law for the interface elements was described via the parameters listed in Table A.1 as explained in Chapter 5.

Table A.1: DCB interface properties.

Property	Value
k	6.0 x 10^6 N/mm^3
σ_{0I}	60.0 MPa
$G_{IC} = G_C$	0.06 J/m^2

Analytical solutions to validate the FE model for the DCB problem can be found via the use of beam theory and fracture mechanics [143]. Before damage starts to grow:

$$F = \frac{3BEI}{a^3}\Delta \tag{A.1}$$

and during the propagation of damage:

$$F = B\sqrt{\frac{(G_C EI)^{3/2}}{3EI\Delta}} \tag{A.2}$$

An investigation was conducted to see how accurately the interface elements in ABAQUS were able to track the analytical solutions. This involved assessing both mesh sensitivity and the viscosity parameter to be used in viscous regularization. Viscous regularization is an analysis technique to overcome the convergence difficulties that arise with material models exhibiting softening behaviour and degradation in their stiffness. This technique modifies the constitutive equations presented earlier, causing the tangent stiffness matrix of the softening material (the interface elements) to be positive for sufficiently small time increments. The addition of viscous regularization permits stresses in the cohesive elements to exist outside the bounds set by the traction-separation law. ABAQUS defines a viscous stiffness degradation variable D_v which is defined by the following evolution equation:

$$\dot{D}_v = \frac{1}{\mu}(D - D_v) \tag{A.3}$$

μ is the viscosity parameter, and represents the relaxation time of the viscous system, and D is the scalar damage variable for the fully inviscid model. The damaged response of the material, with viscous effects included, is then be given by:

$$\boldsymbol{\sigma} = (1 - D_v)\overline{\boldsymbol{\sigma}} \tag{A.4}$$

where $\boldsymbol{\sigma}$ is the stress vector for the damaged model, and $\overline{\boldsymbol{\sigma}}$ the stress vector predicted by the elastic traction-separation behaviour for the current strains without damage. A value for the viscosity parameter μ must be entered in ABAQUS when using this technique. A small value will help improve the rate of convergence, without compromising the results. Too high a value has the danger of modifying the results erroneously. The solution of the viscous system relaxes to the solution of the inviscid case as $t/\mu \rightarrow \infty$ where t represents time.

Parametric studies are presented here for meshes of 100x4, 150x4, 200x4, 300x4, and 400x4. The mesh sensitivity is assessed, but before this is done the effect of changing the viscosity parameter was investigated. This was done by running the problem with decreasing viscosity for different mesh densities. Once a suitable value of the viscosity parameter was found that is not seen to alter the results erroneously for any of the mesh densities, then this was used to asses the mesh sensitivity of the problem. Representative results are shown here, with Figure A.2 pertaining to the 200x4 mesh. Here the viscosity parameter was gradually reduced and the load-displacement numerical curve for the point labelled A in Figure A.2 shown in conjunction with the analytical solution. It is clear how the results do not converge when an excessive amount of viscous regularization is used. As this value is reduced, then results closely match the analytical expressions as can be seen by the green curve. Reducing the viscosity parameter further leads to increases in computational cost with no changes in the results obtained.

Figure A.3 shows results for different mesh densities using a very small amount of viscous regularization, corresponding to a value of 10^{-6}. The coarser 100x4 mesh shows some oscillating behaviour. This could be attributed to the fewer interface elements undergoing the stiffness degradation. This means that as each element damages, a rather sudden load drop occurs. Refined meshes show convergent results, which are very accurate especially in the second portion of the curve relating to the crack propagating along the interface. A difference can be seen in the maximum load attained between the analytical solution and the numerical FE results. This can be explained by the non-linear analysis used by ABAQUS resulting in some elements initiating damage just before the load peak. From the simple DCB problem investigated it can be concluded that the interface elements behaved extremely well in the modelling of pure Mode I loading. In particular, very good agreement is seen between the analytical and numerical curves during crack propagation. Nonetheless, care must be taken in making sure that a sufficiently fine mesh is used and that a small enough value for viscosity parameter is input relating to viscous regularization. This analysis option aids greatly in improving convergence but too high a viscosity parameter can lead to erroneous results.

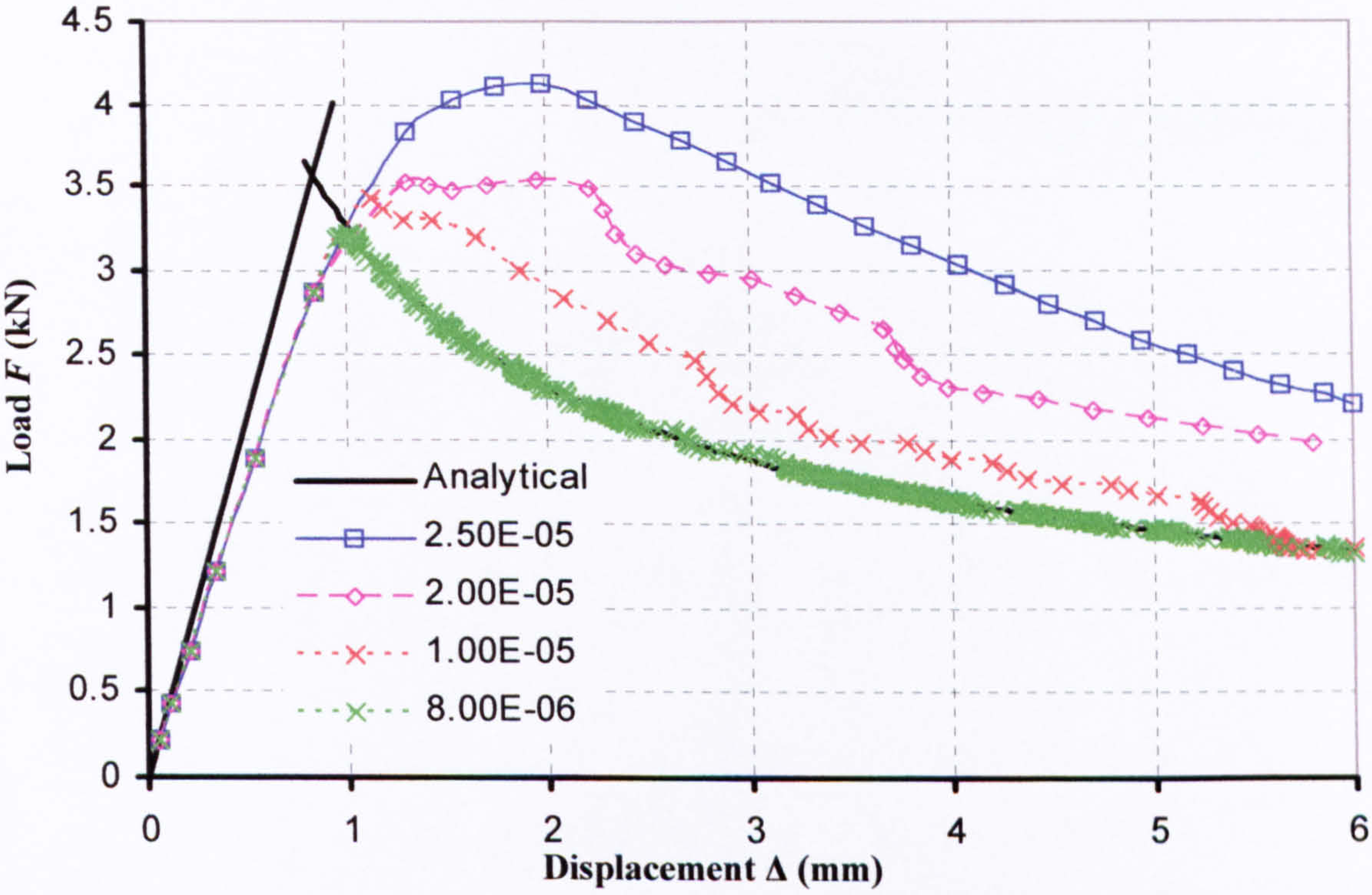

Figure A.2: Sensitivity of DCB model to viscous regularization viscosity parameter μ in interface elements.

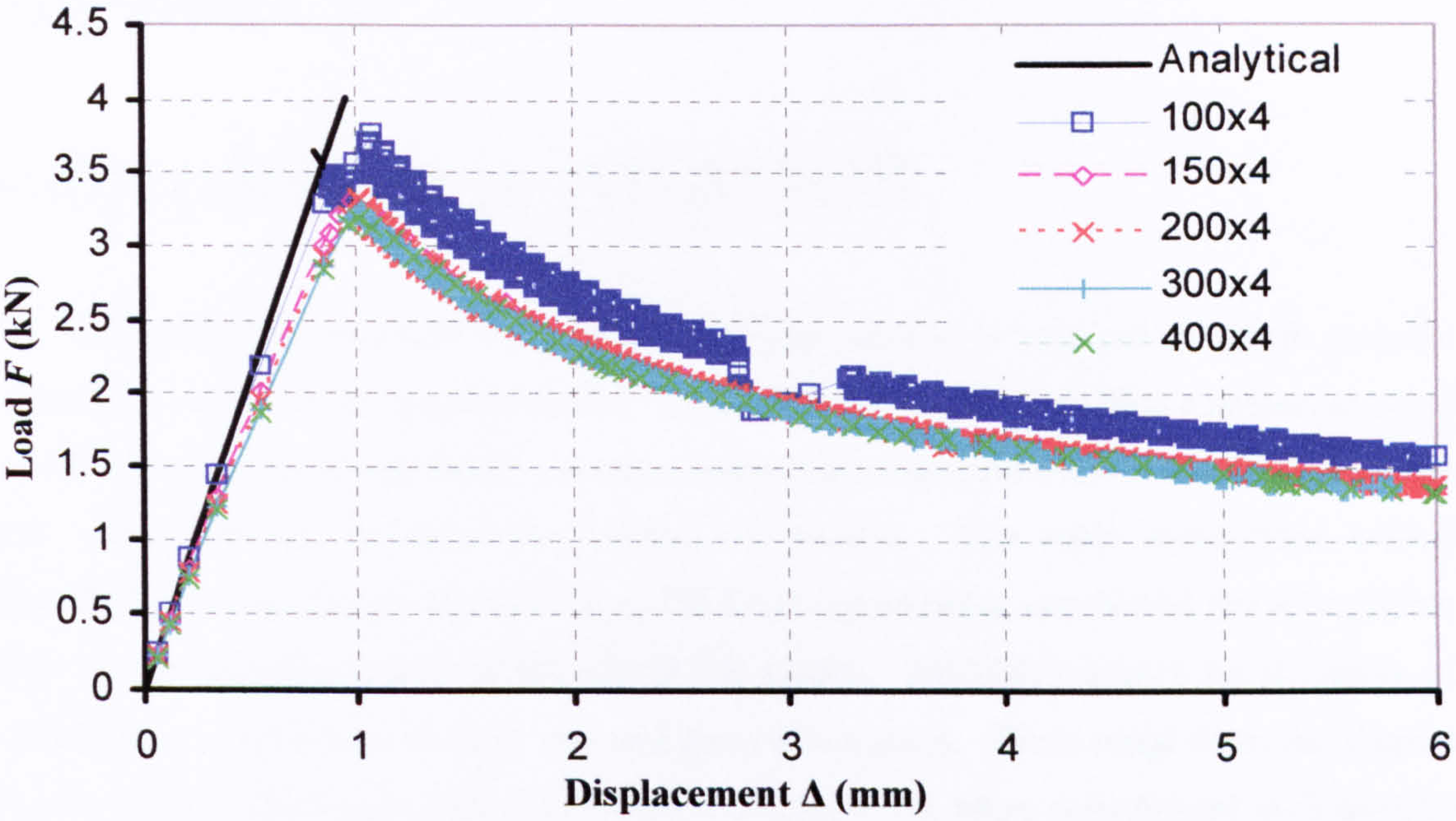

Figure A.3: Mesh sensitivity of DCB model for very low value of viscous regularization.

Appendix B

Submodelling in ABAQUS

Generally, the submodelling technique is used when it is required to obtain accurate results for a local part of a specific model. First a solution is obtained using a coarser mesh of what is termed as the global model, and then interpolation of these results is used to drive the local, more detailed model of the section of interest. The main assumption behind submodelling is that detailed modelling of the local region being considered has a negligible effect on the overall solution of the global FE model. ABAQUS allows for a variety of submodelling capabilities, for both two and three dimensions. These range from the simpler cases of shell-to-shell and solid-to-solid submodelling to the more complicated shell-to-solid submodelling where a shell element global model is used to drive a global model made of solid 3D elements.

A submodelling procedure will require two models, termed the global model and the local model. Once the solution on the global model is found, then this is used to drive the local model. Prior to doing so, the degree of freedoms at nodes on the local model boundary whose values are to be found by interpolation of the global solution need to be defined. These are called driven variables. In ABAQUS the global and local models are run as two completely separate analyses. The only link between the two is the fact that the solution to the global model acts as a boundary condition to the local model by transferring the time-dependent values of variables saved in the global analysis and applying them as prescribed conditions on the refined local model. It is the fashion in which this occurs, coupled with the correct definition of the driven nodes, that will determine the accuracy of the resulting local model analysis. A submodelling procedure can be divided into four distinct steps:

- Development and analysis of the global model and saving of the results in the vicinity of the local model boundary.
- Development of the local model and definition of those nodes which are to be driven by the global model solution.
- Definition of the degrees of freedom to be driven at the local model nodes and any time scaling to be applied on such driven variables.
- Analysis of the local model where the driven degrees of freedom effectively have prescribed boundary conditions from the global model solution.

Figure B.1 shows a simple example of how a global and local model would be linked. The green mesh corresponds to the global model, and the nodes highlighted in blue are those nodes – the driving nodes – which are in the vicinity of the local model boundary at which the solution must be saved. The red line shows the boundary of the local model, which is composed of the driven nodes. The submodelling functionality of ABAQUS is very flexible so that both the global and local models can have nonlinear responses and be analyzed in any sequence of analysis procedures. Time scaling of the solution may also be applied, in the sense that ABAQUS associates a time step even for quasi-static analyses. In this case a time step ranging from zero to one is applied, and in the case of displacement controlled loading, the displacement is ramped linearly over the time step. By default the local model has the same time scale as the global model, but this may be scaled to suit particular design purposes.

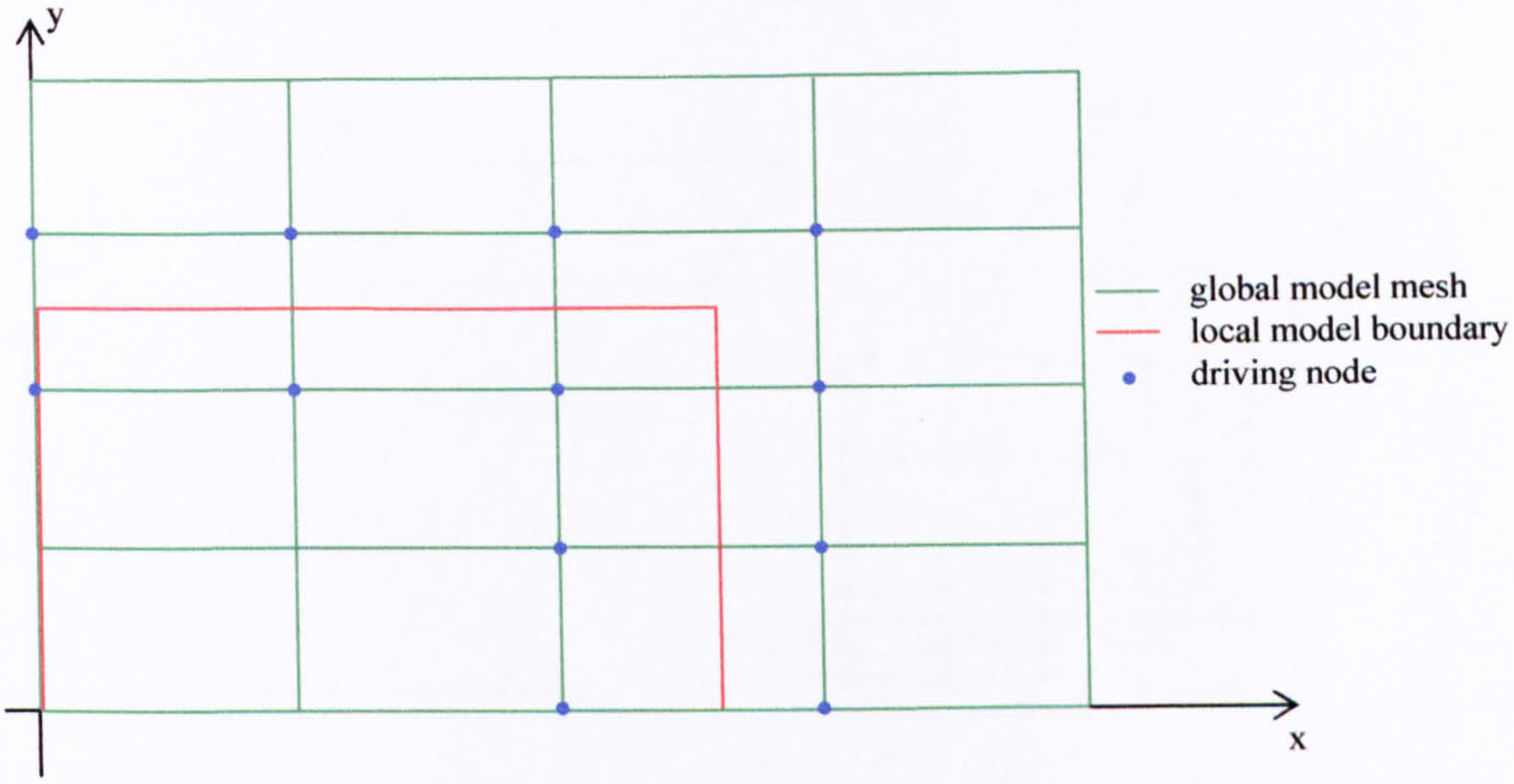

Figure B.1: Simple mesh showing the concept of global-local submodelling.

Figure B.1 is a simple 2D case of a shell-to-shell submodelling where both the global and local models are meshed using conventional shell elements. Particularly powerful however is the possibility to use a global model composed entirely of shell elements and couple this with a local model of solid elements. This guarantees the cheap computational cost of the shell elements in obtaining a solution field for the global model and then using this solution to drive a more detailed local model with solid elements so as to capture particular details and effects. When using such shell-to-solid submodelling, the specification of the driven nodes in the local model as well as which degrees of freedom are driven becomes of paramount importance. This is particularly true since a conventional shell element will have six degrees of freedom at each node, associated with three translations and three rotations at its reference mid-surface. However, a local model with solid elements would have only the three translational degrees of freedom at its nodes, and a physical representation of its geometric thickness unlike the shell element global model.

B.1 Establishing driven nodes in shell-to-solid submodelling

In shell-to-solid submodelling the FE model corresponding to the global model must be meshed solely with conventional shell elements, and the local model with solid elements. These include brick elements as well as the continuum shell elements first discussed in the modelling of the stiffener runout specimens in Chapter 6 as the latter discretize a body in much the same way as the former. The complexity in shell-to-solid submodelling arises form the fact that in the global model the shell reference surface acts as the "driver" for the local model. Hence the shell reference surface – a set of lines – must drive a set of surfaces which exist in the solid local model. This is best shown graphically in Figure B.2.

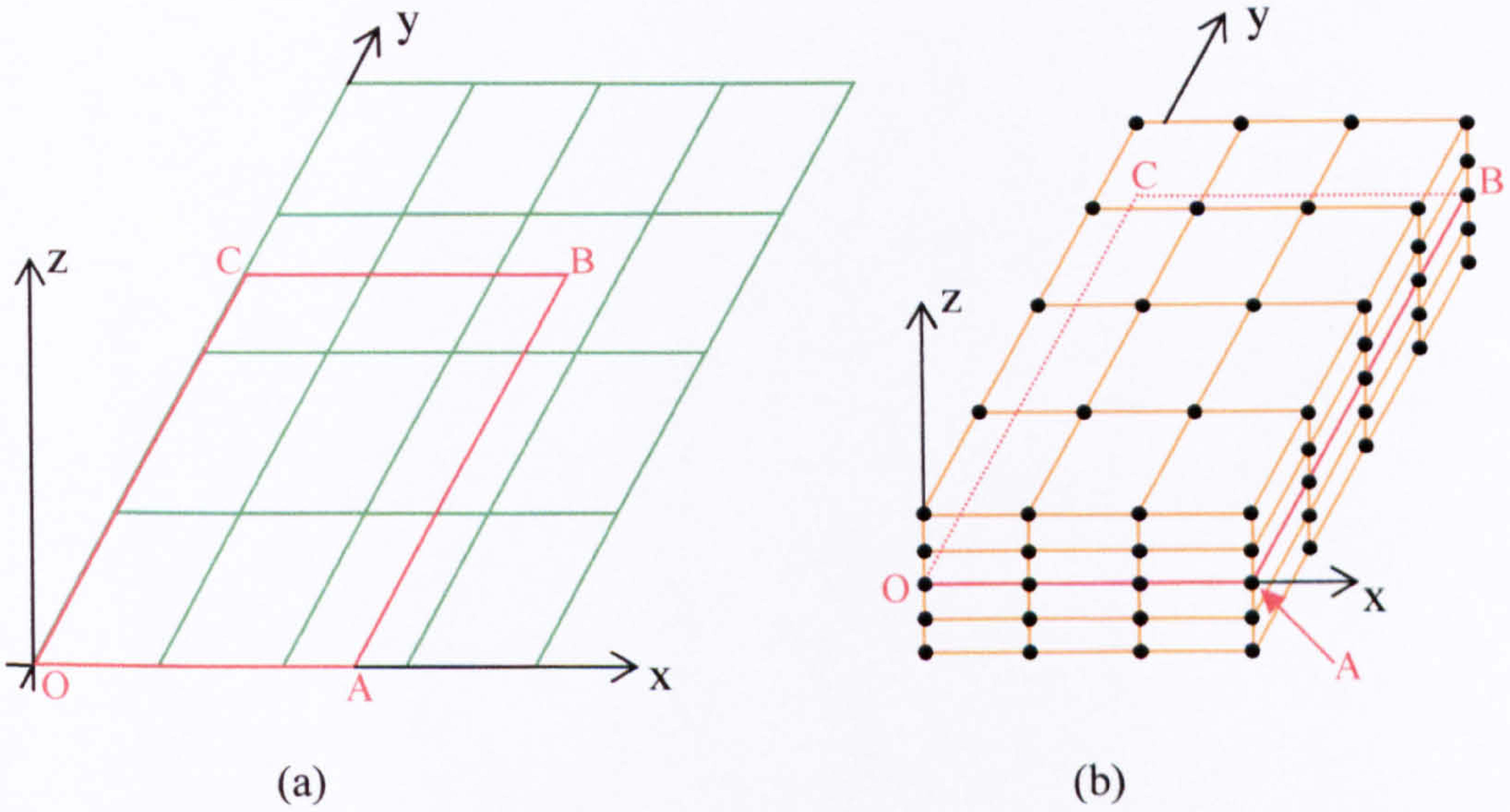

Figure B.2: Schematic showing a shell global model mesh (a) with corresponding solid local model mesh (b).

Figure B.2 (a) shows a simple shell global model, with the area OABC corresponding to the shell mid-surface of the region required to be analyzed in more detail via a local model of solid elements. The same colour coding as in Figure B.1 is used, where the global model mesh is shown in green, whilst red indicates the local model boundary. The corresponding local model is shown in Figure B.2 (b). What was the shell mid-surface has now "acquired" a thickness due to the use of the solid elements, shown in orange. It is clear from Figure B.2 how powerful this method is, particularly when applied to a composite. The mesh shown in Figure B.2 (a) could represent a conventional shell element lay-up of a particular four-ply laminate, and then a particular region of interest could be modelled locally with a solid element per ply in the thickness direction as in Figure B.2 (b).

ABAQUS uses a geometric tolerance system to define how far a node on the boundary of the local model can lie outside the exterior surface of the global model. In shell-to-solid submodelling two tolerances are established so as to determine the exact relationship between the local and global models. Figure B.3 shows part of a local model mesh with its corresponding local model. It is illustrated how an "image" node is produced, corresponding to the closest point on the shell reference surface of the global model. This image node is labelled A in Figure B.3. A user-specified exterior tolerance then determines whether this image node is within the area of influence of the global model. The distance *d* between the image node A and the driven node B on the local solid model is calculated, and if this corresponds to less than half the global model maximum shell thickness *t* plus the specified exterior tolerance *e*, then the node B on the local model is accepted to be driven by the global model.

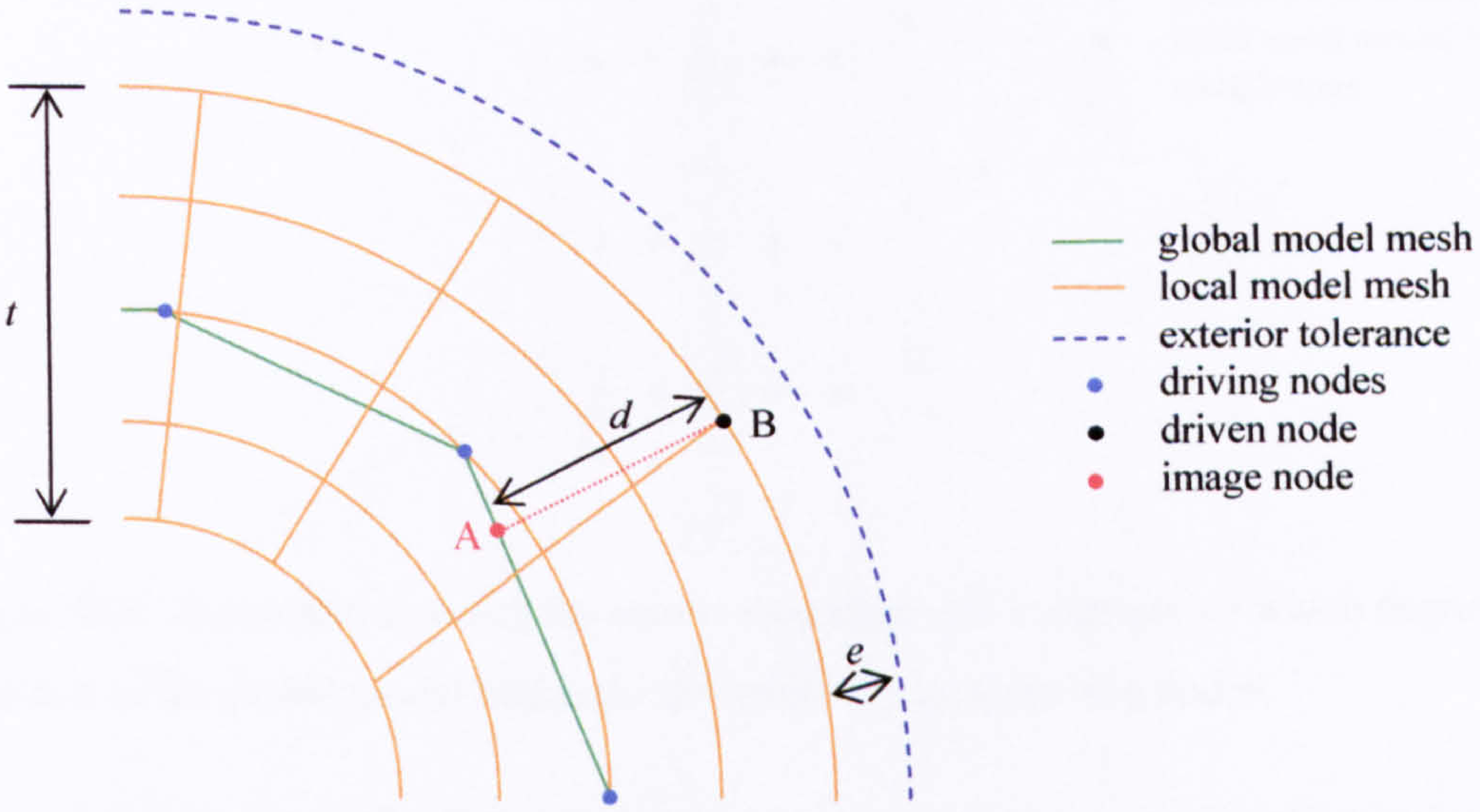

Figure B.3: Schematic showing selection of local model driven nodes in shell-to-solid submodelling.

B.2 Defining driven degrees of freedom in shell-to solid submodelling

As discussed earlier the accuracy of the submodelling procedure will largely depend not only on the correct selection of the driving nodes on the global model, but also on exactly how the degrees of freedom at the nodes of the local variables will be driven by the computed solution on the global model. In the simpler case of shell-to-shell and solid-to-solid submodelling, the user can specify which degrees of freedom are to be driven, relating to translational degrees of freedom for solid elements and translational together with rotational degrees of freedom for conventional shell elements. For shell-to-solid submodelling this is not the case as the global model of conventional shell elements will have rotational degrees of freedom which are not present in the local solid model. However such rotations will have an effect on the translational degrees of freedom at nodes which are not in the same location as the shell mid-surface in the global model. Figure B.4 illustrates this concept together with how ABAQUS automatically chooses those degrees of freedom in the local model which are to be driven based on a user-specified zone – the centre-zone – around the shell mid-surface plane.

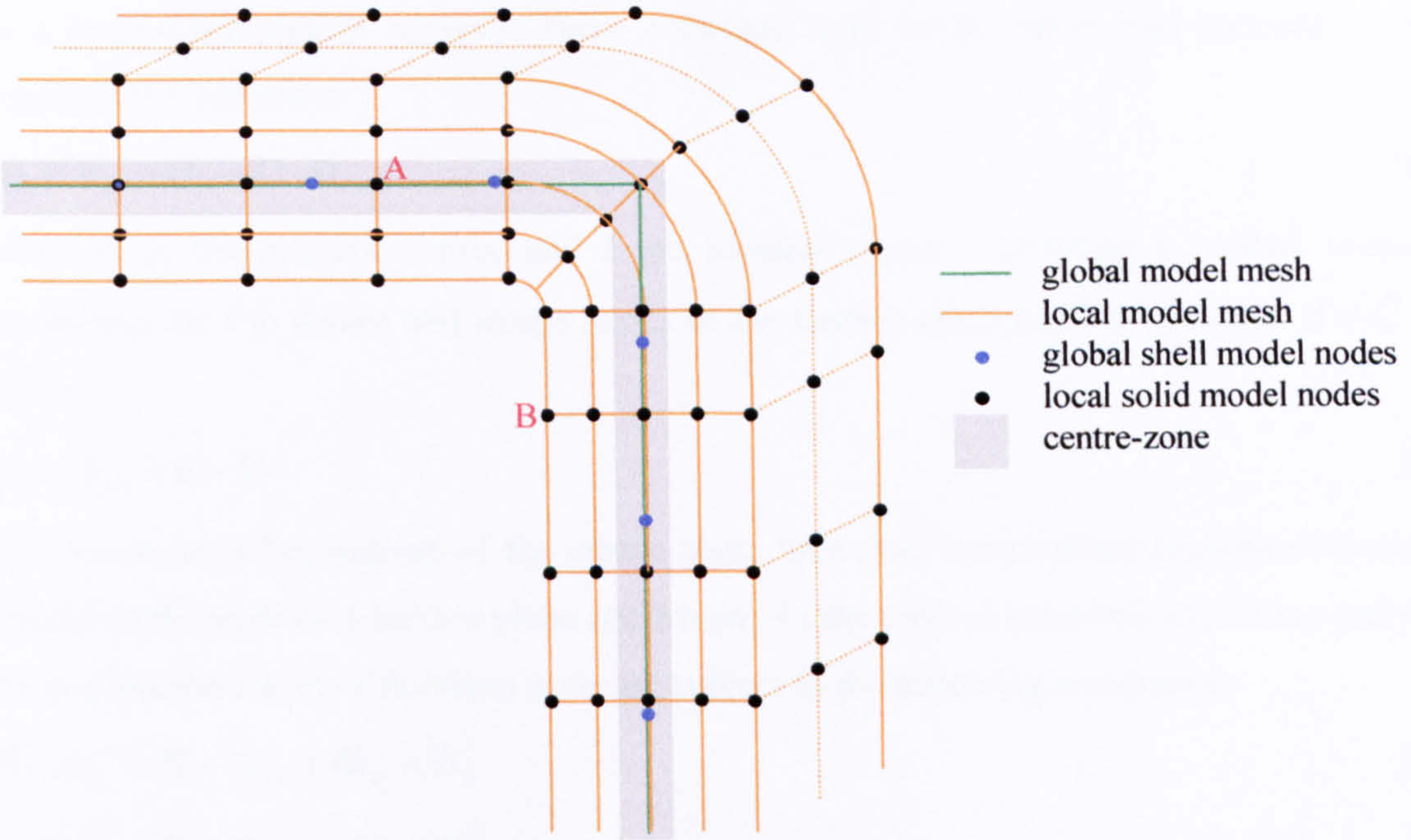

Figure B.4: Schematic showing the centre-zone approach to determine which degrees of freedom of the global model nodes are driven by the local driving nodes.

Again in Figure B.4 the global mesh is shown in green, corresponding to the shell mid-surface. The local model mesh is shown in orange by the solid elements whilst the centre zone is the grey shaded area around the global model shell mid-surface. Those nodes in the local model which lie within the centre zone, such as the node labelled A, will have all their translational degrees of freedom driven by the global model solution. For nodes further away and not within the centre-zone, such as node labelled B, only the translational displacement components parallel to the shell mid-surface plane will be driven. Typically, it is sufficient for just the layer of nodes closest to the shell reference surface to lie within the centre zone as is the case in Figure B.4, but if a very fine mesh is used in the thickness direction in the local model then the centre-zone should be made wider. Two possibilities exist. If a driven node lies within the centre zone, then all its displacement degrees of freedom are driven by the global model solution. In the case of a geometrically linear analysis, the displacements are then found as:

$$\mathbf{u}_L^i = \mathbf{u}_G^i + \mathbf{\Phi}_G^i \times \mathbf{D} \qquad \text{B.1}$$

where the superscript *i* refers to the i'th node, while subscripts *L* and *G* refer to the local and global nodes, the latter being the image nodes. Hence $\mathbf{u}_L^i$ is the displacement vector of the local mode i'th node as a result of being driven by the displacements $\mathbf{u}_G^i$ and rotations $\mathbf{\Phi}_G^i$ of the corresponding image node on the global model. **D** is the vector connecting the image node to the driven node, which have position vectors $\mathbf{X}_G^i$ and $\mathbf{X}_L^i$ respectively:

$$\mathbf{D} = \mathbf{X}_L^i - \mathbf{X}_G^i \tag{B.2}$$

In a large-displacement analysis, finite rotations have to be taken into account so that Equation B.1 becomes:

$$\mathbf{u}_L^i = \mathbf{u}_G^i + (\mathbf{C} - \mathbf{I}) \cdot \mathbf{D} \tag{B.3}$$

where **C** is the rotation matrix and **I** the identity tensor. Defining a rotated vector **d** connecting the i'th driven and image nodes in the current configuration such that $\mathbf{d} = \mathbf{C} \cdot \mathbf{D}$ yields:

$$\mathbf{u}_L^i = \mathbf{u}_G^i + \mathbf{d} - \mathbf{D} \tag{B.4}$$

If a driven node lies outside of the centre zone, then only translational degrees of freedom parallel to the shell mid-surface plane are driven. In the case of geometrically linear analysis, the displacement at the i'th driven node are subject to the following constraints:

$$\mathbf{N}_1 \cdot \mathbf{u}_L^i = \mathbf{N}_1 \cdot \left(\mathbf{u}_G^i + \mathbf{\Phi}_G^i \times \mathbf{D}\right) \tag{B.5}$$

$$\mathbf{N}_2 \cdot \mathbf{u}_L^i = \mathbf{N}_2 \cdot \left(\mathbf{u}_G^i + \mathbf{\Phi}_G^i \times \mathbf{D}\right) \tag{B.6}$$

where $\mathbf{N}_1$ and $\mathbf{N}_2$ are two unit vectors orthogonal to **D**.

In a geometric non-linear analysis the two constraints become:

$$\mathbf{n}_1 \cdot \mathbf{u}_L^i = \mathbf{n}_1 \cdot \left(\mathbf{u}_G^i + \mathbf{d} - \mathbf{D}\right) \tag{B.7}$$

$$\mathbf{n}_2 \cdot \mathbf{u}_L^i = \mathbf{n}_2 \cdot \left(\mathbf{u}_G^i + \mathbf{d} - \mathbf{D}\right) \tag{B.8}$$

where $\mathbf{n}_1$ and $\mathbf{n}_2$ are two unit vectors orthogonal to **d**.

Global-local modelling assumes that a one-to-one correspondence in the time domain of the driving and driven solutions exist. As was mentioned before, even in the case of a quasi-static analysis ABAQUS uses a pseudo-time scale ranging from zero to one, and an applied load will then be incrementally increased across this range. Hence by default, in a submodelling analysis the solution of the global model at a time of for example, 0.2, will be used to drive the local model also at the same time of 0.2. It is not necessary to maintain this one-to-one correspondence, as the time variable of the local model may be scaled relative to that of the global model. The details of the submodelling utility presented here relate mainly to the shell-to-solid submodelling capability, but the other possibilities available in ABAQUS for submodelling such as shell-to-shell and solid-to-solid are discussed in detail in the ABAQUS documentation [39].

Appendix C

Genetic algorithm code for buckling load maximization of a composite plate

The GA presented in Chapter 9 for the buckling load maximization of a composite plate was coded in MATLAB as shown in this Appendix. The main GA is named *Plate_buckle_abaqus_memory* and its proper functioning requires two separate functions named *Critical_buckling_load_memory* and *Constraints*. The former is responsible for providing the autonomous link between the GA and ABAQUS for the function evaluations whilst the latter handles the application of constraints. The GA code *Plate_buckle_abaqus_memory* has a number coding system shown in red which refers back to appropriate sections of Chapter 9 where the code is explained. In all of the code in this Appendix comments are shown in green text, whilst the actual program appears in black.

Plate_buckle_abaqus_memory

```
%This program uses a genetic algorithm to find the best stacking
sequence for a plate with a given number of plies so as to maximize
its buckling load
%The FEA package ABAQUS is used to evaluate the performance of the
laminates, and geometry and loading are defined in the appropriate
ABAQUS input file.

%Clear the MATLAB screen before starting the program
Clc

%Clear all variables before starting the program
clear

%Set some of the composite parameters required (1)
N=16 %Set the total number of plies in the composite
ply_thickness=0.127; %Set the ply thickness
integration_points=3; %Set the number of integration points
material='graphite-epoxy'; %Set the material name in ABAQUS

%Define the required genetic algorithm parameters (2)
NIND=40 %Set the population size
MAXGEN=60 %Set the maximum number of generations
GGAP=0.95 %Set the generation gap
P_CROSS=0.7 %Set the probability of crossover
%Initialize the Chrom matrix and the memory files
```

```
Chrom=[];
memory=[];
gen=0

%Create a matrix size NINDxN/2 of randomly oriented plies, with the 1
to 4 notation (3)
Chrom=randint(NIND,N/2,[1,4])

%Evaluate the buckling load of each individual in ABAQUS by calling
up the "critical_buckling_load_abaqus" function (4)
lamda_crit=critical_buckling_load_memory(Chrom,        ply_thickness,
integration_points, material, memory, gen, GGAP);

%Apply any constraints required by calling up the "constraints"
function (5)
lamda_crit=constraints(lamda_crit, Chrom, NIND, N);

%Start the generational loop (6)
gen=1

%Create the three dimensional memory matrix (7)
for i=1:NIND;
    for j=1:N/2;
        memory(i,j,gen)=Chrom(i,j);
    end
        memory(i,N/2+1,gen)=[lamda_crit(i,1)];
end;

%Start the optimization loop
while gen < MAXGEN,

     %Chrom;

     %Assign fitness values to the entire population (8)
     FitnV=ranking(lamda_crit);

     %Select individuals for breeding (9)
     SelCh=select('sus', Chrom, FitnV, GGAP);

     %Recombine individuals (crossover) (10)
     SelCh=recombin('xovdp', SelCh,P_CROSS);

     %Apply mutation (11)
     %Create a field descriptor variable of horizontal length N/2,
     and      prescrbing bounds of 0 and 4 for the random mutation
     numbers.
     %A number just greater than 0 is used to avoid exactly 0 to be
     generated in the chromosome string
         FieldDR=[rep([0.00000001;4],[1,N/2])];
         %Apply the mutation. Note numbers will now be in decimal
         SelCh=mutbga(SelCh, FieldDR);
         %Round up to the nearest integer value
         SelCh=ceil(SelCh);

     %Evaluate the offspring (12)
     lamda_crit_select=critical_buckling_load_memory(SelCh,
     ply_thickness, integration_points, material, memory, gen, GGAP);
```

```
    %Apply any constraints required by calling up the constraint
    function (13)
    lamda_crit_select=constraints(lamda_crit_select, SelCh,
    NIND*GGAP, N);

    %Reinsert offspring into population (14)
    [Chrom lamda_crit]=reins(Chrom, SelCh, 1,1, lamda_crit,
    lamda_crit_select);

     Chrom

%Apply a condition that if 5 successive individuals are the same then
the algorithm stops since the optimum has been considered found (15)
for k=1:NIND-4; %loop over all the individuals
optimum=Chrom(k,:); %store the first string as the possible optimum
%Check if 4 succesive designs have the same string
if Chrom(k+1,:)==optimum & Chrom(k+2,:)==optimum &
Chrom(k+3,:)==optimum & Chrom(k+4,:)==optimum;

%If they have the same string then end the algorithm
        gen=MAXGEN-1;
        end
    end

%Increment counter (16)
    gen=gen+1

%Update the three dimensional memory matrix (17)
for i=1:NIND;
    for j=1:N/2;
        memory(i,j,gen)=Chrom(i,j);
    end
        memory(i,N/2+1,gen)=[lamda_crit(i,1)];
end


end

%Change "back" lamda_crit since it was changed to turn the problem
from a maximization to a minimization
lamda_crit=2000-lamda_crit;

Chrom;
lamda_crit
```

Critical_buckling_load_memory

```
%This function reads in a population Chrom.  It is coded using ply-
orientation-identity variables so that 1 corresponds to a 0 degree
ply, 2 to 45 degrees, 3 to -45, and 4 to 90.
%Chrom has half the stacking sequence since the laminates are
symmetric.  The leftmost bit in the chromosome string is the ply
closest to the laminate plane of symmetry.
%The function first decodes each individuals string to contain the
stacking sequence, bottom layer to top layer, with actual degree
coding.
%For each individual the section relating to the layup is written in
ABAQUS.
%For each individual an ABAQUS eigenvalue analysis is used to find
the critical buckling load.
%The critical buckling load for each individual is stored into the
column vector lamda_crit and fed back to the GA.

function             lamda_crit=critical_buckling_load_memory(Chrom,
ply_thickness, integration_points, material, memory, gen, GGAP)

%Define the number of individuals NIND and number of layers N
[NIND,half_N] = size(Chrom);
N=half_N*2;

%Create another matrix of the same population but with the actual ply
orientations
%This will be used to "feed" ABAQUS
for m=1:NIND; %loop over the number of individuals
    for k=1:N/2; %loop over the chromosome string
        if Chrom(m,k)==1;
           layups(m,N/2-k+1)=0;
           layups(m,N/2+k)=0;
        end;
        if Chrom(m,k)==2;
           layups(m,N/2-k+1)=45;
           layups(m,N/2+k)=45;
        end;
        if Chrom(m,k)==3;
           layups(m,N/2-k+1)=-45;
           layups(m,N/2+k)=-45;
        end;
        if Chrom(m,k)==4;
           layups(m,N/2-k+1)=90;
           layups(m,N/2+k)=90;
        end
    end
end

%Evaluate the initial population
for m=1:NIND; %loop over the number of individuals
    flag=0;

%Check previous individuals in the same generation
    for p=1:m-1;
        if layups(m,:)==layups(p,:);
            lamda_crit(m,1)=lamda_crit(p,1);
            flag=1;
            disp 'LAYUP FOR INDIVIDUAL ALREADY EVALUATED'
```

```
            disp 'ABAQUS ANALYSES WILL NOT BE COMPUTED FOR THIS
            INDIVIDUAL'
            break %out of p loop
        end %end the if statement
    end %end the p loop
end %end the if m~=0 loop

%Check individuals in all previous populations
if gen~=0 & flag==0
    for layer=1:gen;
    for l=1:NIND/GGAP;
        if Chrom(m,:)== memory(l,1:N/2,layer);
            lamda_crit(m,1)=memory(l,N/2+1,layer);
            lamda_crit(m,1)=2000-lamda_crit(m,1);
            flag=1;
            disp 'LAYUP FOR INDIVIDUAL ALREADY EVALUATED'
            disp 'ABAQUS ANALYSES WILL NOT BE COMPUTED FOR THIS
            INDIVIDUAL'
            break %out of i loop
        end %end the if statement

    end %end the i loop
    if flag==1;
        break
    end %end for flag==1 loop
    end %end the layer loop
end %end the ~=0 loop

    if flag==0  %then run the whole code to evaluate the buckling
load

    fid=fopen('layup.jnp','w'); %open the file where the lay-up data
     required by ABAQUS will be stored

     for k=1:N; %loop across the whole chormosome string to write
     into "layup.jnp" which will be used by ABAQUS

     %Write the ply thickness, number of integration points, material
     name, and lay-up of each layer to the "layup.jnp" file
    fprintf(fid,'%5.5f,    %2d,    %18s,    %3d\r\n',    ply_thickness,
     integration_points, material, layups(m,k) );
    end

    %Close fid
    fclose(fid);

    %Run the ABAQUS job which reads the loads from the created files
    !C:\ABAQUS\6.6-1\exec\abq661.exe job=plate_buckle  interactive

    %Isolate the line with the eigenvalue in the ABAQUS dat file
    using the "grep2 and "tail" commands
    !grep "    1     " plate_buckle.dat > eigenvalue_pre.jnp
    !tail -1 eigenvalue_pre.jnp > eigenvalue.jnp

    %Load in the line into matlab
    eigenvalue=load('eigenvalue.jnp');

    %Isolate and store the eigenvalue
    eigenvalue=eigenvalue(2);
```

```
    %Store the eigenvalue for each individual in column vector
    "lamda_crit"
    lamda_crit(m,1)=eigenvalue;

end %end the flag =0 loop
end

%We seek to maximize the lowest buckling load.  i.e. we seek to
maximize lamda_crit
%Turn the problem into a minimization problem by having
lamda_crit=2000-lamda_crit;
```

Constraints

```
%This function deals with the various constraints to be applied in the problem of finding the optimal stacking sequence for maximum buckling load.
%The function works in terms of binary variables which take on values of 1 if a particular orientation is present and 0 otherwise.
%Designs which do not satisfy the constraints are penalized in terms of a penalty on the buckling load
%The first constraint penalizes designs which correspond to non-blalanced laminates
%The second constraint penalized designs which correspond to laminates wtih more than three contiguous plies in the same direction. This can be introduced so as to prevent matrix cracking problems

function lamda_crit=constraints(lamda_crit, Chrom, NIND, N)

%Momentarily turn the problem back into a maximization for the application of the penalties
lamda_crit=2000-lamda_crit;

%Set the penalty parameter to be used
penalty=0.8;

%Define variables for 0, 45, -45, 90 which are 1 if the corresponding orientation "exists" and 0 otherwise
for m=1:NIND ; %loop over the number of individuals in the population
    for k=1:N/2 ; % loop going across each string
        if Chrom(m,k)==1;
            o_k(m,k)=1;
        else
            o_k(m,k)=0;
        end
        if Chrom(m,k)==2;
            f_p(m,k)=1;
        else
            f_p(m,k)=0;
        end
        if Chrom(m,k)==3;
            f_m(m,k)=1;
        else
            f_m(m,k)=0;
        end
        if Chrom(m,k)==4;
            n_k(m,k)=1;
        else
            n_k(m,k)=0;
        end
    end
end

%The following constraint penalizes those designs which are not balanced
%Check which laminates are balanced
for m=1:NIND; %loop over the number of individuals
        balance(m,1)=0;
        balance_increment(m,1)=sum(f_p(m,:))-sum(f_m(m,:));
        balance(m,1)=balance(m,1)+balance_increment(m,1);
end
```

```
%Penalize those designs which are not balanced
for m=1:NIND; %loop over the number of individuals
    if balance(m,1)~=0;
    lamda_crit(m,1)=(1-penalty)*lamda_crit(m,1);
    end
end

%The following constraint penalizes those designs which have more
than 3 contiguous plies.  This section is omitted when the contiguous
ply constraint is not activated
for m=1:NIND %loop over each individual
      for k=3:N/2-3 %loop across each individual's string, starting
      from the 3rd ply from the symmetry plane onwards
      %Penalize those designs  which have more than 3 plies of the
      same orientation one next to the other
    if o_k(m,k)==1 & o_k(m,k+1)==1 & o_k(m,k+2)==1 & o_k(m,k+3)==1
    lamda_crit(m,1)=(1-penalty)*lamda_crit(m,1);
    end
    if f_p(m,k)==1 & f_p(m,k+1)==1 & f_p(m,k+2)==1 & f_p(m,k+3)==1
    lamda_crit(m,1)=(1-penalty)*lamda_crit(m,1);
    end
    if f_m(m,k)==1 & f_m(m,k+1)==1 & f_m(m,k+2)==1 & f_m(m,k+3)==1
    lamda_crit(m,1)=(1-penalty)*lamda_crit(m,1);
    end
    if n_k(m,k)==1 & n_k(m,k+1)==1 & n_k(m,k+2)==1 & n_k(m,k+3)==1
    lamda_crit(m,1)=(1-penalty)*lamda_crit(m,1);
    end
    end

%Penalize designs where the two plies adjacent to the symmetry plane
have the same orientation.  This section is also omitted in the
absence of the contiguous ply constraint.
    if o_k(m,1)==1 & o_k(m,2)==1;
    lamda_crit(m,1)=(1-penalty)*lamda_crit(m,1);
    end
    if f_p(m,1)==1 & f_p(m,2)==1;
    lamda_crit(m,1)=(1-penalty)*lamda_crit(m,1);
    end
    if f_m(m,1)==1 & f_m(m,2)==1;
    lamda_crit(m,1)=(1-penalty)*lamda_crit(m,1);
    end
    if n_k(m,1)==1 & n_k(m,2)==1;
    lamda_crit(m,1)=(1-penalty)*lamda_crit(m,1);
    end
    end

%We seek to maximize the lowest buclking load.  i.e. we seek to
maximize lamda_crit
%Turn the problem into a minimization problem by having
lamda_crit=2000-lamda_crit
```

Appendix D

Genetic algorithm code for lay-up optimization of composite I-stiffened panel

This Appendix shows the MATLAB code that was developed for the lay-up optimization of the I-stiffened panel as discussed in Chapter 10. Two optimizations are discussed in Chapter 10, one for the flange lay-up of the panel and once for the skin lay-up. The code in this Appendix relates to the skin lay-up optimization, but only slight modifications were made for the flange lay-up optimization, and such modifications are explained in Chapter 10. The main GA is programmed in a MATLAB script called *GA*. This links to the ABAQUS FE models responsible for the function evaluations via the developed MATLAB function *Abaqus_analyses*. The latter function is also responsible for handling the various constraints in the optimization, whilst a third function *Convert* decodes the chromosome strings into the actual ply orientations that they represent. A number coding system in the *GA* script and a letter coding system in the *Abaqus_analyses* function is shown in red so as to cross reference with the explanations of chapter 10.

GA

```
%This is a genetic algorithm to minimize damage in an I-stiffened panel
%THIS CODE REQUIRES the "convert " and "abaqus_analyses" user created MATLAB functions

%Clear all variables before starting the program and the screen
clear;
clc

%Delete the file where data will be written and any ABAQUS lock files
delete ('non_linear_data.jnp');
delete *.lck
delete *.jnp

%Tell the user to set the required parameters
disp 'MAKE SURE GENETIC PARAMETERS ARE SET in GA.m!', disp ' '
disp 'MAKE SURE PARAMETERS REQUIRED BY ABAQUS ARE SET IN ABAQUS_analyses.m!', disp ' '
```

```
%Set the number of plies in the skin which are being optimised for.
type all the plies even if symmetric
plies=8

%Define the required genetic algorithm parameters (1)
NIND=40 ;%Set the population size
MAXGEN=40 ; %Set the maximum number of generations
GGAP=0.95 ;%Set the generation gap
P_CROSS=0.7 ;%Set the probability of crossover
GENERATION=0;

%Display the genetic parameters to the screen
disp 'THE NUMBER OF INDIVIDUALS IN THE GENETIC POPULATION IS:', disp
(NIND)
disp 'THE MAXIMUM NUMBER OF GENERATIONS IS:', disp (MAXGEN)
disp 'THE GENERATION GAP IS:', disp (GGAP)
disp 'THE PROBABILITY OF CROSSOVER IS:', disp(P_CROSS)

%Ask whether it is a restart analysis and write data as required
restart=input('PLEASE ENTER IF THIS IS A RESTART, IF YES TYPE "1", IF
NO THEN ANYTHING ELSE')

if restart~=1;
disp 'THE GA IS STARTING FROM NEW'

%Initialize the Chrom matrix and memory matrix, as well as the
function evaluation counter
Chrom=[];
mem=[];
function_evaluation_counter=0;
dlmwrite('function_evaluation_counter.txt',function_evaluation_counte
r,' ')

%Tell the user the base population will now be calculated
disp 'THE BASE POPULATION WILL NOW BE COMPUTED AND EVALUATED...',
disp ' '
%Create a matrix size NINDxplies of randomly oriented plies, with the
1 to 4 notation (2)
Chrom=randint(NIND,plies,[1,4])

%Set a "tag variable" which is equal to 0 until the optimum design is
found, then becomes 1 when it has been found
tag=0;

%Convert the chromosome string containing the integer ply
represenation to actual ply orientations by calling the "convert"
user created function (3)
Chrom_actual=convert(Chrom);


%Call the "ABAQUS_analyses" user created function to evaluate the
total damage for each member of the population, creating an array
with the objective function of each individual (4)
damage=ABAQUS_analyses(Chrom_actual,tag,mem,GENERATION,GGAP);

%Tell the user the base population has been computed
disp 'THE BASE POPULATION HAS BEEN EVALUATED', disp ' '

%Start the generational loop and tell the user (5)
GENERATION=1;
```

```
%MEMORY - Create the memory matrix for the initial population (6)
for i=1:NIND;
        for j=1:plies;
        mem(i,j,GENERATION)=Chrom_actual(i,j);
        end
mem(i,plies+1,GENERATION)=[damage(i,1)];
end

end %End the case of a restart

%Set a "tag variable" which is equal to 0 until the optimum design is
found, then becomes 1 when it has been found
tag=0;

%If the analysis is not a restart write the generation number,
Chromosome, and damage to appropriate files (7)
        if restart~=1
        %Write the current generation to 'backup_Generation.txt'
        dlmwrite('backup_Generation.txt',GENERATION,' ');
        %Write the current population to 'backup_Chrom.txt'
        dlmwrite('backup_Chrom.txt',Chrom,' ');
        %Write the current damage for each individual to
        'backup_Damage.txt'
        dlmwrite('backup_Damage.txt',damage,' ');
        %Write the memory matrix in 'memory.txt'
        filename=sprintf('memory%3d.txt',GENERATION);    %create a
        filename that depends on the generation number
        dlmwrite(filename,mem(:,:,GENERATION),' ');
        end

if restart==1
disp 'THE GA WILL CONTINUE FROM SAVED BACKUP RESULTS'
end % end the not restart case if

GENERATION=dlmread('backup_Generation.txt',' ');
disp 'GENERATIONAL LOOP STARTING...'
while GENERATION < MAXGEN,

% In the case the program has quit prematurely, load the current
generation number, opulation string, and damage variable
        GENERATION=dlmread('backup_Generation.txt',' ')
        Chrom=dlmread('backup_Chrom.txt',' ')
        damage=dlmread('backup_Damage.txt',' ')
        for k=1:GENERATION;
        filename=sprintf('memory%3d.txt',k);
        mem(:,:,k)=dlmread(filename,' ');
        end

%Tell the user which generation is to be evaluated
disp 'GENERATION TO BE COMPUTED AND EVALUATED:', disp (GENERATION)

%Show Chrom
Chrom

%Assign fitness values to the entire population (8)
FitnV=ranking(damage);

%Select individuals for breeding (9)
SelCh=select('sus', Chrom, FitnV, GGAP);
```

```
%Recombine individuals (crossover) (10)
SelCh=recombin('xovdp', SelCh,P_CROSS);
%Apply mutation (11)
%Create a field descriptor variable of horizontal length
"flanges", and prescribing bounds of 0 and 3 for the random mutation
numbers.
%A number just greater than 0 is used to avoid exactly 0 to be
generated in the chromosome string
FieldDR=[rep([0.00000001;4],[1,plies])];
%Apply the mutation.  Note numbers will now be in decimal
SelCh=mutbga(SelCh, FieldDR);
%Round up to the nearest integer value
SelCh=ceil(SelCh)

%Convert the selected individuals to actual orientations by again
calling the appropriate user created function
SelCh_actual=convert(SelCh);

%Calculate the objective function for the selected individuals by
again calling the appropriate user created function (12)
damage_select=ABAQUS_analyses(SelCh_actual,tag,mem,GENERATION,GGAP);

%Reinsert offspring into population (13)
[Chrom damage]=reins(Chrom, SelCh, 1,1, damage, damage_select);

%Apply a condition that if 5 successive individuals are the same
then the algorithm stops since the optimum has been considered found
(14)
for k=1:NIND-4; %loop over all the individuals
optimum=Chrom(k,:); %store the first string as the possible optimum
%Check if 5 successive designs have the same string
if       Chrom(k+1,:)==optimum       &       Chrom(k+2,:)==optimum       &
Chrom(k+3,:)==optimum & Chrom(k+4,:)==optimum
%if they have the same string then end the algorithm
GENERATION=MAXGEN-1;
end
end

%Increment counter
GENERATION=GENERATION+1

%MEMORY - Create the memory matrix for the current population
%convert to current population to real orientations

Chrom_actual=convert(Chrom);
for i=1:NIND;
        for j=1:plies;
        mem(i,j,GENERATION)=Chrom_actual(i,j);
        end
mem(i,plies+1,GENERATION)=[damage(i,1)];
end

%Save the generation number, current population string, and damage
variables in case a restart is required
%Write the current generation to 'backup_Generation.jnp'
dlmwrite('backup_Generation.txt',GENERATION,' ')
%Write the current population to 'backup_Chrom.jnp'
dlmwrite('backup_Chrom.txt',Chrom,' ')
%Write the current damage for each individual to 'backup_Damage.jnp'
dlmwrite('backup_Damage.txt',damage,' ')
%Write the memory matrix in 'memory.txt'
```

```
filename=sprintf('memory%3d.txt',GENERATION); %create a filename that
depends on the generation number
dlmwrite(filename,mem(:,:,GENERATION),' ');

end

%Tell the user the optimum has been found and change the "tag"
variable to 1
disp 'THE OPTIMUM DESIGN HAS BEEN FOUND...RE-RUNNING OPTIMUM DESIGN',
disp ' '
tag=1;

%Convert the optimum design to its real lay-up representation
optimum_actual=convert(optimum);

%Rerun the ABAQUS analyses for the optimum design after initializing
the damage_opt variable where the least damage will be stored
damage_opt=[]
damage_opt=ABAQUS_analyses(optimum_actual,tag,mem,GENERATION,GGAP);

%Tell the user what the optimum lay-up is and its total damage
optimum_actual=optimum_actual.' ; %transpose the lay-up to a column
disp 'THE OPTIMUM DESIGN HAS THE FOLLOWING FLANGE3_GLOBAL LAYUP:',
disp(optimum_actual)
disp 'THE OPTIMUM DESIGN HAS THE FOLLOWING TOTAL DAMAGE :', disp
(damage_opt)
disp 'DATA FOR THE OPTIMUM DESIGN HAS BEEN APPENDED TO
non_linear_data.jnp AND THE LOAD-DISPLACEMENT CURVE IS ALSO SHOWN',
disp ' '

%close the graphics plot
hold off
```

Abaqus_analyses

```
%This is a function to be used in the genetic algorithm to optimise
the I-stiffened panel model to minimize local failure at the skin-
stiffener interface
%The function takes in a matrix with the lay-up and runs this through
the various ABAQUS analyses
%Buckle, non-linear, and local quasi-static analyses are run
%A load displacement curve is produced for each design
%Details of each design are printed to the non_linear_data.jnp file
%The function outputs an array with the total damage in each member
of the population

function damage=ABAQUS_analyses(Chrom_actual,tag,mem,GENERATION,GGAP)

%Set the ply thickness, number of integration points per ply, and the
name in ABAQUS of the materials as well as the minimum buckling load
and pre-buckling stiffness required (A)
ply_thickness=0.125 ;
integration_points_local=1 ;
integration_points_global=1 ;
material_flange='"T300/914C - compressive"' ;
material_skin='"T300/914C - averaged"' ;
material_web='"T300/914C - compressive"' ;
material_cap='"T300/914C - compressive"' ;
minimum_buckling_load=112.68 %kN minimum buckling load
minimum_stiffness=171.3 %kN/mm minimum pre-buckling stiffness

%Input the lay-ups that do not change in the analysis, ie the cap and
web and flanges (B)

%Input the local flange lay-ups
flange1_local=[0;0];
flange2_local=[0;0];
flange3_local=[45;-45];
flange4_local=[-45;45];

%Using the local flange definitions, create corresponding flange
definitions for the global model
flange1_global=[flange1_local;flange4_local];
flange2_global=[flange1_local;flange3_local;flange4_local];
flange3_global=[flange1_local;flange2_local;flange3_local;flange4_loc
al];

%Using the local flange definitions, create the web definitions
web_bottom=[flipud(flange4_local);
0;flipud(flange3_local);flipud(flange2_local);45;-
45;flipud(flange1_local)];
web_top=[flange1_local;-
45;45;flange2_local;flange3_local;0;flange4_local];

%Using the local flange definitions, create the cap definitions
cap_core=[90;0;0;0;90;90;0;0;0;0;90;90;0;0] ; %half of the cap core
since it is symmetric, specified from bottom up
cap_bottom=[web_bottom;cap_core];
cap_top=[flipud(cap_core);web_top];
%Read the number of individuals
[NIND,columns]=size(Chrom_actual) ;
```

```
for n=1:NIND; %loop over the number of individuals
    flag=0; %flag for memory

%MEMORY - CHECK PREVIOULSY EVALUATED INDIVIDUALS IN THE CURRENT
POPULATION
if n~=1 & tag==0 %omit the first individual from the memory search
and also dont search if re-running the optimum (tag==1 case)
      for p=1:n-1;
      if Chrom_actual(n,:)== Chrom_actual(p,:);
      damage(n,1)=damage(p,1);
      flag=1;
      disp 'THIS INDIVIDUAL HAS BEEN PREVIOUSLY EVALUATED -
      PREVIOUS OBJECTIVE FUNCTION WILL BE USED'
      disp 'THE DAMAGE OF EACH INDIVIDUAL SO FAR IS:', disp (damage)
      break %break out of the p loop
      end %end the if statement
   end %end the p loop
end %end the if m~=0 loop


%MEMORY - CHECK PREVIOUSLY EVALUATED INDIVIDUALS IN PREVIOUS
GENERATIONS
if GENERATION~=0 & flag==0 & tag==0;%only run this check if no
individuals in current population matched and if not evaluation base
population
      for layer=1:GENERATION; %loop over the previously evaluated
      generations
        for i=1:NIND/GGAP; %recover the whole size of the population
        rather than just the number of selected individuals
            if Chrom_actual(n,:)==mem(i,1:columns,layer);
            damage(n,1)=mem(i,columns+1,layer);
            flag=1;
            disp 'THIS INDIVIDUAL HAS BEEN PREVIOUSLY EVALUATED -
            PREVIOUS OBJECTIVE FUNCTION WILL BE USED'
%Display the array of damage values to the user
disp 'THE DAMAGE OF EACH INDIVIDUAL SO FAR IS:', disp (damage)
        break %out of the i loop
            end % end the if statement
        end %end the i loop
        if flag==1;
      break %break out of the layer loop if match found
        end %end for flag==1 if statement
      end %end the layer loop
end %end the GENERATION~=0 & flag==0 loop

%Evaluate the individual if memory search found no matches
if flag==0 %then evaluate the individual
%Tell the user which individual is being evaluated
if tag==0
disp 'INDIVIDUAL TO BE EVALUATED:', disp(n)
end
if tag==1
disp 'OPTIMUM INDIVIDUAL TO BE EVALUATED'
end

%create the skin lay-up (C)
skin_bottom=Chrom_actual(n,:).'
skin_top=flipud(skin_bottom);
```

```
%%%%%%%%%%%%%%%%%%%%%%%%%%%%%%%%%%%%%%%%%%%%%
%%%%%CREATE THE LOCAL FLANGE JNP FILES%%%%%%% (D)
%%%%%%%%%%%%%%%%%%%%%%%%%%%%%%%%%%%%%%%%%%%%%

%%% FLANGE1_LOCAL JNP FILE CREATION %%%
%Read the number of plies in flange1 to the variable m
m=size(flange1_local);
m=m(1,1);
%Create the jnp file which contains the data ABAQUS needs for flange1
fid=fopen('flange1_local.jnp','w'); %open the file where the lay-up
data required by ABAQUS will be stored
      for i=1:m;
      fprintf(fid,'%5.5f,   %2d,   %18s,   %3d\r\n',   ply_thickness,
      integration_points_local, material_flange, flange1_local(i,1));
      end;
fclose(fid);

%%% FLANGE2_LOCAL JNP FILE CREATION %%%
%Read the number of plies in flange2 to the variable m
m=size(flange2_local);
m=m(1,1);
%Create the jnp file which contains the data ABAQUS needs for flange2
fid=fopen('flange2_local.jnp','w'); %open the file where the lay-up
data required by ABAQUS will be stored
      for i=1:m;
      fprintf(fid,'%5.5f,   %2d,   %18s,   %3d\r\n',   ply_thickness,
      integration_points_local, material_flange, flange2_local(i,1));
      end;
fclose(fid);

%%% FLANGE3_LOCAL JNP FILE CREATION %%%
%Read the number of plies in flange1 to the variable m
m=size(flange3_local);
m=m(1,1);
%Create the jnp file which contains the data ABAQUS needs for flange3
      fid=fopen('flange3_local.jnp','w'); %open the file where the
      lay-up data required by ABAQUS will be stored
      for i=1:m;
      fprintf(fid,'%5.5f,   %2d,   %18s,   %3d\r\n',   ply_thickness,
      integration_points_local, material_flange, flange3_local(i,1));
      end;
fclose(fid);

%%% FLANGE4_LOCAL JNP FILE CREATION %%%
%Read the number of plies in flange1 to the variable m
m=size(flange4_local);
m=m(1,1);
%Create the jnp file which contains the data ABAQUS needs for flange4
      fid=fopen('flange4_local.jnp','w') ; %open the file where the
      lay-up data required by ABAQUS will be stored
      for i=1:m;
      fprintf(fid,'%5.5f,   %2d,   %18s,   %3d\r\n',   ply_thickness,
      integration_points_local, material_flange, flange4_local(i,1));
      end;
fclose(fid);
```

```
%%%%%%%%%%%%%%%%%%%%%%%%%%%%%%%%%%%%%%%%%%%%
%%%%%CREATE THE GLOBAL FLANGE JNP FILES%%%%% (D)
%%%%%%%%%%%%%%%%%%%%%%%%%%%%%%%%%%%%%%%%%%%%

%%% FLANGE1_GLOBAL JNP FILE CREATION %%%
%Read the number of plies in flange1 to the variable m
m=size(flange1_global);
m=m(1,1);
%Create the jnp file which contains the data ABAQUS needs for flange1
fid=fopen('flange1_global.jnp','w'); %open the file where the    lay-
up data required by ABAQUS will be stored
      for i=1:m;
      fprintf(fid,'%5.5f,   %2d,   %18s,   %3d\r\n',   ply_thickness,
      integration_points_global,                        material_flange,
      flange1_global(i,1));
      end;
fclose(fid);

%%% FLANGE2_GLOBAL JNP FILE CREATION %%%
%Read the number of plies in flange2 to the variable m
m=size(flange2_global);
m=m(1,1);
%Create the jnp file which contains the data ABAQUS needs for flange2
fid=fopen('flange2_global.jnp','w') ; %open the file where the lay-up
data required by ABAQUS will be stored
      for i=1:m;
      fprintf(fid,'%5.5f,   %2d,   %18s,   %3d\r\n',   ply_thickness,
      integration_points_global,                        material_flange,
      flange2_global(i,1));
      end;
fclose(fid);

%%% FLANGE3_GLOBAL JNP FILE CREATION %%%
%Read the number of plies in flange3 to the variable m
m=size(flange3_global);
m=m(1,1);
%Create the jnp file which contains the data ABAQUS needs for flange3
fid=fopen('flange3_global.jnp','w'); %open the file where the lay-up
data required by ABAQUS will be stored
      for i=1:m;
      fprintf(fid,'%5.5f,   %2d,   %18s,   %3d\r\n',   ply_thickness,
      integration_points_global,                        material_flange,
      flange3_global(i,1));
      end;
fclose(fid);


%%%%%%%%%%%%%%%%%%%%%%%%%%%%%%%%%%%%%%%%%%%%
%%%%%CREATE THE SKIN JNP FILES%%%%%%%%%%%%%% (D)
%%%%%%%%%%%%%%%%%%%%%%%%%%%%%%%%%%%%%%%%%%%%

%%% SKIN BOTTOM JNP FILE CREATION %%%
%Read the number of plies in skin_bottom to the variable m
m=size(skin_bottom);
m=m(1,1);
%Create  the  jnp  file  which  contains  the  data  ABAQUS  needs  for
skin_bottom
fid=fopen('skin_bottom.jnp','w');  %open  the  file  where  the  lay-up
data required by ABAQUS will be stored
      for i=1:m;
```

```
        fprintf(fid,'%5.5f,    %2d,    %18s,    %3d\r\n',    ply_thickness,
        integration_points_local, material_skin, skin_bottom(i,1));
        end;
fclose(fid);

%%% SKIN TOP JNP FILE CREATION %%%
%Read the number of plies in skin_top to the variable m
m=size(skin_top);
m=m(1,1);
%Create  the  jnp  file  which  contains  the  data  ABAQUS  needs  for
skin_top
fid=fopen('skin_top.jnp','w'); %open the file where the lay-up data
required by ABAQUS will be stored
        for i=1:m;
        fprintf(fid,'%5.5f,    %2d,    %18s,    %3d\r\n',    ply_thickness,
        integration_points_local, material_skin, skin_top(i,1));
        end;
fclose(fid);


%%%%%%%%%%%%%%%%%%%%%%%%%%%%%%%%%%%%%%%%%%%%
%%%%%CREATE THE WEB FLANGE JNP FILES%%%%%%%%
%%%%%%%%%%%%%%%%%%%%%%%%%%%%%%%%%%%%%%%%%%%%

%Create the top and bottom web lay-ups
web_bottom=[flipud(flange4_local);      0;      flipud(flange3_local);
flipud(flange2_local); 45;-45; flipud(flange1_local)];

web_top=[flange1_local;   -45;   45;   flange2_local;   flange3_local;
0;flange4_local];

%%% WEB BOTTOM JNP FILE CREATION %%%
%Read the number of plies in web_bottom to the variable m
m=size(web_bottom);
m=m(1,1);
%Create  the  jnp  file  which  contains  the  data  ABAQUS  needs  for
web_bottom
fid=fopen('web_bottom.jnp','w'); %open the file where the lay-up data
required by ABAQUS will be stored
        for i=1:m;
        fprintf(fid,'%5.5f,    %2d,    %18s,    %3d\r\n',    ply_thickness,
        integration_points_local, material_web, web_bottom(i,1));
        end;
fclose(fid);

%%% WEB TOP JNP FILE CREATION %%%
%Read the number of plies in web_top to the variable m
m=size(web_top);
m=m(1,1);
%Create the jnp file which contains the data ABAQUS needs for web_top
fid=fopen('web_top.jnp','w'); %open the file where the lay-up data
required by ABAQUS will be stored
        for i=1:m;
        fprintf(fid,'%5.5f,    %2d,    %18s,    %3d\r\n',    ply_thickness,
        integration_points_local, material_web, web_top(i,1));
        end;
fclose(fid);
```

```
%%%%%%%%%%%%%%%%%%%%%%%%%%%%%%%%%%%%%%%%%%%%
%%%%%CREATE THE CAP JNP FILES%%%%%%%%%%%%%%%
%%%%%%%%%%%%%%%%%%%%%%%%%%%%%%%%%%%%%%%%%%%%

%Create the top and bottom cap lay-ups
cap_bottom=[web_bottom;cap_core];
cap_top=[flipud(cap_core);web_top];

%%% CAP BOTTOM JNP FILE CREATION %%%
%Read the number of plies in cap_top to the variable m
m=size(cap_bottom);
m=m(1,1);
%Create the jnp file which contains the data ABAQUS needs for the cap
fid=fopen('cap_bottom.jnp','w'); %open the file where the lay-up data
required by ABAQUS will be stored
      for i=1:m;
      fprintf(fid,'%5.5f,   %2d,   %18s,   %3d\r\n',   ply_thickness,
      integration_points_local, material_cap, cap_bottom(i,1));
      end;
fclose(fid);

%%% CAP TOP JNP FILE CREATION %%%
%Read the number of plies in cap_top to the variable m
m=size(cap_top);
m=m(1,1);
%Create the jnp file which contains the data ABAQUS needs for the cap
fid=fopen('cap_top.jnp','w'); %open the file where the lay-up data
required by ABAQUS will be stored
      for i=1:m;
      fprintf(fid,'%5.5f,   %2d,   %18s,   %3d\r\n',   ply_thickness,
      integration_points_local, material_cap, cap_top(i,1));
      end;
fclose(fid);


%%%%%%%%%%%%%%%%%%%%%%%%%%%%%%%%%%%%%%%%%%%%%%%%%%%%%%%%%%%%%%%%%%%
%%%%%%%%%%%%%%%%%%%%%%
%%%%%The above creates jnp files ready to be read in directly by the
ABAQUS input files%%%%%
%%%%%%%%%%%%%%%%%%%%%%%%%%%%%%%%%%%%%%%%%%%%%%%%%%%%%%%%%%%%%%%%%%%
%%%%%%%%%%%%%%%%%%%%%%

%Tell the user the ABAQUS global buckling analysis is running
disp 'ABAQUS GLOBAL BUCKLING ANALYSIS CURRENTLY RUNNING...', disp ' '

%Run the linear buckling analyses to feed the nonlinear analysis with
the imperfections (E)
%Instruct the ABAQUS environment file to use 2 CPUs
!C:\ABAQUS\6.6-1\exec\abq661.exe          job=I_panel_optimise_buckle
ask_delete=off cpus=2 interactive
disp ' '
%Tell the user the ABAQUS buckling analysis has completed
if tag==0;
disp 'ABAQUS GLOBAL BUCKLING ANALYSIS COMPLETED', disp ' '
end
if tag==1;
disp 'ABAQUS GLOBAL BUCKLING ANALYSIS FOR OPTIMUM DESIGN COMPLETED',
disp ' '
end
```

```
%Read the first eigenvalue from the buckling analysis dat file
!grep "   1      " I_panel_optimise_buckle.dat > eigenvalue_pre.jnp
!tail -1 eigenvalue_pre.jnp > eigenvalue.jnp
%Load the eigenvalue from the eigenvalue.jnp file into a variable,
then isolate it
eigenvalue=load('eigenvalue.jnp');
eigenvalue=eigenvalue(2);



%Read the maximum_load from the buckling analysis dat file (linear
perturbation step)
!grep  "TOTAL                  "      I_panel_optimise_buckle.dat       >
buckling_load_pre_pre.jnp
!tail  -5 buckling_load_pre_pre.jnp  > buckling_load_pre.jnp
%Extract the required value from the just created jnp file
%Express the maximum load in kN, and then multiply this by the
eigenvalue to get the buckling load
fid=fopen('buckling_load_pre.jnp');
maximum_load=textread('buckling_load_pre.jnp','%*s%15.9f');
fclose(fid);
maximum_load=maximum_load(1)/1000;
buckling_load=maximum_load*eigenvalue;

%Tell the user the ABAQUS global non-linear analysis is running
disp 'ABAQUS GLOBAL NON-LINEAR ANALYSIS CURRENTLY RUNNING...', disp '
'

%Run the non-linear analysis to find the non-linear panel response
%Instruct the ABAQUS environment file to use 2 CPUs (F)
!C:\ABAQUS\6.6-1\exec\abq661.exe       job=I_panel_optimise_nonlinear
ask_delete=off cpus=2 interactive
disp ' '

%Tell the user the ABAQUS global non-linear analysis has completed
if tag==0;
disp 'ABAQUS GLOBAL NON-LINEAR ANALYSIS COMPLETED', disp ' '
end
if tag==1
disp 'ABAQUS GLOBAL NON-LINEAR ANALYSIS FOR OPTIMUM DESIGN
COMPLETED', disp ' '
end

%Read the appropriate lines with the reaction forces to
reaction_pre.jnp
!grep  "TOTAL                  "      I_panel_optimise_nonlinear.dat      >
reactions_pre.jnp

%Store the values of reactions_pre.jnp into a temporary array
reactions2
[reactions2] = textread('reactions_pre.jnp','%*s%15.9f');

%Get rid of the first two numbers which are not reactions but memory
data for the ABAQUS job
%Store the reactions into the array reactions
%Add a 0 reaction for the first increment
%Clear the temporary array reactions2
m=length(reactions2);
       for i=1:m-2;
       reactions(i,1)=reactions2(i+2,1);
       end
```

```
reactions=[0;reactions];
m=length(reactions);
      for i=1:m;
      reactions(i)=reactions(i)/1000;
      end
clear reactions2

%Read the appropriate lines with the applied end displacements to
reaction_pre.jnp
!grep "CURRENT VALUE OF MONITOR NODE"  I_panel_optimise_nonlinear.msg
> displacement_pre.jnp

%The lines contain a lot of unnecessary data, so store all this data,
isolate the displacements into array displacements, and clear all the
other data
%Add a 0 displacement for the first increment
[text1, text2, text3, text4, text5,  text6, text7, text8, text9,
displacements] = textread ('displacement_pre.jnp', '%8s%8s%8s%8s%8s
%6d%10s%3d%3s%10.10f');
clear text1
clear text2
clear text3
clear text4
clear text5
clear text6
clear text7
clear text8
clear text9
displacements=[0;displacements];

%%%%%%%%%%%%%%%%%%%%%%%%%%%%%%%%%%%%%%%%%%%%%%%%%%%%%%%%%%%%%%%%%%
%%%%%PLOT THE LOAD-DISPLACEMENT CURVE AND SAVE VARIOUS DATA TO
non_linear_data FILE  (G) %%%%%%%%%%%%%%%%%%%%%%%%%%%%%%%%%%%%%%%%%
%%%%%%%%%%%%%%%%%%%%%%%%%%%%%%%%%%%%%%%%%%%%%%%%%%%%%%%%%%%%%%%%%%

if tag==0
%Plot the design's load displacement curve
plot(displacements,reactions,'b-')
title('Load against End Displacement')
xlabel('End Displacement (mm)')
ylabel('Load (kN)')
hold on

%Plot the design's buckling point
%First find the buckling displacement which is the maximum
displacement multiplied by the eigenvalue
buckling_displacement = max(displacements)*eigenvalue;
plot(buckling_displacement,buckling_load,'rx')
hold on

%Store the lay-up, buckling load and displacements, and all the non-
liner displacements and reactions into a file "non_linear_data.jnp"
(H)
%Open the file where the data will be stored, and use the "a"
permission to append data and not replace it
fid=fopen('non_linear_data.jnp','a') ; %open the file where the lay-
up data required by ABAQUS will be stored

%Write a heading flange and the appropriate lay-up below it
fprintf(fid,'%22s\r\n','layup skin_bottom');
fprintf(fid,'%3u,%3u,%3u,%3u,%3u,%3u,%3u,%3u\r\n\r\n',skin_bottom)
```

```
%Write headings for the displacement at buckling and buckling load
fprintf(fid,'%26s%26s\r\n','buckling  displacement  (mm)','buckling
load (kN)');
fprintf(fid,'%13.2f
%13.4f\r\n',buckling_displacement, buckling_load);

%Write all the non-linear analysis displacements and reactions
m=length(displacements);
fprintf(fid,'%26s%26s\r\n','end  displacement  (mm)','applied  load
(kN)');
      for i=1:m;
      fprintf(fid,'%13.2f                        %13.4f\r\n\r\n',
      displacements(i), reactions(i));
      end;
fclose(fid);
end %close the if statement for the optimum case

%%%%%%%%%%%%%%%%%%%%%%%%%%%%%%%%%%%%%%%%%%%%%%%%%%%%%%%%%%%%%%
%%%%%PLOT  THE  LOAD-DISPLACEMENT  CURVE  AND  SAVE  VARIOUS  DATA  TO
non_linear_data FILE IN THE CASE OF THE BEST DESIGN%%%%%%%%%%%%%%%%
%%%%%%%%%%%%%%%%%%%%%%%%%%%%%%%%%%%%%%%%%%%%%%%%%%%%%%%%%%%%%%

if tag==1
%Plot the optimum design's load displacement curve
plot(displacements,reactions,'g:')
title('Load against End Displacement')
xlabel('End Displacement (mm)')
ylabel('Load (kN)')
hold on

%Plot the design's buckling point
%First  find  the  buckling  displacement  which  is  the  maximum
displacement multiplied by the eigenvalue
buckling_displacement = max(displacements)*eigenvalue;
plot(buckling_displacement,buckling_load,'mx')
hold on

%Store the lay-up, buckling load and displacements, and all the non-
liner displacements and reactions into a file "non_linear_data.jnp"
%Open  the  file  where  the  data  will  be  stored,  and  use  the  "a"
permission to append data and not replace it
fid=fopen('non_linear_data.jnp','a'); %open the file where the lay-up
data required by ABAQUS will be stored

%Write a heading to notify taht this is the best design
fprintf(fid,'%40s\r\n\r\n','BELOW IS THE BEST DESIGN');

%Write a heading flange and the appropriate lay-up below it
fprintf(fid,'%22s\r\n','layup skin_bottom');

fprintf(fid,'%3u,%3u,%3u,%3u,%3u,%3u,%3u,%3u\r\n\r\n',skin_bottom);

%Write headings for the displacement at buckling and buckling load
fprintf(fid,'%26s%26s\r\n','buckling  displacement  (mm)','buckling
load (kN)');
fprintf(fid,'%13.2f%13.4f\r\n',               buckling_displacement,
buckling_load);
```

```
%Write all the non-linear analysis displacements and reactions
m=length(displacements);
fprintf(fid,'%26s%26s\r\n','end  displacement  (mm)','applied  load
(kN)');
    for i=1:m;
    fprintf(fid,'%13.2f                   %13.4f\r\n\r\n',
    displacements(i), reactions(i));
    end;
fclose(fid);
end %close the if statement for the optimum case

clear reactions
clear displacements


%%%%%%%%%%%%%%%%%%%%%%%%%%%%%%%%%%%%%%%%%%%%%%%%%%%%%%%%%%%
%%%%%The  load-displacement  curve  has  now  been  plotted  and  data
written to the non_linear_data file %%%%%%%%%%%%%%%%%%%%%%%%%%%%%
%%%%%%%%%%%%%%%%%%%%%%%%%%%%%%%%%%%%%%%%%%%%%%%%%%%%%%%%%%%

%Tell the user the ABAQUS local analysis is running
disp 'ABAQUS LOCAL MODEL UPDATED', disp ' '
disp 'ABAQUS LOCAL ANALYSIS CURRENTLY RUNNING...', disp ' '
%Run the local analyses to model the debonding (I)
%Instruct the ABAQUS environment file what the global file to read
from is and also to use 2 CPUs
!C:\ABAQUS\6.6-1\exec\abq661.exe        job=I_panel_optimise_local
globalmodel=I_panel_optimise_nonlinear.fil   ask_delete=off   cpus=2
interactive
disp ' '
    if tag==0
    disp 'ABAQUS LOCAL ANALYSIS COMPLETED', disp ' '
    end
        if tag==1
        disp  'ABAQUS  LOCAL  ANALYSIS  FOR  OPTIMUM  DESIGN
        COMPLETED', disp ' '
        end

%%%%%%%%%%%%%%%%%%%%%%%%%%%%%%%%%%%%%%%%%%%%%%%%%%%%%%%%%%%
%%%%%READ THE DAMAGE IN THE COHESIVE ELEMENTS FROM THE ABAQUS OUTPUT
%%%%%%%%%%%%%%%%%%%%%%%%%%%%%%%%%%%%%%%%%%%%%%%%%%%%%%%%%%%

%Write the sum of the damage in each element to a file damage_pre.jnp
!grep "TOTAL        "  I_panel_optimise_local.dat  > damage_pre.jnp

%Read the last line which contains the damage at the last increment
to final_total_damage.jnp
!tail -1 damage_pre.jnp > final_total_damage.jnp

%Read   the   final   total   damage   value   into   a   variable
"final_total_damage",   ignoring   the   TOTAL   string   in   the
final_total_damage.jnp file
if tag==0
[final_total_damage] = textread('final_total_damage.jnp','%*s%8.5f');
%Tell the user the individual has been evaluated
disp 'INDIVIDUAL EVALUATED', disp ' '
%Store the damage for each individual in an array (J)
damage(n,1)=final_total_damage
```

```
%Display the buckling load and stiffness values for display purposes
buckling_load
stiffness=buckling_load/buckling_displacement

%Apply constraints (K)
%Apply constraint on buckling load
      if  buckling_load  <  minimum_buckling_load;  %penalize  if  the
      buckling load is less than the minimum specified
      damage(n,1)=damage(n,1)+100
      end


%Apply constraint on pre-buckling stiffness
      if  (buckling_load/buckling_displacement)  <  minimum_stiffness;
      %penalize  if  the  pre-buckling  stiffness  is  less  than  the
      minimum specified
      damage(n,1)=damage(n,1)+100
      end

%Display the array of damage values to the user
disp 'THE DAMAGE OF EACH INDIVIDUAL SO FAR IS:', disp (damage)

%Write the damage for the individual to non-linear.dat
fid=fopen('non_linear_data.jnp','a');
fprintf(fid,'%30s\r\n', 'total interface damage');
fprintf(fid,'%6.2f\r\n',final_total_damage);
%Print a line of % signs and empty lines to separate the data from
one design to the next
fprintf(fid,'%10s\r\n\r\n\r\n\r\n',
'%%%%%%%%%%%%%%%%%%%%%%%%%%%%%%%%%%%%%%%%%%%%%%%%%%%%%%%');
fclose(fid)
end

%Read  the  final  optimum  total  damage  value  into  a  variable
"final_total_damage",   ignoring   the   TOTAL   string   in   the
final_total_damage.jnp file
      if tag==1
      [final_total_damage]                                           =
      textread('final_total_damage.jnp','%*s%8.5f');
      %Tell the user the optimum individual has been evaluated
      disp 'OPTIMUM  DESIGN EVALUATED', disp ' '
      %Store the damage for the optimum individual as an array
      least_damage(n,1)=final_total_damage

%Display the buckling load and stiffness for display purposes
buckling_load
stiffness=buckling_load/buckling_displacement

%Apply constraints
%Apply constraint on buckling load
      if  buckling_load  <  minimum_buckling_load;  %penalize  if  the
      buckling load is less than the minimum specified
      least_damage(n,1)=least_damage(n,1)+100
      end
%Apply constraint on pre-buckling stiffness
      if  (buckling_load/buckling_displacement)  <  minimum_stiffness;
      %penalize  if  the  pre-buckling  stiffness  is  less  than  the
      minimum specified
      least_damage(n,1)=least_damage(n,1)+100
      end
```

```
%Write the damage for the optimal individual to non-linear.dat
fid=fopen('non_linear_data.jnp','a');
fprintf(fid,'%30s\r\n', 'total opt. interface damage');
fprintf(fid,'%6.2f\r\n',final_total_damage);
%Print a line of % signs and empty lines to separate the data from
one design to the next
fprintf(fid,'%10s\r\n\r\n\r\n\r\n',
'%%%%%%%%%%%%%%%%%%%%%%%%%%%%%%%%%%%%%%%%%%%%%%%%%%%%');
fclose(fid)
end


%Print the load-displacement curve to load_displacement_curve.jpeg
print -djpeg load_displacement_curve

%If a function evaluation has been calculated, print to file to
remember how many have been evaluated
function_evaluation_counter=dlmread('function_evaluation_counter.txt'
,' ');
function_evaluation_counter=function_evaluation_counter+1;
dlmwrite('function_evaluation_counter.txt',function_evaluation_counte
r,' ');

end %end the if flag==0 loop

%End the do loop as the whole generation has been computed
end

%%%%%%%%%%%%%%%%%%%%%%%%%%%%%%%%%%%%%%%%%%%%%%%%%%%%%%%%%%%%%%%%%%%%%
%%%%%%THE FUNCTION ENDS HAVING FOUND THE TOTAL DAMAGE FOR EACH MEMBER
OF THE POPULATION%%%%%%%%%%%%%%%%%%%%%%%%%%%%%%%%%%%%%%%%%%%%%%%%%%%%
%%%%%%%%%%%%%%%%%%%%%%%%%%%%%%%%%%%%%%%%%%%%%%%%%%%%%%%%%%%%%%%%%%%%%
```

Convert

```
%This function transforms the Chrom population matrix which uses ply
identity variables to a matrix of the same size with the actual ply
orientations
%Each row corresponds to an individual in the population, and the
rows to the relative ply direction in the various flanges

function Chrom_actual_orientations=convert (Chrom)

%Read in the size of Chrom.  The number of rows corresponds to the
number of individuals
[NIND,columns]=size(Chrom);

%Convert the ply identity variables to actual orientations
for k=1:NIND; %loop over the number of individuals
    for i=1:columns %loop over the number of columns
        if Chrom(k,i)==1;
        Chrom_actual_orientations(k,i)=0;
        end

        if Chrom(k,i)==2;
        Chrom_actual_orientations(k,i)=45;
        end

        if Chrom(k,i)==3;
        Chrom_actual_orientations(k,i)=-45;
        end

         if Chrom(k,i)==4;
        Chrom_actual_orientations(k,i)=90;
        end
    end
end

%%%%%%%%%%%%%%%%%%%%%%%%%%%%%%%%%%%%%%%%%%%%%%%%%%%%%%%%%%%%%%%%%%%%%%%%
%%%%%%The function writes back a matrix the same size as Chrom but
with the actual ply-orientations%%%%%%%%%%%%%%%%%%%%%%%%%%%%%%%%%%%%%%%%
%%%%%%%%%%%%%%%%%%%%%%%%%%%%%%%%%%%%%%%%%%%%%%%%%%%%%%%%%%%%%%%%%%%%%%%%
```

Appendix E

Publications

- Faggiani, A. and Falzon, B. G. Optimization Strategy for Minimizing Damage in Postbuckling Stiffened Panels. *AIAA Journal*, 45 (10): 2520-2528, 2007.

- Faggiani, A. and Falzon, B. G. Numerical Analysis of Stiffener Runout Sections. *Applied Composite Materials*, 14 (2): 145-158, 2007.

- Faggiani, A. and Falzon, B. G. "Optimizing Postbuckling Composite Panels for Damage Resistance". *Proceedings of 16th International Conference on Composite Materials*, Kyoto, Japan, 8-13 July 2007.

- Faggiani, A. and Falzon, B. G. An FE Based Optimization Procedure for Postbuckling Stiffened Panels. *Proceedings of 6th ASMO-UK/ISSMO International Conference on Engineering Design Optimization CD-ROM, Oxford*, UK, 3-4 July 2006.